Development and validation of tools for the structural design of
wind turbine blades

by

Louis-Charles FORCIER

THESIS PRESENTED TO ÉCOLE DE TECHNOLOGIE
SUPÉRIEURE
IN PARTIAL FULFILLMENT FOR THE DEGREE OF
DOCTOR OF PHILOSOPHY
Ph. D.

MONTREAL, MARCH 10, 2020

ÉCOLE DE TECHNOLOGIE SUPÉRIEURE
UNIVERSITÉ DU QUÉBEC

BOARD OF EXAMINERS

THIS THESIS HAS BEEN EVALUATED

BY THE FOLLOWING BOARD OF EXAMINERS:

M. Simon Joncas, Thesis Supervisor
Department of systems engineering, École de technologie supérieure

M. Souheil-Antoine Tahan, President of the Board of Examiners
Department of mechanical engineering, École de technologie supérieure

M. Henri Champliaud, Member of the jury
Department of mechanical engineering, École de technologie supérieure

M. Gabriel LaPlante, External Independent Examiner
Department of mechanical engineering, Université de Moncton

THIS THESIS WAS PRESENTED AND DEFENDED

IN THE PRESENCE OF A BOARD OF EXAMINERS AND THE PUBLIC

ON JANUARY 15, 2020

AT ÉCOLE DE TECHNOLOGIE SUPÉRIEURE

ACKNOWLEDGEMENTS

DÉVELOPPEMENT ET VALIDATION D'OUTILS POUR LA CONCEPTION STRUCTURALE DES PALES D'ÉOLIENNES

Louis-Charles FORCIER

RÉSUMÉ

La conception d'une pale d'éolienne est un processus itératif durant lequel on raffine une solution du concept préliminaire jusqu'au concept final. L'objectif de cette thèse est de développer et d'évaluer certains outils en lien avec les différentes étapes du processus de conception d'une pale d'éolienne.

Un premier aspect abordé est la question du transfert des chargements calculés sur un modèle aéroélastique d'une éolienne vers un modèle d'éléments finis à trois dimensions d'une pale. La principale difficulté étant liée au transfert des chargements d'une pale modélisée comme une poutre vers un modèle de pale modélisée en trois dimensions. Pour faire face à cette difficulté, un modèle cinématique d'une éolienne générique a été réalisé. Cela permet de développer une méthode d'application des charges gravitationnelles et inertielles dans le modèle d'éléments finis de la pale en imposant des forces volumiques par l'entremise d'accélérations et de rotations autour d'axes donnés. Les chargements aérodynamiques sont quant à eux appliqués à l'aide d'éléments de type RBE3. Le modèle cinématique a également permis d'obtenir des équations analytiques permettant d'évaluer l'effet des charges gravitationnelles et inertielles, en termes d'efforts internes dans la pale, à partir des paramètres d'opération de l'éolienne (dimensions, vitesses, accélérations) et des paramètres de masse de la pale.

Un deuxième aspect abordé dans cette thèse est le choix du modèle structural pour le dimensionnement et la validation des pales d'éolienne. Quatre modèles de niveau de complexité différents ont été utilisés pour modéliser les pales de l'éolienne de 10 kW du *Wind Energy Strategic Network* (WESNet). Du plus simple au plus raffiné, on retrouve : un modèle de poutre où les chargements ne sont repris que par deux bandes rectangulaires représentant les semelles de longeron ; un modèle de poutre reprenant les théories de la résistance des matériaux appliquées à une section à paroi mince hétérogène ; un modèle de poutre utilisant des éléments finis de section de poutre composite à paroi mince ; et finalement, un modèle d'éléments finis de coques de la pale entière. La comparaison des résultats de ces différents modèles avec les données expérimentales de l'éolienne du WESNet a permis de montrer que le premier modèle donne des résultats sécuritaires et assez précis en ce qui concerne l'évaluation des contraintes, des déformations et de la résistance de la pale pour être en mesure d'évaluer la faisabilité d'une géométrie de pale. Les deuxième et troisième modèles ont quant à eux montré un niveau de précision permettant de les utiliser en dimensionnement et validation préliminaire en ce qui concerne l'évaluation de la flèche, des contraintes, des déformations, de la résistance et des fréquences propres de la pale. Ces deux derniers modèles sont les outils idéaux à utiliser pour calculer les propriétés de section nécessaires pour le modèle aéroélastique de l'éolienne. Finalement,

le modèle d'éléments finis de coques est requis lors du dimensionnement et de la validation finale de la pale puisqu'il est le seul à représenter correctement la complexité du champ de contraintes dans les régions de la pale où la section change de forme rapidement.

Le troisième aspect traité dans cette thèse concerne le développement d'un code d'éléments finis pour l'analyse de section de poutres composites à paroi mince (troisième modèle d'analyse structurale présenté précédemment). Cette méthode est basée sur une implémentation de type paroi mince, utilisant des éléments finis de lignes à trois noeuds, de la méthode *Nonhomogeneous Anisotropic Beam Section Analysis*. L'implémentation proposée permet de mettre en place facilement un modèle d'analyse d'une section de poutre à paroi mince pour en déterminer la distribution des contraintes, des déformations, des efforts de plaque et du gauchissement de même que pour en déterminer les propriétés élastiques de section. La méthode proposée permet d'évaluer avec précision le comportement des poutres composites incluant les effets des couplages géométriques et matériaux (dont les stratifiés non symétriques et non balancés) de même que le comportement en cisaillement transverse.

Mots clés: pales d'éolienne, matériaux composites, conception structurale, éléments finis, poutres à paroi mince, chargements

DEVELOPMENT AND VALIDATION OF TOOLS FOR THE STRUCTURAL DESIGN OF WIND TURBINE BLADES

Louis-Charles FORCIER

ABSTRACT

The design of a wind turbine is an iterative process in which a solution is refined from the preliminary stage to the final concept. The objective of this thesis is to develop and evaluate certain tools used during the different steps of the wind turbine blade structural design process.

A first aspect that is treated in this thesis is the question of the transfer of loads obtained from an aeroelastic model of the wind turbine to a three-dimensional shell finite element model of the blade. The principal difficulty encountered results from the fact that the loads have to be transferred from a model where the blade is idealized as a beam to a three-dimensional model. To manage this difficulty, a kinematic model of a generic wind turbine was built. This model helped develop a method to apply gravitational and inertial loads to the three-dimensional finite element model of a blade by defining accelerations and rotations about given axes. Aerodynamic loads are applied using RBE3-type elements. The developed kinematic model also allows to obtain analytical equations to compute of gravitational and inertial loads when the wind turbine operating parameters (dimensions, velocities, accelerations) and blade mass parameters are known.

A second aspect dealt with in this thesis is the choice of a structural model for the wind turbine blades dimensioning and validation. Four models of different levels of complexity have been used to model the blades of the Wind Energy Strategic Network's (WESNet) 10 kW wind turbine. From the simplest to the most refined, these models are: a beam model where the loads are supported by a cross section idealized as two rectangular strips representing the spar caps; a beam model based on the strength of materials theory adapted for non-homogeneous thin-walled cross sections; a beam model based on thin-walled cross-sectional finite elements; and a shell finite element model of the whole blade. The comparison of the results from these models with different experimental data sets shows that the first model gives conservative results for stresses, strains and blade strength. These results have also enough precision to allow this model to be used for the feasibility evaluation of a blade geometry. The second and third models show a level of precision that allows their use for preliminary dimensioning and validation in regards to blade deflection, stresses, strains, strength and natural frequencies. These last two models are also the ideal tools for the computation of the blade cross-sectional properties needed for wind turbine aeroelastic models. Finally, the shell finite element model is required for the final blade dimensioning and validation because it is the only one that is able to compute correctly the complex stress field in the region of the blade where the cross-sectional shape change rapidly.

X

The third aspect that was addressed in this thesis is the development of a finite element code for the analysis of composite thin-walled beam cross sections. This is the third model presented earlier. This method is based on a thin-walled implementation of the Nonhomogeneous Anisotropic Beam Section Analysis method. This implementation uses 3-node line finite elements with nodes having translational and rotational degrees of freedom. This allows to easily set up a model of a thin-walled composite cross section for the analysis of stress, strain, shell load and warping distributions as well as for the computation of the cross-sectional stiffness properties. The proposed method allows to precisely evaluate the behaviour of composite beams including the effects of geometric (including unbalanced and nonsymmetrical layups) and material couplings as well as the transverse shear behaviour.

TABLE OF CONTENTS

XIV

LIST OF TABLES

LIST OF FIGURES

LIST OF SYMBOLS

a	Line element thickness along the t-direction
a, b	Coordinate system translations in the x- and y-directions
a_j	Thickness of the jth layer
$\mathbf{a}_{j/i}$	Acceleration vector of point j in coordinate system i
A	Cross-sectional area
A_i	Area of the ith cell of a multicell thin-walled cross section
$\mathbf{A}$	Matrix for the computation of cross-sectional properties
$\mathbf{A}_h$	Unit vector of the rotor rotational axis
$\mathbf{A}_n$	Unit vector of the nacelle rotational axis
b	Blade spar cap width; Plate width
b_r	Blade spar cap width normalized by chord length
$\mathbf{B}$	Matrix of the derivatives of the shape functions
c	Blade chord length; Cosine of θ, $\cos\theta$
c_i	Cosine of i, $\cos i$
$\mathbf{C}$	Matrix for the computation of cross-sectional properties
D_{ij}	Components of the plate bending stiffness matrix, i and j takes values 1, 2 and 6
$\mathbf{D}$	Matrix of imposed constraints on cross-sectional nodal warping displacements

e	Failure strain
E	Elastic modulus
E_1, E_2	Longitudinal and transverse elastic moduli
E_z	Elastic modulus in the x-direction
$\overline{EA}$	Beam cross-sectional axial stiffness
$\overline{EI}_x$, $\overline{EI}_y$	Beam cross-sectional bending stiffnesses
$\overline{EI}_1$, $\overline{EI}_2$	Beam cross-sectional bending stiffnesses about the principal axes of bending
$\mathbf{E}$	Matrix for the computation of cross-sectional properties
$\mathbf{f}$	Vector of applied forces per unit volume
F_{TW}	Tsai-Wu failure index
$\mathbf{F}$	Vector of applied forces; Nodal forces vector of a finite element model
$\mathbf{F}_s$	Beam cross-sectional compliance matrix
g	Gravitational acceleration
$\mathbf{g}$	Gravitational acceleration vector; Vector of cross-sectional warping displacement field
G	Shear modulus
G_{12}	In-plane shear modulus
G_{zx}, G_{yz}	Transverse shear moduli
$\overline{GA}_x$, $\overline{GA}_y$	Beam cross-sectional transverse shear stiffnesses

$\overline{GJ}$	Beam cross-sectional torsional stiffness
h	Blade spar cap thickness
h_r	Blade spar cap thickness normalized by chord length
i_x, i_y, i_{xy}	Cross-sectional mass moment of inertia per unit length
$\mathbf{i}$, $\mathbf{j}$, $\mathbf{k}$	Unit vectors in the x-, y- and z-directions
I, I_x, I_y	Cross-sectional inertia
I_0	Blade mass moment of inertia about its root
I_i, I_{ij}	Blade mass moment of inertia, i and j take values x, y or z
$\mathbf{I}_i$	Identity matrix of shape $i \times i$
J	Cross-sectional moment of polar inertia
$\mathbf{J}$	Jacobian matrix
k_x, k_y	Correction factors for transverse shear
$\mathbf{K}$	Stiffness matrix of a finite element model
$\mathbf{K}_s$	Beam cross-sectional stiffness matrix
L	Blade length; Finite element length
L_{nr}	Distance between rotor centre and nacelle yaw axis
$\mathbf{L}$	Matrix for the computation of cross-sectional properties
m	Mass
m'	Mass per unit length
$\mathbf{m}$	Vector of applied moments per unit length

M	Bending moment
M_m	Plate bending moment per unit length, m takes values r, s or rs
M_t	Torsional moment
M_x, M_y	Bending moments
M_1, M_2	Bending moments in the cross-sectional principal axes of bending
$\mathbf{M}$	Vector of blade bending and torsional moments; Mass matrix of a finite element model; Matrix for the computation of cross-sectional properties
$\mathbf{M}_s$	Beam cross-sectional mass matrix
n	Number of degrees of freedom
n_l	Number of layers in the composite layup
n_n	Number of nodes in the finite element
n_s	Number of integration points along the element length
n_t	Number of integration points per layer
N	Axial force; Force per unit length of a plate
N_i	ith shape function
N_m	Plate axial force per unit length, m takes values r, s or rs
N_{cr}	Critical buckling load per unit width of the plate
$\mathbf{N}$	Shape function matrix
$\mathbf{p}$	Vector of applied forces per unit length; Vector of stress components in the cross-sectional plane

$\mathbf{P}$	Matrix for the computation of cross-sectional external work
$\mathbf{P}_{i/j}$	Transformation matrix from coordinate system j to coordinate system i
q_i	Shear flow in the ith cell of a multicell thin-walled cross section
Q_n	Plate transverse shear force per unit length, n takes values rs or st
$\mathbf{Q}$	Material constitutive matrix
r, s, t	Coordinates in system rst
r_h	Hub radius
$\mathbf{r}$	Vector of displacements and rotations of the beam reference axis
$\mathbf{r}_{j/i}$	Position vector of point j in coordinate system i
$\mathbf{R}$	Reaction force vector;
	Matrix for the computation of cross-sectional properties
s	Sine of θ, $\sin\theta$
$\hat{s}$	Unit vector tangent to the axis of a line element
s_i	Sine of i, $\sin i$;
	s-coordinate of the ith node
$\mathbf{s}$	Vector of cross-sectional displacement field
S	Allowable stress
S_1^C	Longitudinal compression strength
S_1^T	Longitudinal tension strength
S_{12}	Shear strength
S_2^C	Transverse compression strength

S_2^T	Transverse tension strength
S	Matrix for the computation of cross-sectional strains
t	Ply thickness;
	Blade airfoil thickness;
	Wall thickness;
	Time
$\hat{t}$	Unit vector normal to the axis of a line element
t_r	Blade airfoil thickness normalized by chord length
T	Matrix for the computation of cross-sectional generalized strains
$\mathbf{T}_s$	Beam cross-sectional property transformation matrix in translation
$\mathbf{T}_\alpha$, $\mathbf{T}_\beta$	Transformation matrices for material constitutive law
$\mathbf{T}_\theta$	Beam cross-sectional property transformation matrix in rotation
u	Vector of nodal cross-sectional warping displacements
U	Nodal displacement vector of a finite element model
V_x, V_y	Shear forces
$\mathbf{v}_{j/i}$	Velocity vector of point j in coordinate system i
V	Vector of beam internal loads;
	Vector shear and axial forces
w_i	Weight of the ith integration point
W_e	External work
W_i	Internal work
x, y, z	Coordinates in system xyz

x_i, y_i	Coordinates of the ith node
x_c, y_c	Beam cross-sectional shear centre coordinates
x_e, y_e	Beam cross-sectional elastic centre coordinates
x_{cg}, y_{cg}	Coordinate of the cross-sectional centre of gravity
X_{cg}, Y_{cg}, Z_{cg}	Coordinates of the blade centre of gravity
z	Radial position along the blade length, distance from blade root
$\mathbf{Z}$	Matrix for the computation of cross-sectional internal loads
α	Orientation of the cross-sectional principal axes of bending
α_{ij}	Coupling coefficients between beam deformation modes
$\boldsymbol{\alpha}_{j/i}$	Angular acceleration vector of body j in coordinate system i
β	Rotor coning angle
γ	Rotor tilt angle
γ_{ij}	Shear strain, i and j take values 1, 2, 3, r, s, t, x, y or z, with $i \neq j$
γ_{zx}^0, γ_{yz}^0	Beam transverse shear deformations
δ	Operator indicating that the associated quantity is virtual
ϵ	Strain
ϵ_i	Normal strain, i takes values 1, 2, 3, r, s, t, x, y or z
ϵ_z^0	Beam reference axis deformation
$\boldsymbol{\epsilon}$	Strain vector
θ	Blade pitch angle; Coordinate system rotation

$\dot{\theta}$	Blade pitch velocity
$\ddot{\theta}$	Blade pitch acceleration
θ_1	Orientation of the cross-sectional principal axes of bending
θ_T	Blade twist angle
$\kappa_x,\ \kappa_y,\ \kappa_z$	Beam axis curvature
$\boldsymbol{\kappa}$	Vector of beam generalized strains
Λ	Nacelle yaw velocity
$\dot{\Lambda}$	Nacelle yaw acceleration
$\boldsymbol{\lambda}$	Vector of Lagrange multipliers for imposed constraints on cross-sectional nodal warping displacements
ν_{12}	Major Poisson ratio
ρ	Density
σ_i	Normal stress, i takes values 1, 2, 3, r, s, t, x, y or z
$\boldsymbol{\sigma}$	Stress vector
τ_{ij}	Shear stress, i and j take values 1, 2, 3, r, s, t, x, y or z with $i \neq j$
$\varphi_x,\ \varphi_y,\ \varphi_z$	Beam cross-sectional rotations
$\boldsymbol{\phi}$	Modal shape solution of a finite element model
$\chi_x,\ \chi_y,\ \chi_z$	Beam reference axis displacements
Ψ	Blade azimuth angle
ω	Natural angular frequency
$\boldsymbol{\omega}_{j/i}$	Angular velocity vector of body j in coordinate system i

Ω	Rotor rotational speed
$\dot{\Omega}$	Rotor rotational acceleration

Superscripts

$^{-1}$	Inverse of a matrix
^{C}	Compressive
^{i}	Quantity evaluated at the ith node
^{T}	Transpose of a matrix; Tensile
$^{-T}$	Inverse of the transpose of a matrix, e.g., $\mathbf{M}^{-T} = (\mathbf{M}^{T})^{-1}$
$'$	Derivative with respect to z, e.g., $f' = \mathrm{d}f/\mathrm{d}z$; Indicate a coordinate transformation in translation
$''$	Second derivative with respect to z, e.g., $f'' = \mathrm{d}^2 f/\mathrm{d}z^2$; Indicate a coordinate transformation in rotation
$\cdot$	Derivative with respect to time, e.g., $\dot{f} = \mathrm{d}f/\mathrm{d}t$
$\cdot\cdot$	Second derivative with respect to time, e.g., $\ddot{f} = \mathrm{d}^2 f/\mathrm{d}t^2$
$\hat{}$	Denotes that a vector is expanded to a matrix where each column contains a vector associated with a different load case; Unit vector

Subscripts

$_{,i}$	Derivative with respect to i, e.g., $f_{a,x} = \mathrm{d}f_a/\mathrm{d}x$

$1, 2, 3$	Axes 1, 2 and 3 of coordinate system 123
$aero$	Aerodynamic force
b	Blade coordinate system
c	Cone coordinate system
e	Finite element index
$grav$	Gravitational force
G	Ground coordinate system
h	Hub coordinate system
$iner$	Inertial force
n	Nacelle coordinate system
r, s, t	Axes r, s and t of coordinate system rst
t	Tilt coordinate system
T	Tower top coordinate system
x, y, z	Axes x, y and z of coordinate system xyz

INTRODUCTION

0.1 Context : wind turbine blades

Since this thesis discusses structural analysis of wind turbine blades, a good starting point is to describe the basic principles of a wind turbine. As shown in Figure 0.1, for a typical modern upwind three-bladed wind turbine, one effect of the wind on the blades is to cause in-plane aerodynamic loads, which produce the rotor torque that is converted into electrical power by the generator located in the nacelle. The other effect of the wind is to cause out-of-plane loads, that do not contribute to the wind turbine power but constitute the most important part of the blade load.

Wind turbine blades are made of airfoil shapes with a chord length increasing from blade tip towards the maximum chord location, where the transition to the circular root begins. The blade pitch angle, which is the angle between the chord line and the rotor plane (positive when the leading edge goes upwind), is almost zero at the tip and somewhere between 15° and 30° at the maximum chord location. Based on this general blade geometry, it can be understood that the most important part of the aerodynamic load causes bending of the blade globally oriented about its weakest axis, the flapwise direction.

For more details concerning the aerodynamics of wind turbines, the interested reader is referred to the author's master's thesis (Forcier, 2010). In addition to the aerodynamic loads, wind turbine blades are also subjected to gravitational and inertial loads. Theses are discussed in detail in Chapter 2.

Modern wind turbines are made of composite materials. Glass fibres are mostly used, but some designs also incorporate carbon fibres. A majority of wind turbine blades are manufactured by resin infusion or prepreg technologies using epoxy or polyester resin
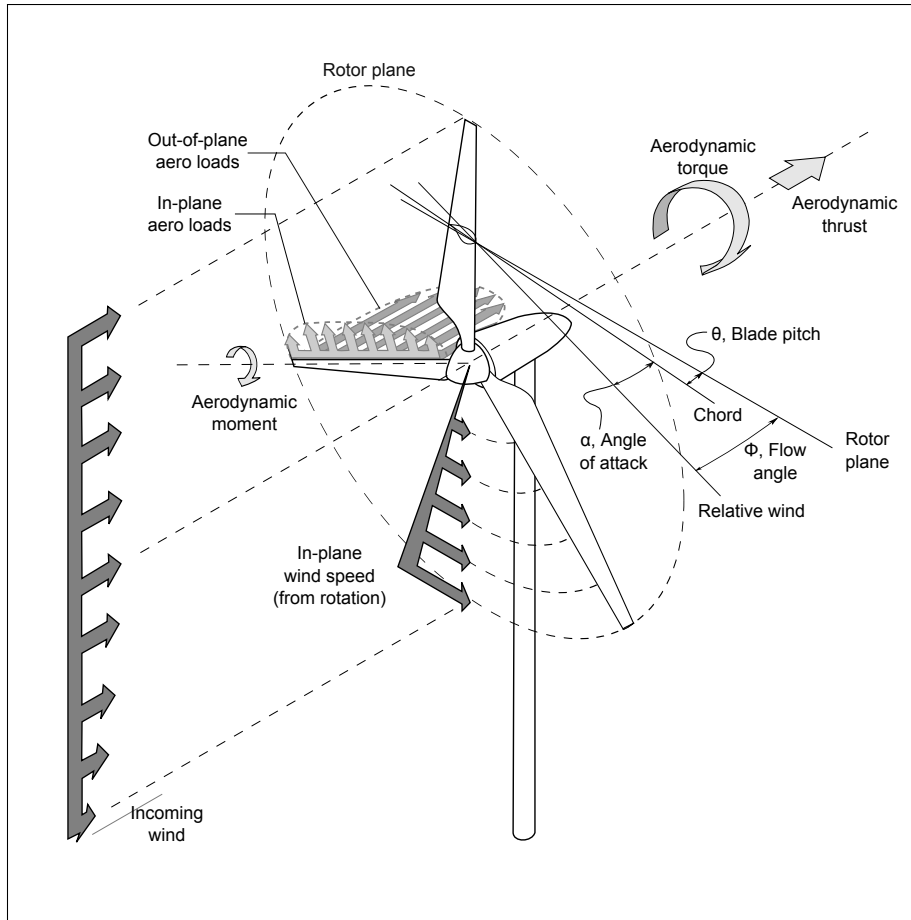
Figure 0.1   Horizontal axis wind turbine. From Cormier
et al. (2016)

systems. Some parts of the blade use a sandwich construction incorporating foam or balsa wood cores. Figure 0.2 shows different structural topologies of modern wind turbine blades. Figure 0.2a and b present the structural shell concept with respectively one and two shear webs. In this design, the shells are thickened at the maximum airfoil thickness to create the spar caps. In the load bearing spar concept (Figure 0.2c), the spar caps and the two shear webs are manufactured in one part on which the shells are later bonded.

As summarized in Figure 0.3, the spar caps are made principally of unidirectional fibres oriented along the blade longitudinal axis to support the flapwise bending moment, which

is the critical load. Aerodynamic shells and shear web includes a large amount of biaxial fibres at $\pm 45°$ (relative to the blade longitudinal axis) to support shear loads due to shear forces and torsional moment. Sandwich panels are often built by incorporating foam or balsa wood core in the laminates to increase their buckling strength in large unsupported panels like the ones near the trailing edge.

4

(a)

(b)

(c)
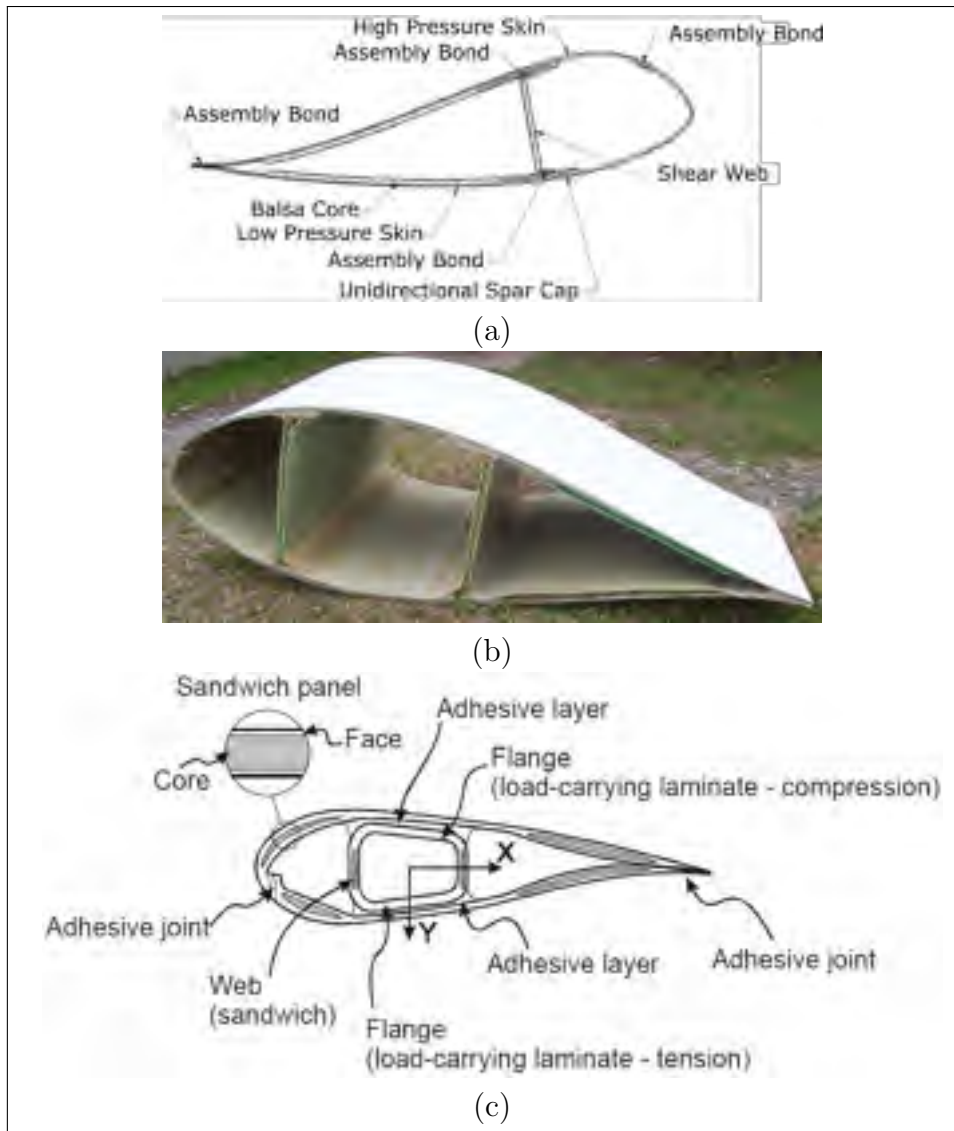
Figure 0.2   Modern wind turbine structures. (a) Structural shell with 1 shear web, adapted from Jackson et al. (2005). (b) Structural shell with 2 shear webs. (c) Load bearing spar, from Sørensen et al. (2004)
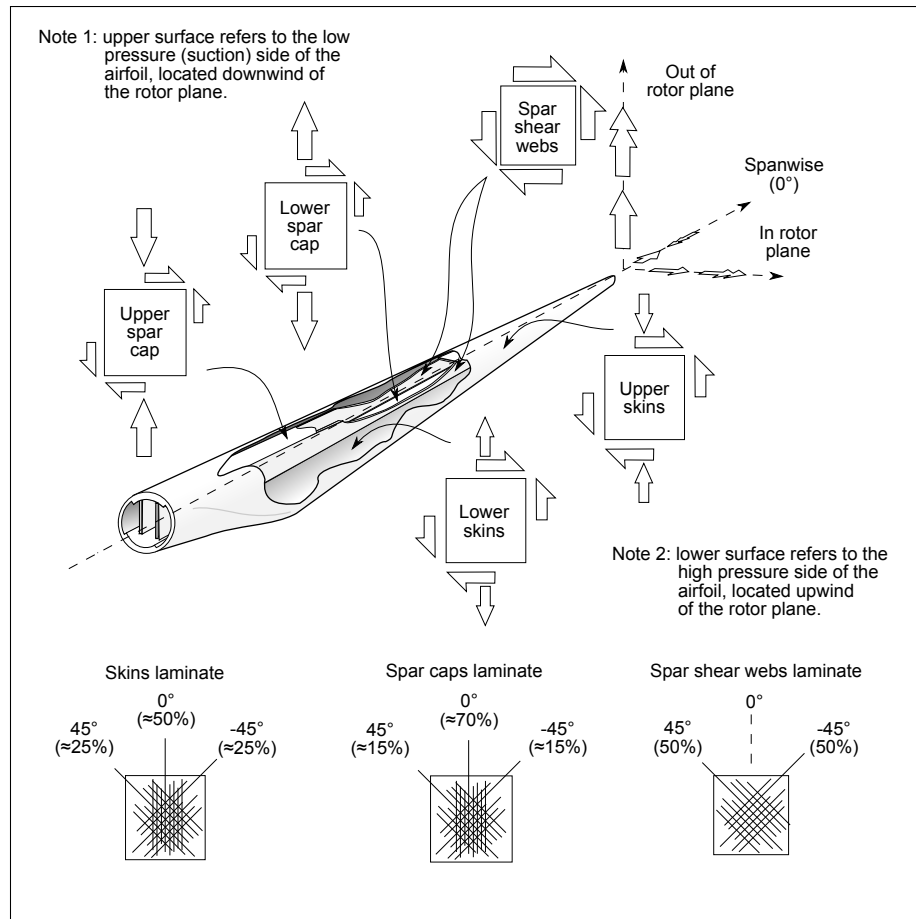
Figure 0.3   Wind turbine blade structure. From Cormier
et al. (2016)

0.2   Structural design process of a wind turbine blade

Like for many other components, the structural design process of a wind turbine blade is an iterative process. The typical design process for a wind turbine blade is represented in Figure 0.4.
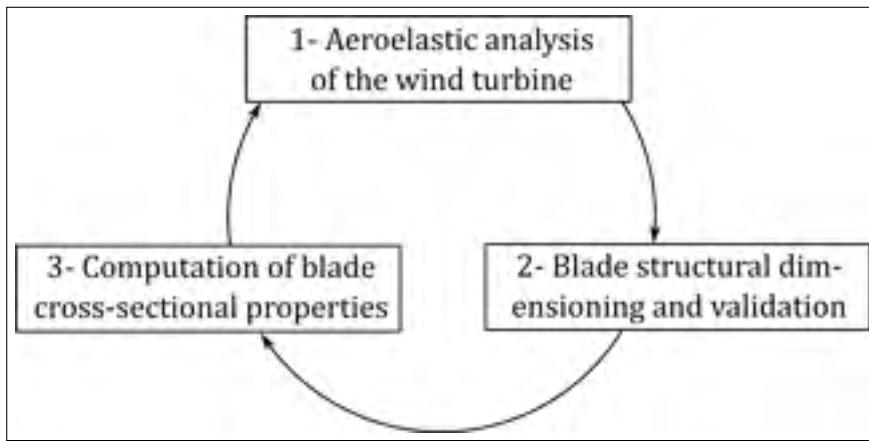
Figure 0.4   Structural Design Process of a Wind Turbine
Blade

The first step of the process consists of the aeroelastic analysis of the wind turbine. This is done with a multibody dynamic model of the whole wind turbine including the effect of wind and the elastic behaviour of some parts like the blades and the tower. This analysis allows the computation of the loads in all components, including the blades, for different loads cases defined by the appropriate standards. These data can then be post-processed in order to obtain a set of critical blade load cases.

These critical load cases then become the inputs for the next step of the design process: the blade structural dimensioning and validation. The design of the blade laminate can be done based on static and fatigue strength, buckling, critical deflection, eigenfrequencies, etc. If the requirements are not met, a recommendation can be made to change the

aerodynamic shape of the blade by increasing chord length or airfoil thickness where it is needed.

The blade being dimensioned and validated, the process can continue to the third step consisting of computing the blade cross-sectional properties (for instance, $\overline{EA}$, $\overline{EI}$, mass per unit length) needed for the aeroelastic analysis of the wind turbine (return to step 1).

Each of these three steps can be the entry point of the blade design process. Using cross-sectional properties from similar blades or modelling the blade as an infinitely rigid part, the aeroelastic analysis of the wind turbine can be the entry point. Using critical load cases from similar blades or simplified conservative load cases, the designer can also start the design process by the blade dimensioning and validation. Finally, guessing a preliminary laminate design from similar blades, it is also possible to start with step 3, the computation of the blade cross-sectional properties.

No matter the entry point in the design process, a few iterations can be needed to reach the final design. So the tools and models used may not be the same at each iteration for a given step. For example, the models needed for final iterations are not necessarily well suited for preliminary stages of the design process where simple and easy to solve models are generally preferred.

0.3   Two contexts of blade structural analysis

When looking at the blade structural design process described in the last section, two different contexts where structural models of the blades are needed can be identified: (1) structural dimensioning and validation of the blade and (2) computation of blade cross-sectional properties for aeroelastic analysis.

0.3.1 Structural dimensioning and validation of the blade

The first context where structural analysis models are needed is when performing the blade structural design and validation. Most of the time, especially in the final stages, 3D shell finite elements are used to ensure that the blade can sustain the loads without any static or fatigue failure, without any buckling and with a reasonable blade deflection.

0.3.2 Computation of blade cross-sectional properties for aeroelastic analysis

The second context where blade structural analysis models are needed is when it is time to get the blade cross-sectional properties needed as input for the wind turbine aeroelastic model. For that purpose, a tool for cross-sectional analysis of the blade is well suited. Different levels of complexity can be included in the beam cross-sectional model used. When only bending properties are needed, the designer can rely on classical strength of material models, but for some designs, for instance, for bend-twist coupling blade used for passive load alleviation, the model needs to be able to manage the couplings between all the blade deformation modes.

0.4 Two types of structural analysis models

As seen in the previous section, two types of structural models are mainly used for blade structural analysis: (1) beam models and (2) 3D shell finite element models.

0.4.1 Beam models

Beam models are based on the strength of material theory. They are the type of model used in most of the aeroelastic codes, and they are well suited and often used for the blade cross-sectional property evaluation. However, they can also yield valuable information for the blade structural validation. Their capabilities for evaluating stresses and strains,

deflection, buckling, and eigenfrequencies are not as good as those of a 3D finite element model (especially in the areas of rapid cross section change like maximum chord to root transition region), but they are sufficient for preliminary dimensioning and validation and they are much faster to set up and get results than 3D shell finite element models.

It is also interesting to note that the most recent aeroelastic codes tend to include beam models that are able to manage all the material and geometric coupling between the different deformation modes of general composite beams (see Section 2.1 for more details). Therefore, complex cross-sectional analysis tools are needed in order to get all the required cross-sectional properties. This issue is addressed in this thesis (see objective 3).

0.4.2 3D shell finite element models

3D shell finite element models are based on surface elements with nodes having translational and rotational degrees of freedom. Commercial software offer shell finite elements with through the thickness layered material definition that are well suited for composite materials. This type of model is often used for the structural dimensioning and validation of the blade. However, with proper post-processing, a 3D shell finite element model can also be used to get the blade cross-sectional properties. This latter point is also addressed in this thesis (see objective 2).

0.4.3 Discussion

When the blade designer uses these two types of structural analysis models, he has to transfer some information from one to another. A good example of that is when taking the loads from an aeroelastic simulation of the wind turbine (which usually use beam model for blades) and transfer them to a 3D shell finite element model of the blade. This is not a straightforward task, and this is addressed in this thesis (see objective 1).

Another issue that is addressed in this thesis is the choice of the right structural analysis model to use in a given situation (see objective 2). 3D finite element models are, of course, more precise, but they are also more time consuming for the pre-processing as well as for the solution. Beam models are easier to set up and the results are obtained quickly, but are not always adequate for the final phases of the design process.

0.5 Thesis objectives

As seen in the previous sections, structural analysis of wind turbine blades is done in different contexts and using different models. The aim of this thesis is to address some issues related to the structural analysis of wind turbine blades. These issues, identified by the author during his activities as a wind turbine blade designer, are related to each step of the blade structural design process presented in Section 0.2. These objectives are:

Objective 1: Develop tools to transfer the blade load obtained from an aeroelastic model of the wind turbine (where the blade is modelled as a beam) to a 3D shell finite element model of the blade.

Objective 2: Compare blade structural models of different levels of complexity with respect to their capability of blade design and analysis and conclude on their use at the different stages of the blade design process.

Objective 3: Develop tools to evaluate the cross-sectional properties of general anisotropic nonhomogeneous thin-walled beam.

0.6 Thesis plan

The first chapter of the thesis will describe the 10 kW WESNet wind turbine blade that was designed by the author at the beginning of his doctoral studies and that is used as an

example through the thesis. This chapter also presents the test setup and methodology used to collect the experimental data presented in this thesis.

Chapter 2 is intended to answer the first objective of the thesis and is dedicated to the study of the different loads to which wind turbine blades are subjected. It also offers a methodology to transfer the blade load obtained from an aeroelastic model of the wind turbine to a 3D shell finite element model of the blade. The content of this chapter was published in the *Wind Engineering* journal (Forcier and Joncas, 2019).

The third chapter presents different models for the structural analysis of wind turbine blades, ranging from the simplest to the more complex : (1) simple model, (2) classical strength of materials model, (3) cross-sectional finite element model and (4) 3D finite element model. This serves as a basis to address objectives 2 and 3.

Chapter 4 is dedicated to the detailed presentation of the cross-sectional finite element model specifically developed in this thesis. It is intended to answer objective 3.

Finally, Chapter 5 offers a comparison of the capabilities of the different models presented in the last two chapters. This theoritical and experimental comparison covers natural frequencies, deflection, stresses and strains, buckling, composite strength and cross-sectional properties. This chapter concludes the work on objective 2.

A summary of the thesis plan is presented in Table 0.1. It indicates the distribution of the work with respect to the different objectives as well as the distribution of the literature review and the original work through the thesis.

Table 0.1   Thesis plan

Chapters	Sections	Objectives			Lit. review	Original work
		1	2	3		
1	1.1–1.7					
2	2.1					
	2.2–2.6					
3	3.1–3.2					
	3.3–3.4					
	3.5					
	3.6–3.7					
4	4.1–4.2					
	4.3–4.5					
5	5.1–5.8					

CHAPTER 1

WESNET BLADE AND TEST METHODOLOGY

In the beginning of his doctoral studies, the author had the chance to participate in the design of a 10 kW wind turbine. This turbine, was designed at ÉTS and manufactured in the course of a project funded by the Natural Sciences and Engineering Research Council of Canada's Wind Energy Strategic Network (NSERC/WESNet). In this project, the author was involved in the structural design and validation of the blades. This wind turbine was designed and manufactured over a 15-month period, between January 2011 and March 2012 and was installed at the Wind Energy Institute of Canada (WEICan) on Prince Edward Island in June 2012.

As all the characteristics of this blade were available and as five blades were available for further testing, this blade design is used throughout this thesis as an example for the numerical and experimental work.

The aim of this chapter is to present the design of this blade. The content of this chapter is principally based on a conference paper presented by the author at the 19th International Conference on Composite Materials (Forcier et al., 2013). The last section of this chapter also presents the methodology for the different tests realized for the purpose of this thesis.

1.1 Introduction

1.2 Wind turbine characteristics

This turbine is a pitch regulated variable speed wind turbine equipped with a direct drive synchronous generator designed at the University of New Brunswick (Canada). The rotor diameter is 8.08 m and the turbine reaches its nominal electric power of 10 kW at a wind speed of 9.5 m/s and a rotor speed of 185 rpm. For wind speeds below this value, the blade pitch angle is fixed and the rotor speed is adjusted to get the maximum

power output. For winds above the nominal speed, the pitch control system is activated to maintain the rotor speed as close as possible to 185 rpm and consequently limit the power output to 10 kW. No yaw control system is needed as the rotor uses a downwind configuration and the nacelle yaw motion is unconstrained. The rotor therefore auto aligns itself when the wind direction changes. Table 1.1 summarizes the wind turbine characteristics and Figures 1.1 and 1.2 show respectively the nacelle without its covers and the assembled wind turbine.

Table 1.1   WESNet 10 kW wind turbine characteristics

Nominal power	10 kW
Cut-in wind speed	3 m/s
Nominal wind speed	9.5 m/s
Number of blades	3
Rotor speed range	0–250 rpm
Nominal rotor speed	185 rpm
Rotor orientation	downwind, free yaw
Rotor diameter	8.08 m
Nominal tip speed ratio	8.5
Hub height	24 m
Control system	active pitch
Hub radius	0.28 m
Rotor coning	3°
Generator	variable speed, direct drive
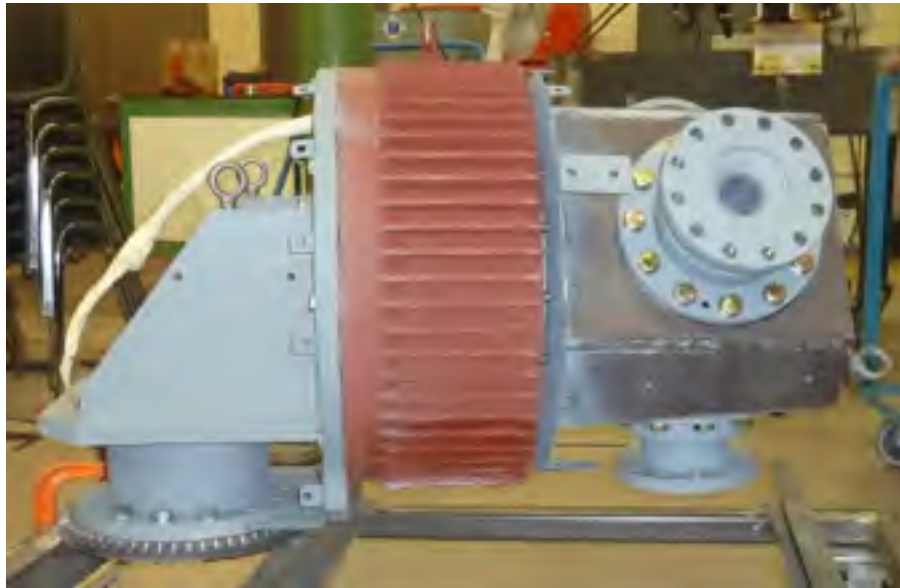
Figure 1.1   WESNet 10 kW wind turbine nacelle without covers

Figure 1.2   WESNet 10 kW wind turbine

1.3   Blade aerodynamic design

The blade aerodynamic design was done by Jon Sumner, Ph.D. student at ÉTS. The blade uses airfoils of the Delft University of Technology family (Timmer and van Rooij, 2003) and was designed using blade element momentum (BEM) theory. As the aerodynamic design has to consider both aerodynamic and structural considerations, in the early stages of the aerodynamic design, conservative characteristic loads were used to verify that the current design met the structural requirements.

Table 1.2 shows the final aerodynamic design of the blade. Thicker airfoils are used near the blade root for structural reasons. Sectional loads are higher at this location and thicker airfoils allow a higher section modulus. Near the blade tip, where the sectional loads are lower, it is possible to use thinner airfoils to get maximum aerodynamic efficiency.

Table 1.2 Blade aerodynamic shape. z is the distance from the blade root, c is the airfoil chord length and θ_T is the airfoil twist angle

z [m]	θ_T [deg.]	c [m]	Airfoil
0.000	15.3	0.200	Circle
0.160	15.3	0.200	Circle
0.560	15.3	0.334	DU-97-W-300
0.760	14.5	0.318	DU-97-W-300
0.960	13.7	0.303	DU-91-W2-250
1.160	12.9	0.287	DU-91-W2-250
1.360	12.1	0.271	DU-91-W2-250
1.560	11.2	0.256	DU-91-W2-250
1.760	10.4	0.240	trans. 212-250
1.960	9.6	0.224	DU-00-W-212
2.160	8.8	0.208	DU-00-W-212
2.360	8.0	0.193	trans. 180-212
2.560	7.2	0.177	DU-96-W-180
2.810	6.2	0.157	DU-96-W-180
3.060	5.2	0.138	DU-96-W-180
3.260	4.3	0.122	DU-96-W-180
3.460	3.2	0.106	DU-96-W-180
3.660	1.3	0.090	DU-96-W-180
3.760	0.0	0.083	DU-96-W-180

1.4 Blade loads computation

Once the aerodynamic design was fixed, to determine the blade design loads, the turbine was analyzed using the aeroelasticity code FAST (Jonkman and Buhl Jr., 2005). This software models the entire wind turbine as an assembly of rigid and flexible bodies. In our analysis, all parts were considered rigid and the only degrees of freedom that were taken into account were the nacelle yaw motion and the variable rotor speed.

As the wind turbine is a free yaw downwind machine, the only control strategies to model were the variable rotor speed and the blade pitch control mechanism. The variable rotor speed control was modelled by specifying the torque vs. rotational speed curve of the

generator as supplied by the designer. The pitch control system uses a proportional-integral controler. The control systems was modelled with Simulink using the FAST's Simulink interface by Tommy Gagnon, a master's degree student at ÉTS.

All the relevant ultimate load cases of the aeroelastic method defined in the International Electrotechnical Commission (IEC) standard on design of small wind turbines (International Electrotechnical Commission, 2005) were evaluated using FAST. These load cases include normal power production, power production with control system fault, shut down, idling and parked wind turbine for different wind conditions.

The fatigue load cases were treated differently. In addition to the aeroelastic method, the IEC standard presents a simplified method to evaluate conservative load cases. The simplified fatigue load case is based on the load range of a wind turbine that operates between 0.5 and 1.5 times the design rotor speed and 0.5 and 1.5 times the rotor aerodynamic torque. The simplified method also includes the possibility to analyze the fatigue load case as a static load case using a safety factor of 10 on static material strengths. The fatigue load case used is based on this procedure. The nominal operation condition was modelled with FAST to get the aerodynamic loads and the gravitational and inertial loads were applied directly in the finite element model.

This analysis of all load cases with FAST allowed the identification, in addition to the fatigue load case, of three critical load cases to use for the blade structural design: maximum root axial force, maximum root edgewise bending moment and maximum root flapwise bending moment. The maximum root axial force and edgewise bending moment occur when the wind turbine in normal operation is submitted to the normal turbulence model with a wind speed of 25 m/s. The maximum root flapwise bending moment happens when the wind turbine in normal operation faces the extreme operating gust at nominal wind speed. During this situation, wind speed increases suddenly from 9.5 m/s to 14 m/s and then reduces to 9.5 m/s. This causes an acceleration of the rotor speed that causes a rapid nacelle yaw movement generating high out-of-plane gyroscopic

forces. These forces are in the opposite direction of the aerodynamics forces so that the blade's upper surface is in tension and the lower surface is in compression.

According to the IEC61400-2 standard, a safety factor of 1.35 was applied to the ultimate loads and no safety factor was applied on fatigue load.

1.5   Blade structural design

Figure 1.3 shows a schematic representation of the topology of the blade cross section. The blade is made of three parts (upper and lower surfaces of the airfoil and shear web) bonded together. Both aerodynamic shells are thicker in the maximum thickness region of the airfoil (between 15 % and 45 % of chord length) to form the spar caps that support most of the blade loads.
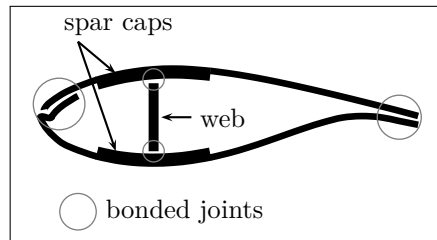
Figure 1.3   Blade internal structure

The materials used in this blade are similar to those of large wind turbines. The main structural material is Saertex glass fibre with Gurit's Prime 20 epoxy resin. Two different non-crimp fabrics (NCF) are used : a 655 g/m^2 unidirectional fabric for plies at 0° (fibre in the blade longitudinal direction) and a 609 g/m^2 bidiagonal fabric containing plies at $+45°$ and $-45°$. 0° plies are 0.50 mm thick and plies at $+45°$ and $-45°$ are 0.23 mm thick each.

The shear web is a sandwich panel made of Gurit Corecell A500 between glass/epoxy skins. On the blade surface, there is also a layer of gelcoat (GC, 0.51 mm thick) and a

ply of chopped strand mat (CSM, glass fibre with vinylester resin, 0.65 mm thick). A methacrylate adhesive is used to bond the aerodynamic skins and shear web together. Table 1.3 shows material properties used for blade design. Note that all material strengths of Table 1.3 have been divided by a safety factor of 3.0 (according to the IEC 61400-2 standard) when entered in the finite element model except for the fatigue load case where the safety factor was 10.

Table 1.3   Material properties used in the finite element models

			UD[a]	CSM[b]	Core[c]	Gelcoat[d]
Longitudinal elastic modulus	E_1	[MPa]	38954	9650	72.5	3440
Tranverse elastic modulus	E_2	[MPa]	14538	9650	72.5	3440
Major Poisson ratio	ν_{12}		0.29	0.30	0.39	0.30
Shear modulus	G_{12}	[MPa]	4239	3860	26	1380
Longitudinal tension strength	S_1^T	[MPa]	776	124	1.3	-
Longitudinal compression strength	S_1^C	[MPa]	522	-	0.9	-
Transverse tension strength	S_2^T	[MPa]	54	124	1.3	-
Transverse compression strength	S_2^C	[MPa]	165	-	0.9	-
Shear strength	S_{12}	[MPa]	56	-	1	-
Density	ρ	[kg/m^3]	1884	1670	92	1230
Ply thickness	t	[mm]	e	0.65	19.05	0.51

[a] From the Optimat Blades project (Nijssen, 2006)

[b] From the WindPACT turbine design studies (Griffin, 2001)

[c] From material technical data sheet

[d] From the WindPACT turbine design studies (Griffin, 2001)

[e] 0.50 mm for 0° plies and 0.23 mm for +45° and -45° plies

Figure 1.4 shows the geometric model and the mesh of the inner part of the blade that was used for the blade design. The mesh is mostly made of four-node shell elements. The chord length is discretized with about 25 elements, and the size of elements is reduced towards the blade tip to get element aspect ratios as close as possible to 1. The finite element model has a total of 21 553 nodes and 21 536 elements. Note that this mesh differs from the mesh used for the work presented in Chapters 3 and 5.
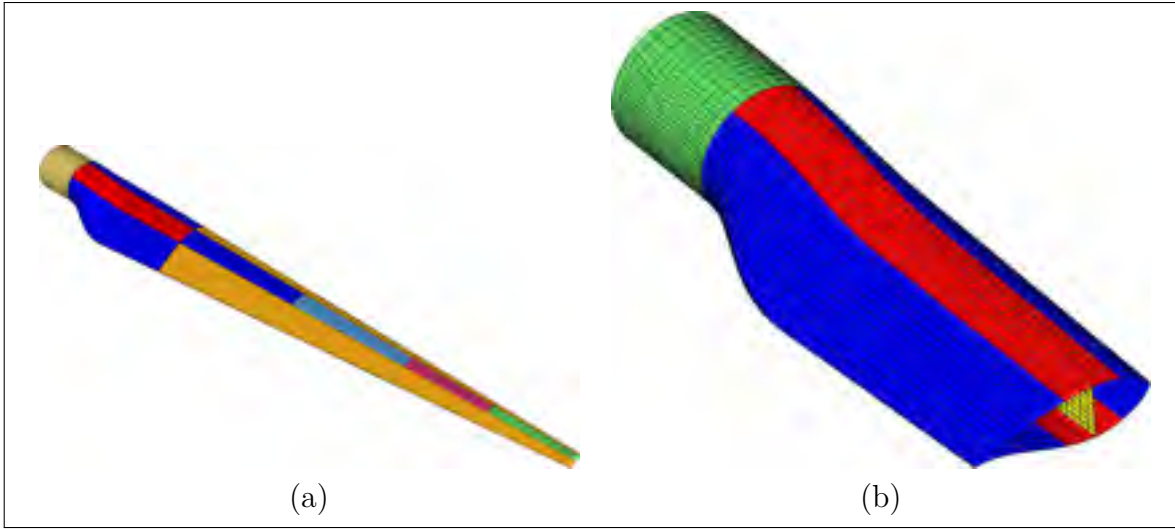
Figure 1.4 Blade model. Regions with different colours have different composite laminates. (a) Surfaces. (b) Mesh of the inner part

The finite element analysis software OptiStruct Altair Engineering (2008) was used for the structural design of the blade. In the early stages of the design process, optimization capabilities of OptiStruct were used. See Forcier and Joncas (2012, Sec. 8) and Forcier (2010, Chap. 8) for an example of this method.

Once this optimization process was completed, the design was adjusted manually to take into account manufacturing constraints that were not included in the optimization run (e.g., discrete ply thickness, increasing layup thicknesses towards blade root, ply sequence). The final blade composite layup is presented in Table 1.4. The longitudinal positions of the first column are the beginning of the ply drops. One ply is dropped each 13 mm (0.5 in).

The blade root to hub attachment system is based on a concept used for the Sandia National Laboratories' Blade System Design Studies (Berry, 2008). M16×2 steel threaded studs are inserted into 15 mm thick steel half-rings at the blade root and incorporated in the blade composite laminates prior to infusion. The length of the studs inside the blade is 155 mm and the studs are tapered for the last 115 mm (see Figure 1.5). An experimental validation of this concept has been done by a tension test on a steel stud embedded

Table 1.4   Blade layup

Blade region, distance from blade root	Laminate
Blade root circular region	
0 mm–210 mm	[GC/CSM/$(+45/-45)_3$/0_6/$(+45/-45)_3$/^{a}/ $(+45/-45)_3$/0_8/$(+45/-45)_3$]
Spar cap, from 15 % to 45 % of chord length	
210 mm–1074 mm	[GC/CSM/$(+45/-45)_2$/0_{11}/$(+45/-45)_2$]
1074 mm–2624 mm	[GC/CSM/$(+45/-45)_2$/0_{10}/$(+45/-45)_2$]
2624 mm–3173 mm	[GC/CSM/$(+45/-45)_2$/0_6/$(+45/-45)_2$]
3173 mm–3776 mm	[GC/CSM/$(+45/-45)_2$/0_2/$(+45/-45)_2$]
Aerodynamic shells, outside spar cap	
210 mm–960 mm	[GC/CSM/$(+45/-45)_2$/0_{11}/$(+45/-45)_2$]
960 mm–3776 mm	[GC/CSM/$(+45/-45)_2$/0_1/$(+45/-45)_2$]
Shear web	
210 mm–3776 mm	[$(+45/-45)_3$/Core/$(+45/-45)_3$]

   ^{a} Steel studs or 0° unidirectional glass-epoxy filler

in a composite laminate similar to the blade root laminate. This test was performed by Jean-François Charron, masters' degree student at ÉTS. The assembly successfully resisted the design load.

1.6   Blade manufacturing

The blades have been manufactured by Composites VCI (Saint-Lin, Québec, Canada). Both aerodynamic skins were manufactured separately in tooling board moulds using vacuum resin infusion. A layer of gelcoat was first applied on the mould and a ply of chopped strand mat (CSM) was laminated by hand layup. Glass fibre plies were then placed incorporating the steel parts at root as shown in Figure 1.5a–c. Near the blade root, where the composite laminate is thick, both skins were bonded together using a butt joint. Counter moulds were used to get a good flat surface for bonding (one counter mould shown on Figure 1.5a–c). In addition to these counter moulds (two for the upper surface skin and two other for the lower surface skin) another counter mould was installed on the lower surface mould along the blade leading edge to create a lap joint as shown

in Figures 1.3 and 1.5e. At the trailing edge, no counter mould was necessary as both skins were bonded on the internal surface of each other.
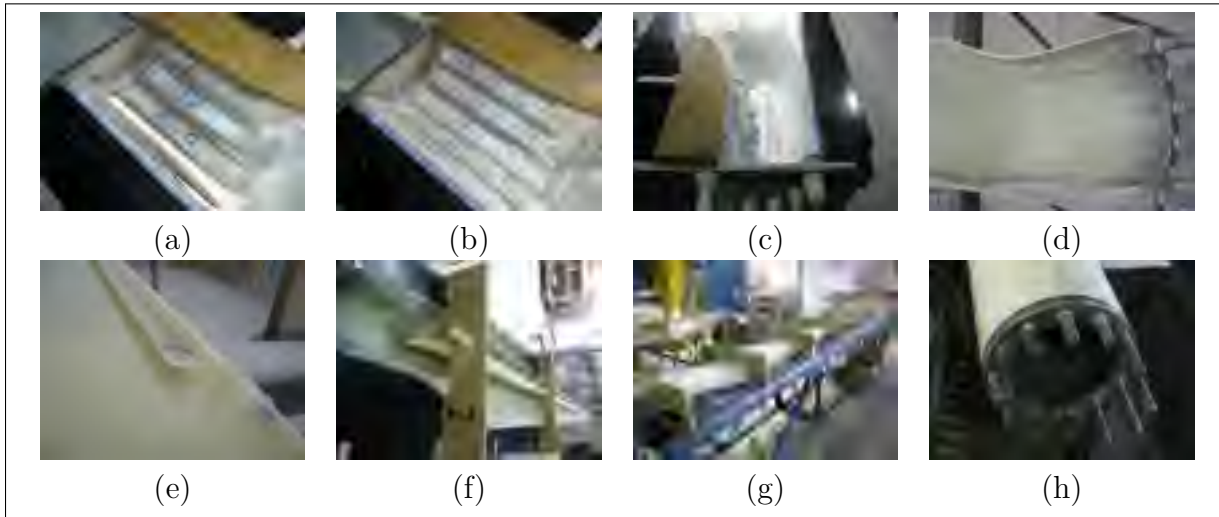
Figure 1.5   Blade manufacturing: (a–c) blade root layup; (d) infused lower surface; (e) bonding lip on the lower surface's leading edge; (f) bonding of shear web on the lower surface, nine positioning jigs are used (only two shown); (g) bonding of the upper surface on the lower surface and shear web assembly; (h) close view of the assembled blade root

Once both aerodynamic skins were infused, they were trimmed and the shear web was bonded to the lower surface as shown in Figure 1.5f. The shear web was cut out from an infused flat sandwich panel. The upper surface was then bonded to the assembly of lower surface and shear web as shown in Figure 1.5g. Figure 1.5h shows the bonded blade near the root region. Once assembled, the blade was finished and post-cured at 65°C for 7 hours. The final blade mass is 28 kg.

1.7   Tests methodology

For the experimental validation of the tools developed in this thesis, five blades were available. The different tests performed on the blades were all different versions of bending tests. These experiments were done on a steel frame as illustrated in Figures 1.6 to 1.10. Two of the available blades were instrumented with strain gauges on their exterior

surface. On the blade surface, reflective targets were also sticked for the blade to be scanned with a 3D scanner. An EXAscan from Creaform was used. The comparison of deflected and undeflected scanned shapes allows the computation of the blade deflection. Note that for all flapwise bending tests, the upper surface of the airfoils is oriented towards the floor and the lower surface in oriented upward.

1.7.1 Modal analysis

The first test performed was a modal analysis of the blades. For that purpose, the blade root was fixed on the test support (see Figure 1.6). The blade tip was manually deflected and then, quickly released. The signal of a strain gauge was recorded during the free vibration phase and a Fourier transform of this signal was used to get the eigenfrequencies of the blade.

1.7.2 Design load test

A second test was performed in order to recreated the critical load case of the blade. This was done by loading the blade at two blade stations ($z = 2.360$ m and $z = 3.500$) as shown in Figure 1.7. The loads were applied with manual winches and were transferred to the blade by aluminum saddles. Loads cells were also installed on the winch cables to monitor the applied loads.

1.7.3 Cross-sectional characterization test

A third test was intended to measure the blade cross-sectional stiffness properties. For that purpose, the blade was loaded with a mass applied near its tip. Flapwise, edgewise and torsional (as shown in Figure 1.8) load cases were realized.

Figure 1.6   Modal analysis test setup

1.7.4   Destructive test

Finally, destructive tests were done. These tests were performed in two steps. In the first step, the blade, fixed at root, is also simply supported in its central part ($z = 2.360$ m) and loaded near its tip ($z = 3.500$ m) to create a failure in its outer part (see Figure 1.9). In the second step of the destructive test, the blade is loaded at $z = 2.360$ m to generate a failure in its inner part (see Figure 1.10).

Figure 1.7   Design load test setup

Figure 1.8   Cross-sectional charaterization test setup

Figure 1.9   Setup for step 1 of the destructive test
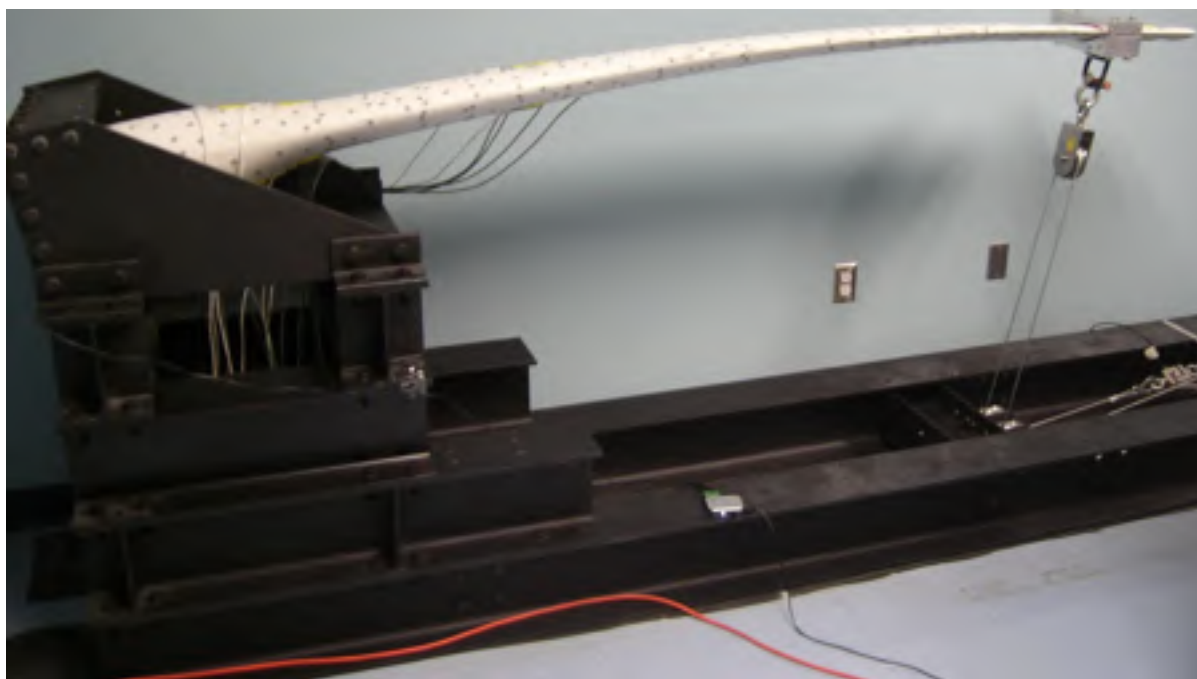
Figure 1.10   Setup for step 2 of the destructive test

LOADS ON A WIND TURBINE BLADE AND THEIR TRANSFER FROM AN AEROELASTIC SIMULATION TO A 3D FINITE ELEMENT MODEL

The aim of this chapter is to answer the first objective of the thesis, that is to propose a methodology to transfer the loads obtained from an aeroelastic model of the wind turbine (where the blades are modelled as beams) to a 3D shell finite element model of the blade. To do so, analytical equations for the computation of blade root loads as function of the wind turbine characteristics and operation parameters are derived. This chapter is based on a paper published in the *Wind Engineering* journal (Forcier and Joncas, 2019).

2.1 Introduction

Aeroelastic simulations are frequently used for the design and analysis of wind turbines. Tools like FAST (Jonkman and Buhl Jr., 2005), GH Bladed (Bossanyi, 2003), HAWC2 (Larsen and Hansen, 2007) or PHATAS, a module of FOCUS6 (Knowledge Centre WMC, 2012; Lindenburg, 2005), allow the simulation of the fully coupled dynamic behaviour of the wind turbine. Three methods are mostly used to model the structural behaviour of the deformable blades: multibody dynamics (a series of rigid bodies linked with springs); beam finite element; and modal superposition (the blade deflection is a weighted sum of its first few modal shapes).

The Elastodyn module of FAST uses modal superposition with the first two flapwise and the first edgewise modes. The blade deformation is then given by 3 parameters (generalized coordinates that are scaling factors for each mode shape). Torsion is not taken into account. GH Bladed also uses this method with up to 6 modes in each blade directions. Like FAST (using the Elastodyn module), no torsional degrees of freedom are modelled. Both software work under the small perturbation assumption for the blade deformation. However, in FAST, the loads are computed on the deformed shape of the

blade, allowing the modelling of some nonlinear effects (Jonkman, 2003; Wilson et al., 1999).

HAWC2 uses a combination of beam finite elements and multibody dynamics. Blades can be modelled with several bodies made of Timoshenko beam finite elements allowing the modelling of all the couplings between the different modes of deformation. This method also takes into account the nonlinear behaviour of the blade even if linear models are used for the beam elements. When using the Beamdyn module of FAST, the blades are modelled using geometric nonlinear beam finite elements. These elements use a Timoshenko beam formulation and have capabilities to model all possible couplings between the different modes of deformation (Wang et al., 2017).

All these methods are based on beam theory and need to evaluate the different cross-sectional properties along the blade length. Tools for that purpose include PreComp (Bir, 2006), VABS (Yu et al., 2002a), CROSTAB (Lindenburg and de Winkel, 2005b), FAROB, a module of FOCUS6 (Lindenburg and de Winkel, 2005b) and BECAS (Blasques, 2012). These software packages, excluding VABS and BECAS, use Euler-Bernoulli beam theory and shear flow analysis of thin-walled beams to compute axial, bending and torsion section moduli as well as coupling terms between these modes of deformation. VABS and BECAS uses the Timoshenko beam theory so they also include shear deformation due to shear forces. For a review of some of these different software packages, see the article by Chen et al. (2010).

Another tool for blade cross-sectional properties calculations is BPE (Malcolm and Laird, 2007), which use a shell or solid finite element model. A set of unit loads is applied to the blade tip and section properties are computed from the analysis of nodal displacement at different cross-section along the blade length.

Once the internal loads have been computed at different blade sections during the aeroelastic simulation, the section modulus can be used to compute strains and stresses in these cross sections. Unfortunately, this method gives good results only in regions away

from the blade attachment and when cross-sectional shape variations are small (Chen et al., 2010), which is not the case at the blade root and near the maximum chord region. It is also possible to evaluate the buckling load of a cross section or of a panel in a cross section, but these methods are less accurate than with three-dimensional finite element models (Lindenburg and de Winkel, 2005a).

Three-dimensional finite element models (using shell or solid elements) can give a more precise strain and stress field on the blade but these models can be included in aeroelastic simulations only at a very prohibitive computational cost. For an example of aeroelastic simulation using shell model of the blade and computation fluid dynamics, see the articles by Bazilevs et al. (2011a,b).

A trade-off between efficient aeroelastic simulations and high precision strain, stress and buckling evaluation of the blade is to use the aeroelastic simulation to identify the critical load cases and reproduce them on a three-dimensional finite element model. However, the transfer from one dimensional beam load to three-dimensional models is not straight-forward.

If the load case to analyze is when the blade is at rest or if the gravitational and inertial forces are negligible, only aerodynamic loads have to be applied to the model. A way of doing that is to apply a concentrated force at the nearest node from each blade element centre corresponding to the aerodynamic force at this blade element (see for example a report by Griffith and Ashwill (2011)). Another way is to try to reproduce the pressure field on the blade surface using the blade airfoil properties and the angles of attack computed by the aerodynamic analysis tool (see for example the work of Knill (2005) and Caous et al. (2018)).

If gravitational loads have to be considered in the analysis, it is easy to apply them as body loads in the finite element model. One just has to compute the gravity vector direction according to the blade orientation in space.

Inertial loads on the blade can be calculated from the blade acceleration relative to an inertial coordinate system and from the blade mass distribution (see for example the work of Lillo, 2011).

Another approach is to use the total load computed by the aeroelastic solver (including aerodynamic, gravitational and inertial) as internal loads given at specific locations along the blade length. The external load distribution that generates this internal load distribution can then be computed and applied to the shell finite element model as point or distributed loads as discussed in Section 2.4.1.

The proposed approach of this thesis is to use the operation parameters of the wind turbine (rotor and nacelle rotational speed and acceleration, blade azimuth, blade pitch, rotor coning and rotor tilt) to characterize the inertial loads on the blade. This facilitates the inclusion of these loads in a finite element model as body loads. In doing so, the mass distribution of the blade around its longitudinal axis is taken into account and a change in the design that affects the blade mass distribution is also taken into account in the applied loads.

The objectives of this chapter are twofold. First, it is to derive analytical expressions for the gravitational and inertial load distribution on a wind turbine blade from the blade mass distribution and the turbine operation parameters. This will allow (1) the separation of the total load obtained from aeroelastic simulation in its different types and; (2) the understanding of the influence of different wind turbine operating parameters on blade loads. The second objective of this chapter is to develop a tool to reproduce the loads from an aeroelastic simulation on a three-dimensional finite element model of the wind turbine blade by separating the different load types.

The next section discusses the different types of loads on a wind turbine blade and the approach used to evaluate them. An expression for the distribution of each type of load on the blade will then be presented with the resulting forces and moments at the blades root. Next, a methodology will be presented to apply all these loads on a three-

dimensional finite element model of a wind turbine blade, and finally, an example of this methodology will be applied on a 10 kW wind turbine.

2.2 Loads on a wind turbine blade and methodology

For a given particle P of mass m on the blade, Newton's second law can be written as

$$\mathbf{F}_{aero} + \mathbf{F}_{grav} + \mathbf{R} = m\mathbf{a}_{P/G} \tag{2.1}$$

where $\mathbf{F}_{aero}$, $\mathbf{F}_{grav}$ and $\mathbf{a}_{P/G}$ are respectively the aerodynamic force vector, the gravitational force vector and the acceleration of point P relative to an inertial coordinate system. Vector $\mathbf{R}$ is the reaction force due to the blade deformation. Note that the damping forces are neglected.

If we want to perform a static analysis of the blade, we can rewrite Newton's second law as

$$\mathbf{F}_{aero} + \mathbf{F}_{grav} + \mathbf{F}_{iner} + \mathbf{R} = 0 \tag{2.2}$$

where the inertial loads are

$$\mathbf{F}_{iner} = -m\mathbf{a}_{P/G} \tag{2.3}$$

It is then possible to apply aerodynamic, gravitational and inertial loads on a static model of the blade to evaluate the displacement, strain and stress fields for a dynamic load case.

The wind turbine model that allows the computation of the different loads has seven coordinate systems as shown in Figure 2.1. The origin of the *blade coordinate system* ($\cdot_b$) is located at the blade root and is fixed to the blade (pitches with the blade). The z-axis is parallel to the blade's longitudinal axis (and pointing towards blade tip) and the x-axis is parallel to the blade tip chord line (and pointing towards leading edge). A positive pitch θ (leading edge goes upwind) is a rotation of the blade around its negative

z-axis. In the finite element model of the blade presented later, the global coordinate system is the blade coordinate system.

The *cone coordinate system* $(\cdot_c)$ is identical to the blade coordinate system but does not pitch with the blade. It is aligned with the blade coordinate system when $\theta = 0$.

The origin of the *hub coordinate system* $(\cdot_h)$ is located at the intersection of the rotor axis of rotation and the blade longitudinal axis. It rotates with the rotor. The z-axis is parallel to the blade's longitudinal axis projection in the rotor plane, and the y-axis is normal to the rotor plane. The rotor turns clockwise (around positive y-axis) when looking from upwind.

The *tilt coordinate system* $(\cdot_t)$ is fixed to the nacelle and tilted. It is the same as the hub coordinate system when the azimuth angle $\Psi = 0$ (blade pointing upward).

The *nacelle coordinate system* $(\cdot_n)$ is fixed to the nacelle, but not tilted. The z-axis is pointing upward and the y-axis is normal to the rotor plane (if $\gamma = 0$) and is pointing downwind (assuming no yaw error). The origin of this coordinate system passes through the tower axis.

The *tower top coordinate system* $(\cdot_T)$ is fixed to the tower top. It is the same as the nacelle coordinate system when the yaw angle is zero.

Finally, the *ground coordinate system* $(\cdot_G)$ is an inertial coordinate system. Its origin is located at the intersection of the tower's longitudinal axis and the ground level. The x- and y-axis of this coordinate system are aligned to the x- and y-axes of the tower top coordinate system respectively.

Here, all wind turbine components, except for the tower and the blades, are considered to be rigid. If $\mathbf{r}_{j/i}$, $\mathbf{v}_{j/i}$, $\mathbf{a}_{j/i}$, $\boldsymbol{\omega}_{j/i}$ and $\boldsymbol{\alpha}_{j/i}$ are respectively the position, velocity, acceleration, angular velocity and angular acceleration of point j (or origin of the coordinate system j) relative to the coordinate system i, we can establish the following relations
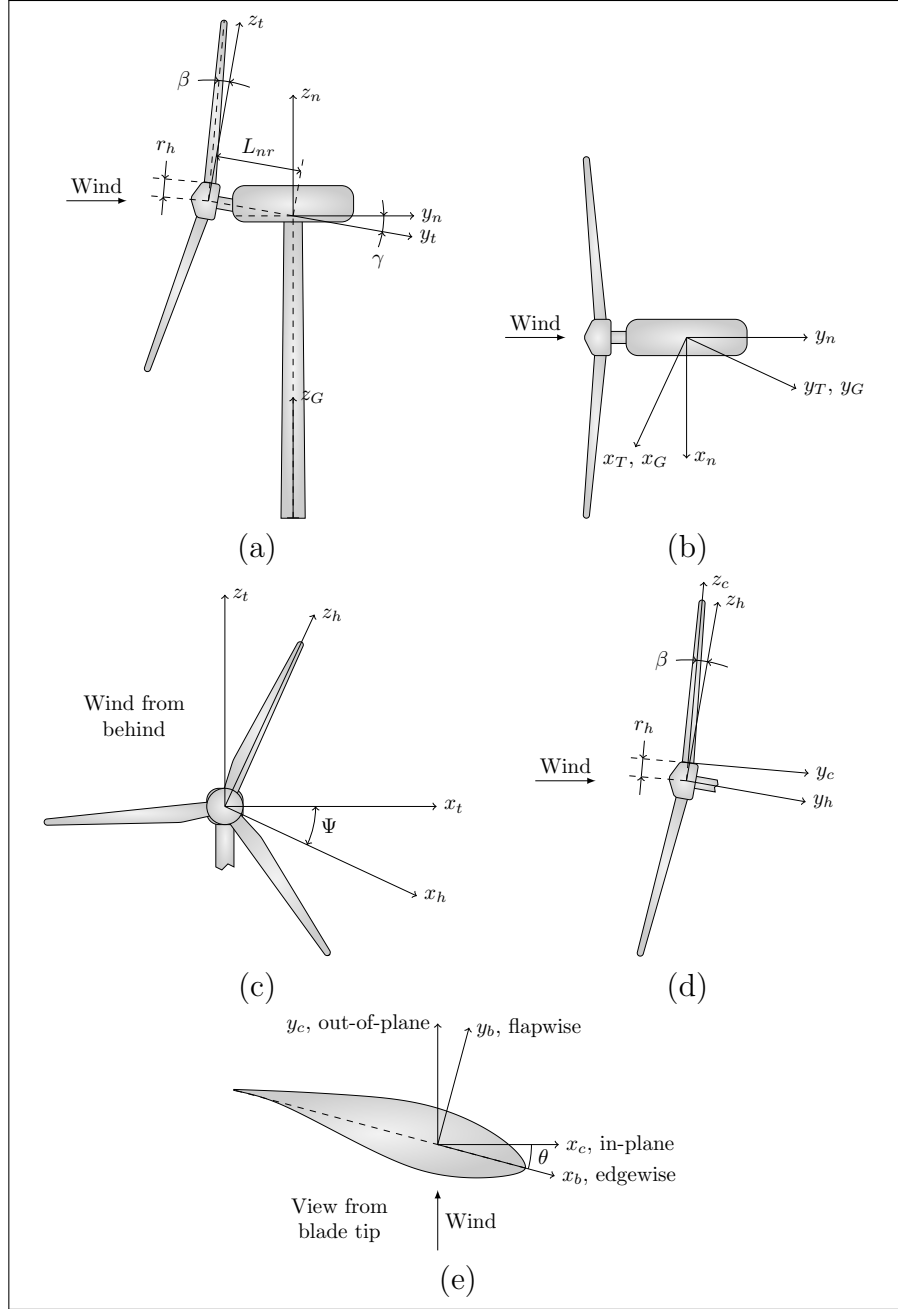
Figure 2.1 Coordinate systems used in the wind turbine model

between coordinate systems: $\boldsymbol{\omega}_{n/T} = [0, 0, \Lambda]_n^T$, $\boldsymbol{\alpha}_{n/T} = [0, 0, \dot{\Lambda}]_n^T$, $\mathbf{r}_{t/n} = [0, -L_{nr}, 0]_t^T$, $\boldsymbol{\omega}_{h/t} = [0, \Omega, 0]_h^T$, $\boldsymbol{\alpha}_{h/t} = [0, \dot{\Omega}, 0]_h^T$, $\mathbf{r}_{c/h} = [0, 0, r_h]_c^T$, $\boldsymbol{\omega}_{b/c} = [0, 0, \dot{\theta}]_b^T$, $\boldsymbol{\alpha}_{b/c} = [0, 0, \ddot{\theta}]_b^T$. The indices after the vectors show in which coordinate system the vector components are expressed. All other position, velocity and acceleration vectors between two adjacent co-

ordinate systems in the kinematic chain (blade, cone, hub, tilt, nacelle, tower top, ground coordinate systems) are zero vectors. Λ and $\dot{\Lambda}$ are respectively the nacelle yaw velocity and acceleration, Ω and $\dot{\Omega}$ are respectively the rotor rotational velocity and acceleration, $\dot{\theta}$ and $\ddot{\theta}$ are respectively the blade pitch angular velocity and acceleration, r_h is the hub radius (distance between blade root and the rotor axis parallel to blade axis), L_{nr} is the distance between the origin of the hub coordinate system and the nacelle yaw axis normal to the rotor axis and γ is the rotor tilt angle.

To the relations between coordinate systems stated above, we have to add the tower top motion relative to the ground. Vectors $\boldsymbol{\omega}_{T/G}$, $\boldsymbol{\alpha}_{T/G}$ and $\mathbf{a}_{T/G}$ are not null when the tower is flexible.

The transformation matrices from one coordinate system to another are:

$$\mathbf{P}_{b/c} = \begin{bmatrix} c_\theta & -s_\theta & 0 \\ s_\theta & c_\theta & 0 \\ 0 & 0 & 1 \end{bmatrix} \tag{2.4}$$

$$\mathbf{P}_{c/h} = \begin{bmatrix} 1 & 0 & 0 \\ 0 & c_\beta & s_\beta \\ 0 & -s_\beta & c_\beta \end{bmatrix} \tag{2.5}$$

$$\mathbf{P}_{h/t} = \begin{bmatrix} c_\Psi & 0 & -s_\Psi \\ 0 & 1 & 0 \\ s_\Psi & 0 & c_\Psi \end{bmatrix} \tag{2.6}$$

$$\mathbf{P}_{t/n} = \begin{bmatrix} 1 & 0 & 0 \\ 0 & c_\gamma & -s_\gamma \\ 0 & s_\gamma & c_\gamma \end{bmatrix} \tag{2.7}$$

where θ, β, Ψ and γ are respectively the pitch, rotor coning, blade azimuth and rotor tilt angles. $c_i = \cos i$ and $s_i = \sin i$.

We know from kinematics that the expressions of acceleration $\mathbf{a}_{P/i}$, velocity $\mathbf{v}_{P/i}$ and position $\mathbf{r}_{P/i}$ of a point P in a coordinate system i when the acceleration $\mathbf{a}_{P/j}$, velocity $\mathbf{v}_{P/j}$ and position $\mathbf{r}_{P/j}$ of this point in coordinate system j are known are:

$$
\begin{cases}
\mathbf{a}_{P/i} = \mathbf{a}_{P/j} + \mathbf{a}_{j/i} + 2\boldsymbol{\omega}_{j/i} \times \mathbf{v}_{P/j} \\
\qquad + \boldsymbol{\omega}_{j/i} \times \boldsymbol{\omega}_{j/i} \times \mathbf{r}_{P/j} + \boldsymbol{\alpha}_{j/i} \times \mathbf{r}_{P/j} \\
\mathbf{v}_{P/i} = \mathbf{v}_{P/j} + \mathbf{v}_{j/i} + \boldsymbol{\omega}_{j/i} \times \mathbf{r}_{P/j} \\
\mathbf{r}_{P/i} = \mathbf{r}_{P/j} + \mathbf{r}_{j/i}
\end{cases}
\tag{2.8}
$$

where $\boldsymbol{\omega}_{j/i}$ and $\boldsymbol{\alpha}_{j/i}$ are respectively the angular velocity and the angular acceleration vectors of coordinate system j relative to coordinate system i. Using these equations, and the already stated relations between the different coordinate systems, from Eq. 2.3,

the inertial force on a mass element P on the blade can be expressed as:

$$
\begin{aligned}
\mathbf{F}_{iner} = & - m\boldsymbol{\omega}_{h/t} \times \boldsymbol{\omega}_{h/t} \times \mathbf{r}_{P/h} && \text{(1- centrifugal, rotor rotation)} \\
& - m\boldsymbol{\alpha}_{h/t} \times \mathbf{r}_{P/h} && \text{(2- inertial, rotor acceleration)} \\
& - m\boldsymbol{\omega}_{n/T} \times \boldsymbol{\omega}_{n/T} \times \mathbf{r}_{P/n} && \text{(3- centrifugal, nacelle rotation)} \\
& - m\boldsymbol{\alpha}_{n/T} \times \mathbf{r}_{P/n} && \text{(4- inertial, nacelle acceleration)} \\
& - 2m\boldsymbol{\omega}_{n/T} \times \boldsymbol{\omega}_{h/t} \times \mathbf{r}_{P/h} && \text{(5- gyrosc., rotor and nacelle rot.)} \\
& - m\boldsymbol{\omega}_{b/c} \times \boldsymbol{\omega}_{b/c} \times \mathbf{r}_{P/b} && \text{(6- centrifugal, blade pitch rotation)} \\
& - m\boldsymbol{\alpha}_{b/c} \times \mathbf{r}_{P/b} && \text{(7- inertial, blade pitch acceleration)} \\
& - 2m\boldsymbol{\omega}_{h/t} \times \boldsymbol{\omega}_{b/c} \times \mathbf{r}_{P/b} && \text{(8- gyrosc., blade pitching and rotor rot.)} \\
& - 2m\boldsymbol{\omega}_{n/T} \times \boldsymbol{\omega}_{b/c} \times \mathbf{r}_{P/b} && \text{(9- gyrosc., blade pitching and nacelle rot.)} \\
& - m\mathbf{a}_{T/G} && \text{(10- tower top motion)} \\
& - 2m\boldsymbol{\omega}_{T/G} \times \mathbf{v}_{P/b} && \text{(11- tower top motion)} \\
& - 2m\boldsymbol{\omega}_{T/G} \times \boldsymbol{\omega}_{b/c} \times \mathbf{r}_{P/b} && \text{(12- tower top motion)} \\
& - 2m\boldsymbol{\omega}_{T/G} \times \boldsymbol{\omega}_{h/t} \times \mathbf{r}_{P/h} && \text{(13- tower top motion)} \\
& - 2m\boldsymbol{\omega}_{T/G} \times \boldsymbol{\omega}_{n/T} \times \mathbf{r}_{P/n} && \text{(14- tower top motion)} \\
& - m\boldsymbol{\omega}_{T/G} \times \boldsymbol{\omega}_{T/G} \times \mathbf{r}_{P/T} && \text{(15- tower top motion)} \\
& - m\boldsymbol{\alpha}_{T/G} \times \mathbf{r}_{P/T} && \text{(16- tower top motion)} \\
& - m\mathbf{a}_{P/b} && \text{(17- blade deformation)} \\
& - 2m\boldsymbol{\omega}_{b/c} \times \mathbf{v}_{P/b} && \text{(18- blade deformation)} \\
& - 2m\boldsymbol{\omega}_{h/t} \times \mathbf{v}_{P/b} && \text{(19- blade deformation)} \\
& - 2m\boldsymbol{\omega}_{n/T} \times \mathbf{v}_{P/b} && \text{(20- blade deformation)}
\end{aligned}
\tag{2.9}
$$

The first two terms of the equation are the inertial loads due to the rotor rotation. The first one is a centrifugal force and the second one is due to the angular acceleration. The 3rd and 4th terms represent the same effects, but due to the nacelle rotation and angular acceleration. The 5th term is the gyroscopic force due to the combination of rotor and

nacelle rotations. Terms 6 to 9 are due to the blade pitch motion and depend on the blade mass distribution around its longitudinal axis. The 7 following terms are the effects of the tower top motion due to the tower deformation and the last 4 terms are due to the blade deformation.

For the development of the next section's equations, two simplifying hypotheses are made. Firstly, we consider that all the blade mass is concentrated on its longitudinal axis, so that terms 6 to 9 vanish. Secondly, the effects of the blade and tower deformation will be neglected. This allows us to more clearly characterize the effects of wind turbine operation parameters on the inertial loads and has the effect that terms 10 to 20 vanish.

With these hypotheses, it is possible to express the inertial load distribution on the blade in terms of force per unit length as:

$$
\begin{aligned}
\mathbf{p}_{iner} = & -m'\boldsymbol{\omega}_{h/t} \times \boldsymbol{\omega}_{h/t} \times \mathbf{r}_{P/h} \\
& -m'\boldsymbol{\alpha}_{h/t} \times \mathbf{r}_{P/h} \\
& -m'\boldsymbol{\omega}_{n/T} \times \boldsymbol{\omega}_{n/T} \times \mathbf{r}_{P/n} \\
& -m'\boldsymbol{\alpha}_{n/T} \times \mathbf{r}_{P/n} \\
& -2m'\boldsymbol{\omega}_{n/T} \times \boldsymbol{\omega}_{h/t} \times \mathbf{r}_{P/h}
\end{aligned}
\tag{2.10}
$$

where m' is the mass per unit length of the blade. The vectors expressed in the blade coordinate system are :

$$
\mathbf{r}_{P/h} = \begin{bmatrix} 0 \\ 0 \\ z + r_h \end{bmatrix}
\tag{2.11}
$$

$$
\mathbf{r}_{P/n} = \begin{bmatrix} L_{nr}c_\beta s_\theta \\ -L_{nr}c_\beta c_\theta \\ z + r_h + L_{nr}s_\beta \end{bmatrix}
\tag{2.12}
$$

$$
\boldsymbol{\omega}_{h/T} = \Omega \mathbf{A}_h
\tag{2.13}
$$

$$\boldsymbol{\omega}_{n/T} = \Lambda \mathbf{A}_n \tag{2.14}$$

$$\boldsymbol{\alpha}_{h/T} = \dot{\Omega} \mathbf{A}_h \tag{2.15}$$

$$\boldsymbol{\alpha}_{n/T} = \dot{\Lambda} \mathbf{A}_n \tag{2.16}$$

where $\mathbf{A}_h$ and $\mathbf{A}_n$ are unit vectors defined as

$$\mathbf{A}_h = \begin{bmatrix} -c_\beta s_\theta \\ c_\beta c_\theta \\ -s_\beta \end{bmatrix} \tag{2.17}$$

and

$$\mathbf{A}_n = \begin{bmatrix} -(s_\beta c_\gamma c_\Psi - c_\beta s_\gamma)s_\theta - c_\gamma s_\Psi c_\theta \\ (s_\beta c_\gamma c_\Psi - c_\beta s_\gamma)c_\theta - c_\gamma s_\Psi s_\theta \\ c_\beta c_\gamma c_\Psi + s_\beta s_\gamma \end{bmatrix} \tag{2.18}$$

2.3 Distribution of loads on the blade and blade root loads

In this section, an analytical expression is given for the loads distribution on the blade for each load type. Internal loads at blade root are also given as they are often used to compare load cases with each other. All vector components are expressed in the blade coordinate system.

Load distribution along blade length is defined by $\mathbf{p}(z) = \begin{bmatrix} p_x(z) & p_y(z) & p_z(z) \end{bmatrix}^T$ and $\mathbf{m}(z) = \begin{bmatrix} m_x(z) & m_y(z) & m_z(z) \end{bmatrix}^T$, which are respectively the applied forces and moments per unit length. The internal loads are $\mathbf{V}(z) = \begin{bmatrix} V_x(z) & V_y(z) & N(z) \end{bmatrix}^T$ where $V_x(z)$ and $V_y(z)$ are the shear forces and $N(z)$ is the normal force; and $\mathbf{M}(z) = \begin{bmatrix} M_x(z) & M_y(z) & M_t(z) \end{bmatrix}^T$ where $M_x(z)$ and $M_y(z)$ are the bending moments and $M_t(z)$ is the torsional moment.

2.3.1 Aerodynamic loads

Aerodynamic loads are computed by the aerodynamic routine of the aeroelasticity code using mostly blade element momentum theory. Aerodynamic forces along blade length are computed in the in-plane (p_{in}) and out-of-plane directions (p_{out}), respectively parallel to the x- and y-axes of the cone coordinate system. The radial aerodynamic force is neglected most of the time. The aerodynamic pitching moment m_p (positive when the pitch angle is decreased) is also computed by the aerodynamic solver.

In the blade coordinate system, the aerodynamic force and moment distributions are given by

$$\mathbf{p}_{aero}(z) = \begin{bmatrix} p_{in}c_\theta - p_{out}s_\theta \\ p_{in}s_\theta + p_{out}c_\theta \\ 0 \end{bmatrix} \tag{2.19}$$

and

$$\mathbf{m}_{aero}(z) = \begin{bmatrix} 0 \\ 0 \\ m_p \end{bmatrix} \tag{2.20}$$

where θ is the blade pitch angle.

The integration of these loads along blade length allows the computation of the blade root internal loads as:

$$\mathbf{V}_{aero}(0) = \int_0^L \mathbf{p}_{aero}dz \tag{2.21}$$

and

$$\mathbf{M}_{aero}(0) = \int_0^L \begin{bmatrix} -zp_{y,aero} \\ zp_{x,aero} \\ m_{z,aero} \end{bmatrix} dz \tag{2.22}$$

where L is the length of the blade. Note that these last two equations are valid for any types of loads.

Depending on the aerodynamic code used, the aerodynamic forces can be distributed forces (per unit length of the blade) computed at some location. Internal loads at blade root are then computed by numerical integration of equations 2.19 and 2.20 using, for instance, linear interpolation between these locations (Hansen, 2008). Other codes (Jonkman and Buhl Jr., 2005) compute concentrated loads at each aerodynamic blade element centre. Internal loads at blade root can then be computed using a summation instead of an integral in equations 2.19 and 2.20.

2.3.2 Gravitational loads

The gravitational force distribution along the blade is given by

$$\mathbf{p}_{grav}(z) = m'\mathbf{g} \tag{2.23}$$

where $\mathbf{g}$ is the gravitational acceleration vector ($\|\mathbf{g}\| = g \approx 9.81$ m/s^2), whose orientation is given by $[0, 0, -1]_n^T$ when expressed in the nacelle coordinate system. The force direction then depends on the orientation of the blade in space, i.e., pitch, azimuth, coning and tilt angles.

In the blade coordinate system, the gravitational force distribution is given by:

$$\mathbf{p}_{grav}(z) = m'g \begin{bmatrix} c_\gamma s_\Psi c_\theta - (c_\beta s_\gamma - s_\beta c_\gamma c_\Psi)s_\theta \\ c_\gamma s_\Psi s_\theta + (c_\beta s_\gamma - s_\beta c_\gamma c_\Psi)c_\theta \\ -s_\beta s_\gamma - c_\beta c_\gamma c_\Psi \end{bmatrix} \tag{2.24}$$

and the internal loads at the blade root are

$$\mathbf{V}_{grav}(0) = mg \begin{bmatrix} c_\gamma s_\Psi c_\theta - (c_\beta s_\gamma - s_\beta c_\gamma c_\Psi)s_\theta \\ c_\gamma s_\Psi s_\theta + (c_\beta s_\gamma - s_\beta c_\gamma c_\Psi)c_\theta \\ -s_\beta s_\gamma - c_\beta c_\gamma c_\Psi \end{bmatrix} \tag{2.25}$$

and

$$\mathbf{M}_{grav}(0) = Z_{cg}mg \begin{bmatrix} -c_\gamma s_\Psi s_\theta - (c_\beta s_\gamma - s_\beta c_\gamma c_\Psi)c_\theta \\ c_\gamma s_\Psi c_\theta - (c_\beta s_\gamma - s_\beta c_\gamma c_\Psi)s_\theta \\ 0 \end{bmatrix} \tag{2.26}$$

where m and Z_{cg} are respectively the total blade mass and the distance between the blade root and the blade centre of gravity:

$$m = \int_0^L m' dz \tag{2.27}$$

and

$$Z_{cg} = \frac{1}{m} \int_0^L m' z dz \tag{2.28}$$

Assuming that the coning and tilt angles are small, which is the case for most horizontal axis wind turbine, and that pitch angle is close to zero, which is the case below nominal wind speed, gravity causes a mostly axial load when the blade is pointing upward and downward and a mostly edgewise load when the blade is in the horizontal position. If the blade is in the feather position (pitch angle close to 90°), in the horizontal position, gravity causes mostly flapwise loading.

2.3.3 Inertial loads due to rotor rotation

This load type is given by the first term of Eq. 2.10. When loads are expressed in the blade coordinate system,

$$\mathbf{p}_{iner,1}(z) = m'\Omega^2(z + r_h)c_\beta \begin{bmatrix} -s_\beta s_\theta \\ s_\beta c_\theta \\ c_\beta \end{bmatrix} \tag{2.29}$$

and the integration over the blade length gives the following expressions for the internal loads at blade root:

$$\mathbf{V}_{iner,1}(0) = m\Omega^2(Z_{cg} + r_h)c_\beta \begin{bmatrix} -s_\beta s_\theta \\ s_\beta c_\theta \\ c_\beta \end{bmatrix} \tag{2.30}$$

and

$$\mathbf{M}_{iner,1}(0) = \Omega^2(I_0 + Z_{cg}mr_h)c_\beta \begin{bmatrix} -s_\beta c_\theta \\ -s_\beta s_\theta \\ 0 \end{bmatrix} \tag{2.31}$$

where I_0 is the blade mass moment of inertia about its root and is given by

$$I_0 = \int_0^L m'z^2 dz \tag{2.32}$$

Rotor rotation causes a centrifugal traction force that is applied in the blade's longitudinal axis direction for a rotor without coning. For an upwind turbine, as the coning angle increase, the out-of-plane component of this inertial force also increases generating loads that are in the same directions as the aerodynamic loads in normal operation. However, this phenomenon is reduced by the out-of-plane deflection of the blade.

2.3.4 Inertial loads due to rotor acceleration

This load component is given by the second term of Eq. 2.10. In the blade coordinate system, these loads are:

$$\mathbf{p}_{iner,2} = -m'\dot{\Omega}(z + r_h)c_\beta \begin{bmatrix} c_\theta \\ s_\theta \\ 0 \end{bmatrix} \tag{2.33}$$

and internal loads at blade root are:

$$\mathbf{V}_{iner,2}(0) = -m\dot{\Omega}(Z_{cg} + r_h)c_\beta \begin{bmatrix} c_\theta \\ s_\theta \\ 0 \end{bmatrix} \tag{2.34}$$

$$\mathbf{M}_{iner,2}(0) = -\dot{\Omega}(I_0 + Z_{cg}mr_h)c_\beta \begin{bmatrix} -s_\theta \\ c_\theta \\ 0 \end{bmatrix} \tag{2.35}$$

Rotor acceleration and deceleration create in-plane loads only. When the rotor is accelerating, the resulting inertial load is in the opposite direction of aerodynamic loads in normal operation. When braking, inertial loads add to aerodynamic loads. The tilt angle has no effect on these loads and a coning tend to slightly reduce them by a factor $\cos\beta$.

2.3.5   Inertial loads due to nacelle rotation

The third term of Eq. 2.10 gives the loads caused by the rotation of the wind turbine nacelle:

$$\mathbf{p}_{iner,3} = -m'(z)\Lambda^2 \begin{bmatrix} (z + r_h)(2c_\beta^2 c_\gamma s_\gamma c_\Psi s_\theta - c_\gamma s_\gamma c_\Psi s_\theta + c_\beta s_\beta s_\gamma^2 s_\theta \\ \quad -c_\beta s_\beta c_\gamma^2 c_\Psi^2 s_\theta - s_\beta c_\gamma s_\gamma s_\Psi c_\theta - c_\beta c_\gamma^2 c_\Psi s_\Psi c_\theta) \\ \quad +L_{nr}(-c_\beta c_\gamma^2 s_\theta - c_\gamma s_\gamma s_\Psi c_\theta - s_\beta c_\gamma s_\gamma c_\Psi s_\theta) \\ (z + r_h)(-2c_\beta^2 c_\gamma s_\gamma c_\Psi c_\theta + c_\beta s_\beta c_\gamma^2 c_\Psi^2 c_\theta - s_\beta c_\gamma s_\gamma s_\Psi s_\theta \\ \quad -c_\beta c_\gamma^2 c_\Psi s_\Psi s_\theta - c_\beta s_\beta s_\gamma^2 c_\theta + c_\gamma s_\gamma c_\Psi c_\theta) \\ \quad +L_{nr}(-c_\gamma s_\gamma s_\Psi s_\theta + s_\beta c_\gamma s_\gamma c_\Psi c_\theta + c_\beta c_\gamma^2 c_\theta) \\ (z + r_h)(+2c_\beta s_\beta c_\gamma s_\gamma c_\Psi + c_\beta^2 c_\gamma^2 c_\Psi^2 - c_\beta^2 s_\gamma^2 - c_\gamma^2) \\ \quad +L_{nr}(+c_\beta c_\gamma s_\gamma c_\Psi - s_\beta c_\gamma^2) \end{bmatrix} \tag{2.36}$$

and the internal loads at blade root are:

$$\mathbf{V}_{iner,3} = -m\Lambda^2 \begin{bmatrix} (Z_{cg} + r_h)(2c_\beta^2 c_\gamma s_\gamma c_\Psi s_\theta - c_\gamma s_\gamma c_\Psi s_\theta + c_\beta s_\beta s_\gamma^2 s_\theta \\ \quad -c_\beta s_\beta c_\gamma^2 c_\Psi^2 s_\theta - s_\beta c_\gamma s_\gamma s_\Psi c_\theta - c_\beta c_\gamma^2 c_\Psi s_\Psi c_\theta) \\ \quad +L_{nr}(-c_\beta c_\gamma^2 s_\theta - c_\gamma s_\gamma s_\Psi c_\theta - s_\beta c_\gamma s_\gamma c_\Psi s_\theta) \\ (Z_{cg} + r_h)(-2c_\beta^2 c_\gamma s_\gamma c_\Psi c_\theta + c_\beta s_\beta c_\gamma^2 c_\Psi^2 c_\theta - s_\beta c_\gamma s_\gamma s_\Psi s_\theta \\ \quad -c_\beta c_\gamma^2 c_\Psi s_\Psi s_\theta - c_\beta s_\beta s_\gamma^2 c_\theta + c_\gamma s_\gamma c_\Psi c_\theta) \\ \quad +L_{nr}(-c_\gamma s_\gamma s_\Psi s_\theta + s_\beta c_\gamma s_\gamma c_\Psi c_\theta + c_\beta c_\gamma^2 c_\theta) \\ (Z_{cg} + r_h)(+2c_\beta s_\beta c_\gamma s_\gamma c_\Psi + c_\beta^2 c_\gamma^2 c_\Psi^2 - c_\beta^2 s_\gamma^2 - c_\gamma^2) \\ \quad +L_{nr}(+c_\beta c_\gamma s_\gamma c_\Psi - s_\beta c_\gamma^2) \end{bmatrix} \tag{2.37}$$

$$\mathbf{M}_{iner,3} = -\Lambda^2 \begin{bmatrix} -(I_0 + m Z_{cg} r_h)(-2c_\beta^2 c_\gamma s_\gamma c_\Psi c_\theta + c_\beta s_\beta c_\gamma^2 c_\Psi^2 c_\theta - s_\beta c_\gamma s_\gamma s_\Psi s_\theta \\ \quad -c_\beta c_\gamma^2 c_\Psi s_\Psi s_\theta - c_\beta s_\beta s_\gamma^2 c_\theta + c_\gamma s_\gamma c_\Psi c_\theta) \\ \quad -m Z_{cg} L_{nr}(-c_\gamma s_\gamma s_\Psi s_\theta + s_\beta c_\gamma s_\gamma c_\Psi c_\theta + c_\beta c_\gamma^2 c_\theta) \\ (I_0 + m Z_{cg} r_h)(2c_\beta^2 c_\gamma s_\gamma c_\Psi s_\theta - c_\gamma s_\gamma c_\Psi s_\theta + c_\beta s_\beta s_\gamma^2 s_\theta \\ \quad -c_\beta s_\beta c_\gamma^2 c_\Psi^2 s_\theta - s_\beta c_\gamma s_\gamma s_\Psi c_\theta - c_\beta c_\gamma^2 c_\Psi s_\Psi c_\theta) \\ \quad +m Z_{cg} L_{nr}(-c_\beta c_\gamma^2 s_\theta - c_\gamma s_\gamma s_\Psi c_\theta - s_\beta c_\gamma s_\gamma c_\Psi s_\theta) \\ 0 \end{bmatrix} \tag{2.38}$$

For the sake of simplicity, the analysis of this load type is made for the particular case where the coning, tilt and pitch angle are zero ($\theta = \gamma = \beta = 0$). To distinguish with the complete solution, the variables are identified with a star (*) superscript symbol. In that case, the rotation and position vectors are

$$\mathbf{r}_{P/n}^* = \begin{bmatrix} 0 \\ -L_{nr} \\ z + r_h \end{bmatrix} \tag{2.39}$$

and

$$\mathbf{A}_n^* = \begin{bmatrix} -s_\Psi \\ 0 \\ c_\Psi \end{bmatrix} \tag{2.40}$$

The load distribution is then given by

$$\mathbf{p}_{iner,3}^* = m'\Lambda^2 \begin{bmatrix} (z + r_h)s_\Psi c_\Psi \\ -L_{nr} \\ (z + r_h)s_\Psi^2 \end{bmatrix} \tag{2.41}$$

and the internal loads at root are

$$\mathbf{V}_{iner,3}^*(0) = m\Lambda^2 \begin{bmatrix} (Z_{cg} + r_h)s_\Psi c_\Psi \\ -L_{nr} \\ (Z_{cg} + r_h)s_\Psi^2 \end{bmatrix} \tag{2.42}$$

$$\mathbf{M}_{iner,3}^*(0) = \Lambda^2 \begin{bmatrix} mZ_{cg}L_{nr} \\ (I_0 + mZ_{cg}r_h)s_\Psi c_\Psi \\ 0 \end{bmatrix} \tag{2.43}$$

Under these conditions, a rotation of the nacelle in any direction causes a constant negative flapwise loading and an edgewise loading that depends on the blade azimuth position. The latter is zero when the blade is in the horizontal and vertical position, reaches a maximum value at azimuth angles of 45° and 225° and a minimum value at azimuth angles of 135° and 315°. An axial force is also created by the nacelle rotation. This force is always null (when the blade is in the vertical position) or positive, reaching a maximum value when the blade is in the horizontal position.

2.3.6 Inertial loads due to nacelle acceleration

The fourth term of Eq. 2.10 gives the load caused by the acceleration of the wind turbine nacelle:

$$
\mathbf{p}_{iner,4} = -m'(z)\dot{\Lambda} \begin{bmatrix} (z+r_h)(s_\beta c_\gamma c_\Psi c_\theta - c_\gamma s_\Psi s_\theta - c_\beta s_\gamma c_\theta) \\ +L_{nr}(c_\gamma c_\Psi c_\theta - s_\beta c_\gamma s_\Psi s_\theta) \\ (z+r_h)(s_\beta c_\gamma c_\Psi s_\theta - c_\beta s_\gamma s_\theta + c_\gamma s_\Psi c_\theta) \\ +L_{nr}(c_\gamma c_\Psi s_\theta + s_\beta c_\gamma s_\Psi c_\theta) \\ L_{nr} c_\beta c_\gamma s_\Psi \end{bmatrix} \tag{2.44}
$$

and the internal loads at blade root are:

$$
\mathbf{V}_{iner,4} = -m\dot{\Lambda} \begin{bmatrix} (Z_{cg}+r_h)(s_\beta c_\gamma c_\Psi c_\theta - c_\gamma s_\Psi s_\theta - c_\beta s_\gamma c_\theta) \\ +L_{nr}(c_\gamma c_\Psi c_\theta - s_\beta c_\gamma s_\Psi s_\theta) \\ (Z_{cg}+r_h)(s_\beta c_\gamma c_\Psi s_\theta - c_\beta s_\gamma s_\theta + c_\gamma s_\Psi c_\theta) \\ +L_{nr}(c_\gamma c_\Psi s_\theta + s_\beta c_\gamma s_\Psi c_\theta) \\ L_{nr} c_\beta c_\gamma s_\Psi \end{bmatrix} \tag{2.45}
$$

$$
\mathbf{M}_{iner,4} = -\dot{\Lambda} \begin{bmatrix} -(I_0 + mZ_{cg}r_h)(s_\beta c_\gamma c_\Psi s_\theta - c_\beta s_\gamma s_\theta + c_\gamma s_\Psi c_\theta) \\ -mZ_{cg}L_{nr}(c_\gamma c_\Psi s_\theta + s_\beta c_\gamma s_\Psi c_\theta) \\ (I_0 + mZ_{cg}r_h)(s_\beta c_\gamma c_\Psi c_\theta - c_\gamma s_\Psi s_\theta - c_\beta s_\gamma c_\theta) \\ +mZ_{cg}L_{nr}(c_\gamma c_\Psi c_\theta - s_\beta c_\gamma s_\Psi s_\theta) \\ 0 \end{bmatrix} \tag{2.46}
$$

As for the previous case, an example is given for a turbine with no coning and tilt and with a pitch angle of 0°. The position and rotation vectors are then the same as stated in the previous section and the load distribution on the blade is:

$$
\mathbf{p}^*_{iner,4} = -m'\dot{\Lambda} \begin{bmatrix} L_{nr}c_\Psi \\ (z+r_h)s_\Psi \\ L_{nr}s_\Psi \end{bmatrix} \tag{2.47}
$$

$$\mathbf{V}^*_{iner,4}(0) = -m\dot{\Lambda} \begin{bmatrix} L_{nr}c_\Psi \\ (Z_{cg} + r_h)s_\Psi \\ L_{nr}s_\Psi \end{bmatrix} \tag{2.48}$$

$$\mathbf{M}^*_{iner,4}(0) = -\dot{\Lambda} \begin{bmatrix} -(I_0 + mZ_{cg}r_h)s_\Psi \\ mZ_{cg}L_{nr}c_\Psi \\ 0 \end{bmatrix} \tag{2.49}$$

In the particular conditions stated above, the nacelle acceleration causes axial, in-plane and out-of-plane loads that depend on the direction of the acceleration. In-plane forces are zero when the blade is in the horizontal position and reach their extremum values when the blade is in the vertical position. The out-of-plane and axial forces are null when the blade is in the vertical position and reach their extremum values when the blade is in the horizontal position.

2.3.7   Inertial loads due to gyroscopic effect

The last inertial effect, given by the fifth term of Eq. 2.10, is the gyroscopic load due to the combination of rotor and nacelle rotations. The distribution of the load along blade length is given by:

$$\mathbf{p}_{iner,5} = -2m'\Lambda\Omega(z + r_h)c_\beta \begin{bmatrix} -(c_\beta c_\gamma c_\Psi + s_\beta s_\gamma)s_\theta \\ (c_\beta c_\gamma c_\Psi + s_\beta s_\gamma)c_\theta \\ -(s_\beta c_\gamma c_\Psi - c_\beta s_\gamma) \end{bmatrix} \tag{2.50}$$

and the forces and bending moments at blade roots are:

$$\mathbf{V}_{iner,5}(0) = -2m\Lambda\Omega(Z_{cg} + r_h)c_\beta \begin{bmatrix} -(c_\beta c_\gamma c_\Psi + s_\beta s_\gamma)s_\theta \\ (c_\beta c_\gamma c_\Psi + s_\beta s_\gamma)c_\theta \\ -(s_\beta c_\gamma c_\Psi - c_\beta s_\gamma) \end{bmatrix} \tag{2.51}$$

$$\mathbf{M}_{iner,5}(0) = 2\Lambda\Omega(I_0 + Z_{cg}mr_h)(c_\beta^2 c_\gamma c_\Psi + s_\beta c_\beta s_\gamma)\begin{bmatrix} c_\theta \\ s_\theta \\ 0 \end{bmatrix} \tag{2.52}$$

Assuming that the coning and tilt angles are small, gyroscopic effects cause loads that are mostly in the out-of-plane direction with extreme values reached when the blade is in the vertical position.

2.4   Application of loads in a three-dimensional finite element model

As discussed in the introduction, different methods can be used to transfer the loads computed by aeroelastic simulations to a finite element model. One of them is to apply the complete set of loads (including aerodynamic, gravitational and inertial loads) at the same time. These loads are often output as internal load distributions. A step of processing is then necessary to obtain the external load distribution that results in the given internal load distribution. Once the load distribution is known, the method of applying them to the finite element model is similar to that of aerodynamic loads presented in the next subsection.

The approach used in the following sections separates the different load types, applying the gravitational and inertial loads as body loads.

2.4.1   Aerodynamic loads

The aerodynamic load on a wind turbine blade is a complex pressure and friction distribution. In some situations, knowing the angle of attack and the relative wind speed at a given location, it is possible to retrieve the pressure and friction distributions from airfoil data and apply them to the finite element model. However, in other situations, this distribution is not known. Airfoil data (lift, drag and moment coefficients from wind tunnel tests or numerical simulations) are often given only for a small range of angles of attack

(approx. $-5°$ to $15°$). They are then extrapolated using empirical relations to cover the $-180°$ to $180°$ range with no information about the pressure and friction distributions. There are also empirical corrections to blade element momentum theory (hub and tip loss factors, Glauert correction for high values of induction factors, stall delay, dynamic stall, ...) that change aerodynamic lift, drag and moment with no information on the pressure and friction distribution modifications (Hansen, 2008; Ning, 2013).

For these reasons, it is difficult to reproduce the exact pressure and friction distributions over the blade surface. But an efficient approach to apply aerodynamic loads on a shell finite element model of a wind turbine blade does not need to do it. It is sufficient to assure that the internal force and moment distributions (beam loads) over the blade are correct, neglecting local load application effects that are not important for structural design purpose. The stress and strain fields at a given location depend mostly on the internal loads at that location (result of applied loads outboard of this location) and very little on the locally applied loads.

Aerodynamic loads could typically be given in two ways : (1) as concentrated forces and moments at the centre of finite length aerodynamic elements or (2) as forces and moments per unit length given at some locations supposing linear interpolation between them. In both cases there are two forces (in-plane and out-of-plane) and a pitching moment (around the blade longitudinal axis). When loads are obtained in the second way, they could be transformed like the first way by dividing the blade in several sections, interpolating to get the load per unit length at the centre of each section and multiplying by the length of each section to get the total load (see Fig. 2.2).

As seen in the introduction, different approaches exist for applying these loads on the shell finite element model. The preferred method is to use interpolation elements (Nastran's RBE3). This kind of element allows the loads applied to a reference node to be transferred to connected nodes with no stiffening of the structure. One interpolation element is created at each blade section or aerodynamic element. The reference node (the one

where the forces and moments are applied) is located at the centre of the section, on the blade's longitudinal axis. The connected nodes are all nodes covered by the blade section or aerodynamic element. Figure 2.2 shows the aerodynamic load application process.
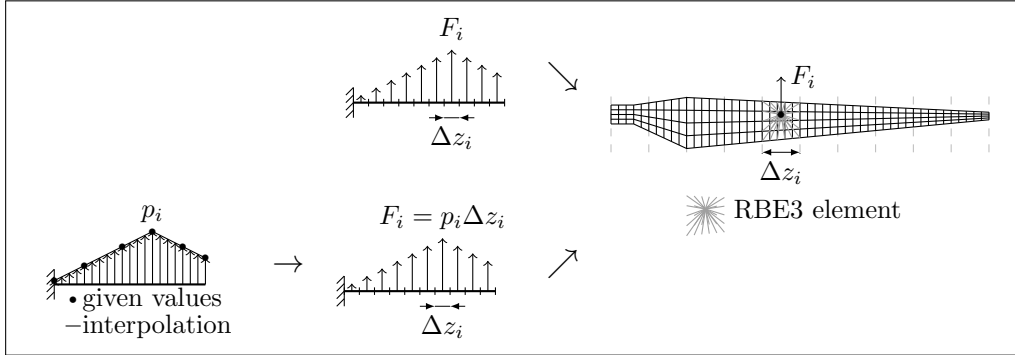
Figure 2.2 Method for the application of aerodynamic loads on a shell finite element model. F_i represents a concentrated force or moment and p_i, a force or moment per unit length

2.4.2 Gravitational loads

In the finite element model, where the global coordinate system is the blade coordinate system, gravity induced loads can easily be accounted for by applying gravity in the **g**-direction. This direction is given by the unit vector (see Eq. 2.24):

$$\hat{\mathbf{g}} = \frac{\mathbf{g}}{g} = \begin{bmatrix} c_\gamma s_\Psi c_\theta - (c_\beta s_\gamma - s_\beta c_\gamma c_\Psi) s_\theta \\ c_\gamma s_\Psi s_\theta + (c_\beta s_\gamma - s_\beta c_\gamma c_\Psi) c_\theta \\ -s_\beta s_\gamma - c_\beta c_\gamma c_\Psi \end{bmatrix} \tag{2.53}$$

where $g = \|\mathbf{g}\| \approx 9.81 \text{ m/s}^2$.

2.4.3 Inertial loads due to rotor speed and acceleration

Finite element software packages allow the definition of this kind of body load by defining an axis of rotation, a point through which this axis pass and rotation speed and

acceleration. In this case, the axis of rotation is the positive y-axis of the hub system:

$$\mathbf{A}_h = \begin{bmatrix} -c_\beta s_\theta \\ c_\beta c_\theta \\ -s_\beta \end{bmatrix} \tag{2.54}$$

and the point corresponding to the rotor centre and through which the axis of rotation passes is

$$\mathbf{n}_h = \begin{bmatrix} 0 \\ 0 \\ -r_h \end{bmatrix} \tag{2.55}$$

When preparing the FE model, the user just has to define body loads by specifying an angular speed Ω and acceleration $\dot{\Omega}$ around an axis defined by the unit vector $\mathbf{A}_h$ and passing through point $\mathbf{n}_h$.

2.4.4   Inertial loads due to nacelle speed and acceleration

Here, (as for the centrifugal loads due to rotor speed and acceleration) an axis of rotation, a point through which this axis passes and a rotation speed and acceleration need to be defined. The axis of rotation is the positive z-axis of the nacelle coordinate system. In the blade coordinate system, the rotation speed and acceleration vector is

$$\mathbf{A}_n = \begin{bmatrix} -(s_\beta c_\gamma c_\Psi - c_\beta s_\gamma)s_\theta - c_\gamma s_\Psi c_\theta \\ (s_\beta c_\gamma c_\Psi - c_\beta s_\gamma)c_\theta - c_\gamma s_\Psi s_\theta \\ c_\beta c_\gamma c_\Psi + s_\beta s_\gamma \end{bmatrix} \tag{2.56}$$

The point on the nacelle rotation axis is selected as the intersection point between the rotor axis and the nacelle rotation axis which is the origin of the nacelle coordinate

system. In the blade coordinate system, this point is

$$\mathbf{n}_n = -L_{nr} \begin{bmatrix} s_\theta c_\beta \\ -c_\beta c_\theta \\ s_\beta + r_h/L_{nr} \end{bmatrix} \tag{2.57}$$

As for the previous case, when preparing the FE model, body loads have to be defined by specifying an angular speed Λ and acceleration $\dot{\Lambda}$ around an axis defined by the unit vector $\mathbf{A}_n$ and passing through point $\mathbf{n}_n$.

2.4.5 Inertial loads due to gyroscopic effects

The gyroscopic loads are harder to apply in a finite element model, although some solvers have the possibility to do it. Making the assumption that all the blade mass is concentrated on its longitudinal axis and neglecting the axial loads (that are small compared to the in-plane and out-of-plane loads, especially if coning and tilt angles are small), it is possible to make an analogy between gyroscopic forces and forces due to an angular acceleration. Taking an angular acceleration of magnitude

$$\alpha_g = -2\Lambda\Omega c_\beta (c_\beta c_\gamma c_\Psi - s_\beta s_\gamma) \tag{2.58}$$

around the unit vector

$$\mathbf{A}_g = \begin{bmatrix} c_\theta \\ s_\theta \\ 0 \end{bmatrix} \tag{2.59}$$

and passing through the intersection point between the blade's longitudinal axis and the rotor axis

$$\mathbf{n}_h = \begin{bmatrix} 0 \\ 0 \\ -r_h \end{bmatrix} \tag{2.60}$$

This results in a force distribution equal to

$$\mathbf{p} = m'\alpha_g \mathbf{A}_g \times \left(\begin{bmatrix} 0 \\ 0 \\ z \end{bmatrix} - \mathbf{n}_h \right) = -2m'\Lambda\Omega c_\beta(c_\beta c_\gamma c_\Psi + s_\beta s_\gamma)(z + r_h) \begin{bmatrix} -s_\theta \\ c_\theta \\ 0 \end{bmatrix} \qquad (2.61)$$

which is the same as Eq. 2.50 except that the axial component is neglected. This gives a practical way to include gyroscopic loads in the finite element model even if this kind of load is not implemented in the solver used. The resulting applied load distribution will be close to the real distribution if the coning and tilt angles are small and if the blade mass is concentrated close to its longitudinal axis.

2.5 Application on the WESNet 10 kW wind turbine

To illustrate the method described above, one of the critical load cases of the WESNet 10 kW wind turbine (described in Chapter 1) is studied. This turbine, with its downwind free yaw configuration and its variable speed rotor, offers a good example as all the load components discussed in this chapter are likely to occur. The turbine and blade characteristics that are necessary to compute the loads are as follows: $m = 28.00$ kg, $Z_{cg} = 0.9100$ m, $I_0 = 47.66$ kg·m^2, $L_{nr} = -0.63$ m, $r_h = 0.28$ m, $\beta = -3°$, $\gamma = 0°$. Note that since the rotor has a downwind configuration with a downwind coning, the overhang length and coning angle have negative values.

The studied load case was obtained from a simulation using the NREL's FAST aeroelastic software (Jonkman and Buhl Jr., 2005). To conform to the hypotheses of this chapter, the blade, tower and shaft deformation degrees of freedom were disabled during the FAST simulation (to get rigid blades, tower and shaft). This software supposes, as in this chapter, that the blade mass is concentrated on its longitudinal axis. In the FAST models, the generalized dynamic wake and blade element momentum models with the Beddoes dynamic stall model were used and the time step was set to 0.005 s.

The example load case arises during an extreme operating gust (IEC 61400-2 design load case 1.3 at rated wind speed of 9.5 m/s). The gust causes an acceleration of the rotor, which causes yawing of the free yaw nacelle. The result is a combination of inertial loads due to rotor speed and acceleration; nacelle speed and acceleration; and gyroscopic effect due to rotor and nacelle rotation. Table 2.1 presents the aerodynamic loads and wind turbine operation parameters for this particular load case.

Taking the information of Table 2.1 and the mass, inertia and turbine configuration data presented above, Eq. 2.21, 2.22, 2.25, 2.26, 2.30, 2.31, 2.34, 2.35, 2.37, 2.38, 2.45, 2.46, 2.51 and 2.52 can be used to compute loads of all types. Theses results are presented in Table 2.2 ("This work" column). Also presented in this table are the internal forces and moments at root given by the aeroelastic model ("FAST" column). Only total loads are presented as FAST does not output separated load types. A shell finite element model of the blade has been made and loads have been applied as presented in Section 2.4. The Altair's Optistruct finite element solver was used to evaluate all load types separately and then, all together and the total applied loads were output and presented in Table 2.2 ("FEM" column). For a description of the FE model, see Section 1.5.

Reminding that the critical load component is frequently the flapwise bending moment, we will now focus our attention on it. According to the blade coordinate system used here, this bending moment is M_x and should be negative in normal operation (i.e., when aerodynamic loads are dominant; see Figure 2.1). However, one of the critical load cases resulting from the analysis of the WESNet wind turbine (the one studied in this section) yields a flapwise bending moment that is in the opposite direction (positive value of M_x). The equations developed in Section 2.3 are useful to understand this load case.

First, we can observe that the aerodynamic flapwise bending moment is effectively in the normal direction. The dominant load types in this load case are the inertial loads due to rotor rotation ($M_{x,iner,1}$) and to the gyroscopic effects due to a combination of rotor and nacelle rotations ($M_{x,iner,5}$), the latter being the most important. This analysis

Table 2.1 Load case used in the numerical application. z and Δz are respectively the blade's aerodynamic element centre and length. F_T and F_N are respectively the tangential and normal aerodynamic forces on the element. F_T is in the x-direction of the cone coordinate system of this paper and F_N is in the y-direction of this same coordinate system. M_P is the pitching moment, positive when leading edge goes downwind (around z-axis of the blade or cone coordinate system)

z [m]	Δz [m]	F_T [N]	F_N [N]	M_P [N·m]
0.1034	0.207	0.000	0.000	0.243
0.3334	0.253	0.000	0.000	1.097
0.5600	0.200	31.160	13.133	-0.744
0.7600	0.200	40.094	15.693	-0.812
0.9600	0.200	34.318	12.698	-1.126
1.1600	0.200	37.074	12.307	-1.085
1.3600	0.200	41.319	13.582	-0.289
1.5600	0.200	49.033	15.036	0.031
1.7600	0.200	51.525	13.360	-0.275
1.9600	0.200	45.504	9.104	-0.270
2.1600	0.200	38.053	5.495	-0.517
2.3600	0.200	22.920	2.056	-0.601
2.5600	0.200	19.079	0.812	-0.638
2.8100	0.300	12.848	-0.688	-1.116
3.0600	0.200	-0.345	-0.875	-0.768
3.2600	0.200	-5.879	-0.752	-0.730
3.4600	0.200	-7.169	-0.534	-0.639
3.6600	0.200	-0.067	-0.794	-0.495
$\theta = -2.021° = -0.03527$ rad				
$\Psi = 183.9° = 3.210$ rad				
$\Omega = 222.1$ rpm $= 23.26$ rad/s				
$\dot{\Omega} = 65.47°/s^2 = 1.143$ rad/s^2				
$\Lambda = -71.22°/s = -1.243$ rad/s				
$\dot{\Lambda} = -234.9°/s^2 = -4.100$ rad/s^2				
$g = 9.81$ m/s^2				

gives insight about some solutions to reduce the loads associated with this load case. The installation of a damping system to reduce the nacelle rotation speed would reduce

the gyroscopic loads. Another solution could be to limit the rotation speed of the rotor. Finally, looking at Equation 2.31, we can conclude that a reduction of the coning angle would reduce the flapwise bending moment due to rotor rotation. Nevertheless we have to take into account that the blade is not perfectly rigid so that the blade will deform and this could slightly change the conclusion drawn from an analysis with rigid blades.

When comparing the total load values of this work with values output by the FAST aeroelastic solver (Table 2.2), all differences are within a margin of 0.05 % except for the difference in M_y value. This is probably caused by a rounding error of the azimuth angle (for that angle, sine computation amplifies the error). However, when comparing the root load values obtained from the equations of Section 2.3 with the summed loads at root in the finite element model, some load types and directions show an important difference. This is due to the fact that, in the finite element model, blade mass is not concentrated on its longitudinal axis. The values obtained from the finite element model are more precise because they take into account the real mass distribution of the blade. This causes loads on blade that are slightly different than what is predicted by the equations of Section 2.3 and by an aeroelastic solver that suppose that blade mass is concentrated on its longitudinal axis. These differences are noticed in the edgewise loads and torsional moment. On the other hand, the error in flapwise loads and axial force (that are the critical loads) is minimal.

To get the same values as those obtained in the finite element model, it is possible to recompute the equations of Section 2.3 by using a different form of Equation 2.10 where the blade mass is not supposed to be concentrated on its longitudinal axis:

$$
\begin{aligned}
\mathbf{f}_{iner} = & -\rho \boldsymbol{\omega}_{h/t} \times \boldsymbol{\omega}_{h/t} \times \mathbf{r}_{P/h} \\
& -\rho \boldsymbol{\alpha}_{h/t} \times \mathbf{r}_{P/h} \\
& -\rho \boldsymbol{\omega}_{n/T} \times \boldsymbol{\omega}_{n/T} \times \mathbf{r}_{P/n} \\
& -\rho \boldsymbol{\alpha}_{n/T} \times \mathbf{r}_{P/n} \\
& -2\rho \boldsymbol{\omega}_{n/T} \times \boldsymbol{\omega}_{h/t} \times \mathbf{r}_{P/h}
\end{aligned}
\tag{2.62}
$$

where ρ is the material density and $\mathbf{f}_{iner}$ is the inertial force per unit volume at a given infinitesimal point on the blade. When using the position vector $\mathbf{r}_{P/b} = [x, y, z]^T$ instead of $\mathbf{r}_{P/b} = [0, 0, z]^T$ and integrating over the surface of each cross section, the distribution of force and moment per unit length of the blade can be expressed in function of each cross-sectional mass per unit length (m'), centre of gravity (x_{cg} and y_{cg}) and mass moment of inertia per unit length (i_x, i_y and i_{xy}). After that, integration over blade length gives internal loads at root that are functions of blade's mass (m), centre of gravity (X_{cg}, Y_{cg} and Z_{cg}) and mass moment of inertia (I_x, I_y, I_z, I_{xy}, I_{xz} and I_{yz}).

Blade root internal loads computed this way for the example wind turbine are reported in Table 2.2 ("Detailed" column) and show really small differences when compared to the finite element model values. The only noticeable difference is for the axial load caused by the gyroscopic effect ($N_{x,iner,5}$) but that difference is expected since the axial force is not taken into account by the method of applying this type of load in the finite element model as explained earlier. This confirms that the differences observed between values computed using equations of Section 2.3 and the finite element model values are due to the different blade mass distribution in both models. One of the advantages of the proposed method is that the inertial loads are applied correctly using the real mass distribution of the blade.

Table 2.2 Internal forces and moments at blade root. Forces are in N and moments, in N·m. Column "This work" computed from the equations of Section 2.3. For the "FAST" column, loads are converted from FAST blade coordinate system to this work coordinate system: $V_x = -$ RootFyb1, $V_y =$ RootFxb1, $N =$ RootFzb1, $M_x = -$ RootMyb1, $M_y =$ RootMxb1, $M_t =$ RootMzc1

Load	This work	FAST	Detailed	FEM	Diff. 1	Diff. 2	Diff. 3
$V_{x,aero}$	124.0	-	124.0	124.0	-	0.00	0.00
$V_{y,aero}$	405.3	-	405.3	405.3	-	0.01	0.01
N_{aero}	0.000	-	0.000	0	-	-	-
$M_{x,aero}$	-607.2	-	-607.2	-607.2	-	0.00	0.00
$M_{y,aero}$	157.5	-	157.5	157.5	-	0.02	0.02
$M_{t,aero}$	-8.734	-	-8.734	-8.734	-	0.00	0.00
$V_{x,grav}$	-19.18	-	-19.18	-19.18	-	-0.02	-0.03
$V_{y,grav}$	-13.68	-	-13.67	-13.67	-	0.04	0.03
N_{grav}	273.7	-	273.7	273.6	-	0.02	0.02
$M_{x,grav}$	12.44	-	13.87	13.87	-	-10.28	-0.01
$M_{y,grav}$	-17.45	-	-12.34	-12.34	-	41.42	-0.04
$M_{t,grav}$	0.000	-	0.3555	0.3549	-	-100.00	0.03
$V_{x,iner,1}$	-33.22	-	-319.0	-318.6	-	-89.57	0.13
$V_{y,iner,1}$	-941.4	-	-931.3	-931.4	-	1.08	-0.01
$N_{iner,1}$	17970	-	17970	17980	-	-0.03	-0.03
$M_{x,iner,1}$	1548	-	1645	1644	-	-5.83	0.05
$M_{y,iner,1}$	-54.63	-	20.39	20.29	-	-369.26	0.48
$M_{t,iner,1}$	0.000	-	32.32	32.27	-	-100.00	0.17
$V_{x,iner,2}$	-38.00	-	-38.00	-38.00	-	-0.01	-0.01
$V_{y,iner,2}$	1.341	-	1.372	1.372	-	-2.26	0.00
$N_{iner,2}$	0.000	-	-0.6032	-0.6023	-	-100.00	0.12
$M_{x,iner,2}$	-2.205	-	-2.267	-2.268	-	-2.78	-0.04
$M_{y,iner,2}$	-62.49	-	-62.56	-62.58	-	-0.15	-0.03
$M_{t,iner,2}$	0.000	-	0.1946	0.1928	-	-100.00	1.14
$V_{x,iner,3}$	4.541	-	3.735	3.737	-	21.51	-0.05
$V_{y,iner,3}$	29.76	-	29.98	29.98	-	-0.75	0.00
$N_{iner,3}$	1.805	-	1.760	1.760	-	2.56	0.00
$M_{x,iner,3}$	-28.95	-	-29.20	-29.20	-	-0.85	0.01
$M_{y,iner,3}$	6.762	-	5.863	5.865	-	15.29	-0.03
$M_{t,iner,3}$	0.000	-	-0.5934	-0.5925	-	-100.00	0.08
$V_{x,iner,4}$	78.90	-	79.49	79.49	-	-0.74	0.00
$V_{y,iner,4}$	-12.34	-	-10.20	-10.20	-	20.97	0.01
$N_{iner,4}$	4.912	-	5.060	5.060	-	-2.92	0.00
$M_{x,iner,4}$	18.23	-	15.85	15.86	-	14.96	-0.09
$M_{y,iner,4}$	76.79	-	77.61	77.62	-	-1.07	-0.01
$M_{t,iner,4}$	0.000	-	-1.107	-1.201	-	-100.00	-7.83
$V_{x,iner,5}$	-67.60	-	-67.67	-67.62	-	-0.03	0.08
$V_{y,iner,5}$	-1916	-	-1918	-1916	-	-0.02	0.09
$N_{iner,5}$	-100.5	-	-100.6	7.290	-	-1478.04	-1479.51
$M_{x,iner,5}$	3150	-	3147	3151	-	-0.02	-0.13
$M_{y,iner,5}$	-111.2	-	-113.3	-110.0	-	1.06	3.02
$M_{t,iner,5}$	0.000	-	43.42	42.77	-	-100.00	1.53
$V_{x,total}$	49.45	49.47	-236.6	-236.1	-0.04	-120.94	0.22
$V_{y,total}$	-2447	-2446	-2436	-2435	0.03	0.48	0.05
N_{total}	18150	18150	18150	18260	0.03	-0.58	-0.58
$M_{x,total}$	4091	4091	4183	4186	0.00	-2.27	-0.08
$M_{y,total}$	-4.653	-4.626	73.17	76.39	0.58	-106.09	-4.21
$M_{t,total}$	-8.734	-8.733	65.86	65.06	0.01	-113.42	1.24
Diff. 1: (This work−FAST)/(FAST)×100							
Diff. 2: (This work−FEM)/(FEM)×100							
Diff. 3: (Detailed−FEM)/(FEM)×100							

2.6 Conclusion

One of the objectives of this chapter was to propose a method to study the contributions of different load types in the total load on a wind turbine blade computed during an aeroelastic simulation. This has been done by developing analytical equations allowing the computation of the values of the different load types as a function of the wind turbine operation parameters (speed and acceleration of the rotor and the nacelle; azimuth and pitch angles), geometry (tilt and coning angle; rotor hub radius; distance between the tower axis and the rotor plane) and blade mass parameters. This set of equations could also be useful to determine the effects of some geometric and operation parameters on the wind turbine blade loads, especially at the preliminary stages of the design process.

The second objective of the chapter was to describe a method to take the loads computed by an aeroelastic simulation and apply them to a three-dimensional finite element model of a blade. The proposed method consists in applying the aerodynamic loads using RBE3 elements and applying gravitational and inertial loads as body forces. All the axes and points of rotation and acceleration are defined in order to apply the different inertial load types.

The advantages of this method are:

- The applied inertial loads take into account the real blade mass distribution around its longitudinal axis (with an exception for the gyroscopic load).

- A modification of the blade design that results in a change of its mass properties is directly accounted for in the applied loads of the finite element model. This is particularly useful for a finite element model using structural optimization: inertial and gravitational loads are automatically adjusted according to the blade mass properties during the optimization process.

- It is possible to apply a different safety factor on different load types if the standard used prescribes it.

- It is possible to study the effects of the wind turbine's geometric characteristics and operating conditions without the necessity of simulating a particular situation in an aeroelastic simulation.

All the methods and equations proposed in this chapter are based on the hypothesis that the blade and the tower are rigid. Consequently, they are well designed for use in the preliminary stages of the design process, if the tower and the blades are considered rigid in the aeroelastic simulation. This allows the designer to get a first set of loads to start the design with minimal information about the blade mass.

However, even when modelling the blade and tower flexibility, the proposed equations could yield useful information for understanding the effects of the different load types on the total blade load.

WIND TURBINE BLADE STRUCTURAL MODELS

3.1 Introduction

This chapter concentrates on the second and third objectives of this thesis. It presents four different models for blade structural analysis, from the simplest to the more complex: (1) simple model, (2) classical strength of materials model, (3) cross-sectional finite element model and (4) 3D shell finite element model. For each model, the methods for the computation of eigenfrequencies, deflection, stresses, strains, buckling, strength and cross-sectional properties are presented, where applicable. The first two models are built based on the literature. The last two models are contributions of the author.

Before the description of these four models, a section is dedicated to a review of some generalities about beam cross-sectional properties.

3.2 Generalities about beam cross-sectional properties

3.2.1 Cross-sectional stiffness matrix $\mathbf{K}_s$

The relation between beam internal loads $\mathbf{V}$ and beam generalized strains $\boldsymbol{\kappa}$, for a given cross section is

$$\mathbf{V} = \mathbf{K}_s \boldsymbol{\kappa} \tag{3.1}$$

In the case of a Timoshenko beam and for a general case where coupling exists between all deformation modes, Eq. 3.1 could be expressed as

$$
\begin{bmatrix} V_x \\ V_y \\ N \\ M_x \\ M_y \\ M_t \end{bmatrix} = \begin{bmatrix} K_{s11} & K_{s12} & K_{s13} & K_{s14} & K_{s15} & K_{s16} \\ K_{s12} & K_{s22} & K_{s23} & K_{s24} & K_{s25} & K_{s26} \\ K_{s13} & K_{s23} & K_{s33} & K_{s34} & K_{s35} & K_{s36} \\ K_{s14} & K_{s24} & K_{s34} & K_{s44} & K_{s45} & K_{s46} \\ K_{s15} & K_{s25} & K_{s35} & K_{s45} & K_{s55} & K_{s56} \\ K_{s16} & K_{s26} & K_{s36} & K_{s46} & K_{s56} & K_{s66} \end{bmatrix} \begin{bmatrix} \gamma_{zx}^0 \\ \gamma_{yz}^0 \\ \epsilon_z^0 \\ \kappa_x \\ \kappa_y \\ \kappa_z \end{bmatrix}
\tag{3.2}
$$

where V_x and V_y are the shear forces, N is the axial force, M_x and M_y are the bending moments and M_t is the torsional moment. Note that $\mathbf{K}_s$ is a symmetric matrix and that here, the beam longitudinal axis is along the z-axis. The beam generalized strains can be expressed as functions of the displacements of the beam reference axis and their derivatives :

$$
\begin{aligned}
\gamma_{zx}^0 &= \frac{\partial \chi_x}{\partial z} - \varphi_y \\
\gamma_{yz}^0 &= \frac{\partial \chi_y}{\partial z} + \varphi_x \\
\epsilon_z^0 &= \frac{\partial \chi_z}{\partial z} \\
\kappa_x &= \frac{\partial \varphi_x}{\partial z} \\
\kappa_y &= \frac{\partial \varphi_y}{\partial z} \\
\kappa_z &= \frac{\partial \varphi_z}{\partial z}
\end{aligned}
\tag{3.3}
$$

where χ_x, χ_y and χ_z are the displacement of the beam reference axis and φ_x, φ_y and φ_z are the rotations of its section (see Figure 3.1).

For the particular case where the origin of the cross-sectional coordinate system is coincident with the elastic and shear centres, and the x and y-axes are the principal axes of
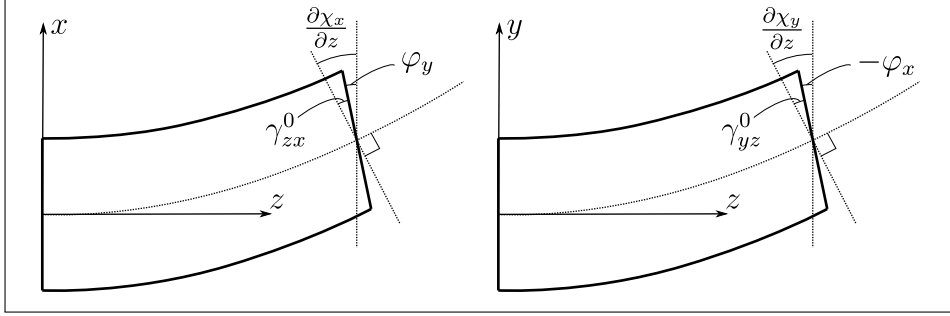
Figure 3.1   Variables for the beam generalized strains

bending, Equation 3.1 reduces to

$$
\begin{bmatrix} V_x \\ V_y \\ N \\ M_x \\ M_y \\ M_t \end{bmatrix} = \begin{bmatrix} k_x\overline{GA}_x & 0 & 0 & 0 & 0 & 0 \\ 0 & k_y\overline{GA}_y & 0 & 0 & 0 & 0 \\ 0 & 0 & \overline{EA} & 0 & 0 & 0 \\ 0 & 0 & 0 & \overline{EI}_x & 0 & 0 \\ 0 & 0 & 0 & 0 & \overline{EI}_y & 0 \\ 0 & 0 & 0 & 0 & 0 & \overline{GJ} \end{bmatrix} \begin{bmatrix} \gamma_{zx}^0 \\ \gamma_{yz}^0 \\ \epsilon_z^0 \\ \kappa_x \\ \kappa_y \\ \kappa_z \end{bmatrix} \tag{3.4}
$$

where

$$
\overline{GA}_x = \int G_{zx}\,\mathrm{d}A \tag{3.5}
$$

$$
\overline{GA}_y = \int G_{yz}\,\mathrm{d}A \tag{3.6}
$$

$$
\overline{EA} = \int E_z\,\mathrm{d}A \tag{3.7}
$$

$$
\overline{EI}_x = \int E_z y^2\,\mathrm{d}A \tag{3.8}
$$

$$
\overline{EI}_y = \int E_z x^2\,\mathrm{d}A \tag{3.9}
$$

k_x and k_y are the correction factors for transverse shear (Cowper, 1966) and $\overline{GJ}$ is obtained from the solution of the torsion problem. Note that for an axisymmetric cross section:

$$
\overline{GJ} = \int (x^2 G_{yz} + y^2 G_{zx})\,\mathrm{d}A \tag{3.10}
$$

As seen in Section 2.1, some aeroelastic software like FAST (with Elastodyn module) and Bladed requires only the bending stiffnesses of the blade cross section ($\overline{EI}_1$ and $\overline{EI}_2$, where the 12-coordinate system is aligned with the principal axes of bending). However, more recent software like HAWC2 and FAST (with Beamdyn module) requires a full 6×6 cross-sectional stiffness matrix.

Returning to a general cross section, in the case of an Euler beam, the shear forces effects are neglected and the behaviour law of the beam's cross section is

$$
\begin{bmatrix} N \\ M_x \\ M_y \\ M_t \end{bmatrix} = \begin{bmatrix} K_{s11} & K_{s12} & K_{s13} & K_{s14} \\ K_{s12} & K_{s22} & K_{s23} & K_{s24} \\ K_{s13} & K_{s23} & K_{s33} & K_{s34} \\ K_{s14} & K_{s24} & K_{s34} & K_{s44} \end{bmatrix} \begin{bmatrix} \epsilon_z^0 \\ \kappa_x \\ \kappa_y \\ \kappa_z \end{bmatrix}
\tag{3.11}
$$

Note that the Euler cross-sectional stiffness matrix will be equal to the Timoshenko cross-sectional stiffness matrix (with removed first two lines and column) only if there is no coupling between the beam transverse shear and the other deformation modes. In Equation 3.11, $\mathbf{K}_s$ is still a symmetric matrix and the beam generalized strains are expressed as:

$$
\begin{aligned}
\gamma_{zx}^0 &= \frac{\partial \chi_x}{\partial z} - \varphi_y = 0 \Rightarrow \frac{\partial \chi_x}{\partial z} = \varphi_y \\
\gamma_{yz}^0 &= \frac{\partial \chi_y}{\partial z} + \varphi_x = 0 \Rightarrow \frac{\partial \chi_y}{\partial z} = -\varphi_x \\
\epsilon_z^0 &= \frac{\partial \chi_z}{\partial z} \\
\kappa_x &= \frac{\partial \varphi_x}{\partial z} = -\frac{\partial^2 \chi_y}{\partial z^2} \\
\kappa_y &= \frac{\partial \varphi_y}{\partial z} = \frac{\partial^2 \chi_x}{\partial z^2} \\
\kappa_z &= \frac{\partial \varphi_z}{\partial z}
\end{aligned}
\tag{3.12}
$$

An error could occur in using this model if the beam's reference axis is not coincident with the cross section's shear centre. In that case, the shear forces induce a torsional deformation and this phenomenon is not taken into account as the shear forces effects

are neglected. Thus, an Euler beam model stiffness matrix should be computed using a reference axis that is coincident with the shear centre (Hodges and Yu, 2007).

The relation between beam internal load and generalized strains could also be expressed using the cross-sectional compliance matrix as

$$\boldsymbol{\kappa} = \mathbf{K}_s^{-1}\mathbf{V} = \mathbf{F}_s\mathbf{V} \tag{3.13}$$

or, in the developed form,

$$
\begin{bmatrix} \gamma_{zx}^0 \\ \gamma_{yz}^0 \\ \epsilon_z^0 \\ \kappa_x \\ \kappa_y \\ \kappa_z \end{bmatrix} = \begin{bmatrix} F_{s11} & F_{s12} & F_{s13} & F_{s14} & F_{s15} & F_{s16} \\ F_{s12} & F_{s22} & F_{s23} & F_{s24} & F_{s25} & F_{s26} \\ F_{s13} & F_{s23} & F_{s33} & F_{s34} & F_{s35} & F_{s36} \\ F_{s14} & F_{s24} & F_{s34} & F_{s44} & F_{s45} & F_{s46} \\ F_{s15} & F_{s25} & F_{s35} & F_{s45} & F_{s55} & F_{s56} \\ F_{s16} & F_{s26} & F_{s36} & F_{s46} & F_{s56} & F_{s66} \end{bmatrix} \begin{bmatrix} V_x \\ V_y \\ N \\ M_x \\ M_y \\ M_t \end{bmatrix} \tag{3.14}
$$

The compliance matrix of an Euler beam model is equal to the compliance matrix of a Timoshenko beam model from which the first two rows and columns are removed.

3.2.2 Coordinate system transformation

The relation between the displacements of the reference axis in two parallel coordinate systems (Figure 3.2) is

$$
\begin{aligned}
\chi_x &= \chi_x' + b\varphi_z' \\
\chi_y &= \chi_y' - a\varphi_z' \\
\chi_z &= \chi_z' - b\varphi_x' + a\varphi_y' \\
\varphi_x &= \varphi_x' \\
\varphi_y &= \varphi_y' \\
\varphi_z &= \varphi_z'
\end{aligned} \tag{3.15}
$$
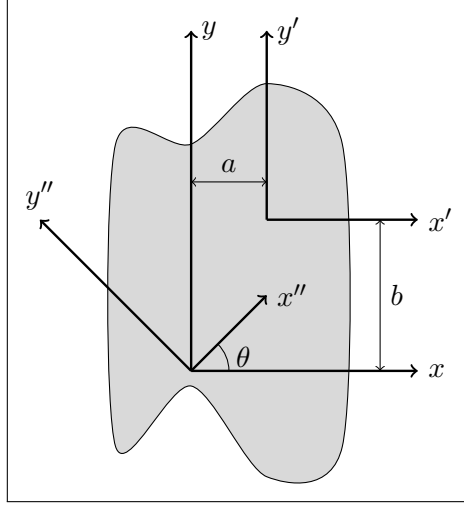
Figure 3.2   Coordinate systems
used for the transformation of the
cross-sectional stiffness and
compliance matrices

Replacing these relations in the definitions of the beam generalized strains (Eq. 3.3), we get (knowing that $z = z'$):

$$
\begin{aligned}
\gamma_{zx}^0 &= \frac{\partial \chi_x}{\partial z} - \varphi_y = \frac{\partial \chi_x'}{\partial z} + b\frac{\partial \varphi_z'}{\partial z} - \varphi_y' = {\gamma_{zx}^0}' + b\kappa_z' \\
\gamma_{yz}^0 &= \frac{\partial \chi_y}{\partial z} + \varphi_x = \frac{\partial \chi_y'}{\partial z} - a\frac{\partial \varphi_z'}{\partial z} + \varphi_x' = {\gamma_{zy}^0}' - a\kappa_z' \\
\epsilon_z^0 &= \frac{\partial \chi_z}{\partial z} = \frac{\partial \chi_z'}{\partial z} - b\frac{\partial \varphi_x'}{\partial z} + a\frac{\partial \varphi_y'}{\partial z} = {\epsilon_z^0}' - b\kappa_x' + a\kappa_y' \\
\kappa_x &= \frac{\partial \varphi_x}{\partial z} = \frac{\partial \varphi_x'}{\partial z} = \kappa_x' \\
\kappa_y &= \frac{\partial \varphi_y}{\partial z} = \frac{\partial \varphi_y'}{\partial z} = \kappa_y' \\
\kappa_z &= \frac{\partial \varphi_z}{\partial z} = \frac{\partial \varphi_z'}{\partial z} = \kappa_z'
\end{aligned}
\tag{3.16}
$$

Expressed in a matrix form, this becomes:

$$
\begin{bmatrix} \gamma_{zx}^0 \\ \gamma_{yz}^0 \\ \epsilon_z^0 \\ \kappa_x \\ \kappa_y \\ \kappa_z \end{bmatrix} = \begin{bmatrix} 1 & 0 & 0 & 0 & 0 & b \\ 0 & 1 & 0 & 0 & 0 & -a \\ 0 & 0 & 1 & -b & a & 0 \\ 0 & 0 & 0 & 1 & 0 & 0 \\ 0 & 0 & 0 & 0 & 1 & 0 \\ 0 & 0 & 0 & 0 & 0 & 1 \end{bmatrix} \begin{bmatrix} \gamma_{zx}^{0\,'} \\ \gamma_{yz}^{0\,'} \\ \epsilon_z^{0'} \\ \kappa_x' \\ \kappa_y' \\ \kappa_z' \end{bmatrix} \tag{3.17}
$$

or

$$
\boldsymbol{\kappa} = \mathbf{T}_s \boldsymbol{\kappa}' \tag{3.18}
$$

The relation between two sets of internal loads expressed in these same coordinate systems (see Fig. 3.2) is:

$$
\begin{bmatrix} V_x \\ V_y \\ N \\ M_x \\ M_y \\ M_t \end{bmatrix} = \begin{bmatrix} 1 & 0 & 0 & 0 & 0 & 0 \\ 0 & 1 & 0 & 0 & 0 & 0 \\ 0 & 0 & 1 & 0 & 0 & 0 \\ 0 & 0 & b & 1 & 0 & 0 \\ 0 & 0 & -a & 0 & 1 & 0 \\ -b & a & 0 & 0 & 0 & 1 \end{bmatrix} \begin{bmatrix} V_x' \\ V_y' \\ N' \\ M_x' \\ M_y' \\ M_t' \end{bmatrix} \tag{3.19}
$$

or

$$
\mathbf{V} = \mathbf{T}_s^{-T} \mathbf{V}' \tag{3.20}
$$

The compliance matrix in the prime coordinate system is then:

$$
\begin{aligned}
\boldsymbol{\kappa} &= \mathbf{F}_s \mathbf{V} \\
\mathbf{T}_s \boldsymbol{\kappa}' &= \mathbf{F}_s \mathbf{T}_s^{-T} \mathbf{V}' \\
\boldsymbol{\kappa}' &= \mathbf{T}_s^{-1} \mathbf{F}_s \mathbf{T}_s^{-T} \mathbf{V}' \\
\boldsymbol{\kappa}' &= \mathbf{F}_s' \mathbf{V}' \text{ with } \mathbf{F}_s' = \mathbf{T}_s^{-1} \mathbf{F}_s \mathbf{T}_s^{-T}
\end{aligned} \tag{3.21}
$$

In a similar way, the cross-sectional stiffness matrix in the prime coordinate system is

$$
\begin{aligned}
\mathbf{V} &= \mathbf{K}_s \boldsymbol{\kappa} \\
\mathbf{T}_s^{-T} \mathbf{V}' &= \mathbf{K}_s \mathbf{T}_s \boldsymbol{\kappa}' \\
\mathbf{V}' &= \mathbf{T}_s^T \mathbf{K}_s \mathbf{T}_s \boldsymbol{\kappa}' \\
\mathbf{V}' &= \mathbf{K}_s' \boldsymbol{\kappa}' \text{ with } \mathbf{K}_s' = \mathbf{T}_s^T \mathbf{K}_s \mathbf{T}_s
\end{aligned}
\tag{3.22}
$$

In a developed form, the cross-sectional stiffness and compliance matrices in the prime coordinate system are repectively (taking into account the symmetry of the matrices):

$$K'_{s11} = K_{s11}$$

$$K'_{s12} = K_{s12}$$

$$K'_{s13} = K_{s13}$$

$$K'_{s14} = -bK_{s13} + K_{s14}$$

$$K'_{s15} = aK_{s13} + K_{s15}$$

$$K'_{s16} = bK_{s11} - aK_{s12} + K_{s16}$$

$$K'_{s22} = K_{s22}$$

$$K'_{s23} = K_{s23}$$

$$K'_{s24} = -bK_{s23} + K_{s24}$$

$$K'_{s25} = aK_{s23} + K_{s25}$$

$$K'_{s26} = bK_{s12} - aK_{s22} + K_{s26} \tag{3.23}$$

$$K'_{s33} = K_{s33}$$

$$K'_{s34} = -bK_{s33} + K_{s34}$$

$$K'_{s35} = aK_{s33} + K_{s35}$$

$$K'_{s36} = bK_{s13} - aK_{s23} + K_{s36}$$

$$K'_{s44} = b^2 K_{s33} - 2bK_{s34} + K_{s44}$$

$$K'_{s45} = -abK_{s33} + aK_{s34} - bK_{s35} + K_{s45}$$

$$K'_{s46} = -b^2 K_{s13} + bK_{s14} + abK_{s23} - aK_{s24} - bK_{s36} + K_{s46}$$

$$K'_{s55} = a^2 K_{s33} + 2aK_{s35} + K_{s55}$$

$$K'_{s56} = abK_{s13} + bK_{s15} - a^2 K_{s23} - aK_{s25} + aK_{s36} + K_{s56}$$

$$K'_{s66} = b^2 K_{s11} - 2abK_{s12} + 2bK_{s16} + a^2 K_{s22} - 2aK_{s26} + K_{s66}$$

and

$$F'_{s11} = F_{s11} - 2bF_{s16} + b^2 F_{s66}$$

$$F'_{s12} = F_{s12} + aF_{s16} - bF_{s26} - abF_{s66}$$

$$F'_{s13} = F_{s13} + bF_{s14} - aF_{s15} - bF_{s36} - b^2 F_{s46} + abF_{s56}$$

$$F'_{s14} = F_{s14} - bF_{s46}$$

$$F'_{s15} = F_{s15} - bF_{s56}$$

$$F'_{s16} = F_{s16} - bF_{s66}$$

$$F'_{s22} = F_{s22} + 2aF_{s26} + a^2 F_{s66}$$

$$F'_{s23} = F_{s23} + bF_{s24} - aF_{s25} + aF_{s36} + abF_{s46} - a^2 F_{s56}$$

$$F'_{s24} = F_{s24} + aF_{s46}$$

$$F'_{s25} = F_{s25} + aF_{s56}$$

$$F'_{s26} = F_{s26} + aF_{s66} \tag{3.24}$$

$$F'_{s33} = F_{s33} + 2bF_{s34} - 2aF_{s35} + b^2 F_{s44} - 2abF_{s45} + a^2 F_{s55}$$

$$F'_{s34} = F_{s34} + bF_{s44} - aF_{s45}$$

$$F'_{s35} = F_{s35} + bF_{s45} - aF_{s55}$$

$$F'_{s36} = F_{s36} + bF_{s46} - aF_{s56}$$

$$F'_{s44} = F_{s44}$$

$$F'_{s45} = F_{s45}$$

$$F'_{s46} = F_{s46}$$

$$F'_{s55} = F_{s55}$$

$$F'_{s56} = F_{s56}$$

$$F'_{s66} = F_{s66}$$

In a similar way, we could express the relation between two sets of generalized strains and internal forces after a rotation of the coordinate system (see Fig. 3.2) as:

$$
\begin{bmatrix} \gamma_{zx}^0 \\ \gamma_{yz}^0 \\ \epsilon_z^0 \\ \kappa_x \\ \kappa_y \\ \kappa_z \end{bmatrix}
=
\begin{bmatrix}
c & -s & 0 & 0 & 0 & 0 \\
s & c & 0 & 0 & 0 & 0 \\
0 & 0 & 1 & 0 & 0 & 0 \\
0 & 0 & 0 & c & -s & 0 \\
0 & 0 & 0 & s & c & 0 \\
0 & 0 & 0 & 0 & 0 & 1
\end{bmatrix}
\begin{bmatrix} \gamma_{zx}^{0\,''} \\ \gamma_{yz}^{0\,''} \\ \epsilon_z^{0''} \\ \kappa_x'' \\ \kappa_y'' \\ \kappa_z'' \end{bmatrix}
\tag{3.25}
$$

or

$$
\boldsymbol{\kappa} = \mathbf{T}_\theta \boldsymbol{\kappa}''
\tag{3.26}
$$

and

$$
\begin{bmatrix} V_x \\ V_y \\ N \\ M_x \\ M_y \\ M_t \end{bmatrix}
=
\begin{bmatrix}
c & -s & 0 & 0 & 0 & 0 \\
s & c & 0 & 0 & 0 & 0 \\
0 & 0 & 1 & 0 & 0 & 0 \\
0 & 0 & 0 & c & -s & 0 \\
0 & 0 & 0 & s & c & 0 \\
0 & 0 & 0 & 0 & 0 & 1
\end{bmatrix}
\begin{bmatrix} V_x'' \\ V_y'' \\ N'' \\ M_x'' \\ M_y'' \\ M_t'' \end{bmatrix}
\tag{3.27}
$$

or

$$
\mathbf{V} = \mathbf{T}_\theta \mathbf{V}''
\tag{3.28}
$$

where $s = \sin\theta$ and $c = \cos\theta$.

The cross-sectional stiffness matrix in the double prime coordinate system is then:

$$
\begin{aligned}
\boldsymbol{\kappa} &= \mathbf{F}_s \mathbf{V} \\
\mathbf{T}_\theta \boldsymbol{\kappa}'' &= \mathbf{F}_s \mathbf{T}_\theta \mathbf{V}'' \\
\boldsymbol{\kappa}'' &= \mathbf{T}_\theta^{-1} \mathbf{F}_s \mathbf{T}_\theta \mathbf{V}'' \\
\boldsymbol{\kappa}'' &= \mathbf{F}_s'' \mathbf{V}'' \text{ with } \mathbf{F}_s'' = \mathbf{T}_\theta^{-1} \mathbf{F}_s \mathbf{T}_\theta
\end{aligned}
\tag{3.29}
$$

and the cross-sectional stiffness matrix in the double prime coordinate system is

$$\mathbf{V} = \mathbf{K}_s \boldsymbol{\kappa}$$
$$\mathbf{T}_\theta \mathbf{V}'' = \mathbf{K}_s \mathbf{T}_\theta \boldsymbol{\kappa}''$$
$$\mathbf{V}'' = \mathbf{T}_\theta^{-1} \mathbf{K}_s \mathbf{T}_\theta \boldsymbol{\kappa}''$$
$$\mathbf{V}'' = \mathbf{K}_s'' \boldsymbol{\kappa}'' \text{ with } \mathbf{K}_s'' = \mathbf{T}_\theta^{-1} \mathbf{K}_s \mathbf{T}_\theta$$

$$(3.30)$$

In a developed form, the cross-sectional stiffness matrix in the double prime coordinate system is (taking into account the symmetry of the matrices):

$$K''_{s11} = c^2 K_{s11} + 2cs K_{s12} + s^2 K_{s22}$$

$$K''_{s12} = -cs K_{s11} + c^2 K_{s12} - s^2 K_{s12} + cs K_{s22}$$

$$K''_{s13} = c K_{s13} + s K_{s23}$$

$$K''_{s14} = c^2 K_{s14} + cs K_{s15} + cs K_{s24} + s^2 K_{s25}$$

$$K''_{s15} = -cs K_{s14} + c^2 K_{s15} - s^2 K_{s24} + cs K_{s25}$$

$$K''_{s16} = c K_{s16} + s K_{s26}$$

$$K''_{s22} = s^2 K_{s11} - 2cs K_{s12} + c^2 K_{s22}$$

$$K''_{s23} = -s K_{s13} + c K_{s23}$$

$$K''_{s24} = -cs K_{s14} - s^2 K_{s15} + c^2 K_{s24} + cs K_{s25}$$

$$K''_{s25} = s^2 K_{s14} - cs K_{s15} - cs K_{s24} + c^2 K_{s25}$$

$$K''_{s26} = -s K_{s16} + c K_{s26} \qquad (3.31)$$

$$K''_{s33} = K_{s33}$$

$$K''_{s34} = c K_{s34} + s K_{s35}$$

$$K''_{s35} = -s K_{s34} + c K_{s35}$$

$$K''_{s36} = K_{s36}$$

$$K''_{s44} = c^2 K_{s44} + 2cs K_{s45} + s^2 K_{s55}$$

$$K''_{s45} = -cs K_{s44} + c^2 K_{s45} - s^2 K_{s45} + cs K_{s55}$$

$$K''_{s46} = c K_{s46} + s K_{s56}$$

$$K''_{s55} = s^2 K_{s44} - 2cs K_{s45} + c^2 K_{s55}$$

$$K''_{s56} = -s K_{s46} + c K_{s56}$$

$$K''_{s66} = K_{s66}$$

The expressions of the components of $\mathbf{F}_s$ follows the same transformation rules, i.e., K can be replaced by F in Equation 3.31.

3.2.3 Shear centre

The shear centre is defined as the point where the application of a shear force does not results in a torsion of the beam. So in order for a and b to be the coordinates of this point, the shear-twist coupling terms of the compliance matrix (F'_{s16} and F'_{s26} of Equation 3.24) have to be null. The coordinates of the shear centre is then:

$$
\begin{aligned}
x_c &= -\frac{F_{s26}}{F_{s66}} \\
y_c &= \frac{F_{s16}}{F_{s66}}
\end{aligned}
\tag{3.32}
$$

3.2.4 Elastic centre

The elastic centre is defined as the point where an applied axial force does not cause bending of the beam. In order for a and b to be the coordinates of this point, the extension-bending coupling terms (F'_{s34} and F'_{s35} of Equation 3.24) of the cross-sectional compliance matrix have to be zero. The coordinates of the elastic centre is then:

$$
\begin{aligned}
x_e &= \frac{F_{s44}F_{s35} - F_{s45}F_{s34}}{F_{s44}F_{s55} - F_{s45}^2} \\
y_e &= \frac{F_{s45}F_{s35} - F_{s55}F_{s34}}{F_{s44}F_{s55} - F_{s45}^2}
\end{aligned}
\tag{3.33}
$$

3.2.5 Principal axes of bending

When the origin of the coordinate system is located at the elastic centre, this coordinate system could be rotated by an angle $\theta = \theta_1$ to get the principal axes of bending. These axes are characterized by the fact that there is no coupling between bending about these two axes, i.e., $F''_{s45} = 0$. The orientation of the principal axes of bending is then:

$$\theta_1 = \frac{1}{2}\arctan\left(\frac{-2F_{s45}}{F_{s55} - F_{s44}}\right) \tag{3.34}$$

Note that θ_1 has always a value between $-45°$ and $+45°$, so that it represents the smallest angle between the xy-coordinate system and the principal axes of bending, even if the bending stiffness about the first principal axis is smaller than about the second.

3.3 Model 1: Simple model

Several simple models for blade preliminary analysis have been proposed (Giguère and Selig, 2000; Hillmer et al., 2007; Mikkelsen, 2016, for instance). The one proposed here is based on Hansen (2008), the cross section is represented as shown in Figure 3.3. The only parts modelled are the spar caps idealized as two rectangular strips. c is the chord length and t is the airfoil thickness. For instance, for the airfoils used in the WESNet wind turbine, t/c ranges from 18 % to 30%. b is the spar caps width which is generally equal to approximately 30 % of the chord length ($b/c = 0.30$) and h is the spar cap thickness.
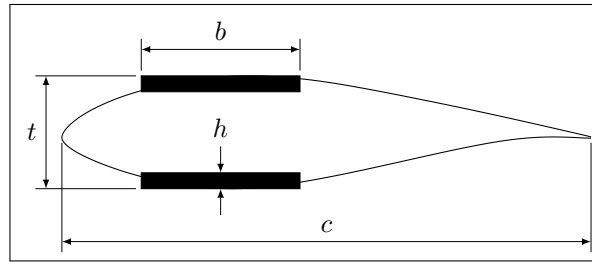
Figure 3.3   Simplified blade model

The cross-sectional inertia (about an axis parallel to the chord line and passing through the mid distance between both spar caps) is

$$I = \frac{bt^3}{12} - \frac{b(t - 2h)^3}{12} \tag{3.35}$$

and the maximum strain (and absolute value of minimum strain) is

$$\epsilon = \frac{M(t/2)}{EI} \tag{3.36}$$

where M is the bending moment. As a simple and conservative assumption, the resultant of the in-plane and out-of-plane bending moments is supposed to be applied about an axis parallel to the chord line. E is the spar cap elastic modulus.

From Equation 3.36, the required section inertia is

$$I = \frac{Mt}{2Ee} \tag{3.37}$$

where e is the failure strain.

From Equation 3.35, the required spar cap thickness for a given inertia value can be derived as

$$h = \frac{t}{2} - \frac{1}{2}\sqrt[3]{t^3 - \frac{12I}{b}} \tag{3.38}$$

Inserting Equation 3.37 into Equation 3.38, the required spar cap thickness as a function of airfoil shape, material properties and bending moment is

$$h = \frac{t}{2} - \frac{1}{2}\sqrt[3]{t^3 - \frac{6Mt}{Eeb}} \tag{3.39}$$

Note that in the previous equations, the substitutions $E\epsilon = \sigma$ and $Ee = S$ allow to work using stress instead of strain. σ is the applied stress and S is the allowable stress.

Using thicknesses that are normalized by the chord length:

$$h_r = h/c$$
$$t_r = t/c \tag{3.40}$$
$$b_r = b/c$$

Equation 3.39 becomes

$$h_r = \frac{t_r}{2} - \frac{1}{2}\sqrt[3]{t_r^3 - \frac{6Mt_r}{Eeb_rc^3}} \tag{3.41}$$

This model can then be used for the dimensioning of the blade spar caps with equation 3.39 or 3.41. Once the spar cap thickness is known, at several cross sections along the blade length, a blade mass can be estimated using typical relations between spar cap mass and whole blade mass. The model can also be used for the stress and strain analysis with equations 3.36 and 3.35.

A conservative value of the limit strain e can also be determined. For instance, the DNVGL-ST-0376 standard (DNV GL, 2015) proposes simplified design values of 0.35 % for tensile strain and 0.25 % for compressive strain. The smallest among these values can be used, so $e = 0.25$ %.

As just demonstrated, this model is well suited for preliminary structural dimensioning of wind turbine blades based on strength. However, it is not usable to evaluate natural frequencies, deflection and buckling. Also, the only cross-sectional stiffness property it computes is the flapwise bending stiffness.

3.4 Model 2: Classical strength of materials model

This model is based on classical strength of materials theory. After some basics about cross-sectional integral computation, the analysis of extension and bending behaviour is presented. The torsion analysis based on Bredt theory is then discussed. Finally, the analysis of deflection, modal analysis and buckling behaviour of the beam are presented.

3.4.1 Surface integral computation

Figure 3.4 shows the different coordinate systems used for this analysis. The z-axis is the blade's longitudinal axis, the x-axis lie in the rotor plane and the y-axis is normal to the rotor plane and pointing downwind. Taking into account the thin-walled nature of

the wind turbine blade, the integral over the area A of the cross section is computed as a line integral over the walls:

$$\int_A f \, dA = \int_s ft \, ds \tag{3.42}$$

where t is the wall thickness, s is the variable along the walls and f is the quantity to integrate.

This integral is then evaluated numerically by discretizing the contour in several segments and summing over these segments:

$$\int_s ft \, ds \approx \sum_i f_i t_i \Delta s_i \tag{3.43}$$

Before performing these calculations, the contour points are translated towards the interior of the cross section by a distance of half of the wall thickness. The coordinates of the contour point then represent the mid thickness surface of the walls.
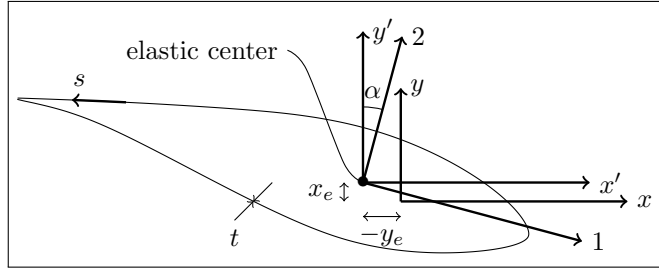
Figure 3.4   Coordinate systems for the classical strength of materials model

3.4.2   Analysis of extension and bending

For the analysis of the extension and bending behaviour, a first set of cross-sectional properties relative to the reference coordinate system (xy) can be computed as (Hansen, 2008):

$$\overline{EA} = \int_A E \, dA \tag{3.44}$$

$$\overline{ES}_x = \int_A yE \, \mathrm{d}A \tag{3.45}$$

$$\overline{ES}_y = \int_A xE \, \mathrm{d}A \tag{3.46}$$

$$\overline{EI}_x = \int_A y^2 E \, \mathrm{d}A \tag{3.47}$$

$$\overline{EI}_y = \int_A x^2 E \, \mathrm{d}A \tag{3.48}$$

$$\overline{EI}_{xy} = \int_A xyE \, \mathrm{d}A \tag{3.49}$$

E is the material's elastic modulus in the z-direction. For laminates, the effective elastic modulus is used. From these properties, the coordinates of the elastic centre are:

$$x_e = \frac{\overline{ES}_y}{\overline{EA}} \tag{3.50}$$

$$y_e = \frac{\overline{ES}_x}{\overline{EA}} \tag{3.51}$$

Knowing the location of the elastic centre, the bending stiffness relative to this point are:

$$\overline{EI}_{x'} = \int_A (y')^2 E \, \mathrm{d}A = \overline{EI}_x - y_e^2 \overline{EA} \tag{3.52}$$

$$\overline{EI}_{y'} = \int_A (x')^2 E \, \mathrm{d}A = \overline{EI}_y - x_e^2 \overline{EA} \tag{3.53}$$

$$\overline{EI}_{x'y'} = \int_A x'y' E \, \mathrm{d}A = \overline{EI}_{xy} - x_e y_e \overline{EA} \tag{3.54}$$

Finally, the angle between the x'-axis and the closest principal axes of bending is:

$$\alpha = \frac{1}{2} \arctan \left(\frac{2\overline{EI}_{x'y'}}{\overline{EI}_{x'} - \overline{EI}_{y'}} \right) \tag{3.55}$$

and the bending stiffnesses around these axes are

$$\overline{EI}_1 = \overline{EI}_{x'}(\alpha) = \frac{\overline{EI}_x + \overline{EI}_y}{2} + \frac{\overline{EI}_x - \overline{EI}_y}{2} \cos 2\alpha + \overline{EI}_{xy} \sin 2\alpha \tag{3.56}$$

$$\overline{EI}_2 = \overline{EI}_{y'}(\alpha) = \frac{\overline{EI}_x + \overline{EI}_y}{2} - \frac{\overline{EI}_x - \overline{EI}_y}{2}\cos 2\alpha - \overline{EI}_{xy}\sin 2\alpha \qquad (3.57)$$

$\overline{EI}_1$ is the flapwise bending stiffness and $\overline{EI}_2$ is the edgewise bending stiffness. Generally, for a wind turbine blade, $\overline{EI}_2 > \overline{EI}_1$.

For a given cross section, if the flapwise bending moment M_1, the edgewise bending moment M_2 and the axial force N are known, it is possible to compute the axial strain of a point using:

$$\epsilon_z = \frac{M_1 y_p}{\overline{EI}_1} - \frac{M_2 x_p}{\overline{EI}_2} + \frac{N}{\overline{EA}} \qquad (3.58)$$

where x_p and y_p are the coordinates along the 1- and 2-axes respectively and M_1 and M_2 are computed as:

$$M_1 = M_x \cos \alpha - M_y \sin \alpha$$
$$M_2 = M_x \sin \alpha + M_y \cos \alpha \qquad (3.59)$$

3.4.3 Analysis of torsion

From strength of materials textbooks (Rivello, 1969; Bazergui et al., 2002), the unit torsion angle of one of the cells of a multicell thin-walled beam is:

$$\kappa_z = \frac{1}{2A_i}\left(q_i \oint_i \frac{\mathrm{d}s}{Gt} - q_{i-1}\int_{i-1,i}\frac{\mathrm{d}s}{Gt} - q_{i+1}\int_{i,i+1}\frac{\mathrm{d}s}{Gt}\right) \qquad (3.60)$$

t and G are respectively the wall thickness and shear modulus. For laminates, the effective shear modulus is used. A_i is the surface enclosed by the ith cell and q_i, q_{i-1} and q_{i+1} are respectively the shear flow in the walls of the ith cell, the shear flow in the web left to the ith cell and the shear flow in the web right to the ith cell (see Figure 3.5). Integrals over (i), $(i-1,i)$ and $(i,i+1)$ are respectively integral over the ith cell, the web to the

left to the ith cell and the web to the right to the ith cell. Using the following notation,

$$
\begin{aligned}
\delta_i &= \oint_i \frac{\mathrm{d}s}{Gt} \\
\delta_{i,j} &= \int_{i,j} \frac{\mathrm{d}s}{Gt}
\end{aligned}
\tag{3.61}
$$

Equation 3.60 can be written as

$$
2A_i\kappa_z = q_i\delta_i - q_{i-1}\delta_{i-1,i} - q_{i+1}\delta_{i,i+1}
\tag{3.62}
$$

Knowing that each cell must have the same unit torsion angle κ_z, the previous equation is repeated for each of the n cells of the beam. This results in a system of n equations to compute the shear flow q_i in each cell;

$$
\begin{aligned}
2A_1\kappa_z &= & +q_1\delta_1 - q_2\delta_{1,2} \\
2A_2\kappa_z &= -q_1\delta_{1,2} & +q_2\delta_2 - q_3\delta_{2,3} \\
2A_3\kappa_z &= -q_2\delta_{2,3} & +q_3\delta_3 - q_4\delta_{3,4} \\
&\cdots \\
2A_n\kappa_z &= -q_{n-1}\delta_{n-1,n} & +q_n\delta_n
\end{aligned}
\tag{3.63}
$$

Or in matrix form:

$$
2\kappa_z \mathbf{A} = \boldsymbol{\delta}\mathbf{q}
\tag{3.64}
$$

where

$$
\begin{aligned}
\mathbf{A} &= \begin{bmatrix} A_1 & A_2 & A_3 & \cdots & A_n \end{bmatrix}^T \\
\mathbf{q} &= \begin{bmatrix} q_1 & q_2 & q_3 & \cdots & q_n \end{bmatrix}^T \\
\boldsymbol{\delta} &= \begin{bmatrix}
\delta_1 & -\delta_{1,2} & 0 & 0 & \cdots & 0 & 0 \\
-\delta_{1,2} & \delta_2 & -\delta_{2,3} & 0 & \cdots & 0 & 0 \\
0 & -\delta_{2,3} & \delta_3 & -\delta_{3,4} & \cdots & 0 & 0 \\
\vdots & \vdots & \vdots & \vdots & \ddots & 0 & 0 \\
0 & 0 & 0 & 0 & 0 & -\delta_{n-1,n} & \delta_n
\end{bmatrix}
\end{aligned}
\tag{3.65}
$$

From equilibrium,

$$M_t = 2\mathbf{A}^T\mathbf{q} \tag{3.66}$$

where M_t is the torsion moment. Introducing the torsional stiffness $\overline{GJ}$:

$$M_t = \overline{GJ}\kappa_z \tag{3.67}$$

From Eq. 3.64, 3.66 and 3.67, the torsional rigidity can be computed as:

$$\overline{GJ} = 4\mathbf{A}^T\boldsymbol{\delta}^{-1}\mathbf{A} \tag{3.68}$$
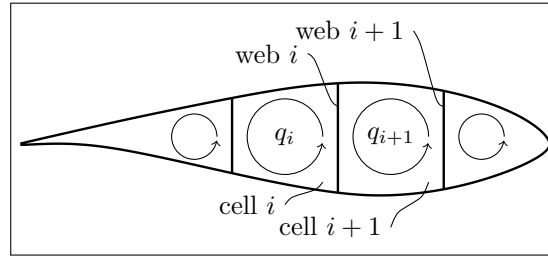
Figure 3.5   Torsion analysis of a
multicell thin-walled beam

3.4.4   Deflection analysis

The deflection analysis procedure presented in this section is based on Hansen (2008).
Assuming that the applied forces (p_x, p_y and p_z) and moments (m_x, m_y and m_z) per unit
length are known at n different points from the blade root to the blade tip and assuming
a linear variation between these points, the internal load distribution can be computed

as:

$$V_x^i = V_x^{i+1} + \frac{(p_x^{i+1} + p_x^i)}{2}(z^{i+1} - z^i)$$

$$V_y^i = V_y^{i+1} + \frac{(p_y^{i+1} + p_y^i)}{2}(z^{i+1} - z^i)$$

$$N^i = N^{i+1} + \frac{(p_z^{i+1} + p_z^i)}{2}(z^{i+1} - z^i)$$

$$M_x^i = M_x^{i+1} - V_y^{i+1}(z^{i+1} - z^i) + \frac{(m_x^{i+1} + m_x^i)}{2}(z^{i+1} - z^i) - \left(\frac{p_y^{i+1}}{3} + \frac{p_y^i}{6}\right)(z^{i+1} - z^i)^2$$

$$M_y^i = M_y^{i+1} + V_x^{i+1}(z^{i+1} - z^i) + \frac{(m_y^{i+1} + m_y^i)}{2}(z^{i+1} - z^i) + \left(\frac{p_x^{i+1}}{3} + \frac{p_x^i}{6}\right)(z^{i+1} - z^i)^2$$

$$M_t^i = M_t^{i+1} + \frac{(m_z^{i+1} + m_z^i)}{2}(z^{i+1} - z^i)$$

$$(3.69)$$

where the superscript indicates the point number, i ranging from 1 at the blade root to n at the blade tip. As the internal loads are null at the blade tip, the computation process can begin at that point and then progress towards the blade root.

For each point, the beam curvature can be computed by first transferring the bending moments in the principal axis of bending:

$$M_1^i = +M_x^i \cos \alpha^i - M_y^i \sin \alpha^i$$
$$M_2^i = +M_x^i \sin \alpha^i + M_y^i \cos \alpha^i$$

$$(3.70)$$

and then, by evaluating the curvatures around these axes:

$$\kappa_1^i = \frac{M_1^i}{EI_1^i}$$
$$\kappa_2^i = \frac{M_2^i}{EI_2^i}$$

$$(3.71)$$

and finally by converting these curvatures into the xy-coordinate system:

$$\kappa_x^i = +\kappa_1^i \cos \alpha^i + \kappa_2^i \sin \alpha^i$$
$$\kappa_y^i = -\kappa_1^i \sin \alpha^i + \kappa_2^i \cos \alpha^i$$

$$(3.72)$$

The axial and torsional beam generalized deformations can be evaluated with:

$$\epsilon_x^{0,i} = \frac{N^i}{\overline{EA}^i}$$
$$\kappa_z^i = \frac{M_t^i}{\overline{GJ}^i}$$

(3.73)

Assuming a linear variation of these beam deformations between loading points, the beam rotations and deflections can be computed starting at the blade root where they are null and progressing towards the blade tip:

$$\varphi_x^i = \varphi_x^{i-1} + \frac{1}{2}(\kappa_x^i + \kappa_x^{i-1})(z^i - z^{i-1})$$
$$\varphi_y^i = \varphi_y^{i-1} + \frac{1}{2}(\kappa_y^i + \kappa_y^{i-1})(z^i - z^{i-1})$$
$$\varphi_z^i = \varphi_z^{i-1} + \frac{1}{2}(\kappa_z^i + \kappa_z^{i-1})(z^i - z^{i-1})$$
$$\chi_x^i = \chi_x^{i-1} + \varphi_y^{i-1}(z^i - z^{i-1}) + \left(\frac{\kappa_y^i}{6} + \frac{\kappa_y^{i-1}}{3}\right)(z^i - z^{i-1})^2$$
$$\chi_y^i = \chi_y^{i-1} - \varphi_x^{i-1}(z^i - z^{i-1}) - \left(\frac{\kappa_x^i}{6} + \frac{\kappa_x^{i-1}}{3}\right)(z^i - z^{i-1})^2$$
$$\chi_z^i = \chi_z^{i-1} + \frac{1}{2}(\epsilon_z^{0,i} + \epsilon_z^{0,i-1})(z^i - z^{i-1})$$

(3.74)

By doing so, the effect of transverse shear is neglected, following the Euler-Bernoulli hypothesis.

3.4.5 Modal analysis

For the modal analysis, the blade mass distribution is required. Following the same procedure as for the calculation of the cross-sectional stiffness properties, the mass per unit length m' can be computed at some location along the blade length as:

$$m' = \int_A \rho \, dA$$

(3.75)

where ρ is the material density.

The procedure presented here (Hansen, 2008) allows the computation of the first flapwise and edgewise bending modes, the most important for blade design.

The beam equilibrium equations in bending are:

$$p_x + \frac{\partial V_x}{\partial z} = m' \ddot{\chi}_x$$
$$p_y + \frac{\partial V_y}{\partial z} = m' \ddot{\chi}_y \tag{3.76}$$

For a modal analysis, there is no external load so the equilibrium equations become:

$$\frac{\partial V_x}{\partial z} = m' \ddot{\chi}_x$$
$$\frac{\partial V_y}{\partial z} = m' \ddot{\chi}_y \tag{3.77}$$

The solution of this problem has the form

$$\chi_i = A \sin(\omega(t - t_0)) \tag{3.78}$$

where A, ω, t and t_0 are respectively, the amplitude, the angular frequency, the time and the phase variable. So the second derivative of the solution is:

$$\ddot{\chi}_i = -A\omega^2 \sin(\omega(t - t_0)) = -\omega^2 \chi_i \tag{3.79}$$

Replacing this solution in Equation 3.77 yields:

$$\frac{\partial V_x}{\partial z} = -m' \omega^2 \chi_x$$
$$\frac{\partial V_y}{\partial z} = -m' \omega^2 \chi_y \tag{3.80}$$

This Equation has a form that is similar to the equilibrium equation of a static beam (equation 3.76 with $\ddot{\chi}_x = \ddot{\chi}_y = 0$) with

$$p_x = m'\omega^2\chi_x$$
$$p_y = m'\omega^2\chi_y$$

(3.81)

Then, χ_x and χ_y are an eigenmode and ω^2 is an eigenvalue of the blade if the loads of Equation 3.81 cause blade deflections equal to χ_x and χ_y. A solution is found iteratively by starting, for instance, from $p_x = p_y = m'$ and $\omega^2 = 1$. The new deflection is then computed using the method presented in Section 3.4.4 and the eigenvalue is computed at the blade tip as

$$\omega^2 = \frac{p_y^n}{\chi_y^n m'^n}$$

(3.82)

where n is the last point on the blade (tip). The new loads can then be computed as

$$p_x = \frac{m'\omega^2\chi_x}{\sqrt{(\chi_x^n)^2 + (\chi_y^n)^2}}$$
$$p_y = \frac{m'\omega^2\chi_y}{\sqrt{(\chi_x^n)^2 + (\chi_y^n)^2}}$$

(3.83)

where the deflection is normalized to get a unit tip deflection. When ω^2 does not change anymore from one iteration to the next one, the solution for the first mode is obtained.

The procedure is similar for the second mode with the difference that a way to avoid converging towards the first mode needs to be implemented. This is done by removing, each time a new deflection is computed, $C_1\chi_{x,\text{mode 1}}$ to χ_x and $C_1\chi_{y,\text{mode 1}}$ to χ_y. C_1 is a constant equal to:

$$C_1 = \frac{\int \chi_{x,\text{mode 1}} m'\chi_x \, \mathrm{d}L + \int \chi_{y,\text{mode 1}} m'\chi_y \, \mathrm{d}L}{\int \chi_{x,\text{mode 1}} m'\chi_{x,\text{mode 1}} \, \mathrm{d}L + \int \chi_{y,\text{mode 1}} m'\chi_{y,\text{mode 1}} \, \mathrm{d}L}$$

(3.84)

where the integrals are performed over the blade length.

For the third mode, to avoid converging towards the first two modes, each time a new deflection is computed, $C_1\chi_{x,\text{mode 1}} + C_2\chi_{x,\text{mode 2}}$ is removed to χ_x and $C_1\chi_{y,\text{mode 1}} + C_2\chi_{y,\text{mode 2}}$ to χ_y. The C_2 constant is equal to:

$$C_2 = \frac{\int \chi_{x,\text{mode 2}} m' \chi_x \, \mathrm{d}L + \int \chi_{y,\text{mode 2}} m' \chi_y \, \mathrm{d}L}{\int \chi_{x,\text{mode 2}} m' \chi_{x,\text{mode 2}} \, \mathrm{d}L + \int \chi_{y,\text{mode 2}} m' \chi_{y,\text{mode 2}} \, \mathrm{d}L} \tag{3.85}$$

The procedure follows the same rules for the other modes.

3.4.6 Buckling analysis

For the buckling analysis, at a given cross section, the blade exterior surface is separated in different panels. A separation between two adjacent panels occurs each time (1) a web is connected to the blade surface and (2) there is a change in the laminate. For instance, in Figure 3.6, the cross section is separated in 8 panels. For each panel, the width b is computed as the sum of the length of the elements forming the panel and the critical compressive force per unit length is calculated using the conservative infinite length (in the blade longitudinal direction) buckling solution for flat panel simply supported on each sides (Kollár and Springer, 2003) :

$$N_{cr} = \frac{2\pi^2}{b^2} \left(\sqrt{D_{11}D_{22}} + D_{12} + 2D_{66} \right) \tag{3.86}$$

where D_{11}, D_{22}, D_{12} and D_{66} are the panel bending stiffnesses obtained from the classical lamination theory (Barbero, 1999; Berthelot, 2012; Kollár and Springer, 2003; Gibson, 2007).

For each panel, the mean (along its width) compressive force per unit length N_z is also computed. For each element, N_z is computed as:

$$N_z = \sigma_z t = E_z \epsilon_z t \tag{3.87}$$

where t is the panel thickness and E_z is its modulus of elasticity (effective modulus for laminates).
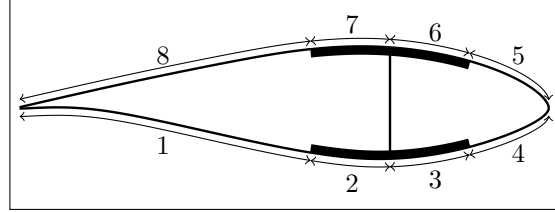
Figure 3.6   Example of panels for
cross-sectional analysis

A buckling failure index can then be computed as:

$$F_{\text{buckling}} = \frac{N_z}{N_{cr}} \tag{3.88}$$

3.5   Model 3: Cross-sectional finite element model

The third model for blade structural analysis is based on a finite element discretization of the cross section. Capitalizing on the fact that wind turbine blades are thin-walled structures, line finite elements are used. As the development of this finite element is a considerable part of the thesis, it is presented in its own chapter (Chapter 4). That chapter shows how stresses and strains in the cross section can be computed using this method and how a full 6×6 cross-sectional stiffness matrix can be obtained for general composite thin-walled cross sections including unbalanced and nonsymmetrical layups.

A methodology for buckling evaluation like the one presented in Section 3.4.6 for the classical strength of materials model could be used but has not been implemented yet. For more advanced methods for buckling evaluation of thin-walled composite beams, see Lindenburg and de Winkel (2005a).

For the analysis of blade deflection and natural frequencies, the blade length is discretized using three-node beam finite elements with reduced integration. This element is formulated as follows. The principle of virtual work for a beam is

$$\int \delta \mathbf{r}^T \mathbf{M}_s \ddot{\mathbf{r}} \, dL + \int \delta \boldsymbol{\kappa}^T \mathbf{K}_s \boldsymbol{\kappa} \, dL = \int \delta \mathbf{r}^T \mathbf{p} \, dL$$

where $\mathbf{M}_s$ and $\mathbf{K}_s$ are respectively the cross-sectional mass and stiffness matrices. $\mathbf{r} = \begin{bmatrix} \chi_x & \chi_y & \chi_z & \varphi_x & \varphi_y & \varphi_z \end{bmatrix}^T$ contains the displacements and rotations of the beam reference axis and $\boldsymbol{\kappa} = \begin{bmatrix} \gamma_{zx}^0 & \gamma_{yz}^0 & \epsilon_z^0 & \kappa_x & \kappa_y & \kappa_z \end{bmatrix}^T$ is the beam generalized strain vector. The δ operator denotes that the associated quantity is virtual and the double dot notation means a double derivative with respect to time (acceleration). Finally, $\mathbf{p} = \begin{bmatrix} p_x & p_y & p_z & m_x & m_y & m_z \end{bmatrix}^T$ is the vector of applied forces (p_x, p_y and p_z) and moments (m_x, m_y and m_z) per unit length of the blade. With the finite element discretization:

$$\delta \mathbf{r} = \mathbf{N} \delta \mathbf{u}$$

$$\mathbf{r} = \mathbf{N} \mathbf{u}$$

$$\ddot{\mathbf{r}} = \mathbf{N} \ddot{\mathbf{u}}$$

$$\delta \boldsymbol{\kappa} = \boldsymbol{\partial} \mathbf{N} \delta \mathbf{u} = \mathbf{B} \delta \mathbf{u}$$

$$\boldsymbol{\kappa} = \boldsymbol{\partial} \mathbf{N} \mathbf{u} = \mathbf{B} \mathbf{u}$$

where $\mathbf{u} = \begin{bmatrix} \ldots & \chi_x^i & \chi_y^i & \chi_z^i & \varphi_x^i & \varphi_y^i & \varphi_z^i & \ldots \end{bmatrix}^T$ is the vector of the element's nodal displacement and rotations. $\mathbf{N}$ and $\mathbf{B}$ are respectively the element's shape function and derivative of shape function matrices. The principle of virtual work then becomes

$$\mathbf{M} \ddot{\mathbf{U}} + \mathbf{K} \mathbf{U} = \mathbf{F}$$

where $\mathbf{U}$ is the nodal displacements and rotation vector expanded to the whole model. The mass matrix $\mathbf{M}$, the stiffness matrix $\mathbf{K}$ and the applied load vector $\mathbf{F}$ are respectively:

$$\mathbf{M} = \sum_e \int \mathbf{N}^T \mathbf{M}_s \mathbf{N} \, \mathrm{d}L$$

$$\mathbf{K} = \sum_e \int \mathbf{B}^T \mathbf{K}_s \mathbf{B} \, \mathrm{d}L$$

$$\mathbf{F} = \sum_e \int \mathbf{N}^T \mathbf{p} \, \mathrm{d}L$$

where the sum is taken over all the model elements. For a three-node Timoshenko beam element, the shape function matrix is

$$\mathbf{N} = \begin{bmatrix} N_1 \mathbf{I}_6 & N_2 \mathbf{I}_6 & N_3 \mathbf{I}_6 \end{bmatrix}$$

where $N_1 = -\frac{1}{2}r(1-r)$, $N_2 = \frac{1}{2}r(1+r)$, $N_3 = 1 - r^2$ and $\mathbf{I}_6$ is a 6×6 identity matrix. Nodes 1, 2 and 3 are respectively located at $r = -1$, $r = 1$ and $r = 0$. The $\mathbf{B}$ matrix is

$$\mathbf{B} = \frac{2}{L} \begin{bmatrix} \mathbf{B}_1 & \mathbf{B}_2 & \mathbf{B}_3 \end{bmatrix}$$

with

$$\mathbf{B}_i = \begin{bmatrix} N_{i,r} & 0 & 0 & 0 & -\frac{L}{2}N_i & 0 \\ 0 & N_{i,r} & 0 & \frac{L}{2}N_i & 0 & 0 \\ 0 & 0 & N_{i,r} & 0 & 0 & 0 \\ 0 & 0 & 0 & N_{i,r} & 0 & 0 \\ 0 & 0 & 0 & 0 & N_{i,r} & 0 \\ 0 & 0 & 0 & 0 & 0 & N_{i,r} \end{bmatrix}$$

and $N_{i,r} = \frac{dN_i}{dr}$ so that $N_{1,r} = -\frac{1}{2} + r$, $N_{2,r} = \frac{1}{2} + r$ and $N_{3,r} = -2r$. L is the element length. The integration over the element length to compute the mass matrix $\mathbf{M}$, the stiffness matrix $\mathbf{K}$ and the load vector $\mathbf{F}$ are evaluated numerically over the reference element :

$$\int f(z) \, \mathrm{d}L = \frac{L}{2} \int f(r) \, \mathrm{d}r \approx \frac{L}{2} \sum_i f(r_i) w_i$$

Using a reduced integration on two points to avoid shear locking, i ranges from 1 to 2 with $w_i = 1$ and $r_i = \pm\frac{1}{\sqrt{3}}$.

The solution of the modal analysis is as follows (Bathe, 2006). Starting from the equilibrium equation with no load vector, we get

$$\mathbf{M}\ddot{\mathbf{U}} + \mathbf{K}\mathbf{U} = 0$$

Under these conditions, the solution vector has the following form:

$$\mathbf{U} = \boldsymbol{\phi}\sin\omega(t - t_0)$$

so that

$$\ddot{\mathbf{U}} = -\omega^2\boldsymbol{\phi}\sin\omega(t - t_0)$$

Replacing in the equilibrium equation gives

$$\mathbf{M}\left(-\omega^2\boldsymbol{\phi}\sin\omega(t - t_0)\right) + \mathbf{K}\left(\boldsymbol{\phi}\sin\omega(t - t_0)\right) = 0$$

or

$$\mathbf{K}\boldsymbol{\phi} = \omega^2\mathbf{M}\boldsymbol{\phi}$$

which is an eigenproblem yielding as many solutions for natural angular frequency ω and associated mode shape $\boldsymbol{\phi}$ as there are degrees of freedom in the model.

3.6   Model 4: 3D shell finite element model

The use of 3D finite element models for the structural analysis of wind turbine blades is common. Most of the time, due to the thin-walled topology of these structures, shell finite elements are employed. As the exterior shape of the blade is the reference shape for aerodynamics, the finite element mesh is frequently located on this surface and the element thickness is built towards the blade interior.

The particularity of this model over the three previous is that it is able to manage the effects of the variation of the cross-sectional shape of the beam along its length. However, it takes more work to set up the model.

The use of this kind of model is well documented for the computation of natural frequencies, deflection, stresses, strains and buckling (Berggreen et al., 2007; Jensen, 2008; Lillo, 2011; Paquette and Veers, 2008; Tarfaoui et al., 2012, for instance). However, a difficulty arises for computing the blade cross-sectional properties needed for the aeroelastic analysis and it is to this task that the remaining of this section is dedicated.

3.6.1 Computation of cross-sectional stiffness matrix

To compute the cross-sectional properties from a 3D finite element model, we need to know, at different locations along blade length, the internal loads and the beam generalized deformations. Knowing the internal loads is the easiest task, but extracting the generalized deformation is not straightforward. Usually, to do so, the blade reference axis displacements and rotations are computed from the nodal displacements and rotations of the nodes forming the cross section. The longitudinal distribution of these reference axis displacements is then derived using Equation 3.3 to compute the generalized deformations.

The method proposed here is highly inspired by Malcolm and Laird (2007). The particularity of the proposed method is that the computation of cross-sectional displacements and rotations are performed using a formulation similar to an interpolation element like the NASTRAN's RBE3 element.

The procedure to compute the distribution of cross-sectional properties along the blade length is as follows:

- The blade is subjected to a set of linearly independent loads cases. N load cases are needed for a $N \times N$ cross-sectional stiffness matrix.

- n stations where the cross-sectional properties are to be computed are determined.

- For each of these stations, the displacements (translation and rotation) of the reference point is computed using the kinematic relation linking the reference node to the connected nodes of a NASTRAN's RBE3 element. (see appendix I). The reference node of the element is the point that is located at the intersection of the beam's reference axis and cross-sectional plane. The connected nodes are all the nodes within a given distance on both sides of the cross-sectional plane. This distance should be as small as possible (but large enough to get nodes to cover the entire cross section) to get a good representation of the transverse shear strains.

- Once the displacements of the beam's reference axis are known at each stations along its length, Equation 3.3 is used to compute the generalized strains at each station. The derivatives are computed using second order numerical derivations on 3 points.

- For each station, the cross-sectional stiffness matrix is computed by solving the following system:

$$
\left[\begin{bmatrix} V_x \\ V_y \\ N \\ M_x \\ M_y \\ M_z \end{bmatrix}_1 \quad \dots \quad \begin{bmatrix} V_x \\ V_y \\ N \\ M_x \\ M_y \\ M_z \end{bmatrix}_6 \right] = \mathbf{K}_s \left[\begin{bmatrix} \gamma_{zx}^0 \\ \gamma_{zy}^0 \\ \epsilon_z^0 \\ \kappa_x \\ \kappa_y \\ \kappa_z \end{bmatrix}_1 \quad \dots \quad \begin{bmatrix} \gamma_{zx}^0 \\ \gamma_{zy}^0 \\ \epsilon_z^0 \\ \kappa_x \\ \kappa_y \\ \kappa_z \end{bmatrix}_6 \right] \tag{3.89}
$$

  where the index of a vector designates the load case to which it is associated.

For the particular case of a Timoshenko beam, the simplest way to proceed is to use point forces in the x-, y- and z-directions and moments around the x-, y- and z-axes

applied at the blade tip. For a blade of length L, Eq. 3.89 becomes:

$$
\begin{bmatrix}
1 & 0 & 0 & 0 & 0 & 0 \\
0 & 1 & 0 & 0 & 0 & 0 \\
0 & 0 & 1 & 0 & 0 & 0 \\
0 & z-L & 0 & 1 & 0 & 0 \\
L-z & 0 & 0 & 0 & 1 & 0 \\
0 & 0 & 0 & 0 & 0 & 1
\end{bmatrix}
= \mathbf{K}_s
\begin{bmatrix}
\begin{bmatrix}
\gamma_{zx}^0 \\
\gamma_{zy}^0 \\
\epsilon_z^0 \\
\kappa_x \\
\kappa_y \\
\kappa_z
\end{bmatrix}_1
\cdots
\begin{bmatrix}
\gamma_{zx}^0 \\
\gamma_{zy}^0 \\
\epsilon_z^0 \\
\kappa_x \\
\kappa_y \\
\kappa_z
\end{bmatrix}_6
\end{bmatrix}
\tag{3.90}
$$

so that

$$
\mathbf{K}_s =
\begin{bmatrix}
1 & 0 & 0 & 0 & 0 & 0 \\
0 & 1 & 0 & 0 & 0 & 0 \\
0 & 0 & 1 & 0 & 0 & 0 \\
0 & z-L & 0 & 1 & 0 & 0 \\
L-z & 0 & 0 & 0 & 1 & 0 \\
0 & 0 & 0 & 0 & 0 & 1
\end{bmatrix}
\begin{bmatrix}
\begin{bmatrix}
\gamma_{zx}^0 \\
\gamma_{zy}^0 \\
\epsilon_z^0 \\
\kappa_x \\
\kappa_y \\
\kappa_z
\end{bmatrix}_1
\cdots
\begin{bmatrix}
\gamma_{zx}^0 \\
\gamma_{zy}^0 \\
\epsilon_z^0 \\
\kappa_x \\
\kappa_y \\
\kappa_z
\end{bmatrix}_6
\end{bmatrix}^{-1}
\tag{3.91}
$$

If some deformation modes are not needed, the same method can be used by removing the corresponding lines and columns from the matrices. For instance, to get the cross-sectional 4×4 stiffness matrix for an Euler beam, only 4 load cases are needed. These are point forces in the z-direction and moments around the x-, y- and z-axes applied at the blade tip. For a blade of length L, Equation 3.89 then becomes:

$$
\begin{bmatrix}
1 & 0 & 0 & 0 \\
0 & 1 & 0 & 0 \\
0 & 0 & 1 & 0 \\
0 & 0 & 0 & 1
\end{bmatrix}
= \mathbf{K}_s
\begin{bmatrix}
\begin{bmatrix}
\epsilon_z^0 \\
\kappa_x \\
\kappa_y \\
\kappa_z
\end{bmatrix}_1
\cdots
\begin{bmatrix}
\epsilon_z^0 \\
\kappa_x \\
\kappa_y \\
\kappa_z
\end{bmatrix}_4
\end{bmatrix}
\tag{3.92}
$$

so that

$$\mathbf{K}_s = \begin{bmatrix} 1 & 0 & 0 & 0 \\ 0 & 1 & 0 & 0 \\ 0 & 0 & 1 & 0 \\ 0 & 0 & 0 & 1 \end{bmatrix} \left[\begin{bmatrix} \epsilon_z^0 \\ \kappa_x \\ \kappa_y \\ \kappa_z \end{bmatrix}_1 \cdots \begin{bmatrix} \epsilon_z^0 \\ \kappa_x \\ \kappa_y \\ \kappa_z \end{bmatrix}_4 \right]^{-1}$$

$$= \left[\begin{bmatrix} \epsilon_z^0 \\ \kappa_x \\ \kappa_y \\ \kappa_z \end{bmatrix}_1 \cdots \begin{bmatrix} \epsilon_z^0 \\ \kappa_x \\ \kappa_y \\ \kappa_z \end{bmatrix}_4 \right]^{-1}$$

(3.93)

In that case, $\mathbf{F}_s = \hat{\boldsymbol{\kappa}}$.

The procedure for the cross-sectional properties evaluation from a 3D finite element model is summarized in Figure 3.7
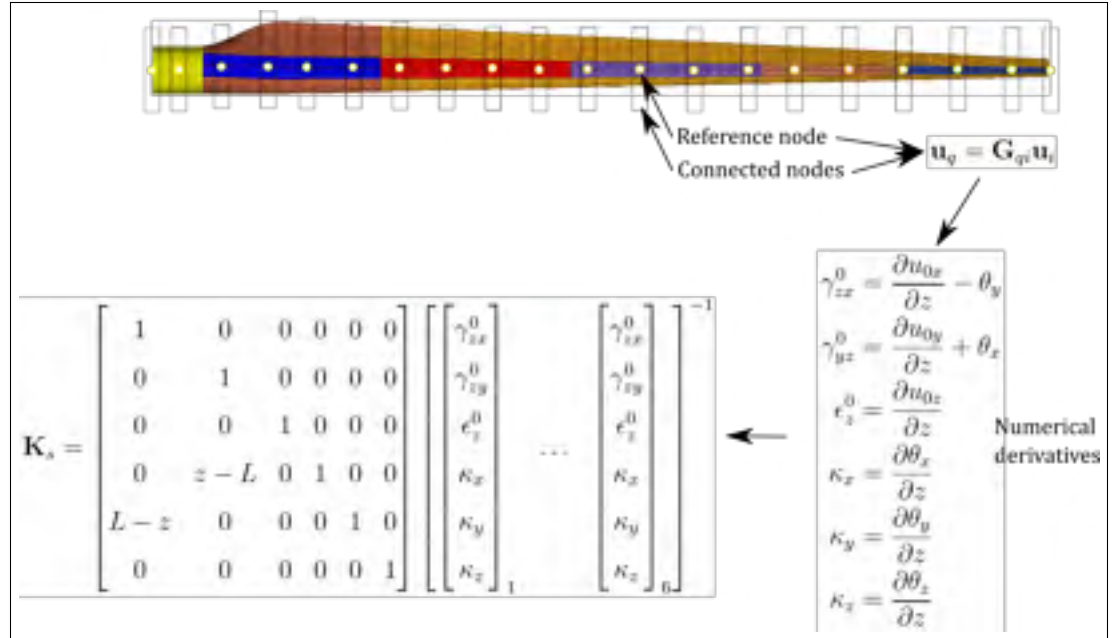
Figure 3.7   Procedure for the cross-sectional properties evaluation from a
3D finite element model

3.6.2 Application to the experimental cross-sectional analysis

The method presented in the last subsection can also be used for the evaluation of the cross-sectional properties of a blade during a bending test. As described in Section 1.7, this test has been performed on the WESNet blade. Instead of using the displacements of connected nodes to compute the cross-sectional generalized deformations, the displacements of the 3D scanner's reflective target were used.

Only 3 modes of deformation were considered in this analysis: flapwise bending, edgewise bending and torsion. Then, the following system has to be solved to get a 3×3 stiffness matrix:

$$\left[\begin{bmatrix} M_x \\ M_y \\ M_z \end{bmatrix}_1 \quad \cdots \quad \begin{bmatrix} M_x \\ M_y \\ M_z \end{bmatrix}_3 \right] = \mathbf{K}_s \left[\begin{bmatrix} \kappa_x \\ \kappa_y \\ \kappa_z \end{bmatrix}_1 \quad \cdots \quad \begin{bmatrix} \kappa_x \\ \kappa_y \\ \kappa_z \end{bmatrix}_3 \right] \tag{3.94}$$

The 3 load cases used was a flapwise force near the blade tip, an edgewise force near the blade tip and an excentric force close to the blade tip (coupled torsion and flapwise bending).

3.7 Summary of model capabilities

To conclude this section, Table 3.1 presents a summary of the capabilities of the 4 structural models described above.

Table 3.1   Summary of model capabilities

	Model 1: beam model; cross section idealized as two rectangular strips	Model 2: beam model; strength of materials theory for thin-walled composite beams	Model 3: beam model; thin-walled cross-sectional finite elements	Model 4: shell finite element model of the whole blade
Cross-sectional properties	Flapwise bending	Extension, two-plane bending, and their couplings; torsion	Full 6 × 6 cross-sectional stiffness matrix	Full 6 × 6 cross-sectional stiffness matrix
Natural frequencies	No	Edgewise and flapwise modes for Euler beam	Eigenvalue solution for Timoshenko beam finite elements	Eigenvalue solution for 3D shell finite elements
Deflection	No	Edgewise and flapwise deflection for Euler beam	Beam axis displacements and rotations for Timoshenko beam finite elements	Full field displacements and rotations for 3D shell finite elements
Strains	Longitudinal strain	Longitudinal strain due to extension and bending, shear strain due to torsion	Full 3D strains	Full 3D strains
Buckling	No	Linear buckling of long plates	Not implemented	Linear buckling
Strength (see Sec. 5.7 for more details)	Based on longitudinal strain	Based on longitudinal strain	Based on fibre direction stress	Based on fibre direction stress

CHAPTER 4

DEVELOPMENT OF A NEW FINITE ELEMENT FOR THE EVALUATION OF CROSS-SECTIONAL PROPERTIES OF THIN-WALLED COMPOSITE BEAMS

4.1   Introduction

Composite beams are a type of structure that is commonly used for airplane wings, helicopter rotor blades or wind turbine blades, in particular. Unlike classic metallic structures, composite beams offer the possibility of using non-homogeneous cross sections and can enable coupling between all deformation modes due to fibre orientation. This latter phenomenon can be used as a load alleviation system if a bend-twist coupling exists in the behaviour of the beam, for instance (Fedorov and Berggreen, 2014). As the structures mentioned earlier are often modelled as beams, especially for aeroelastic analyses, their cross-sectional properties need to be computed. In order to consider all the possibilities offered by composite beams, it is needed to develop models that are more elaborated than the classical strength of material method applied to homogeneous cross sections.

For that purpose, a reference tool is the Variational Asymptotic Beam Section analysis available in the commercial VABS software (Yu et al., 2002c,b, 2012; Hodges and Yu, 2007; Cesnik and Hodges, 1997). The beam cross section is discretized using two-dimensional finite elements and a 6×6 cross-sectional stiffness matrix is calculated. Shear effects are therefore taken into account so the beam can be considered a Timoshenko beam. Giavotto et al. (1983), based on a different methodology, have also developed a tool to compute a 6×6 cross-sectional stiffness matrix for a Timoshenko beam using again a two-dimensional finite element discretization of the cross section. This framework is sometimes called Nonhomogeneous Anisotropic Beam Section Analysis (NABSA). This work has been updated in software called BECAS that also includes optimization capabilities (Blasques et al., 2016; Blasques, 2011, 2012; Blasques and Stolpe, 2012).

However, as airplane wings, helicopter rotor blades and wind turbine blades are often thin-walled structures, it is possible to use methods based on the theory of strength of materials. Of course, these methods have to be adjusted to take into account the composite nature of these structures. These methods allow the computation of the terms of the cross-sectional stiffness matrix by the evaluation of integrals over the beam cross section. They are based on hypotheses about how the section deforms.

The first distinction that can be made between strength of material based models is the way the transverse shear effects are taken into account. Some formulations are based on Timoshenko beams and include these effects (Saravia et al., 2012; Saravia, 2014; Saravanos et al., 2006; Pluszik and Kollár, 2002; Librescu and Song, 2006; Sheikh and Thomsen, 2008; Zhang et al., 2012; Fernandes da Silva et al., 2011; Massa and Barbero, 1998) and others are based on Euler beams and neglect transverse shear effects (Kollár and Pluszik, 2002; Victorazzo and De Jesus, 2016; Cárdenas et al., 2012; Gúnay and Timarci, 2017; Zhang and Wang, 2014; Wang and Zhang, 2014; Wang et al., 2014; Cardoso et al., 2009).

In both of these cases, different ways to model the torsional behaviour of the beam are used. Some authors build their model based on uniform torsion, i.e., Bredt theory for thin-walled beams (Saravia et al., 2012; Saravia, 2014; Saravanos et al., 2006; Kollár and Pluszik, 2002; Victorazzo and De Jesus, 2016; Zhang et al., 2012; Fernandes da Silva et al., 2011; Wang et al., 2014). This means that the beam has a constant section, that it is loaded by torques at its ends only and that the effects of the supports are neglected. However, this theory is still valid for slightly variable cross sections and slightly variable distributed torques as well as for sections away from the effects of supports. Other models are based on non-uniform torsion, i.e. Vlasov torsion, where variable cross section, variable torque distribution or support effects cause restraint to the out-of-plane warping of the cross section (Pluszik and Kollár, 2002; Librescu and Song, 2006; Sheikh and Thomsen, 2008; Cárdenas et al., 2012; Gúnay and Timarci, 2017; Zhang and Wang, 2014; Wang and Zhang, 2014; Massa and Barbero, 1998; Cardoso et al., 2009). According

to Volovoi and Hodges (2000) and Yu et al. (2005), the Vlasov correction for restrained warping is not necessary for closed thin-walled beam as this effect has minimal impact on that kind of structure.

Among the cited models, some are able to consider general composite plate stacking sequences with all coupling implied (Saravia et al., 2012; Saravia, 2014; Saravanos et al., 2006; Pluszik and Kollár, 2002; Librescu and Song, 2006; Sheikh and Thomsen, 2008; Kollár and Pluszik, 2002; Victorazzo and De Jesus, 2016; Cárdenas et al., 2012; Gúnay and Timarci, 2017; Zhang and Wang, 2014; Wang and Zhang, 2014). This allows the modelling of the bend-twist coupling of the beam. With some exceptions (Zhang et al., 2012; Fernandes da Silva et al., 2011; Wang et al., 2014; Cárdenas et al., 2012; Cardoso et al., 2009) all these models take into account the bending rigidity of the walls.

All the cited models can process closed single section beams. Some are also able to model open section beams (Kollár and Pluszik, 2002; Victorazzo and De Jesus, 2016; Zhang et al., 2012; Pluszik and Kollár, 2002; Librescu and Song, 2006; Sheikh and Thomsen, 2008; Massa and Barbero, 1998; Cardoso et al., 2009) and others, closed multicell section beams (Victorazzo and De Jesus, 2016; Zhang et al., 2012; Fernandes da Silva et al., 2011; Wang et al., 2014; Pluszik and Kollár, 2002; Cárdenas et al., 2012; Wang and Zhang, 2014).

Coming back to the more complex VABS and NABSA methods, the modelling of thin-walled cross section with these tools (using line finite elements instead of 2D finite elements) is also interesting. Thin-walled implementations of the VABS method have already been proposed. Some are based on classical Euler beam model with (Yu et al., 2005) or without (Volovoi and Hodges, 2000, 2002) the Vlasov correction. Others are based on Timoshenko beam model (Ferede and Abdalla, 2014; Gupta and Hodges, 2017).

The contribution of this chapter is a thin-walled implementation of the theory behind NABSA. This leads to a 6×6 Timoshenko cross-sectional stiffness matrix. Instead of discretizing the cross section with 2D elements with three displacement degrees of freedom

per node, the section is discretized with line elements containing three translation degrees of freedom and three rotation degrees of freedom per node. This allows the reduction of the computation time (not evaluated in this work), because of the reduced number of degrees of freedom in the cross-sectional model. This is particularly valuable when performing structural optimization. It also allows, at the post-processing stage, the computation of the plate generalized stress (by integrating the stress distribution through the wall thickness) which gives rich information for the analysis of the beam under the applied load. This thin-walled formulation also facilitates the pre-processing of the model as the direction of the laminate stacking is already determined by the cross-sectional mesh.

The next section is a literature review dedicated to the presentation of the classical NABSA theory. Then, the following section describes the proposed finite element implementation of this method. Finally, a validation of the proposed method against analytical and numerical solutions is presented.

4.2 Review of the theory behind NABSA

This section presents the NABSA theory as developed by Giavotto et al. (1983) and extended for optimization by Blasques *et al.* (Blasques and Stolpe, 2012; Blasques, 2012, 2011; Blasques et al., 2016). The nomenclature adopted in this chapter is similar to the one used by the latter. In that theory it is assumed that the beam has a constant cross section and is loaded at its ends only.

4.2.1 Coordinate systems

Figure 4.1 shows the different coordinate systems used: a global coordinate system xyz, an element coordinate system rst and a material coordinate system 123. The x- and y-axes are in the cross-sectional plane and the z-axis is the beam reference axis. The r-axis is parallel to z and the s- and t-axes are respectively parallel and normal to the

beam wall. Finally, the 3-axis of the material coordinate system is parallel to the t-axis and the 1- and 2-axes are in the plane of the beam wall and are the material's principal direction of orthotropy (1-axis being typically aligned with the fibre direction).
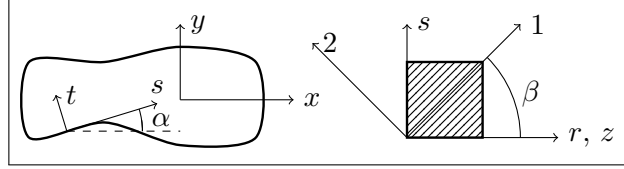
Figure 4.1   Coordinate systems

4.2.2   Stress and strain

The stress and strain components are used in a vectorial form defined as

$$\boldsymbol{\sigma} = \begin{bmatrix} \sigma_x & \sigma_y & \tau_{xy} & \tau_{xz} & \tau_{yz} & \sigma_z \end{bmatrix}^T$$
$$\boldsymbol{\epsilon} = \begin{bmatrix} \epsilon_x & \epsilon_y & \gamma_{xy} & \gamma_{xz} & \gamma_{yz} & \epsilon_z \end{bmatrix}^T \tag{4.1}$$

and the stress-strain relationship is

$$\boldsymbol{\sigma} = \mathbf{Q}\boldsymbol{\epsilon} \tag{4.2}$$

where $\mathbf{Q}$ is the material constitutive matrix. The second half of the stress vector contains the out-of-plane components of stress and is designated as

$$\mathbf{p} = \begin{bmatrix} \tau_{xz} & \tau_{yz} & \sigma_z \end{bmatrix}^T \tag{4.3}$$

4.2.3   Internal loads

The vector of the beam internal loads is defined as

$$\mathbf{V} = \begin{bmatrix} V_x & V_y & N & M_x & M_y & M_t \end{bmatrix}^T \tag{4.4}$$

where V_x and V_y are the shear forces, N is the axial force, M_x and M_y are the bending moments and M_t is the torsional moment. These internal loads are the resultants of the out-of-plane components of stress on the blade cross section:

$$\mathbf{V} = \int_A \mathbf{Z}^T \mathbf{p} \, dA \tag{4.5}$$

where

$$\mathbf{Z} = \begin{bmatrix} 1 & 0 & 0 & 0 & 0 & -y \\ 0 & 1 & 0 & 0 & 0 & x \\ 0 & 0 & 1 & y & -x & 0 \end{bmatrix} \tag{4.6}$$

4.2.4 Generalized strain

Defining the beam reference axis displacements χ_i and rotations φ_i as

$$\mathbf{r} = \begin{bmatrix} \chi_x & \chi_y & \chi_z & \varphi_x & \varphi_y & \varphi_z \end{bmatrix}^T \tag{4.7}$$

and defining the Timoshenko beam generalized strains as

$$\boldsymbol{\kappa} = \begin{bmatrix} \chi_x' - \varphi_y & \chi_y' + \varphi_x & \chi_z' & \varphi_x' & \varphi_y' & \varphi_z' \end{bmatrix}^T \tag{4.8}$$

we can show that

$$\boldsymbol{\kappa} = \mathbf{Tr} + \mathbf{r}' \tag{4.9}$$

where

$$\mathbf{T} = \begin{bmatrix} 0 & 0 & 0 & 0 & -1 & 0 \\ 0 & 0 & 0 & 1 & 0 & 0 \\ 0 & 0 & 0 & 0 & 0 & 0 \\ 0 & 0 & 0 & 0 & 0 & 0 \\ 0 & 0 & 0 & 0 & 0 & 0 \\ 0 & 0 & 0 & 0 & 0 & 0 \end{bmatrix} \tag{4.10}$$

and the prime symbol ($'$) denotes a derivative with respect to z.

4.2.5 Kinematics of the cross section

The displacement of an arbitrary point in the cross section $\mathbf{s} = \begin{bmatrix} s_x & s_y & s_z \end{bmatrix}^T$ is separated in two terms:

$$\mathbf{s} = \mathbf{Zr} + \mathbf{g} \tag{4.11}$$

The first term $\mathbf{Zr}$ is the displacement due to the cross-sectional rigid body motion and the second term $\mathbf{g} = \begin{bmatrix} g_x & g_y & g_z \end{bmatrix}^T$ is the displacement due to cross section warping.

4.2.6 Strain-displacement relations

By separation of the derivative with respect to x and y (in the cross-sectional plane) from the derivative with respect to z (along the beam longitudinal axis), the strain-displacement relation is

$$\boldsymbol{\epsilon} = \mathbf{Bs} + \mathbf{Ss}' \tag{4.12}$$

where

$$\mathbf{B} = \begin{bmatrix} \partial/\partial x & 0 & 0 \\ 0 & \partial/\partial y & 0 \\ \partial/\partial y & \partial/\partial x & 0 \\ 0 & 0 & \partial/\partial x \\ 0 & 0 & \partial/\partial y \\ 0 & 0 & 0 \end{bmatrix} \tag{4.13}$$

and

$$\mathbf{S} = \begin{bmatrix} 0 & 0 & 0 \\ 0 & 0 & 0 \\ 0 & 0 & 0 \\ 1 & 0 & 0 \\ 0 & 1 & 0 \\ 0 & 0 & 1 \end{bmatrix} \tag{4.14}$$

Using Equation 4.11, noticing that $\mathbf{BZ} = \mathbf{SZT}$ and using Equation 4.9, the strain vector becomes

$$\boldsymbol{\epsilon} = \mathbf{SZ\kappa} + \mathbf{Bg} + \mathbf{Sg}' \tag{4.15}$$

Finally, the warping function $\mathbf{g}$ is expressed using a finite element discretization of the cross section so that

$$\mathbf{g} = \mathbf{Nu} \tag{4.16}$$

where $\mathbf{N}$ is a matrix containing the shape functions and $\mathbf{u}$ is a vector containing the warping displacements at nodes. The strain vector then becomes

$$\boldsymbol{\epsilon} = \mathbf{SZ\kappa} + \mathbf{BNu} + \mathbf{SNu}' \tag{4.17}$$

4.2.7 Principle of virtual work for a beam slice

The virtual work (per unit length of the beam) for a beam slice is

$$\underbrace{\int_A \delta\boldsymbol{\epsilon}^T \boldsymbol{\sigma} \, \mathrm{d}A}_{\delta W_i} = \underbrace{\int_A (\delta\mathbf{s}^T \mathbf{p})' \, \mathrm{d}A}_{\delta W_e} \tag{4.18}$$

where the integrals are performed over the cross section A.

Using Equations 4.2 and 4.17, the internal virtual work becomes

$$\delta W_i = \begin{bmatrix} \delta\boldsymbol{\kappa} \\ \delta\mathbf{u} \\ \delta\mathbf{u}' \end{bmatrix}^T \begin{bmatrix} \mathbf{A} & \mathbf{R}^T & \mathbf{L}^T \\ \mathbf{R} & \mathbf{E} & \mathbf{C}^T \\ \mathbf{L} & \mathbf{C} & \mathbf{M} \end{bmatrix} \begin{bmatrix} \boldsymbol{\kappa} \\ \mathbf{u} \\ \mathbf{u}' \end{bmatrix} \tag{4.19}$$

where

$$\begin{aligned}
\underset{6\times6}{\mathbf{A}} &= \sum_e \int \mathbf{Z}^T \mathbf{S}^T \mathbf{Q} \mathbf{S} \mathbf{Z} \, \mathrm{d}A \\
\underset{n\times6}{\mathbf{R}} &= \sum_e \int \mathbf{N}_e^T \mathbf{B}^T \mathbf{Q} \mathbf{S} \mathbf{Z} \, \mathrm{d}A \\
\underset{n\times n}{\mathbf{E}} &= \sum_e \int \mathbf{N}_e^T \mathbf{B}^T \mathbf{Q} \mathbf{B} \mathbf{N}_e \, \mathrm{d}A \\
\underset{n\times n}{\mathbf{C}} &= \sum_e \int \mathbf{N}_e^T \mathbf{S}^T \mathbf{Q} \mathbf{B} \mathbf{N}_e \, \mathrm{d}A \\
\underset{n\times6}{\mathbf{L}} &= \sum_e \int \mathbf{N}_e^T \mathbf{S}^T \mathbf{Q} \mathbf{S} \mathbf{Z} \, \mathrm{d}A \\
\underset{n\times n}{\mathbf{M}} &= \sum_e \int \mathbf{N}_e^T \mathbf{S}^T \mathbf{Q} \mathbf{S} \mathbf{N}_e \, \mathrm{d}A
\end{aligned} \tag{4.20}$$

and n is the number of degrees of freedom in the model. The sums are performed over each element e.

Using Equations 4.11, 4.16, 4.5 and 4.9, the external work is

$$\delta W_e = \begin{bmatrix} \delta\boldsymbol{\kappa} \\ \delta\mathbf{u} \\ \delta\mathbf{u}' \\ \delta\mathbf{r} \end{bmatrix}^T \begin{bmatrix} \mathbf{V} \\ \mathbf{P}' \\ \mathbf{P} \\ \mathbf{V}' - \mathbf{T}^T\mathbf{V} \end{bmatrix} \tag{4.21}$$

where

$$\mathbf{P} = \int_A \mathbf{N}^T \mathbf{p} \, \mathrm{d}A \tag{4.22}$$

Using the expressions of Equations 4.19 and 4.21 in Equation 4.18, the principle of virtual work becomes:

$$
\begin{bmatrix} \delta\boldsymbol{\kappa} \\ \delta\mathbf{u} \\ \delta\mathbf{u}' \\ \delta\mathbf{r} \end{bmatrix}^T
\begin{bmatrix} \mathbf{A} & \mathbf{R}^T & \mathbf{L}^T \\ \mathbf{R} & \mathbf{E} & \mathbf{C}^T \\ \mathbf{L} & \mathbf{C} & \mathbf{M} \\ \mathbf{0} & \mathbf{0} & \mathbf{0} \end{bmatrix}
\begin{bmatrix} \boldsymbol{\kappa} \\ \mathbf{u} \\ \mathbf{u}' \end{bmatrix}
=
\begin{bmatrix} \delta\boldsymbol{\kappa} \\ \delta\mathbf{u} \\ \delta\mathbf{u}' \\ \delta\mathbf{r} \end{bmatrix}^T
\begin{bmatrix} \mathbf{V} \\ \mathbf{P}' \\ \mathbf{P} \\ \mathbf{V}' - \mathbf{T}^T\mathbf{V} \end{bmatrix}
\tag{4.23}
$$

And since these equations must be true for any values of $\delta\boldsymbol{\kappa}$, $\delta\mathbf{u}$, $\delta\mathbf{u}'$ and $\delta\mathbf{r}$, we get

$$
\begin{bmatrix} \mathbf{A} & \mathbf{R}^T & \mathbf{L}^T \\ \mathbf{R} & \mathbf{E} & \mathbf{C}^T \\ \mathbf{L} & \mathbf{C} & \mathbf{M} \\ \mathbf{0} & \mathbf{0} & \mathbf{0} \end{bmatrix}
\begin{bmatrix} \boldsymbol{\kappa} \\ \mathbf{u} \\ \mathbf{u}' \end{bmatrix}
=
\begin{bmatrix} \mathbf{V} \\ \mathbf{P}' \\ \mathbf{P} \\ \mathbf{V}' - \mathbf{T}^T\mathbf{V} \end{bmatrix}
\tag{4.24}
$$

which corresponds to the following system of equations:

$$
\begin{aligned}
\mathbf{A}\boldsymbol{\kappa} + \mathbf{R}^T\mathbf{u} + \mathbf{L}^T\mathbf{u}' &= \mathbf{V} \\
\mathbf{R}\boldsymbol{\kappa} + \mathbf{E}\mathbf{u} + \mathbf{C}^T\mathbf{u}' &= \mathbf{P}' \\
\mathbf{L}\boldsymbol{\kappa} + \mathbf{C}\mathbf{u} + \mathbf{M}\mathbf{u}' &= \mathbf{P} \\
\mathbf{V}' &= \mathbf{T}^T\mathbf{V}
\end{aligned}
\tag{4.25}
$$

By differentiating the third equation with respect to z, merging the second and third equations and rearranging, we get

$$
\begin{aligned}
\mathbf{V}' &= \mathbf{T}^T\mathbf{V} \\
\mathbf{E}\mathbf{u} + \mathbf{R}\boldsymbol{\kappa} &= (\mathbf{C} - \mathbf{C}^T)\mathbf{u}' + \mathbf{L}\boldsymbol{\kappa}' + \mathbf{M}\mathbf{u}'' \\
\mathbf{R}^T\mathbf{u} + \mathbf{A}\boldsymbol{\kappa} &= -\mathbf{L}^T\mathbf{u}' + \mathbf{V}
\end{aligned}
\tag{4.26}
$$

4.2.8   Solution

It could be shown (Blasques, 2012; Giavotto et al., 1983) that $\mathbf{u}$ and $\boldsymbol{\kappa}$ are polynomial functions of z. The solution of Equation 4.26 is obtained as follows for the centre of the beam (far from the boundary conditions). If n is the highest degree of this polynomial, $\frac{\mathrm{d}^{(n+1)}\mathbf{u}}{\mathrm{d}z^{(n+1)}} = \mathbf{u}^{(n+1)} = 0$ and $\frac{\mathrm{d}^{(n+1)}\boldsymbol{\kappa}}{\mathrm{d}z^{(n+1)}} = \boldsymbol{\kappa}^{(n+1)} = 0$. Also, knowing that the beam is loaded at its ends only, $\mathbf{V}'' = 0$.

By successive differentiation of Equation 4.26, we can show that $\mathbf{u}$ and $\boldsymbol{\kappa}$ are, at most, linear functions of z and the system to solve consists in:

$$
\begin{aligned}
\mathbf{E}\mathbf{u}' + \mathbf{R}\boldsymbol{\kappa}' &= 0 \\
\mathbf{R}^T\mathbf{u}' + \mathbf{A}\boldsymbol{\kappa}' &= \mathbf{T}^T\mathbf{V} \\
\mathbf{E}\mathbf{u} + \mathbf{R}\boldsymbol{\kappa} &= (\mathbf{C} - \mathbf{C}^T)\mathbf{u}' + \mathbf{L}\boldsymbol{\kappa}' \\
\mathbf{R}^T\mathbf{u} + \mathbf{A}\boldsymbol{\kappa} &= -\mathbf{L}^T\mathbf{u}' + \mathbf{V}
\end{aligned}
\tag{4.27}
$$

or in matrix form:

$$
\begin{aligned}
\begin{bmatrix} \mathbf{E} & \mathbf{R} \\ \mathbf{R}^T & \mathbf{A} \end{bmatrix} \begin{bmatrix} \mathbf{u}' \\ \boldsymbol{\kappa}' \end{bmatrix} &= \begin{bmatrix} \mathbf{0} \\ \mathbf{T}^T\mathbf{V} \end{bmatrix} \\
\begin{bmatrix} \mathbf{E} & \mathbf{R} \\ \mathbf{R}^T & \mathbf{A} \end{bmatrix} \begin{bmatrix} \mathbf{u} \\ \boldsymbol{\kappa} \end{bmatrix} &= \begin{bmatrix} (\mathbf{C} - \mathbf{C}^T)\mathbf{u}' + \mathbf{L}\boldsymbol{\kappa}' \\ -\mathbf{L}^T\mathbf{u}' + \mathbf{V} \end{bmatrix}
\end{aligned}
\tag{4.28}
$$

4.2.9   Constraints to rigid body motion

Equation 4.28 cannot be solved because the rigid body motion of the cross section described by the $\boldsymbol{\kappa}$ vector is also taken into account by the warping function $\mathbf{u}$. The solution is to impose linear relations between the components of $\mathbf{u}$ so that the mean translation and rotation of the cross section due to warping are zero. Here, the retained solution differs from the ones used by Giavotto, Blasques *et al.* (Giavotto et al., 1983; Blasques and Stolpe, 2012; Blasques, 2012, 2011; Blasques et al., 2016). Noticing that the linear

relations to impose between the components of the warping vector are of the same type as the relations generated by an RBE3 element (see Appendix I), the proposed method is to use this kind of interpolation element. This has the advantage of allowing the easy management of the rotation degrees of freedom of the warping vector. The method consists of imposing that the displacements and rotations of a fictive reference node (located at the origin of the global coordinate system) is zero. Only the displacement degrees of freedom of the connected nodes (all the mesh nodes) are used. An exception to that arises when all the model's nodes are aligned along the x- or the y-axes. In that particular case (in validation case 9 of this paper for instance), the rotational degree of freedom of the connected nodes around the axis on which they are aligned is used.

These constraints result in relations of this form:

$$\mathbf{D}^T \mathbf{u} = \mathbf{0}$$
$$\mathbf{D}^T \mathbf{u}' = \mathbf{0}$$

$$(4.29)$$

that can be added to Equation 4.28 using the Lagrange multiplier method (Bathe, 2006). This gives Equation 4.30.

4.2.10   Solving the problem for a given load case

Given the internal load vector $\mathbf{V} = [V_x \ V_y \ N \ M_x \ M_y \ M_t]^T$, the following system:

$$
\begin{bmatrix} \mathbf{E} & \mathbf{R} & \mathbf{D} \\ \mathbf{R}^T & \mathbf{A} & \mathbf{0} \\ \mathbf{D}^T & \mathbf{0} & \mathbf{0} \end{bmatrix} \begin{bmatrix} \mathbf{u}' \\ \boldsymbol{\kappa}' \\ \boldsymbol{\lambda}_1 \end{bmatrix} = \begin{bmatrix} \mathbf{0} \\ \mathbf{T}^T \mathbf{V} \\ \mathbf{0} \end{bmatrix}
$$

$$
\begin{bmatrix} \mathbf{E} & \mathbf{R} & \mathbf{D} \\ \mathbf{R}^T & \mathbf{A} & \mathbf{0} \\ \mathbf{D}^T & \mathbf{0} & \mathbf{0} \end{bmatrix} \begin{bmatrix} \mathbf{u} \\ \boldsymbol{\kappa} \\ \boldsymbol{\lambda}_2 \end{bmatrix} = \begin{bmatrix} (\mathbf{C} - \mathbf{C}^T)\mathbf{u}' + \mathbf{L}\boldsymbol{\kappa}' \\ -\mathbf{L}^T \mathbf{u}' + \mathbf{V} \\ \mathbf{0} \end{bmatrix}
$$

$$(4.30)$$

can be solved to get the beam deformation vector $\boldsymbol{\kappa} = [\gamma_{zx}^0 \ \gamma_{zy}^0 \ \epsilon_z^0 \ \kappa_x \ \kappa_y \ \kappa_z]^T$ and the node warping displacement vector $\mathbf{u}$.

4.2.11 Cross-sectional stiffness matrix

To get the beam cross-sectional stiffness matrix $\mathbf{K}_s$ and compliance matrix $\mathbf{F}_s$ so that $\mathbf{V} = \mathbf{K}_s \boldsymbol{\kappa}$, $\boldsymbol{\kappa} = \mathbf{F}_s \mathbf{V}$ and $\mathbf{K}_s = \mathbf{F}_s^{-1}$, we can solve Equation 4.30 but replacing the $\mathbf{V}$ vector by a 6×6 matrix $\hat{\mathbf{V}}$, in which each column contains a linearly independent load case:

$$
\begin{bmatrix} \mathbf{E} & \mathbf{R} & \mathbf{D} \\ \mathbf{R}^T & \mathbf{A} & \mathbf{0} \\ \mathbf{D}^T & \mathbf{0} & \mathbf{0} \end{bmatrix} \begin{bmatrix} \hat{\mathbf{u}}' \\ \hat{\boldsymbol{\kappa}}' \\ \hat{\boldsymbol{\lambda}}_1 \end{bmatrix} = \begin{bmatrix} \mathbf{0} \\ \mathbf{T}^T \hat{\mathbf{V}} \\ \mathbf{0} \end{bmatrix}
$$

$$
\begin{bmatrix} \mathbf{E} & \mathbf{R} & \mathbf{D} \\ \mathbf{R}^T & \mathbf{A} & \mathbf{0} \\ \mathbf{D}^T & \mathbf{0} & \mathbf{0} \end{bmatrix} \begin{bmatrix} \hat{\mathbf{u}} \\ \hat{\boldsymbol{\kappa}} \\ \hat{\boldsymbol{\lambda}}_2 \end{bmatrix} = \begin{bmatrix} (\mathbf{C} - \mathbf{C}^T)\hat{\mathbf{u}}' + \mathbf{L}\hat{\boldsymbol{\kappa}}' \\ -\mathbf{L}^T \hat{\mathbf{u}}' + \hat{\mathbf{V}} \\ \mathbf{0} \end{bmatrix} \tag{4.31}
$$

This consists in solving at the same time 6 different load cases. The results ($\hat{\mathbf{u}}$, $\hat{\boldsymbol{\kappa}}$, $\hat{\boldsymbol{\lambda}}_2$, $\hat{\mathbf{u}}'$, $\hat{\boldsymbol{\kappa}}'$, $\hat{\boldsymbol{\lambda}}_1$) are matrices with 6 columns, each one containing the results of a particular load case. Then,

$$
\hat{\mathbf{V}} = \mathbf{K}_s \hat{\boldsymbol{\kappa}} \tag{4.32}
$$

The simplest way to proceed is to choose $\hat{\mathbf{V}} = \mathbf{I}_6$, i.e. the six different load cases contain a unit load component and all others are set to zero. In that case,

$$
\begin{aligned}
\mathbf{u} &= \hat{\mathbf{u}}\mathbf{V} \\
\boldsymbol{\kappa} &= \hat{\boldsymbol{\kappa}}\mathbf{V} \\
\boldsymbol{\lambda}_2 &= \hat{\boldsymbol{\lambda}}_2 \mathbf{V} \\
\mathbf{u}' &= \hat{\mathbf{u}}'\mathbf{V} \\
\boldsymbol{\kappa}' &= \hat{\boldsymbol{\kappa}}'\mathbf{V} \\
\boldsymbol{\lambda}_1 &= \hat{\boldsymbol{\lambda}}_1 \mathbf{V}
\end{aligned} \tag{4.33}
$$

and the cross-sectional stiffness matrix is

$$\mathbf{K}_s = \hat{\mathbf{V}}\hat{\boldsymbol{\kappa}}^{-1} = \hat{\boldsymbol{\kappa}}^{-1} \tag{4.34}$$

Note that this method of computing the beam cross-sectional stiffness matrix differs from the method used by Giavotto, Blasques *et al.* (Giavotto et al., 1983; Blasques and Stolpe, 2012; Blasques, 2012, 2011; Blasques et al., 2016) that was based on the principle of virtual work.

4.3 Implementation of the line finite element

In order to be able to perform a cross-sectional analysis, the matrices of Equation 4.20 have to be evaluated. This section presents the procedure for the computation of a general n-node line element based on a pure displacement formulation similar to the one used for shell finite elements (Ahmad et al., 1970).

4.3.1 Shape functions

The real and reference elements used are represented in Fig. 4.2. For instance, for a 3-node line element, the node position, the shape functions and their derivatives are:

$$
\begin{aligned}
s_1 &= -1 & s_2 &= +1 & s_3 &= 0 \\
N_1 &= \tfrac{1}{2}s(s-1) & N_2 &= \tfrac{1}{2}s(s+1) & N_3 &= 1 - s^2 \\
N_{1,s} &= s - \tfrac{1}{2} & N_{2,s} &= s + \tfrac{1}{2} & N_{3,s} &= -2s
\end{aligned}
\tag{4.35}
$$
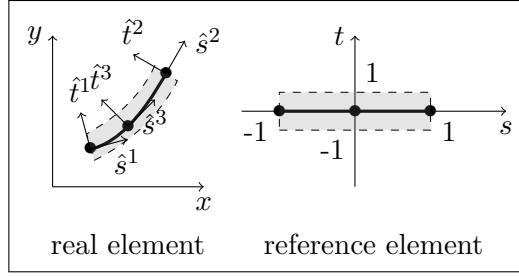
Figure 4.2   Real and reference
element (example for $n = 3$)

4.3.2   Element coordinate system at node

To define the element coordinate system rst, we start by defining a vector in the direction
of the element:

$$\hat{\mathbf{s}}^* = \begin{bmatrix} \partial x/\partial s \\ \partial y/\partial s \\ \partial z/\partial s \end{bmatrix} = \begin{bmatrix} \sum_{i=1}^{n_n} N_{i,s} x_i \\ \sum_{i=1}^{n_n} N_{i,s} y_i \\ 0 \end{bmatrix} \tag{4.36}$$

and by taking the norm of this vector.

$$\hat{\mathbf{s}} = \frac{\hat{\mathbf{s}}^*}{|\hat{\mathbf{s}}^*|} \tag{4.37}$$

We then compute a vector that is normal to the element direction and that lies in the
cross-sectional plane:

$$\hat{\mathbf{t}} = \mathbf{k} \times \hat{\mathbf{s}} = \begin{vmatrix} \mathbf{i} & \mathbf{j} & \mathbf{k} \\ 0 & 0 & 1 \\ \hat{s}_x & \hat{s}_y & 0 \end{vmatrix} = -\hat{s}_y \mathbf{i} + \hat{s}_x \mathbf{j} = \begin{bmatrix} -\hat{s}_y \\ \hat{s}_x \\ 0 \end{bmatrix} = \begin{bmatrix} \hat{t}_x \\ \hat{t}_y \\ 0 \end{bmatrix} \tag{4.38}$$

$\hat{\mathbf{s}}$ and $\hat{\mathbf{t}}$ form an orthonormal coordinate system that corresponds to the s- and t-axes
of the element coordinate system (the r-axis being parallel to the z-axis of the global
coordinate system). $\hat{\mathbf{s}}$ and $\hat{\mathbf{t}}$ can be computed at any point along the element length,
starting with the s-coordinate and using Equations 4.36, 4.37 and 4.38. n_n is the number

of nodes in the element. x_i and y_i are respectively the x- and y-coordinates of the ith node.

The values of the $\hat{\mathbf{t}}$ and $\hat{\mathbf{s}}$ vectors are of particular importance at node for the expression of the shape functions and are expressed as:

$$\hat{\mathbf{t}}^i = \hat{\mathbf{t}}(s_i)$$
$$\hat{\mathbf{s}}^i = \hat{\mathbf{s}}(s_i)$$

(4.39)

for node i.

4.3.3 Coordinate of a point in the element

The x-, y- and z-coordinates of a point in an element can be computed as a function of the s- and t-coordinates as (Bathe, 2006; Cook et al., 2002):

$$x = \sum_{i=1}^{n_n} N_i x_i + \frac{ta}{2} \sum_{i=1}^{n_n} N_i \hat{t}_x^i$$
$$y = \sum_{i=1}^{n_n} N_i y_i + \frac{ta}{2} \sum_{i=1}^{n_n} N_i \hat{t}_y^i$$
$$z = \sum_{i=1}^{n_n} N_i z_i + \frac{ta}{2} \sum_{i=1}^{n_n} N_i \hat{t}_z^i$$

(4.40)

where a is the element thickness (along the t-direction) and z_i is the z-coordinate of the ith node.

4.3.4 Jacobian matrix

The Jacobian matrix $\mathbf{J}$ is defined as:

$$\begin{bmatrix} \partial/\partial s \\ \partial/\partial t \end{bmatrix} = \underbrace{\begin{bmatrix} \partial x/\partial s & \partial y/\partial s \\ \partial x/\partial t & \partial y/\partial t \end{bmatrix}}_{\mathbf{J}} \begin{bmatrix} \partial/\partial x \\ \partial/\partial y \end{bmatrix}$$

(4.41)

So, using Equation 4.40, the Jacobian matrix could be expressed as

$$\mathbf{J} = \sum_{i=1}^{n_n} \begin{bmatrix} N_{i,s}x_i + \frac{ta}{2}N_{i,s}\hat{t}_x^i & N_{i,s}y_i + \frac{ta}{2}N_{i,s}\hat{t}_y^i \\ \frac{a}{2}N_i\hat{t}_x^i & \frac{a}{2}N_i\hat{t}_y^i \end{bmatrix} \tag{4.42}$$

4.3.5 Displacement field, shape function and derivative of shape function matrices

The displacement field can be evaluated by the subtraction of final and initial position of each node using Equation 4.40 (Bathe, 2006). The warping displacement field is then:

$$\mathbf{g} = \mathbf{N}_e\mathbf{u}_e \tag{4.43}$$

where the shape function matrix is

$$\mathbf{N}_e = \begin{bmatrix} & N_i & 0 & 0 & 0 & 0 & -\frac{ta}{2}N_i\hat{t}_y^i \\ \dots & 0 & N_i & 0 & 0 & 0 & \frac{ta}{2}N_i\hat{t}_x^i & \dots \\ & 0 & 0 & N_i & \frac{ta}{2}N_i\hat{t}_y^i & -\frac{ta}{2}N_i\hat{t}_x^i & 0 \end{bmatrix} \tag{4.44}$$

and the nodal displacement vector is

$$\mathbf{u}_e = \begin{bmatrix} \dots & u_x^i & u_y^i & u_z^i & \theta_x^i & \theta_y^i & \theta_z^i & \dots \end{bmatrix}^T \tag{4.45}$$

i ranges from 1 to n_n where n_n is the number of nodes of the element.

Derivation of the shape function matrix using Equation 4.41 yields:

$$\mathbf{B}_e\mathbf{N}_e = \cdots \begin{bmatrix} N_{i,x} & 0 & 0 & 0 & 0 & -\frac{a}{2}\hat{t}^i_y(tN_i)_{,x} \\ 0 & N_{i,y} & 0 & 0 & 0 & \frac{a}{2}\hat{t}^i_x(tN_i)_{,y} \\ N_{i,y} & N_{i,x} & 0 & 0 & 0 & -\frac{a}{2}\hat{t}^i_y(tN_i)_{,y} + \frac{a}{2}\hat{t}^i_x(tN_i)_{,x} \\ 0 & 0 & N_{i,x} & \frac{a}{2}\hat{t}^i_y(tN_i)_{,x} & -\frac{a}{2}\hat{t}^i_x(tN_i)_{,x} & 0 \\ 0 & 0 & N_{i,y} & \frac{a}{2}\hat{t}^i_y(tN_i)_{,y} & -\frac{a}{2}\hat{t}^i_x(tN_i)_{,y} & 0 \\ 0 & 0 & 0 & 0 & 0 & 0 \end{bmatrix} \cdots \tag{4.46}$$

where

$$\begin{cases} N_{i,x} = j_{11}N_{i,s} \\ N_{i,y} = j_{21}N_{i,s} \\ (tN_i)_{,x} = j_{11}tN_{i,s} + j_{12}N_i \\ (tN_i)_{,y} = j_{21}tN_{i,s} + j_{22}N_i \end{cases} \tag{4.47}$$

and i is again ranging from 1 to n_n. j_{11}, j_{12}, j_{21} and j_{22} are the components of the $\mathbf{j}$ matrix, which is the invert of the Jacobian matrix, i.e., $\mathbf{j} = \mathbf{J}^{-1}$.

4.3.6 Material properties

As the material's stress–strain relationship has to be expressed in the xyz-global coordinate system and the elastic properties are known in the 123-material coordinate system, a transformation of the material constitutive law has to be performed. The stress-strain relationship of a specially orthotropic lamina is

$$\mathbf{Q}_{123} = \begin{bmatrix} \frac{E_1}{1-\nu_{12}\nu_{21}} & \frac{\nu_{12}E_2}{1-\nu_{12}\nu_{21}} & 0 & 0 & 0 & 0 \\ & \frac{E_2}{1-\nu_{12}\nu_{21}} & 0 & 0 & 0 & 0 \\ & & G_{12} & 0 & 0 & 0 \\ & & & \frac{5}{6}G_{13} & 0 & 0 \\ & \text{sym.} & & & \frac{5}{6}G_{23} & 0 \\ & & & & & 0 \end{bmatrix} \tag{4.48}$$

where $\nu_{21} = \frac{E_2}{E_1}\nu_{12}$. The 1 and 2-axes are the principal direction of the material properties of the lamina, where the 1-axis is typically the direction of the fibres and the 3-axis is normal to the plate plane. The 5/6 factor in front of the shear modulus in planes 13 and 23 is a correcting factor for the transverse shear stress. This value is correct for homogeneous plates and could be adjusted for composite plates (Berthelot, 2012), which is not done here. There is no rigidity in the thickness direction as a plate cannot transfer stress in that direction. Note that a generally orthotropic stress-strain relationship (with no rigidity in the 3-direction) could be used as well.

The transformation of the constitutive matrix to the global coordinate system is performed in two steps. The first step consists of a transformation in the element coordinate system:

$$\mathbf{Q}_{rst} = \mathbf{T}_\beta^T \mathbf{Q}_{123} \mathbf{T}_\beta \tag{4.49}$$

and the second step, in the global coordinate system:

$$\mathbf{Q} = \mathbf{T}_\alpha^T \mathbf{Q}_{rst} \mathbf{T}_\alpha \tag{4.50}$$

where the transformation matrices are

$$\mathbf{T}_{\alpha/\beta} = \begin{bmatrix} l_1^2 & m_1^2 & l_1 m_1 & n_1 l_1 & m_1 n_1 & n_1^2 \\ l_2^2 & m_2^2 & l_2 m_2 & n_2 l_2 & m_2 n_2 & n_2^2 \\ 2l_1 l_2 & 2m_1 m_2 & l_1 m_2 + l_2 m_1 & n_1 l_2 + n_2 l_1 & m_1 n_2 + m_2 n_1 & 2n_1 n_2 \\ 2l_3 l_1 & 2m_3 m_1 & l_3 m_1 + l_1 m_3 & n_3 l_1 + n_1 l_3 & m_3 n_1 + m_1 n_3 & 2n_3 n_1 \\ 2l_2 l_3 & 2m_2 m_3 & l_2 m_3 + l_3 m_2 & n_2 l_3 + n_3 l_2 & m_2 n_3 + m_3 n_2 & 2n_2 n_3 \\ l_3^2 & m_3^2 & l_3 m_3 & n_3 l_3 & m_3 n_3 & n_3^2 \end{bmatrix} \tag{4.51}$$

For $\mathbf{T}_\beta$,

$$\begin{aligned}
l_1 = \mathbf{e}_r \cdot \mathbf{e}_1 \qquad m_1 = \mathbf{e}_s \cdot \mathbf{e}_1 \qquad n_1 = \mathbf{e}_t \cdot \mathbf{e}_1 \\
l_2 = \mathbf{e}_r \cdot \mathbf{e}_2 \qquad m_2 = \mathbf{e}_s \cdot \mathbf{e}_2 \qquad n_2 = \mathbf{e}_t \cdot \mathbf{e}_2 \\
l_3 = \mathbf{e}_r \cdot \mathbf{e}_3 \qquad m_3 = \mathbf{e}_s \cdot \mathbf{e}_3 \qquad n_3 = \mathbf{e}_t \cdot \mathbf{e}_3
\end{aligned} \tag{4.52}$$

and

$$\mathbf{e}_r = \begin{bmatrix} 1 & 0 & 0 \end{bmatrix} \qquad \mathbf{e}_1 = \begin{bmatrix} \sin\beta & 0 & \cos\beta \end{bmatrix}$$

$$\mathbf{e}_s = \begin{bmatrix} 0 & 1 & 0 \end{bmatrix} \qquad \mathbf{e}_2 = \begin{bmatrix} \cos\beta & 0 & -\sin\beta \end{bmatrix} \qquad (4.53)$$

$$\mathbf{e}_t = \begin{bmatrix} 0 & 0 & 1 \end{bmatrix} \qquad \mathbf{e}_3 = \begin{bmatrix} 0 & 1 & 0 \end{bmatrix}$$

where β is the angle between the fibre direction and the beam longitudinal axis (see Fig. 4.1). For $\mathbf{T}_\alpha$,

$$l_1 = \mathbf{e}_x \cdot \mathbf{e}_r \qquad m_1 = \mathbf{e}_y \cdot \mathbf{e}_r \qquad n_1 = \mathbf{e}_z \cdot \mathbf{e}_r$$

$$l_2 = \mathbf{e}_x \cdot \mathbf{e}_s \qquad m_2 = \mathbf{e}_y \cdot \mathbf{e}_s \qquad n_2 = \mathbf{e}_z \cdot \mathbf{e}_s \qquad (4.54)$$

$$l_3 = \mathbf{e}_x \cdot \mathbf{e}_t \qquad m_3 = \mathbf{e}_y \cdot \mathbf{e}_t \qquad n_3 = \mathbf{e}_z \cdot \mathbf{e}_t$$

and

$$\mathbf{e}_x = \begin{bmatrix} 1 & 0 & 0 \end{bmatrix} \qquad \mathbf{e}_r = \begin{bmatrix} \cos\alpha & \sin\alpha & 0 \end{bmatrix}$$

$$\mathbf{e}_y = \begin{bmatrix} 0 & 1 & 0 \end{bmatrix} \qquad \mathbf{e}_s = \begin{bmatrix} -\sin\alpha & \cos\alpha & 0 \end{bmatrix} \qquad (4.55)$$

$$\mathbf{e}_z = \begin{bmatrix} 0 & 0 & 1 \end{bmatrix} \qquad \mathbf{e}_t = \begin{bmatrix} 0 & 0 & 1 \end{bmatrix}$$

where $\alpha = \arctan2(\hat{s}_y, \hat{s}_x) = \arctan2(-\hat{t}_x, \hat{t}_y)$ is the angle between the element direction and the global x-axis (see Fig. 4.1).

4.3.7 Numerical integration

The integration of Equation 4.20 over the area of the elements is computed numerically using Gauss formula. A full integration is used in the s-direction and $n_t = 2$ integration points per layer are used in the t-direction. The integral of a function of s and t over the area of the element then become (Batoz and Dhatt, 1992)

$$F = \int f(s,t)\,\mathrm{d}A = \sum_{i=1}^{n_s}\sum_{j=1}^{n_l}\sum_{k=1}^{n_t} \omega_i \frac{a_j}{a}\omega_k f(s_i, t_{jk}) \qquad (4.56)$$

where n_s is the number of integration points along the element length (s-direction), n_l is the number of layers along the element thickness (t-direction), n_t is the number of

integration points per layer in the thickness (t) direction and

$$t_{jk} = t_j + \frac{a_j}{a}(1 + t'_k) \tag{4.57}$$

so that t ranges from -1 to $+1$ along the element thickness and t' ranges from -1 to $+1$ along each layer thickness. a_j is the thickness of the jth layer and t_j is the t-coordinate of the bottom of the jth layer. The sampling points position (s_i and t'_k) and weight (ω_i and ω_k) are presented in Table 4.1.

Table 4.1 Sampling point position and weight for Gauss numerical integration in one dimension (Bathe, 2006; Dhatt et al., 2005)

2 int. points			3 int. points		
i	ω_i	s_i	i	ω_i	s_i
1	1	$-1/\sqrt{3}$	1	5/9	$-\sqrt{3/5}$
2	1	$+1/\sqrt{3}$	2	8/9	0
			3	5/9	$+\sqrt{3/5}$
$\int_{-1}^{1} f \ ds \approx \sum_{i=1}^{n_i} \omega_i f(s_i)$					

4.3.8 Fictive rigidity for drilling degrees of freedom

Because the drilling degree of freedom (rotation about the $\hat{\mathbf{t}}$-axis, normal to the beam wall) of the nodes has no associated stiffness, singular or ill-conditioned matrices can arise when two adjacent elements are parallel. To avoid this problem, small stiffness terms are added to the $\mathbf{E}$ matrix (in Eq. 4.30 or 4.31) using a procedure similar to the one presented by Cook et al. (2002).

4.3.9 Post-processing

For a given load case, once the nodal displacements $\mathbf{u}$, their derivatives $\mathbf{u}'$ and the beam generalized strains $\boldsymbol{\kappa}$ are known, the strains in each element can be computed

using Equation 4.17 and then, the stresses with Equation 4.2. Using the transformation matrices defined in Equations 4.51 to 4.55, the stresses and strains can be computed in the other coordinate systems as (Cook et al., 2002):

$$\boldsymbol{\sigma}_{rst} = \mathbf{T}_\alpha^{-T}\boldsymbol{\sigma}$$

$$\boldsymbol{\sigma}_{123} = \mathbf{T}_\beta^{-T}\boldsymbol{\sigma}_{rst}$$

$$\boldsymbol{\epsilon}_{rst} = \mathbf{T}_\alpha\boldsymbol{\epsilon}$$

$$\boldsymbol{\epsilon}_{123} = \mathbf{T}_\beta\boldsymbol{\epsilon}_{rst}$$

$$(4.58)$$

Once this is done, other interesting derived results to compute are the shell internal loads. They are computed as integrals of the stress components over the element thickness:

$$N_m = \int_{-a/2}^{a/2} \sigma_m \, \mathrm{d}\hat{t} = \sum_{j=1}^{n_l}\sum_{k=1}^{n_t} \frac{a_j}{2}\sigma_m\omega_t \tag{4.59}$$

$$Q_n = \int_{-a/2}^{a/2} \sigma_n \, \mathrm{d}\hat{t} = \sum_{j=1}^{n_l}\sum_{k=1}^{n_t} \frac{a_j}{2}\sigma_n\omega_t \tag{4.60}$$

$$M_m = \int_{-a/2}^{a/2} \hat{t}\sigma_m \, \mathrm{d}\hat{t} = \sum_{j=1}^{n_l}\sum_{k=1}^{n_t} \frac{a_j a}{4}t_{jk}\sigma_m\omega_t \tag{4.61}$$

for $m = (r, \ s, \ rs)$ and $n = (rt, \ st)$. The other variables for numerical integration are the same as those of Equation 4.56.

4.3.10 Implemented elements

For the validation presented in the next section, a three-node element ($n_n = 3$) has been implemented using the Python programming language. This element has $n_s = 3$ integration points along the element length (full integration) and $n_t = 2$ integration points along each layer in the thickness direction. Preliminary results not presented here have shown that the three-node element yields better performance than its two-node counterpart by allowing a better representation of the actual geometry of a curved cross section wall. Its convergence rate is then much faster.

4.4 Validation of the implemented element

This section proposes different validation cases intended to verify the performance of the proposed method for the analysis of different types of nonhomogeneous anisotropic thin-walled beams. The pre- and post-processing of the models is done with the Gmsh software (Geuzaine and Remacle, 2009). Note that all the gradient results presented (stresses, strains and shell internal loads) are computed at the centre of the element, i.e., at $s = 0$.

4.4.1 Validation case 1

The first validation case consists of a homogeneous thin-walled circular cross section of radius $R = 1$ and thickness $t = 0.01$ made of an isotropic material with $E = E_1 = E_2 = 207 \times 10^9$, $G = G_{12} = G_{13} = G_{23} = 79.3 \times 10^9$ and $\nu = \nu_{12} = E/(2G) - 1 = 0.3052$. This cross section is centred at the origin of the global coordinate system so that its stiffness matrix is

$$
\mathbf{K}_s = \begin{bmatrix}
2.646 & 0 & 0 & 0 & 0 & 0 \\
0 & 2.646 & 0 & 0 & 0 & 0 \\
0 & 0 & 13.01 & 0 & 0 & 0 \\
0 & 0 & 0 & 6.503 & 0 & 0 \\
0 & 0 & 0 & 0 & 6.503 & 0 \\
0 & 0 & 0 & 0 & 0 & 4.983
\end{bmatrix} \times 10^9
\tag{4.62}
$$

when using the analytical solution for a hollow circle section ($\mathbf{K}_s = \text{diag}(k_x GA, k_y GA, EA, EI_x, EI_y, GJ)$) and where the shear correction factors (k_x and k_y) are computed as per Cowper (1966). The Cowper shear correction factor is used because it is defined for static analysis as the one performed here. A, I_x, I_y and J are respectively the cross-sectional area, moment of inertia about x-axis, moment of inertia about y-axis and polar moment of inertia.

With the proposed model using 100 quadratic elements, we get, when looking at the stress, strain and shear flow values for the 6 different unit load cases, differences with the analytical solutions that are all under 1 % and decrease if the finite element mesh is refined. As an example of the results obtained from the proposed model, Figure 4.3 shows the distribution of σ_{rr} in the middle of the wall over the cross section for the case where the only load is $M_x = 1$. Figure 4.4 shows the shear flow distribution obtained with $V_x = 1$, the other load components being null.
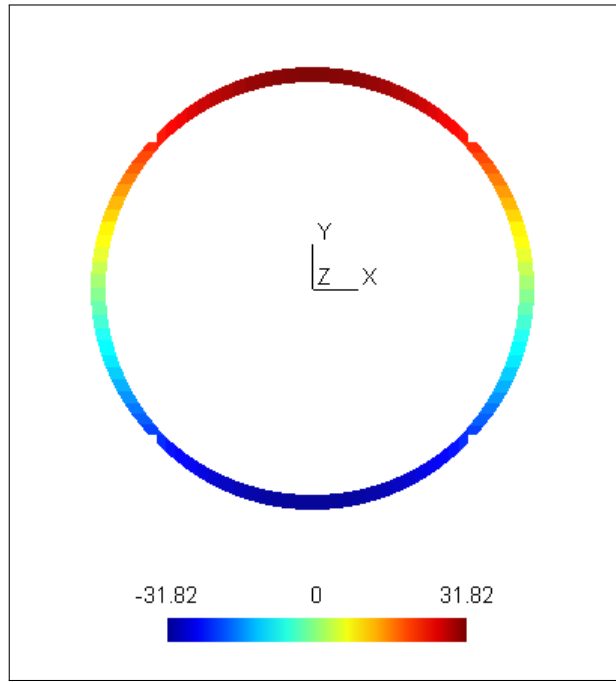
Figure 4.3   Normal stress σ_{rr} for validation
case 1 and $M_x = 1$

4.4.2   Validation case 2

In order to verify if the model is able to manage the geometric coupling correctly, we use the same cross section as validation case 1 but translate the centre of the circle to coordinate $x = -0.5$ and $y = 1$. In that case, the proposed model gives the following
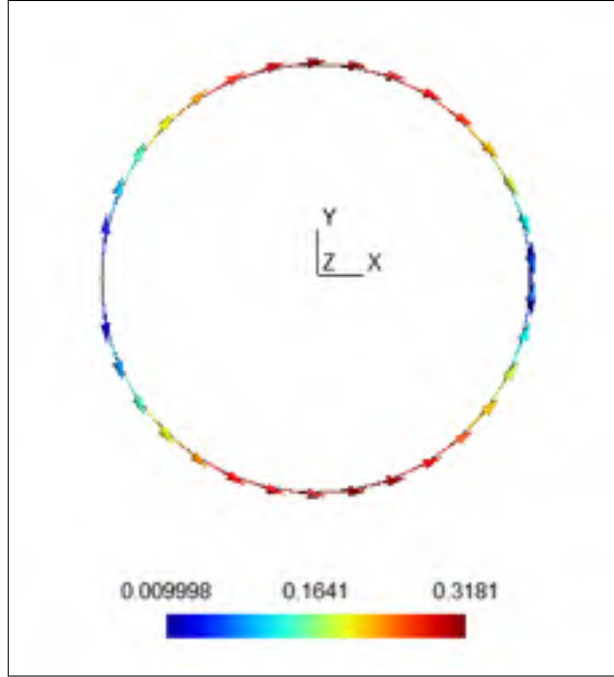
Figure 4.4   Shear flow N_{rs} for validation
case 1 and $V_x = 1$

stiffness and compliance matrices:

$$
\mathbf{K}_s = \begin{bmatrix}
2.646 & 0 & 0 & 0 & 0 & -2.646 \\
0 & 2.646 & 0 & 0 & 0 & -1.323 \\
0 & 0 & 13.01 & 13.01 & 6.503 & 0 \\
0 & 0 & 13.01 & 19.51 & 6.503 & 0 \\
0 & 0 & 6.503 & 6.503 & 9.755 & 0 \\
-2.646 & -1.323 & 0 & 0 & 0 & 8.290
\end{bmatrix} \times 10^9 \tag{4.63}
$$

$$
\mathbf{F}_s = \begin{bmatrix}
578.6 & 100.3 & 0 & 0 & 0 & 200.7 \\
100.3 & 428.1 & 0 & 0 & 0 & 100.3 \\
0 & 0 & 269.1 & -153.8 & -76.88 & 0 \\
0 & 0 & -153.8 & 153.8 & 0 & 0 \\
0 & 0 & -76.88 & 0 & 153.8 & 0 \\
200.7 & 100.3 & 0 & 0 & 0 & 200.7
\end{bmatrix} \times 10^{-12} \tag{4.64}
$$

Looking at the compliance matrix $\mathbf{F}_s$, we can observe that a shear force in a direction now causes a shear deformation in the other direction as well as a torsional deformation. An axial force generates axial deformation and bending in both directions. A bending moment about an axis creates a bending around that axis and an axial deformation. Finally, a torsional moment causes a shear deformation in both directions in addition to a torsional deformation. All those phenomena are expected. If we compute the position of the shear and elastic centre, using Equations 3.32 and 3.33, we get $x_c = x_e = -0.5$ and $y_c = y_e = 1$. This corresponds to the centre of the circle, as expected. If we perform a transformation of the cross-sectional stiffness matrix using Equation 3.22 or 3.23 with $a = -0.5$ and $b = 1$ (i.e., transferring the cross-sectional stiffness matrix to the centre of the circle), we get the same results as for validation case 1, as expected.

4.4.3 Validation case 3

This case consists of a rectangular thin-walled section with the same material as validation case 1. The section has a base $b = 1$, a height $h = 2$ and a thickness $t = 0.01$ and is centred at the origin of the global coordinate system. The cross-sectional stiffness matrix is then:

$$\mathbf{K}_s = \begin{bmatrix} 1.149 & 0 & 0 & 0 & 0 & 0 \\ 0 & 2.987 & 0 & 0 & 0 & 0 \\ 0 & 0 & 12.42 & 0 & 0 & 0 \\ 0 & 0 & 0 & 6.900 & 0 & 0 \\ 0 & 0 & 0 & 0 & 2.415 & 0 \\ 0 & 0 & 0 & 0 & 0 & 2.115 \end{bmatrix} \times 10^9 \tag{4.65}$$

when computed using thin-walled approximation and when the shear coefficients are computed according to Cowper (1966). The proposed model, with 150 quadratic elements

gives:

$$\mathbf{K}_s = \begin{bmatrix} 1.149 & 0 & 0 & 0 & 0 & 0 \\ 0 & 2.988 & 0 & 0 & 0 & 0 \\ 0 & 0 & 12.42 & 0 & 0 & 0 \\ 0 & 0 & 0 & 6.900 & 0 & 0 \\ 0 & 0 & 0 & 0 & 2.415 & 0 \\ 0 & 0 & 0 & 0 & 0 & 2.115 \end{bmatrix} \times 10^9 \tag{4.66}$$

The model gives the same values as the analytical solution up to 4 significant digits except for the transverse shear stiffness in the y-direction where the error is less than 0.1 % and is decreasing as the number of elements in the model is increased.

For that geometry, if the beam is subjected to a torsional moment, the cross section does not remain plane anymore. An analytical solution shows that for a unit torsional moment, the upper right and lower left corners should see a warping displacement in the z-direction of 78.81×10^{-12} and that the upper left and lower right corners should see a displacement of the opposite value. As we can see in Fig. 4.5, this is what the proposed model predicts.

Another interesting value to validate is the shear flow due to a shear force. The analytical solution for V_x indicate that the shear flow varies from 0 at $y = 0$ to a maximum value of 0.5356 at $x = 0$. This is what we get from the proposed model as we can see in Fig. 4.6.

4.4.4   Validation case 4

Starting with load case 3, if we rotate the mesh of the cross section by an angle of 20° around the positive z-axis, the proposed model returns the following cross-sectional
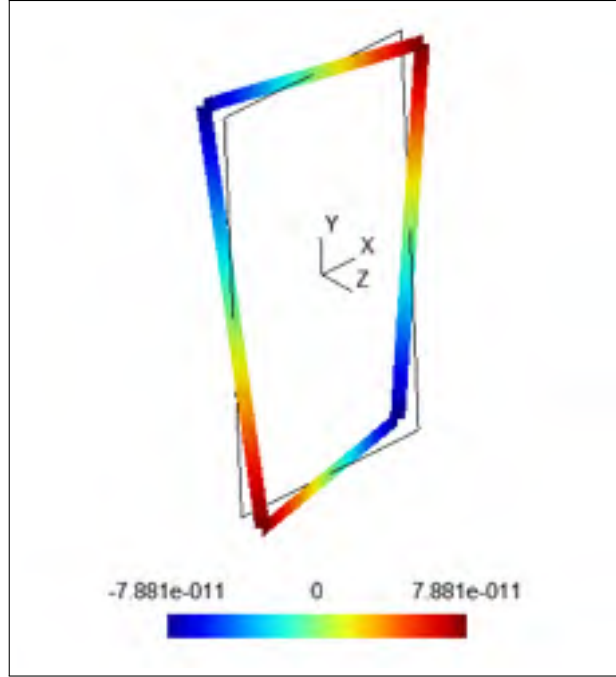
Figure 4.5 Warping displacement u_z for validation case 3 and $M_t = 1$

stiffness matrix:

$$\mathbf{K}_s = \begin{bmatrix} 1.364 & -0.5909 & 0 & 0 & 0 & 0 \\ -0.5909 & 2.773 & 0 & 0 & 0 & 0 \\ 0 & 0 & 12.42 & 0 & 0 & 0 \\ 0 & 0 & 0 & 6.375 & 1.441 & 0 \\ 0 & 0 & 0 & 1.441 & 2.940 & 0 \\ 0 & 0 & 0 & 0 & 0 & 2.115 \end{bmatrix} \times 10^9 \qquad (4.67)$$

As expected, we observe a coupling between bending in both directions. The same kind of coupling also exists for shear. If we compute the angle between the xy-coordinate system and the principal inertia coordinate system using Equation 3.34, we get the right value of $20°$ and if we use Equation 3.30 or 3.31 to transform the cross-sectional stiffness matrix into the principal inertia coordinate system, we get the same result as for the non-rotated rectangular cross section, as expected.
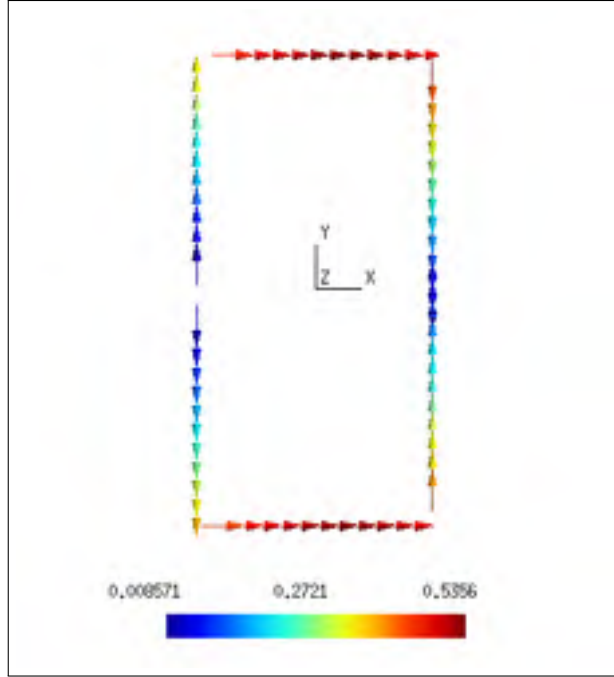
Figure 4.6   Shear flow N_{rs} for validation
case 3 and $V_x = 1$

4.4.5   Validation case 5

In this case, we study a thin-walled circular beam cross section with the same geometry
as validation case 1 (radius $R = 1$ and thickness $t = 0.01$). This section is made with
one layer of an orthotropic material (fibre reinforced polymer) with fibres rotated by an
angle of $45°$ relative to the beam longitudinal axis as illustrated in Fig. 4.7. The material
properties are $E_1 = 39.0 \times 10^9$, $E_2 = 14.5 \times 10^9$, $\nu_{12} = 0.290$ and $G_{12} = 4.24 \times 10^9$.
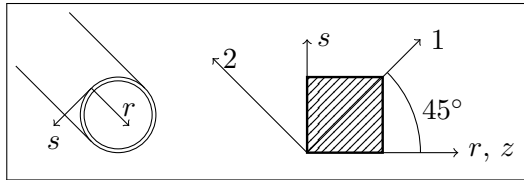
Figure 4.7   Validation case 5

The cross-sectional compliance matrix can be obtained analytically by computing the generalized strain vector for six unit internal force load cases. For that analysis, the shear correction factor is taken as 0.5. The resulting compliance matrix is

$$
\mathbf{F}_s =
\begin{bmatrix}
3485 & 0 & 0 & 689.5 & 0 & 0 \\
0 & 3485 & 0 & 0 & 689.5 & 0 \\
0 & 0 & 1256 & 0 & 0 & -344.9 \\
689.5 & 0 & 0 & 2511 & 0 & 0 \\
0 & 689.5 & 0 & 0 & 2511 & 0 \\
0 & 0 & -344.9 & 0 & 0 & 1743
\end{bmatrix}
\times 10^{-12}
\qquad (4.68)
$$

The solution obtained from the proposed model using 100 quadratic elements is

$$
\mathbf{F}_s =
\begin{bmatrix}
2864 & 0 & 0 & 689.5 & 0 & 0 \\
0 & 2864 & 0 & 0 & 689.5 & 0 \\
0 & 0 & 1256 & 0 & 0 & -344.8 \\
689.5 & 0 & 0 & 2511 & 0 & 0 \\
0 & 689.5 & 0 & 0 & 2511 & 0 \\
0 & 0 & -344.8 & 0 & 0 & 1742
\end{bmatrix}
\times 10^{-12}
\qquad (4.69)
$$

These solutions are really similar. Except for the transverse shear compliances, the differences are under 0.1 %. The difference in the transverse shear compliances is about 18 % and is probably due to the incorrect evaluation of the shear correction factor in the analytical solution which is hard to evaluate due to the presence of off-axis fibres. This shows that the proposed model is able to manage correctly the transverse shear-bending and the extension-torsion couplings due to the presence of off-axis fibres.

4.4.6 Validation case 6

In this validation load case, we study an open thin-walled section. The cross-sectional shape and material are the same as validation case 1 excepted that the section is open at the point of coordinate $x = R$ and $y = 0$.

Using the proposed model with 100 quadratic elements, we get the following cross-sectional stiffness matrix:

$$\mathbf{K}_s = \begin{bmatrix} 2.820 & 0 & 0 & 0 & 0 & 0 \\ 0 & 0.8472 & 0 & 0 & 0 & -1.694 \\ 0 & 0 & 13.01 & 0 & 0 & 0 \\ 0 & 0 & 0 & 6.503 & 0 & 0 \\ 0 & 0 & 0 & 0 & 6.503 & 0 \\ 0 & -1.694 & 0 & 0 & 0 & 3.389 \end{bmatrix} \times 10^9 \qquad (4.70)$$

As expected, we can observe a coupling between the shear force in the y-direction and the torsion. If we compute the position of the shear centre using Equation 3.32, we get the same values as the analytical solution for an open thin-walled beam: $x_s = -2$ and $y_s = 0$. If we transfer the cross-sectional stiffness matrix to an origin located at the shear centre using Equation 3.22 or 3.23, the stiffness matrix becomes:

$$\mathbf{K}_s = \begin{bmatrix} 2820 & 0 & 0 & 0 & 0 & 0 \\ 0 & 847.2 & 0 & 0 & 0 & 0 \\ 0 & 0 & 13010 & 0 & -26010 & 0 \\ 0 & 0 & 0 & 6503 & 0 & 0 \\ 0 & 0 & -26010 & 0 & 58520 & 0 \\ 0 & 0 & 0 & 0 & 0 & 0.1658 \end{bmatrix} \times 10^6 \qquad (4.71)$$

and there is now a coupling between the extension and the bending about y-axis, as expected.

As we can see, the torsional stiffness $K_{s66} = 165.8 \times 10^3$ is really close to the analytical solution of $\overline{GJ} = 166.1 \times 10^3$ (0.18 % difference). It is also possible to compute analytically the warping displacement at the cross section's opening. This analytical solution predicts that the upper and lower parts have respectively warping displacement of $u_z = \pm 18.91 \times 10^{-6}$. As we can see in Fig. 4.8, the proposed model solution is really close to this value (0.16 % difference).
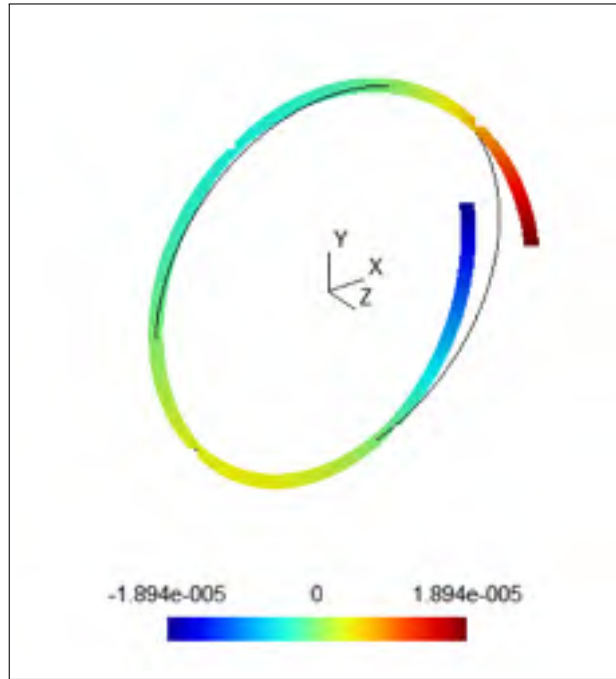
Figure 4.8   Warping displacement u_z for
validation case 6 and $M_t = 1$

Under a unit torsional moment, the shear stress varies linearly within the wall thickness. The analytical solution predicts that the shear stress is zero at mid thickness and reaches extremum values of ± 4775 at the bottom and the top of the element respectively. Fig. 4.9, showing the stress distribution at the top of the wall (interior) computed by the proposed model, presents values that are constant over the cross section (as expected) excepted near the opening. With a value of -4861, the numerical model is 1.8 % higher than the analytical solution. The stress at the bottom of the wall shows a distribution that is

similar to the one of Figure 4.9 with a value of 4688, which is 1.8 % lower than the analytical solution. This shift in the numerical values is also observed for the stress in the middle of the wall, where the numerical model predicts a value of -75 instead of 0. If we look at the torsional flow, the analytical solution yields $M_{rs} = -79.58 \times 10^{-3}$ which is exactly what the numerical model returns.
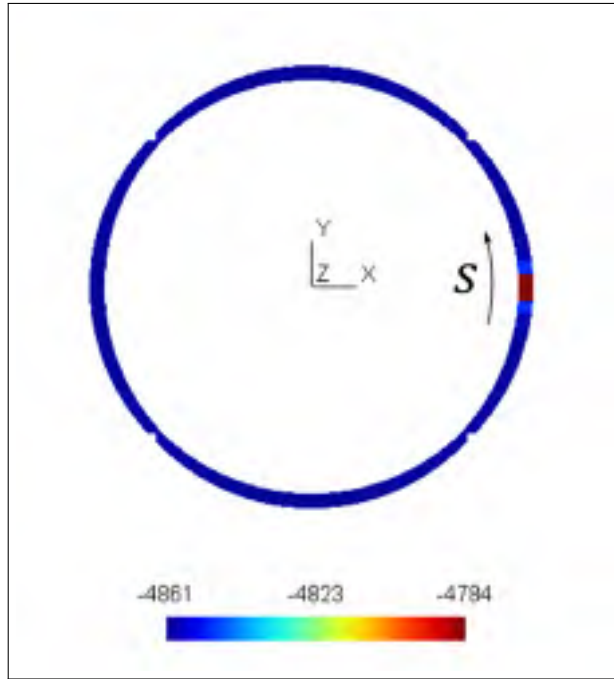
Figure 4.9 Shear stress τ_{rs} at the top of the wall (interior) for validation case 6 and $M_t = 1$

All the differences observed here could be reduced by increasing the number of finite elements in the mesh. This validation case shows that the proposed model correctly manages open sections and geometric shear-torsion coupling.

4.4.7 Validation case 7

This validation case consists of a thin-walled multicell cross section. The geometry is represented in Fig. 4.10 and the material is the same as validation case 1. The analytic

solution to this problem shows that the torsional stiffness of this cross section is $GJ = 10.86 \times 10^9$. When subjected to a unit torsional moment, the shear flow in the left cell is $N_{rs1} = 0.08088$ and the shear flow in the right cell is $N_{rs2} = 0.09324$. The shear flow in the central wall is $N_{rs2} - N_{rs1} = 0.01236$.
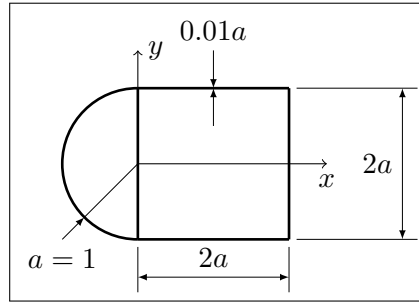
Figure 4.10   Validation case 7

For a model with 124 quadratic elements, the proposed model finds that the shear centre is located at $x = 0.3788$ and $y = 0$. If we transfer the cross-sectional stiffness matrix to this point, we get:

$$\mathbf{K}_s = \begin{bmatrix} 4.096 & 0 & 0 & 0 & 0 & 0 \\ 0 & 3.951 & 0 & 0 & 0 & 0 \\ 0 & 0 & 23.06 & 0 & -3.683 & 0 \\ 0 & 0 & 0 & 14.29 & 0 & 0 \\ 0 & 0 & -3.683 & 0 & 24.75 & 0 \\ 0 & 0 & 0 & 0 & 0 & 10.86 \end{bmatrix} \times 10^9 \qquad (4.72)$$

and we can see that the cross-sectional torsional rigidity $K_{s66} = 10.86 \times 10^9$ is as computed by the analytical solution (GJ). Fig. 4.11 shows the shear flow distribution as calculated by the proposed model. With values of 0.08089, 0.09324 and 0.01235 for the left cell, right cell and central wall respectively, the error relative to the analytical solution is limited to less than 0.1 %. This shows that the proposed model correctly models multicell cross sections.
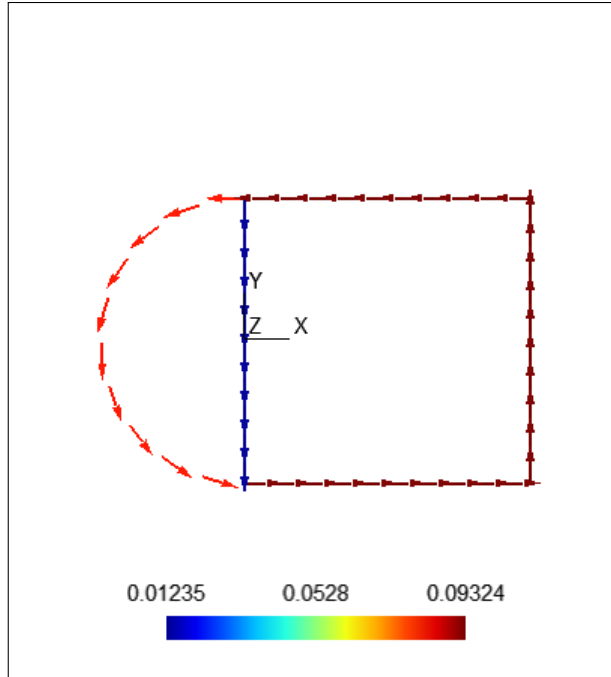
Figure 4.11   Shear flow N_{rs} for validation
case 7 and $M_t = 1$

4.4.8   Validation case 8

In the previous examples, the mesh line was always representing the middle of the shell thickness. However, the reference geometry is often located at one of the shell surfaces. Wind turbine blades and airplane wings are examples where the reference geometry is the exterior surface. It is then sometimes more useful to be able to build the model in order for the mesh to represent the bottom of the plate, i.e., the thickness is built only on one side of the mesh. This could be done by integrating in the thickness direction from $t = 0$ to $t = 2$ instead of integrating from $t = -1$ to $t = 1$ in Equation 4.56. If we model validation case 6 this way, the mesh being located on the exterior surface, the predicted shear centre location is $x_c = -1.995$ and $y_c = 0$ and the cross-sectional stiffness matrix,

when transferred to a coordinate system centred at the shear centre is

$$
\mathbf{K}_s =
\begin{bmatrix}
2824 & 0.0 & 0.0 & 0.0 & 0.0 & 0.0 \\
0.0 & 975.1 & 0.0 & 0.0 & 0.0 & 0.0 \\
0.0 & 0.0 & 13010 & 0.0 & -25950 & 0.0 \\
0.0 & 0.0 & 0.0 & 6503 & 0.0 & 0.0 \\
0.0 & 0.0 & -25950 & 0.0 & 58270 & 0.0 \\
0.0 & 0.0 & 0.0 & 0.0 & 0.0 & 0.1659
\end{bmatrix}
\times 10^6
\tag{4.73}
$$

The only important error is the transverse shear stiffness in the y-direction $(+15.1\ \%)$. This is probably due to the slight difference in the evaluation of the shear centre location. For all other results, we get exactly the same results as those obtained for validation case 6.

4.4.9   Validation case 9

With this validation case, we want to see if the model reacts correctly to a nonsymmetrical and unbalanced layup. Considering the difficulty of obtaining an analytical solution for that kind of layup, the beam section used here is a simple plate of unit width lying along the global x-axis made with 12 quadratic elements. The layup is made of 4 layers of the same material as validation case 5 with orientation $[0/15/-30/90]$ for a total thickness of 0.01 (each layer having a thickness of 0.0025). Classical lamination theory allows us to see that the $\mathbf{A}$, $\mathbf{B}$ and $\mathbf{D}$ matrices (not to be confused with the matrices of Equations 4.13, 4.20 and 4.29) of this laminate are fully populated indicating that couplings exists between each deformation modes. If this beam section is subjected to a unit axial force, it means that the plate is subjected to a membrane force $N_{rr} = 1$. The stress distribution in this plate should then vary only along its thickness. Table 4.2 shows the stress distribution along the plate thickness expressed in the layer coordinate system as computed using the classical lamination theory.

Table 4.2   Stress distribution in the plate
for validation case 9.

location	σ_1	σ_2	τ_{12}
layer 1, bot.	63.38	-12.68	-7.535
layer 1, mid.	87.13	-9.590	-5.069
layer 1, top	110.9	-6.504	-2.604
layer 2, bot.	95.34	-1.908	-11.08
layer 2, mid.	123.0	0.02439	-10.11
layer 2, top	150.6	1.957	-9.144
layer 3, bot.	102.6	16.18	20.49
layer 3, mid.	112.3	23.40	23.74
layer 3, top	122.1	30.62	27.00
layer 4, bot.	-22.69	73.47	-7.259
layer 4, mid.	-18.69	82.39	-9.724
layer 4, top	-14.68	91.32	-12.19

Using the proposed model, we get the same results up to 4 significant digits. These results are also obtained when using the option to place the nodes at the bottom of the laminate as explained in validation case 8.

4.4.10   Validation case 10

As a last validation case, a nonsymmetrical multicell cross section is analyzed. This is similar to wind turbine blade cross sections. As seen in Figure 4.12, the cross section is shifted to produce a geometrical coupling and unbalanced laminates are used to induce a bend-twist coupling. Laminates 1, 2 and 3 have their bottom side on the exterior of the cross section and their thickness is built from the mesh to the interior of the section. Laminate 4 is centred on the mesh line. All layers are made of the same material as validation case 5 and have a thickness of 0.001. Using the proposed methodology, when this cross section is meshed using 198 nodes and 100 quadratic elements, the resulting

138

cross-sectional stiffness matrix is

$$
\mathbf{K}_s = \begin{bmatrix}
100.7 & 13.16 & 7.777 & 7.780 & -7.811 & -85.97 \\
13.16 & 39.79 & 0.2969 & 0.4594 & -0.3280 & 25.80 \\
7.777 & 0.2969 & 371.1 & 382.1 & -422.7 & -7.335 \\
7.780 & 0.4594 & 382.1 & 398.8 & -439.5 & -7.403 \\
-7.811 & -0.3280 & -422.7 & -439.5 & 511.9 & 7.339 \\
-85.97 & 25.80 & -7.335 & -7.403 & 7.339 & 113.8
\end{bmatrix} \times 10^6
\qquad (4.74)
$$

Figure 4.13 shows the mesh used and the warping result for a unit torsional moment.
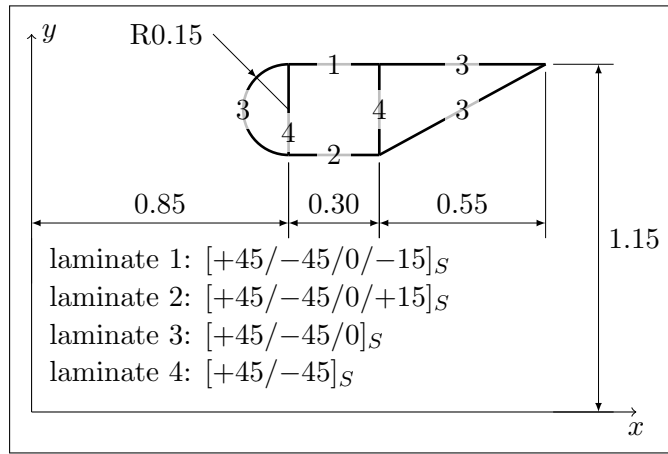
Figure 4.12   Validation case 10

These results are compared with results from a 3D shell finite element model of a beam of length 50.0 that uses the methodology presented in Section 3.6.1. For that model, the beam is meshed with 296 198 nodes and 100 000 8-node shell elements (100 in the cross section and 1000 along the beam length). Figure 4.14 shows this model. RBE2 elements are used at both ends to apply loads and supports. The cross-sectional stiffness matrix
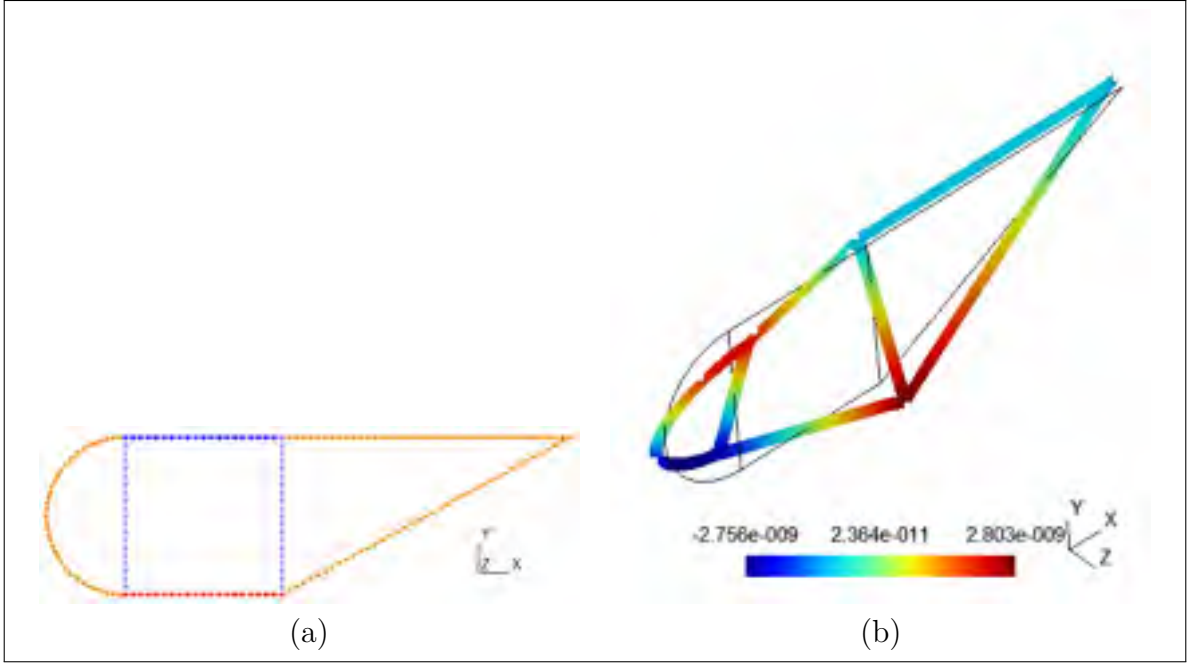
Figure 4.13 Validation case 10. (a) Mesh. (b) Warping displacement u_z for $M_t = 1$.

resulting from this 3D shell finite element model is

$$\mathbf{K}_s = \begin{bmatrix} 102.9 & 13.52 & 7.941 & 7.943 & -7.979 & -87.69 \\ 13.52 & 41.55 & 0.3026 & 0.4525 & -0.3393 & 27.59 \\ 7.941 & 0.3026 & 372.4 & 383.4 & -423.7 & -7.494 \\ 7.943 & 0.4525 & 383.4 & 400.1 & -440.5 & -7.564 \\ -7.979 & -0.3393 & -423.7 & -440.5 & 512.7 & 7.495 \\ -87.69 & 27.59 & -7.494 & -7.564 & 7.495 & 117.4 \end{bmatrix} \times 10^6 \qquad (4.75)$$
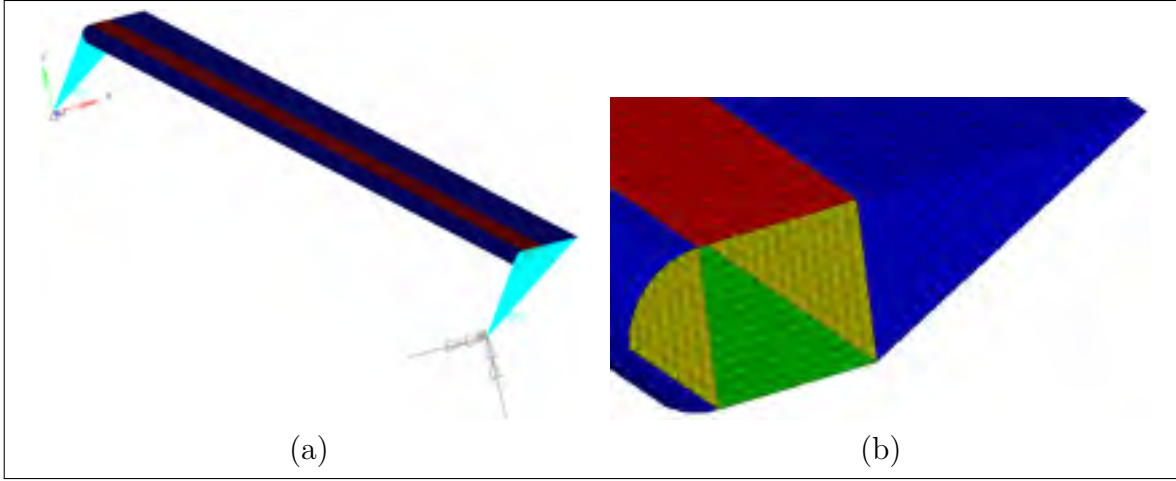
Figure 4.14   3D shell finite element model of validation case 10.
(a) Full model. (b) Zoomed view

When comparing both models, the difference is (absolute value of the difference normalized by the mean of both values):

$$
\begin{bmatrix}
2.2 & 2.7 & 2.1 & 2.1 & 2.1 & 2.0 \\
2.7 & 4.3 & 1.9 & 1.5 & 3.4 & 6.7 \\
2.1 & 1.9 & 0.3 & 0.3 & 0.2 & 2.1 \\
2.1 & 1.5 & 0.3 & 0.3 & 0.2 & 2.2 \\
2.1 & 3.4 & 0.2 & 0.2 & 0.2 & 2.1 \\
2.0 & 6.7 & 2.1 & 2.2 & 2.1 & 3.1
\end{bmatrix} \%
\tag{4.76}
$$

For the extension-bending behaviour, the differences are well under 1 %. The differences are more significant for terms associated with transverse shear and torsion but are, however, limited to 7 %, which is judged satisfactory.

4.5   Conclusion

In this chapter, a thin-walled implementation of the Nonhomogeneous Anisotropic Beam Section Analysis (NABSA) method has been proposed using a finite element formulation similar to the pure displacement formulation used for shell elements. After a recall of the

NABSA method, its thin-walled implementation was presented for a general n-node line element.

A 3-node element implementation was then validated against different validation cases for which an analytical or numerical solution was obtained. These validation cases covered a broad range of possible behaviour of composite beams: geometric coupling, material couplings due to off-axis fibre, open sections, multicell sections, nodes located on the shell bottom surface, nonsymmetrical and unbalanced laminates. The results obtained from the proposed model showed really good agreement with the analytical and numerical solutions.

The proposed method allows the computation of the beam cross-sectional stiffness matrix as the classical NABSA or VABS methods does, but it facilitates the construction of the model by providing a natural through-the-thickness direction to define the material coordinate system. It also facilitates, in addition to the computation of the stresses and strains in each layer of the laminates, the computation of the shell internal loads (shear flow for instance). It also results in models that are smaller and compute faster than the classical NABSA or VABS methods that use a two-dimensional discretization of the cross section with triangular or quadrangular elements.

CHAPTER 5

COMPARISON OF DIFFERENT WIND TURBINE BLADE MODELS AGAINST EXPERIMENTAL RESULTS

5.1 Introduction and methodology

The purpose of this chapter is to compare the performance of the four different models presented in Chapter 3 (see Table 3.1 for a summary of their capabilities) to evaluate strain, stiffness, natural frequencies, buckling and failure. This comparison is made on the WESNet blade presented in Chapter 1 for which experimental data are available.

The next section will present the characteristics of each model as well as the resulting cross-sectional properties. The remaining sections will compare results with respect to modal analysis, deflection, strains, buckling and composite strength.

In each model, the z-axis is the blade longitudinal axis and is pointing towards the tip, the x-axis is parallel to the chord line at tip and pointing towards the leading edge. The orientation of the y-axis follows the right-hand rule.

5.2 Model descriptions and cross-sectional properties

5.2.1 Model 1: simple model

The simple model of the WESNet blade is built as presented in Section 3.3. Table 5.1 presents the different geometrical and material parameters as well as the computed flapwise moment of inertia I (using Equation 3.35) and flapwise bending stiffness EI. These characteristics are given at each blade longitudinal station of Table 1.2 as well as at other points of interest like ply drops.

Table 5.1   Simple model of the WESNet blade (model 1). Variables are as defined in Section 3.3

z [m]	b [mm]	t [mm]	h [mm]	E [GPa]	I [mm^4]	EI [kN·m^2]
0.000	100.2	200.0	13.12	25.78	22 990 000	592.8
0.160	100.2	200.0	13.12	25.78	22 990 000	592.8
0.180	100.3	199.8	13.12	25.78	22 970 000	592.1
0.200	100.2	198.9	13.12	25.78	22 720 000	585.6
0.210	100.1	198.0	13.12	25.78	22 480 000	579.5
0.211	100.1	197.9	13.12	25.78	22 470 000	579.4
0.337	100.4	164.4	13.12	25.78	15 110 000	389.6
0.340	100.5	163.1	8.060	28.87	9 746 000	281.4
0.360	100.3	153.9	8.060	28.87	8 607 000	248.5
0.380	100.3	145.0	8.060	28.87	7 590 000	219.1
0.400	100.1	136.2	8.060	28.87	6 632 000	191.5
0.420	100.2	127.9	8.060	28.87	5 812 000	167.8
0.440	100.4	120.6	8.060	28.87	5 134 000	148.3
0.460	100.5	114.2	8.060	28.87	4 568 000	131.9
0.480	100.1	108.9	8.060	28.87	4 109 000	118.6
0.500	100.3	105.3	8.060	28.87	3 831 000	110.6
0.520	100.2	102.9	8.060	28.87	3 642 000	105.2
0.540	100.5	101.5	8.060	28.87	3 545 000	102.4
0.560	100.2	100.2	8.060	28.87	3 437 000	99.24
0.760	95.40	91.58	8.060	28.87	2 690 000	77.68
0.960	90.90	83.63	8.060	28.87	2 100 000	60.63
0.961	90.88	83.59	7.600	28.26	2 001 000	56.53
1.074	88.16	78.93	7.600	28.26	1 711 000	48.35
1.160	86.10	75.48	7.600	28.26	1 514 000	42.78
1.360	81.30	68.02	7.600	28.26	1 134 000	32.04
1.560	77.06	60.67	7.600	28.26	830 400	23.46
1.760	72.24	52.80	7.600	28.26	566 100	16.00
1.960	67.65	45.25	7.600	28.26	369 300	10.44
2.160	62.82	39.10	7.600	28.26	241 500	6.824
2.359	58.50	34.95	7.600	28.26	170 600	4.821
2.360	58.48	34.93	7.600	28.26	170 300	4.812
2.361	58.46	34.92	7.600	28.26	170 000	4.805
2.560	53.81	31.86	7.600	28.26	124 300	3.512
2.624	52.30	30.98	7.600	28.26	112 500	3.178
2.662	51.40	30.46	5.760	24.79	91 940	2.279
2.810	47.89	28.42	5.760	24.79	72 320	1.793
3.060	42.23	25.12	5.760	24.79	46 910	1.163
3.173	39.61	23.47	5.760	24.79	37 040	0.9183
3.211	38.72	22.92	3.920	18.00	27 780	0.5000
3.260	37.58	22.20	3.920	18.00	25 000	0.4500
3.460	32.75	19.29	3.920	18.00	15 500	0.2790
3.499	31.85	18.70	3.920	18.00	13 960	0.2513
3.500	31.83	18.69	3.920	18.00	13 930	0.2507
3.501	31.80	18.67	3.920	18.00	13 890	0.2500
3.660	28.08	16.29	3.920	18.00	8703	0.1567
3.760	25.98	14.94	3.920	18.00	6444	0.1160
3.776	0.000	0.000	0.000	0.000	0.000	0.000

5.2.2   Model 2: classical strength of materials model

The classical strength of materials model for the WESNet blade is built using the methodology presented in Section 3.4. Each studied longitudinal station is discretized using 100 (for circular sections) to 210 (for airfoil sections) segments. Table 5.2 shows the WES-

Net blade's cross-sectional properties as computed by the classical strength of materials model. As for the simple model, these data are given at each blade longitudinal station of Table 1.2 as well as at other points of interest like ply drops.

Table 5.2   Classical strength of materials model of the WESNet blade (model 2). Variables are as defined in Section 3.4

z [m]	$\overline{EA}$ [kN]	$\overline{ES_x}$ [kN·m]	$\overline{ES_y}$ [kN·m]	$\overline{EI_x}$ [kN·m^2]	$\overline{EI_y}$ [kN·m^2]	$\overline{EI_{xy}}$ [kN·m^2]	$\overline{GJ}$ [kN·m^2]
0.0000	198 700	3.437	-12.56	866.0	867.0	-0.3099	485.9
0.1600	198 700	3.437	-12.56	866.0	867.0	-0.3099	485.9
0.1800	198 900	26.31	-96.65	866.7	873.0	-2.231	488.4
0.2000	199 700	85.64	-315.5	866.6	893.6	-9.651	493.8
0.2100	200 100	131.4	-484.7	863.7	907.6	-15.62	496.3
0.2110	207 900	136.7	-505.9	887.3	911.9	-10.01	497.7
0.3370	209 900	1029	-4005	678.5	1216	-193.1	434.7
0.3400	150 000	739.5	-2899	506.5	904.9	-143.1	229.0
0.3600	149 400	862.0	-3403	458.4	943.6	-173.3	206.0
0.3800	150 400	1049	-4047	423.7	1025	-213.0	188.0
0.4000	151 300	1224	-4652	391.0	1105	-251.6	168.8
0.4200	153 000	1434	-5373	364.0	1211	-297.1	148.8
0.4400	154 900	1636	-6058	342.7	1319	-341.3	130.3
0.4600	156 200	1813	-6663	325.4	1411	-379.1	114.3
0.4800	156 900	1935	-7082	310.7	1477	-406.5	100.9
0.5000	157 300	2013	-7350	301.0	1518	-424.1	92.29
0.5200	158 400	2117	-7716	298.1	1582	-446.4	86.24
0.5400	159 000	2168	-7904	295.8	1615	-457.6	82.71
0.5600	158 400	2158	-7880	289.4	1605	-455.0	79.71
0.7600	149 700	1949	-7056	227.7	1373	-377.1	62.52
0.9600	140 200	1737	-6246	176.7	1146	-304.4	49.02
0.9610	137 000	1740	-6240	173.1	1143	-304.4	48.57
1.074	132 300	1649	-5880	149.4	1042	-272.3	41.35
1.160	60 350	336.6	-1282	61.67	248.4	-56.22	28.42
1.360	56 680	349.0	-1129	46.29	208.5	-45.28	21.45
1.560	53 180	319.5	-1014	33.64	175.7	-35.89	15.84
1.760	49 460	291.6	-897.8	22.97	144.5	-27.52	10.93
1.960	45 650	277.0	-753.6	15.40	113.5	-20.17	7.568
2.160	42 240	263.3	-650.0	10.66	91.14	-15.14	5.299
2.359	39 150	233.0	-561.7	7.663	73.08	-11.23	3.870
2.360	39 130	232.8	-561.3	7.650	73.00	-11.21	3.864
2.361	39 110	232.6	-560.8	7.637	72.91	-11.19	3.858
2.560	35 870	190.6	-474.4	5.447	56.36	-7.943	2.824
2.624	34 830	177.2	-448.2	4.872	51.62	-7.065	2.549
2.662	26 840	140.1	-421.3	3.876	45.77	-6.284	2.487
2.810	24 940	115.4	-359.1	2.922	36.84	-4.630	1.935
3.060	22 190	82.34	-285.8	1.800	25.16	-2.717	1.229
3.173	20 720	69.86	-250.2	1.390	20.53	-2.066	0.9577
3.211	14 680	52.30	-239.7	0.9757	18.40	-1.904	0.9082
3.260	14 220	48.29	-225.2	0.8658	16.73	-1.676	0.8105
3.460	12 150	32.25	-159.4	0.4955	10.25	-0.8426	0.4936
3.499	11 780	29.41	-150.0	0.4366	9.352	-0.7105	0.4409
3.500	11 770	29.34	-149.8	0.4351	9.330	-0.7073	0.4396
3.501	11 760	29.27	-149.6	0.4337	9.307	-0.7042	0.4383
3.660	10 270	19.45	-114.4	0.2501	6.205	-0.3110	0.2627
3.760	9447	14.48	-96.85	0.1763	4.841	-0.1382	0.1888
3.776	0.000	0.000	0.000	0.000	0.000	0.000	0.000

5.2.3   Model 3: cross-sectional finite element model

The WESNet blade is also modelled using the cross-sectional finite element method presented in Chapter 4. Each section was discretized using 100 to 117 quadratic elements (depending on whether the shear web was present or not). The aerodynamic surface elements use the offset node option, i.e., the nodes are on the exterior surface of the blade and the element thickness is built towards the blade interior. The shear web elements use the conventional mid thickness surface definition. The resulting cross-sectional properties are presented in Tables 5.3 to 5.5 using the same longitudinal stations as for models 1 and 2.

Table 5.3   Components of the cross-sectional stiffness matrix of the WESNet blade obtained from the cross-sectional finite element model (model 3). Part 1 of 3

z	K_{s11}	K_{s12}	K_{s13}	K_{s14}	K_{s15}	K_{s16}	K_{s22}
[m]	[kN]	[kN]	[kN]	[kN·m]	[kN·m]	[kN·m]	[kN]
0.000	30 760	52.24	-0.00001085	-1.700	0.01260	0.2999	30 950
0.160	30 760	52.24	-0.00001085	-1.700	0.01260	0.2999	30 950
0.180	30 880	-1525	-0.003874	-1.768	-0.3320	107.8	25 520
0.200	30 970	-1795	-0.001630	-1.877	-0.3456	40.96	23 910
0.210	30 670	-1867	0.0002664	-2.031	-0.3259	-16.98	23 090
0.211	33 700	9708	0.0001982	-2.173	-0.6324	-27.42	68 020
0.337	28 210	1323	0.02527	-3.643	0.3347	-670.4	43 400
0.340	14 830	2120	0.01479	-1.642	0.3340	-345.0	28 180
0.360	19 830	1206	0.0006188	-0.7432	-0.4316	-12.12	26 430
0.380	20 400	1376	0.0004799	-0.7219	-0.4038	0.4850	23 240
0.400	20 690	-8352	0.0005146	-0.7400	-0.3865	11.97	20 050
0.420	20 640	-1484	-0.001098	-0.8391	-0.4054	52.47	17 120
0.440	21 320	-2394	-0.0004337	-0.7714	-0.3141	59.01	15 040
0.460	21 590	-3149	-0.00009843	-0.7581	-0.2616	69.04	13 600
0.480	21 660	-3387	-0.0005396	-0.7911	-0.3067	85.62	12 240
0.500	21 820	-3701	-0.0003141	-0.7813	-0.2953	92.31	11 370
0.520	22 010	-3899	-0.0001783	-0.7815	-0.2970	96.54	10 840
0.540	22 100	-4140	0.0001317	-0.7721	-0.2799	96.37	10 710
0.560	21 040	-3884	0.001002	-0.9358	-0.2461	81.09	10 380
0.760	20 310	-3987	0.003612	-0.8282	-0.2093	16.69	9382
0.960	19 690	-3507	0.001405	-0.7205	-0.2729	15.02	8097
0.961	19 480	-3609	0.002051	-0.6989	-0.2489	8.090	8015
1.074	19 140	-3541	0.001969	-0.6192	-0.1915	-4.369	7411
1.160	13 780	-1898	0.002606	-0.6730	-0.4470	-2.126	7052
1.360	13 160	-1755	0.001053	-0.5319	-0.3348	-10.66	5967
1.560	12 450	-1617	0.001690	-0.5033	-0.3055	-22.47	4839
1.760	11 690	-1447	0.0007260	-0.4451	-0.2390	-28.56	3695
1.960	10 850	-1283	0.0002834	-0.3821	-0.1568	-40.21	2836
2.160	10 020	-1098	-0.0005415	-0.3460	-0.08233	-47.17	2174
2.359	9268	-932.4	-0.0004540	-0.3203	-0.04868	-46.57	1776
2.360	9202	-911.9	-0.0005788	-0.3240	-0.05521	-45.78	1756
2.361	9250	-932.3	-0.0004814	-0.3204	-0.04766	-46.43	1773
2.560	8456	-755.7	-0.0005117	-0.2931	-0.03650	-39.54	1507
2.624	8166	-688.5	-0.0007070	-0.2866	-0.03891	-36.51	1432
2.662	7625	-574.3	-0.001560	-0.2919	-0.04834	-31.79	1283
2.810	7081	-448.6	-0.001486	-0.2684	-0.04545	-27.00	1124
3.060	6273	-335.2	-0.001005	-0.2276	-0.02901	-20.95	937.4
3.173	5865	-274.6	0.0002083	-0.2138	-0.05244	-18.25	839.5
3.211	5304	-242.2	-0.001148	-0.2114	-0.03001	-15.45	704.4
3.260	5140	-222.6	-0.001082	-0.2038	-0.02861	-14.58	667.6
3.460	4432	-118.5	-0.001090	-0.1724	-0.02027	-10.85	536.9
3.499	4290	-84.18	-0.001393	-0.1665	-0.01437	-10.12	512.4
3.500	4271	-101.3	-0.004789	-0.1573	0.06883	-11.05	507.2
3.501	4289	-82.18	-0.001117	-0.1666	-0.02029	-10.01	515.1
3.660	3751	10.79	-0.001239	-0.1340	-0.01295	-7.983	395.6
3.760	3419	87.99	-0.001288	-0.1285	-0.01105	-6.599	366.6
3.776	0.000	0.000	0.000	0.000	0.000	0.000	0.000

Table 5.4   Components of the cross-sectional stiffness matrix
of the WESNet blade obtained from the cross-sectional finite
element model (model 3). Part 2 of 3

z	K_{s23}	K_{s24}	K_{s25}	K_{s26}	K_{s33}	K_{s34}	K_{s35}
[m]	[kN]	[kN·m]	[kN·m]	[kN·m]	[kN]	[kN·m]	[kN·m]
0.000	-0.3170	0.01259	-1.655	87.52	197 500	0.0000	0.0000
0.160	-0.3170	0.01259	-1.655	87.52	197 500	0.0000	0.0000
0.180	-12.24	-0.3322	-2.948	340.5	198 500	40.65	149.0
0.200	-6.412	-0.3509	-3.320	161.2	199 600	108.2	397.7
0.210	-6.185	-0.3368	-3.509	138.3	200 100	154.8	570.6
0.211	-9.127	-0.8083	-4.668	175.2	207 800	160.1	592.1
0.337	-8.157	-0.9395	-5.657	-48.34	212 200	1139	4379
0.340	-1.222	-0.5308	-2.517	-133.1	150 800	789.2	3068
0.360	1.889	-0.4779	-2.232	-147.5	150 300	917.8	3606
0.380	2.026	-0.4388	-2.153	-131.4	151 400	1112	4276
0.400	0.6560	-0.4369	-2.209	-87.20	152 300	1293	4898
0.420	1.818	-0.3656	-2.130	-75.31	154 000	1507	5628
0.440	0.9272	-0.4098	-2.194	-27.71	155 800	1709	6316
0.460	1.459	-0.4038	-2.077	-14.46	157 200	1896	6949
0.480	1.912	-0.3481	-1.975	2.833	158 100	2024	7390
0.500	1.910	-0.3463	-1.941	15.32	158 800	2127	7739
0.520	2.107	-0.3340	-1.881	22.53	160 000	2234	8115
0.540	1.813	-0.3473	-1.853	32.44	160 500	2286	8308
0.560	6.985	-0.1956	-1.516	-21.98	159 800	2269	8251
0.760	5.373	-0.2015	-1.375	6.984	150 900	2044	7392
0.960	4.828	-0.1393	-1.166	11.49	141 400	1818	6548
0.961	4.423	-0.1586	-1.180	15.16	138 200	1822	6542
1.074	3.750	-0.1465	-1.092	22.56	133 400	1722	6160
1.160	6.386	-0.3753	-1.991	30.89	60 670	363.9	1344
1.360	5.710	-0.2843	-1.729	34.58	56 960	351.5	1189
1.560	5.160	-0.2300	-1.541	25.88	53 470	320.7	1068
1.760	4.925	-0.1767	-1.344	17.34	49 690	291.6	944.8
1.960	3.181	-0.1250	-1.109	14.43	45 890	276.1	791.4
2.160	2.506	-0.08525	-0.9376	11.15	42 460	262.6	681.3
2.359	2.146	-0.06302	-0.8173	8.761	39 340	232.0	589.8
2.360	2.206	-0.06151	-0.8132	8.411	39 330	231.8	589.4
2.361	2.144	-0.06280	-0.8163	8.761	39 310	231.6	588.9
2.560	1.833	-0.04601	-0.7022	7.354	36 020	189.2	499.2
2.624	1.815	-0.04022	-0.6661	6.828	34 970	175.7	471.9
2.662	1.883	-0.03714	-0.6649	5.951	27 060	140.6	443.5
2.810	1.592	-0.02825	-0.5828	5.205	25 140	116.8	385.5
3.060	1.287	-0.01944	-0.4798	4.982	22 060	84.14	300.7
3.173	3.028	-0.01248	-0.4788	4.653	20 590	71.24	263.9
3.211	0.9559	-0.01450	-0.4229	5.424	14 710	53.53	253.8
3.260	0.9024	-0.01310	-0.4006	5.096	14 240	49.40	238.7
3.460	0.4650	-0.008040	-0.3142	3.948	12 230	33.26	175.4
3.499	0.06135	-0.008220	-0.2890	3.834	11 860	30.29	165.5
3.500	-8.865	-0.04243	-0.07231	3.721	11 880	30.34	164.7
3.501	0.5668	-0.005967	-0.3016	3.940	11 840	30.13	165.1
3.660	-3.844	0.007662	-0.1548	2.604	10 330	19.82	128.0
3.760	-0.1139	-0.0004187	-0.1984	2.687	9502	14.56	109.5
3.776	0.000	0.000	0.000	0.000	0.000	0.000	0.000

Table 5.5   Components of the cross-sectional stiffness matrix
of the WESNet blade obtained from the cross-sectional finite
element model (model 3). Part 3 of 3

z	K_{s36}	K_{s44}	K_{s45}	K_{s46}	K_{s55}	K_{s56}	K_{s66}
[m]	[kN·m]	[kN·m^2]	[kN·m^2]	[kN·m^2]	[kN·m^2]	[kN·m^2]	[kN·m^2]
0.000	4.874	856.5	-0.0008583	0.00007246	856.5	0.0002119	451.3
0.160	4.874	856.5	-0.0008583	0.00007246	856.5	0.0002119	451.3
0.180	5.468	858.1	3.371	0.02712	868.2	0.08633	435.2
0.200	5.980	859.1	11.27	0.01478	891.7	0.05714	425.0
0.210	6.307	856.1	17.38	0.004900	906.1	0.06528	418.2
0.211	6.534	880.0	11.96	0.001965	911.3	0.07200	437.5
0.337	8.589	676.1	207.8	-0.04542	1261	0.2693	318.1
0.340	4.008	503.1	149.9	-0.04467	923.3	0.1220	185.5
0.360	2.696	456.0	181.6	0.01271	967.3	0.05160	190.4
0.380	2.634	422.1	222.9	0.01484	1055	0.05678	173.7
0.400	2.670	390.1	262.8	0.01807	1139	0.07223	153.9
0.420	2.746	363.7	309.2	0.02589	1248	0.08146	133.3
0.440	2.722	342.9	354.2	0.02493	1359	0.08246	116.0
0.460	2.646	326.6	394.0	0.02271	1458	0.07650	101.9
0.480	2.606	312.5	422.9	0.02164	1529	0.07431	90.03
0.500	2.566	304.6	445.7	0.02163	1587	0.07651	82.45
0.520	2.530	302.1	468.9	0.02086	1655	0.07641	77.55
0.540	2.497	300.0	480.6	0.01969	1690	0.07534	74.84
0.560	2.651	292.3	475.2	0.007372	1671	0.03937	68.78
0.760	2.389	229.8	393.7	0.002702	1430	0.03325	54.49
0.960	2.075	178.2	317.8	0.007220	1194	0.03350	44.38
0.961	2.050	174.7	317.8	0.006477	1191	0.03318	44.29
1.074	1.877	150.7	284.1	0.007716	1085	0.03237	38.76
1.160	2.361	61.00	57.78	0.001824	255.5	0.008699	27.43
1.360	1.999	45.96	47.09	0.006455	214.4	0.01400	21.76
1.560	1.826	33.28	37.29	0.005839	181.0	0.01403	16.37
1.760	1.609	22.59	28.52	0.006919	149.2	0.01505	11.74
1.960	1.327	15.07	20.92	0.007816	117.4	0.01935	8.737
2.160	1.148	10.37	15.68	0.007940	94.45	0.01947	6.531
2.359	1.027	7.417	11.61	0.006982	75.83	0.01759	5.056
2.360	1.028	7.404	11.59	0.007035	75.75	0.01769	5.038
2.361	1.026	7.392	11.57	0.006984	75.65	0.01758	5.043
2.560	0.9070	5.239	8.202	0.005686	58.58	0.01523	3.946
2.624	0.8716	4.674	7.288	0.005315	53.68	0.01453	3.642
2.662	0.8523	3.744	6.516	0.005159	47.70	0.01334	3.472
2.810	0.7666	2.835	4.866	0.004252	38.40	0.01168	2.866
3.060	0.6422	1.728	2.880	0.002959	26.11	0.008503	2.058
3.173	0.6494	1.328	2.192	0.002580	21.31	0.005446	1.724
3.211	0.5526	0.9437	2.003	0.002259	19.20	0.006093	1.634
3.260	0.5284	0.8359	1.764	0.002067	17.46	0.005637	1.501
3.460	0.4282	0.4759	0.9168	0.001384	11.03	0.004030	1.039
3.499	0.3991	0.4182	0.7755	0.001211	10.08	0.004008	0.9628
3.500	0.1314	0.4174	0.7691	0.000009869	10.08	0.01055	0.9661
3.501	0.4132	0.4154	0.7690	0.001284	10.03	0.003587	0.9615
3.660	0.2273	0.2375	0.3470	0.001172	6.746	0.004742	0.6622
3.760	0.2908	0.1672	0.1618	0.0006684	5.288	0.002250	0.5426
3.776	0.000	0.000	0.000	0.000	0.000	0.000	0.000

5.2.4   Model 4: 3D shell finite element model

A 3D shell finite element model of the blade is built using the Altair HyperWorks suite. Hypermesh, Optistruct and Hyperview are used respectively as pre-processor, solver and post-processor. Note that the OptiStruct solver uses the same input format as NASTRAN. The model uses 4-node linear shell elements. As seen in Figure 5.1, the blade is discretized with 38 elements along its chords length and the element size reduces towards the blade tip to keep their aspect as square as possible. The model uses a total of 46 763 nodes and 47 272 elements (all but 3 are quadrangular). Laminates are defined using the PCOMPP method of OptiStruct. As for the cross-sectional finite element model, nodes are on the blade's exterior surface and the element thickness is built towards the blade interior. The shear web elements use the conventional mid thickness surface definition.
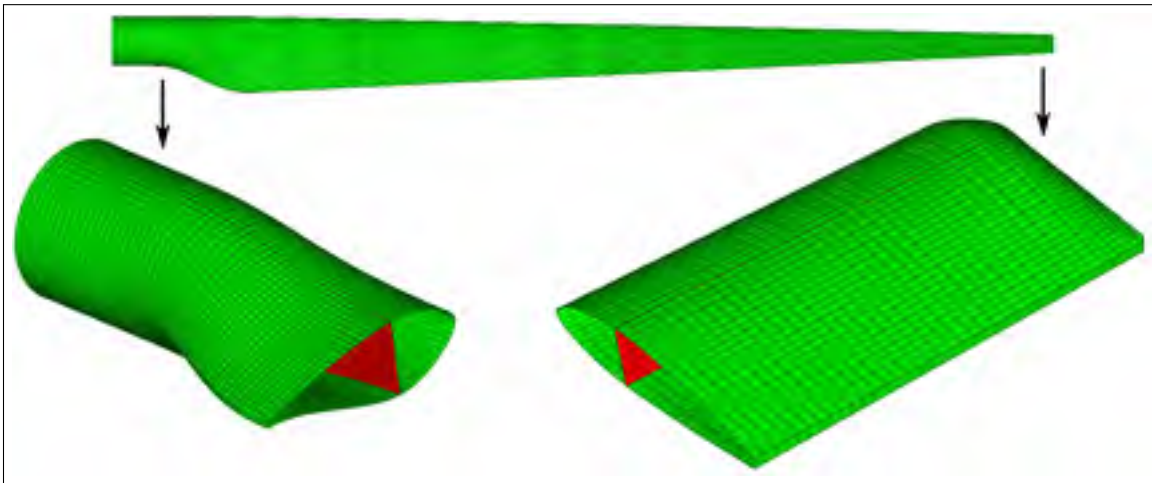
Figure 5.1   Mesh of the WESNet 3D shell finite element model

With this 3D shell finite element model, the methodology presented in Section 3.6.1 is used to compute the cross-sectional properties of the WESNet blade. 75 computation points are used along the blade length. This analysis results in the properties presented in Tables 5.6 to 5.8.

Table 5.6   Components of the cross-sectional stiffness matrix of the WESNet blade obtained from the 3D shell finite element model (model 4).

Part 1 of 3

z [m]	Ks_{11} [kN]	Ks_{12} [kN]	Ks_{13} [kN]	Ks_{14} [kN·m]	Ks_{15} [kN·m]	Ks_{16} [kN·m]	Ks_{22} [kN]
0.02517	27 680	1083	450.9	-126.2	-133.9	-78.28	29 360
0.07552	29 490	1904	2329	-78.49	259.5	-115.4	32 880
0.1259	30 510	2400	2764	-12.81	399.8	-134.0	34 880
0.1762	32 220	-774.8	-4545	-47.92	-113.1	28.68	28 290
0.2266	27 890	-2687	-14880	-481.0	-923.7	153.0	19 500
0.2769	18 990	-2827	-14600	-580.4	-938.3	147.5	11 250
0.3273	15 040	-1806	-12720	-641.8	-897.4	187.7	10 580
0.3776	14 600	-1004	-5433	-545.8	-393.8	244.6	10 700
0.4279	17 320	-3134	812.3	-228.2	-37.59	194.1	8812
0.4783	22 000	-5176	104.8	-123.9	-48.33	167.9	7751
0.5286	25 140	-6294	-4150	-223.4	-485.7	197.4	7321
0.5790	23 450	-5917	-4723	-204.6	-529.0	149.4	7231
0.6293	23 040	-5738	-2875	-82.00	-159.0	127.6	6855
0.6797	22 640	-5442	-1619	-22.49	30.39	111.8	6767
0.7300	22 590	-5465	-406.0	-0.6442	70.03	65.22	6683
0.7804	22 270	-5294	-145.7	27.66	127.7	48.71	6257
0.8307	20 790	-4675	187.3	42.16	161.1	33.38	5952
0.8811	21 060	-4565	705.5	43.23	206.7	38.32	5879
0.9314	21 100	-4693	-4.219	35.31	129.9	43.08	6112
0.9818	18 940	-4271	-1204	14.45	-45.57	41.72	5498
1.032	16 030	-3603	-613.2	-34.25	-169.4	52.79	4653
1.082	14 780	-3347	276.4	9.828	21.21	72.47	3999
1.133	15 450	-3427	1094	32.43	114.0	67.29	3986
1.183	14 540	-3079	1345	7.053	56.97	19.85	3913
1.233	13 860	-2865	514.0	2.313	38.26	-14.79	3705
1.284	14 240	-2842	197.0	-0.03381	23.26	-7.208	3570
1.334	13 880	-2759	164.7	-3.956	13.58	-10.95	3464
1.385	13 210	-2551	586.2	12.22	-0.5892	-27.21	3348
1.435	13 610	-2451	186.4	-9.287	-1.768	-15.250	3202
1.485	13 690	-2638	-181.6	-17.34	-10.80	-22.45	3128
1.536	12 990	-2394	345.6	-24.66	-29.05	-30.41	2932
1.586	11 960	-2331	11.47	-5.153	4.035	-30.20	2711
1.636	11 730	-2132	121.7	22.32	53.67	-33.16	2512
1.687	12 460	-2186	329.3	12.44	83.04	-29.31	2555
1.737	13 060	-2350	266.1	5.964	66.43	-11.00	2541
1.787	12 520	-2194	175.8	3.442	32.83	-55.25	2336
1.838	12 100	-1999	64.88	-2.328	21.11	-70.94	2182
1.888	12 010	-2022	232.8	3.491	23.89	-56.63	2078
1.938	12 050	-1919	197.8	0.6285	19.39	-58.00	1923
1.989	11 920	-1919	204.5	0.6015	15.61	-60.97	1854
2.039	11 720	-1798	161.9	1.6790	19.15	-55.22	1729
2.089	11 510	-1794	364.4	4.5060	4.152	-62.43	1665
2.140	11 290	-1576	85.17	2.5890	0.6678	-65.16	1478
2.190	11 200	-1549	272.6	2.8390	7.206	-63.40	1597
2.240	10 490	-1366	179.8	-0.9155	15.55	-59.81	1288
2.291	11 110	-1514	-3.093	1.491	30.63	-61.67	1341
2.341	10 810	-1360	10.05	2.629	26.70	-59.10	1244
2.391	10 620	-1346	-28.33	0.7454	23.83	-57.00	1238
2.442	10 350	-1258	36.99	2.3520	19.07	-54.31	1184
2.492	10 070	-1180	109.8	1.4220	14.88	-51.10	1145
2.543	10 140	-1166	312.9	0.6208	4.520	-50.02	1135
2.593	9323	-1032	92.40	1.0610	10.44	-44.55	1048
2.643	9289	-983.5	91.18	1.7920	17.81	-42.51	1076
2.694	9210	-925.5	30.21	-0.7521	5.296	-41.12	1078
2.744	8212	-800.4	131.3	1.459	10.70	-35.95	987.5
2.794	8249	-740.3	104.3	3.915	25.17	-34.58	941.0
2.845	8400	-712.0	92.60	2.598	27.41	-33.25	943.0
2.895	8105	-652.7	293.2	2.495	28.22	-31.22	938.7
2.945	8090	-650.6	148.0	1.700	18.80	-30.37	904.5
2.996	7852	-580.2	39.03	0.6680	9.129	-29.04	879.7
3.046	7797	-546.8	144.5	0.5724	8.258	-27.16	843.9
3.096	7629	-519.8	104.4	0.2259	3.786	-25.51	826.3
3.147	7172	-459.2	41.84	0.2943	5.750	-23.09	763.6
3.197	6762	-380.5	65.07	0.2899	11.57	-20.66	777.9
3.247	6483	-323.3	81.77	0.5318	14.04	-18.99	840.4
3.298	6509	-274.0	-37.28	0.8909	13.05	-18.62	887.8
3.348	6275	-214.4	16.71	0.4852	5.510	-16.86	821.7
3.398	6003	-182.2	138.8	0.3032	4.350	-15.65	825.0
3.449	5920	-138.7	46.25	0.5478	9.735	-14.88	800.6
3.499	5961	-57.56	99.07	0.2562	10.51	-14.40	847.6
3.549	5987	-61.02	79.72	-0.4130	4.992	-14.25	1025
3.600	5751	-35.38	72.74	-0.1728	4.519	-13.95	829.0
3.650	5665	-18.04	155.7	0.1956	9.432	-12.92	912.2
3.700	5643	67.29	74.64	-0.7692	9.400	-12.59	949.4
3.751	2303	-12.55	11.25	-0.2973	0.8490	-5.041	120.2

Table 5.7   Components of the cross-sectional
stiffness matrix of the WESNet blade obtained from
the 3D shell finite element model (model 4).
Part 2 of 3

z [m]	Ks_{23} [kN]	Ks_{24} [kN·m]	Ks_{25} [kN·m]	Ks_{26} [kN·m]	Ks_{33} [kN]	Ks_{34} [kN·m]	Ks_{35} [kN·m]
0.02517	52.33	-186.800	159.3	-197.2	266 800	158.8	328.8
0.07552	-635.1	-481.400	101.3	-278.7	244 100	126.1	353.1
0.1259	-921.6	-473.000	28.10	-314.2	226 000	-6.621	51.16
0.1762	1100	-41.160	61.60	24.25	223 100	-235.0	-538.3
0.2266	3327	-350.400	473.6	157.0	198 700	-509.4	-685.3
0.2769	3692	-575.500	584.5	178.5	148 700	-312.1	-281.0
0.3273	3502	-752.900	665.2	95.54	137 100	-50.04	1241
0.3776	1163	-976.200	503.7	-62.92	129 600	-314.6	1113
0.4279	-248.4	-573.400	276.7	112.5	105 400	-259.1	423.9
0.4783	352.6	-278.900	167.4	98.16	112 400	243.1	1784
0.5286	2065	-73.070	206.7	71.80	153 500	1275	5091
0.5790	1467	-77.540	139.8	64.81	178 900	2326	8514
0.6293	308.9	-115.400	-61.05	51.04	179 000	2461	8997
0.6797	647.0	-73.730	-89.85	75.40	176 400	2392	8634
0.7300	1093	-127.400	-128.7	61.79	169 800	2250	8115
0.7804	917.5	-121.500	-133.8	48.91	165 500	2143	7756
0.8307	-1213	-54.730	-50.74	59.42	163 700	2050	7403
0.8811	-1287	-40.530	-114.3	65.99	159 700	1919	6997
0.9314	640.4	-49.110	-118.4	65.50	146 900	1589	5897
0.9818	912.3	-10.740	-5.099	56.76	124 100	1153	4276
1.032	752.5	18.890	60.26	46.18	92 840	693.1	2638
1.082	90.70	-10.130	-18.04	35.90	69 560	474.0	1785
1.133	-277.6	-31.580	-54.08	34.20	61 880	367.6	1373
1.183	-100.5	-31.310	-16.48	41.11	62 870	328.7	1239
1.233	40.11	-25.600	-14.41	44.95	62 660	337.5	1214
1.284	19.29	-21.360	-20.99	43.16	62 180	346.8	1202
1.334	38.10	-18.690	-17.41	42.80	61 300	348.8	1170
1.385	40.86	-18.660	-13.77	45.24	60 440	345.9	1136
1.435	156.1	-12.370	-14.53	41.02	59 350	338.3	1102
1.485	194.7	-10.470	-11.49	37.95	58 560	334.4	1066
1.536	52.43	-4.625	-9.406	37.07	56 770	352.7	1022
1.586	206.7	-18.840	-10.85	33.11	51 490	301.9	897.1
1.636	175.2	-32.550	-19.75	30.32	51 420	289.2	873.5
1.687	75.96	-27.360	-25.66	26.91	54 450	331.5	921.3
1.737	86.86	-22.590	-21.56	20.15	55 070	339.9	915.1
1.787	7.619	-20.640	-20.85	28.42	52 330	329.2	859.0
1.838	51.00	-17.770	-19.87	28.03	51 390	325.8	830.1
1.888	-32.64	-16.390	-15.81	23.42	50 350	321.2	792.6
1.938	0.6086	-12.560	-14.87	21.30	49 440	318.8	765.3
1.989	-14.18	-10.550	-14.28	19.75	48 420	313.1	736.0
2.039	-1.266	-8.920	-13.11	16.00	47 390	306.6	708.5
2.089	-188.8	-11.280	-11.00	16.19	46 560	299.7	680.4
2.14	-136.7	-5.375	-12.75	15.43	45 270	278.1	640.7
2.19	-168.6	-9.544	-16.01	10.84	44 680	284.3	635.0
2.24	-156.6	-9.471	-10.83	10.84	41 620	268.2	587.3
2.291	-132.1	-6.405	-13.27	11.31	43 020	261.9	585.0
2.341	-117.0	-4.880	-12.55	9.704	42 150	249.4	560.4
2.391	-98.06	-2.943	-11.60	9.121	41 310	237.6	538.9
2.442	-147.3	-2.979	-10.79	8.308	40 320	224.7	513.9
2.492	-150.7	-2.113	-9.504	7.238	39 510	212.2	493.8
2.543	-217.0	-2.003	-7.572	6.521	39 000	201.3	481.0
2.593	-165.5	-2.737	-7.886	5.159	34 560	173.9	433.9
2.643	-155.8	-3.466	-8.287	4.817	32 420	159.6	438.0
2.694	-139.7	-1.274	-7.249	5.161	29 860	142.9	425.9
2.744	-142.7	-1.027	-7.162	2.999	26 340	121.4	380.6
2.794	-103.9	-3.048	-8.325	2.980	25 690	113.8	366.7
2.845	-133.1	-3.684	-7.744	2.034	26 230	110.1	359.2
2.895	-169.1	-2.812	-6.518	1.801	25 560	101.7	340.1
2.945	-136.4	-2.336	-6.482	2.004	24 900	94.20	324.6
2.996	-132.7	-1.810	-5.961	1.036	24 240	87.07	308.3
3.046	-140.8	-1.084	-5.317	1.377	23 550	79.67	289.9
3.096	-131.2	-0.7970	-4.586	1.151	22 840	72.96	273.4
3.147	-107.6	-1.399	-4.114	0.2480	20 320	61.85	250.0
3.197	-113.1	-2.330	-4.585	0.2589	17 080	50.04	237.2
3.247	-114.7	-2.473	-4.825	0.0579	15 000	41.99	224.6
3.298	-76.65	-1.237	-5.030	-0.4645	14 440	38.21	215.0
3.348	-74.03	-0.1395	-4.257	-0.6352	14 000	34.01	199.2
3.398	-99.30	-0.5580	-4.036	-0.2785	13 080	29.52	177.3
3.449	-82.27	-1.209	-4.214	-0.4803	12 550	26.31	163.3
3.499	-76.57	-1.243	-3.421	-1.198	12 410	24.83	157.5
3.549	-138.2	-1.386	-3.226	-0.7024	11 990	22.64	144.4
3.600	-97.96	-0.7962	-3.881	-1.023	11 210	19.79	127.5
3.650	-50.90	-0.7408	-4.563	-0.3338	10 660	17.89	115.9
3.700	-227.5	-3.672	-7.522	-0.2404	10 360	16.24	110.3
3.751	-24.08	-0.4638	-0.4910	-0.02256	10 210	14.67	109.0

Table 5.8   Components of the cross-sectional
stiffness matrix of the WESNet blade obtained from
the 3D shell finite element model (model 4).
Part 3 of 3

z	Ks_{36}	Ks_{44}	Ks_{45}	Ks_{46}	Ks_{55}	Ks_{56}	Ks_{66}
[m]	[kN·m]	[kN·m^2]	[kN·m^2]	[kN·m^2]	[kN·m^2]	[kN·m^2]	[kN·m^2]
0.02517	-23.08	1079	22.56	74.79	1121	-25.37	485.0
0.07552	-13.89	997.4	20.86	55.38	1044	-19.24	484.1
0.1259	-2.463	943.5	12.20	36.38	973.8	-12.31	479.7
0.1762	20.32	965.8	-6.971	16.20	952.6	-3.985	443.6
0.2266	52.56	812.8	14.40	30.12	854.2	-7.163	401.2
0.2769	145.0	640.1	40.21	14.04	739.2	-6.303	324.4
0.3273	111.6	531.6	109.2	22.32	819.3	-12.23	333.0
0.3776	-156.5	436.6	107.5	68.40	724.7	-21.21	171.0
0.4279	33.32	254.6	138.0	8.406	643.4	0.7881	81.79
0.4783	115.1	225.3	245.0	0.7871	918.1	5.362	55.21
0.5286	98.85	272.1	384.7	5.129	1370	2.076	49.92
0.5790	15.21	306.0	503.4	1.161	1768	5.330	50.58
0.6293	3.910	297.2	504.1	2.245	1778	3.546	54.49
0.6797	89.58	281.6	475.0	5.073	1693	2.783	58.80
0.7300	112.9	260.8	447.3	0.7150	1609	3.397	56.95
0.7804	100.2	245.2	422.6	2.099	1532	6.027	56.34
0.8307	15.65	229.9	398.0	5.541	1460	12.71	56.55
0.8811	48.84	211.6	370.5	4.871	1376	11.29	54.75
0.9314	58.43	188.6	321.7	2.885	1206	4.446	52.17
0.9818	-23.13	149.6	231.5	-0.1869	897.2	-3.624	46.71
1.032	-85.75	103.0	128.4	-3.691	522.2	-11.41	38.08
1.082	-24.93	77.09	78.73	-0.9380	332.1	-3.515	32.13
1.133	30.87	66.07	60.66	1.873	265.5	3.420	28.79
1.183	28.97	61.25	54.70	1.909	246.9	3.464	26.86
1.233	21.53	57.79	52.76	1.528	238.8	2.614	24.93
1.284	16.80	53.98	50.69	0.8902	230.8	1.851	23.62
1.334	16.33	50.19	48.10	0.6882	220.9	1.597	22.32
1.385	19.19	46.75	45.56	0.8585	211.2	1.733	20.90
1.435	15.20	43.34	43.05	0.5097	201.4	1.430	19.57
1.485	13.33	40.22	40.62	0.4764	192.2	1.357	18.03
1.536	15.24	35.64	38.95	0.6151	184.1	1.257	16.73
1.586	13.99	30.74	32.61	0.3261	158.2	1.122	13.82
1.636	12.86	29.33	30.53	0.2076	150.8	1.042	12.67
1.687	11.49	28.13	31.86	0.1312	157.7	0.7530	13.00
1.737	8.216	26.30	30.76	-0.1150	154.5	0.4893	12.84
1.787	14.37	23.09	27.93	0.3947	142.1	1.124	10.14
1.838	17.41	21.13	26.35	0.5466	135.5	1.390	9.016
1.888	10.91	19.01	24.23	0.2585	127.2	0.9062	8.547
1.938	11.08	17.29	22.68	0.2432	121.1	0.8741	7.779
1.989	10.12	15.56	21.01	0.2461	114.3	0.8655	7.005
2.039	10.61	14.06	19.58	0.09784	108.4	0.6606	6.484
2.089	7.954	12.73	18.07	0.1959	102.3	0.8712	5.799
2.140	7.738	11.08	16.28	0.1045	96.10	0.9856	5.204
2.190	7.869	10.64	15.46	0.1720	91.08	0.7638	4.828
2.240	8.132	9.483	13.73	0.2713	81.43	0.5737	4.246
2.291	7.500	8.756	13.11	0.1166	81.35	0.5300	4.143
2.341	7.925	7.968	11.93	0.1303	76.15	0.5187	3.819
2.391	7.752	7.327	10.98	0.1195	71.88	0.4886	3.560
2.442	7.062	6.629	9.951	0.1160	67.04	0.4691	3.292
2.492	6.327	6.092	9.140	0.09673	63.25	0.4579	3.074
2.543	4.693	5.580	8.397	0.08433	59.99	0.4862	2.900
2.593	5.163	4.686	7.171	0.07170	52.61	0.3918	2.547
2.643	5.252	4.279	6.760	0.05426	50.71	0.3469	2.475
2.694	5.374	3.853	6.141	0.06892	47.31	0.3771	2.345
2.744	4.559	3.128	5.163	0.06379	41.17	0.3004	2.019
2.794	5.601	2.820	4.711	0.02993	38.71	0.1808	1.865
2.845	4.282	2.693	4.333	0.04011	37.09	0.1923	1.765
2.895	1.927	2.423	3.834	0.01864	34.21	0.1709	1.611
2.945	3.410	2.181	3.407	0.03030	31.65	0.1759	1.477
2.996	3.710	1.954	3.009	0.04449	29.16	0.1977	1.350
3.046	2.869	1.741	2.626	0.02909	26.70	0.1697	1.212
3.096	2.825	1.546	2.293	0.02308	24.44	0.1699	1.089
3.147	2.855	1.257	1.925	0.02301	21.45	0.1462	0.9436
3.197	2.510	0.9942	1.679	0.02149	19.29	0.1086	0.8535
3.247	2.321	0.8112	1.456	0.01901	17.44	0.09064	0.7760
3.298	2.830	0.7245	1.268	0.01705	16.07	0.08018	0.7001
3.348	2.364	0.6130	1.058	0.01349	14.45	0.09085	0.6141
3.398	1.598	0.5173	0.8575	0.006964	12.50	0.08025	0.5186
3.449	1.989	0.4486	0.7066	0.009488	11.09	0.04836	0.4496
3.499	1.789	0.3965	0.6043	0.008937	10.22	0.04510	0.4017
3.549	1.175	0.3420	0.4715	0.008272	8.988	0.05500	0.3461
3.600	1.212	0.2843	0.3614	0.008310	7.660	0.04064	0.2902
3.650	0.9826	0.2379	0.2790	0.007660	6.660	0.01984	0.2404
3.700	1.306	0.1867	0.2067	0.01490	5.979	0.02206	0.1992
3.751	1.160	0.1404	0.1561	0.004087	5.514	0.01962	0.1562

5.2.5 Experimental cross-sectional stiffness properties

Using the methodology presented in Section 3.6.2, the WESNet blade cross-sectional properties are also computed and shown in Table 5.9. As the test jig does not allow the application of axial load cases and as the precision of the measurements do not allow the computation of transverse shear deformation, a 3×3 cross-sectional stiffness matrix is obtained. The cross-sectional characterization test was performed on one blade.

Table 5.9 Experimental cross-sectional properties of the WESNet blade

z [m]	K_{s44} [kN·m²]	K_{s45} [kN·m²]	K_{s46} [kN·m²]	K_{s55} [kN·m²]	K_{s56} [kN·m²]	K_{s66} [kN·m²]
0.5000	40.72	38.99	-60.87	636.8	-403.7	19.35
0.8222	57.04	41.22	-33.07	293.5	-126.6	27.25
1.144	52.44	54.34	-2.284	293.4	2.239	28.09
1.467	27.62	22.16	6.191	170.7	27.31	20.49
1.789	15.19	10.85	3.768	107.6	13.30	12.95
2.111	8.708	7.378	1.035	80.19	2.011	6.736
2.433	4.621	2.943	0.07785	48.88	-0.3003	3.380
2.756	2.513	1.325	0.02809	29.32	0.3176	1.938
3.078	1.277	0.6689	0.003744	12.57	0.08737	1.253
3.400	0.2872	0.1396	-0.03863	1.859	-0.01391	0.8930

5.2.6 Comparison

The cross-sectional stiffness properties computed from the different models of the WES-Net blade are now compared. Due to the blade configuration, for which there are no significant couplings at the laminate level (see Table 1.4), the blade cross-sectional stiff-

ness matrix should take the following form:

$$\mathbf{K}_s = \begin{bmatrix} K_{s11} & K_{s12} & 0 & 0 & 0 & K_{s16} \\ K_{s12} & K_{s22} & 0 & 0 & 0 & K_{s26} \\ 0 & 0 & K_{s33} & K_{s34} & K_{s35} & 0 \\ 0 & 0 & K_{s34} & K_{s44} & K_{s45} & 0 \\ 0 & 0 & K_{s35} & K_{s45} & K_{s55} & 0 \\ K_{s16} & K_{s26} & 0 & 0 & 0 & K_{s66} \end{bmatrix} \tag{5.1}$$

There is coupling between extension and bending because the reference axes are not necessarily centred at the elastic centre (K_{s34} and K_{s35} terms) nor aligned with the principal axes of bending (K_{s45} term). There is also coupling between both transverse shear deformation (K_{s12} term). Finally, there is a coupling between the transverse shears and the torsion deformations because the reference axes are not necessarily centred at the shear centre (K_{s16} and K_{s26} terms).

It is not easy to evaluate the importance of the coupling terms of the cross-sectional stiffness matrix when compared to the diagonal terms as the units are not the same. For that purpose, the concept of coupling coefficient is used (Couturier et al., 2015; Fedorov and Berggreen, 2014; Lobitz and Veers, 1998). The coupling coefficients are defined as

$$\alpha_{ij} = \frac{K_{sij}}{\sqrt{K_{sii}K_{sjj}}} \tag{5.2}$$

These coefficients vary from -1 to 1. A value of 0 indicates no coupling and values of -1 or 1 indicate strong coupling. As seen in Figure 5.2, the coupling coefficients that should be null (α_{s13}, α_{s14}, α_{s15}, α_{s23}, α_{s24}, α_{s25}, α_{s36}, α_{s46}, α_{s56}) are effectively null as computed by model 3. When looking at the coupling coefficients from model 4 (Figure 5.3), we can see that they are not null but they are really close to zero and small when compared to the non-null coupling coefficients (α_{s12}, α_{s16}, α_{s26}, α_{s34}, α_{s35}, α_{s45}).
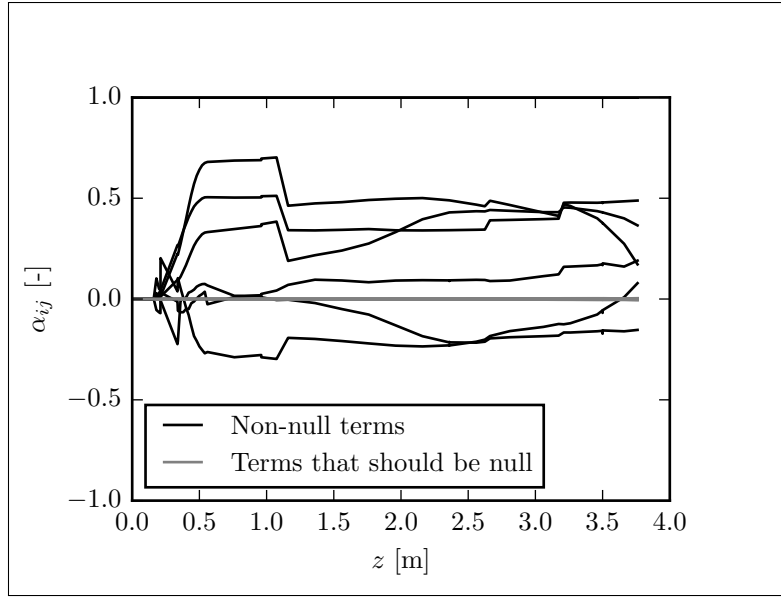
Figure 5.2   Blade cross-sectional coupling coefficients
from model 3
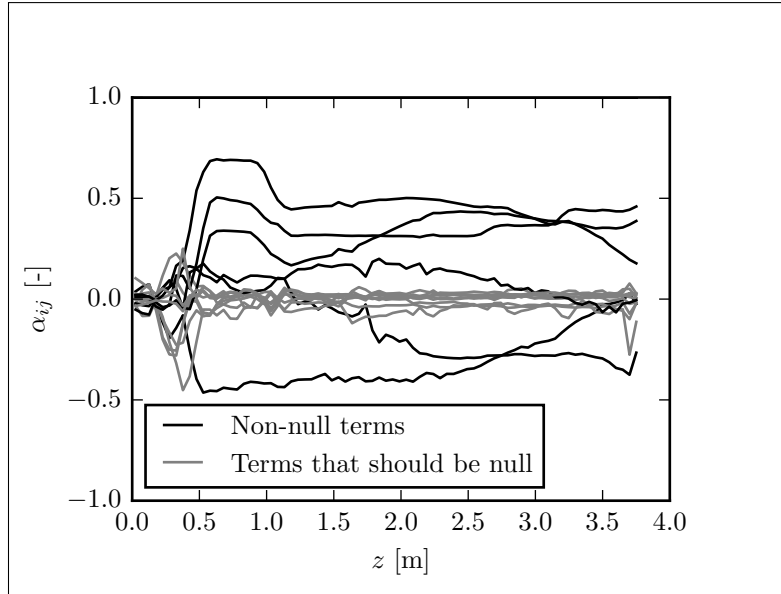
Figure 5.3   Blade cross-sectional coupling coefficients
from model 4

Note that models 3 and 4 are able to evaluate all the terms of the 6×6 cross-sectional

stiffness matrix. Model 2 only evaluates those associated with the extension, bending

and torsion deformations (K_{s33}, K_{s44}, K_{s55}, K_{s34}, K_{s35}, K_{s45} and K_{s66}). Model 1 only evaluate the flapwise bending stiffness (K_{s44}, when the x are is the flapwise principal axis of bending). Finally, the experimentations allow computing terms associated with the bending and torsion behaviour only (K_{s44}, K_{s55}, K_{s45} and K_{s66}).

The detailed results for each of the non-null terms are then presented. Figure 5.4, 5.5 and 5.6 present the results obtained for the terms associated with the transverse shear deformation. We can see that both models show the same trends but a significant error is observable. This is due to the imprecision of model 4 to evaluate transverse shear properties. This imprecision is due to the fact that transverse shear deformation is small in this blade and hard to capture with the used method so a small error results in a larger relative difference.
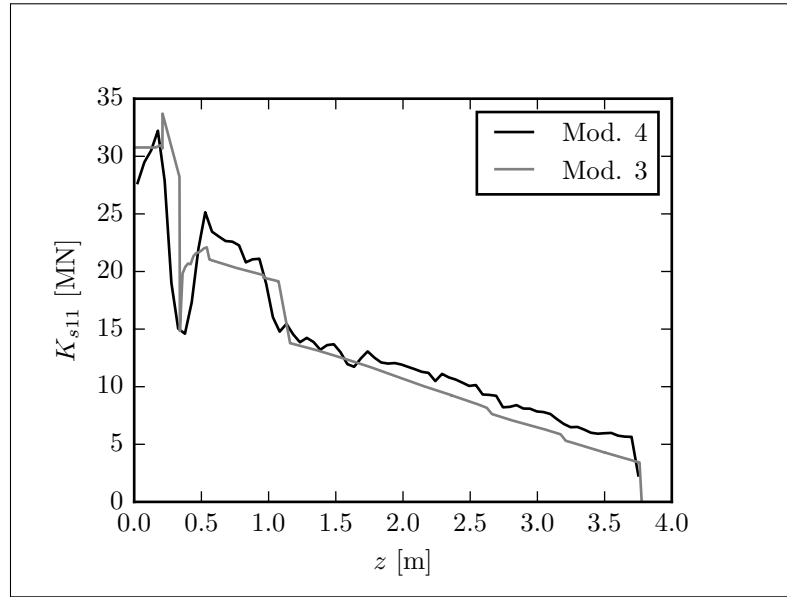
Figure 5.4   In-plane transverse shear stiffness K_{s11}
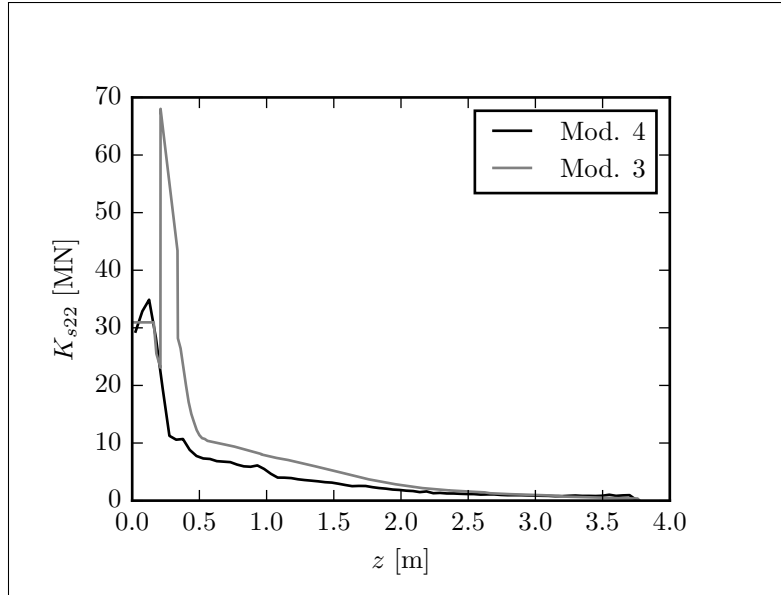
Figure 5.5   Out-of-plane transverse shear stiffness K_{s22}
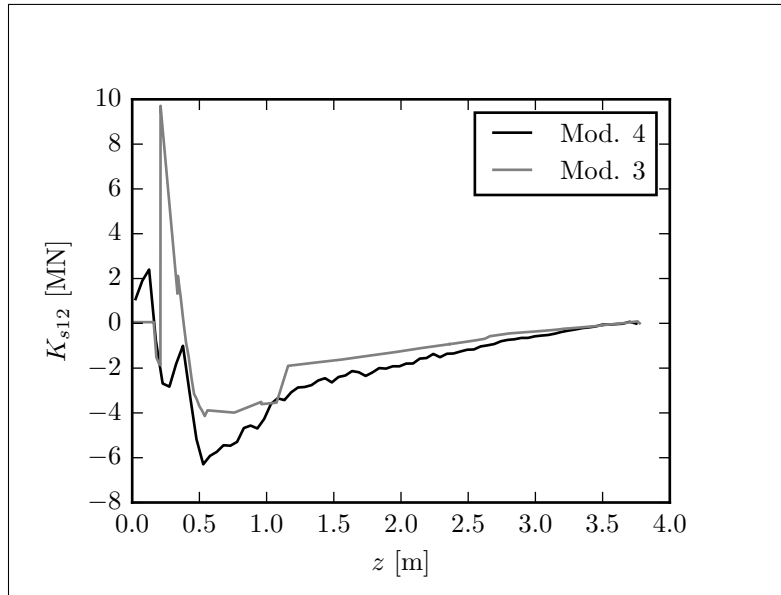
Figure 5.6   Transverse shear stiffness coupling term K_{s12}

As shown in Figure 5.7, the axial stiffness from models 2, 3 and 4 are really similar in the outboard region of the blade. In the inboard region, model 4 shows the same trends but with important differences. This is due to the fact that this model (3D shell finite element) is able to take into account the effects of the rapidly changing cross section

shape in this part of the blade. On their side, models 2 and 3 suppose a constant cross-sectional shape. The same conclusion can be made when looking at the bending stiffness of Figures 5.8 and 5.9.
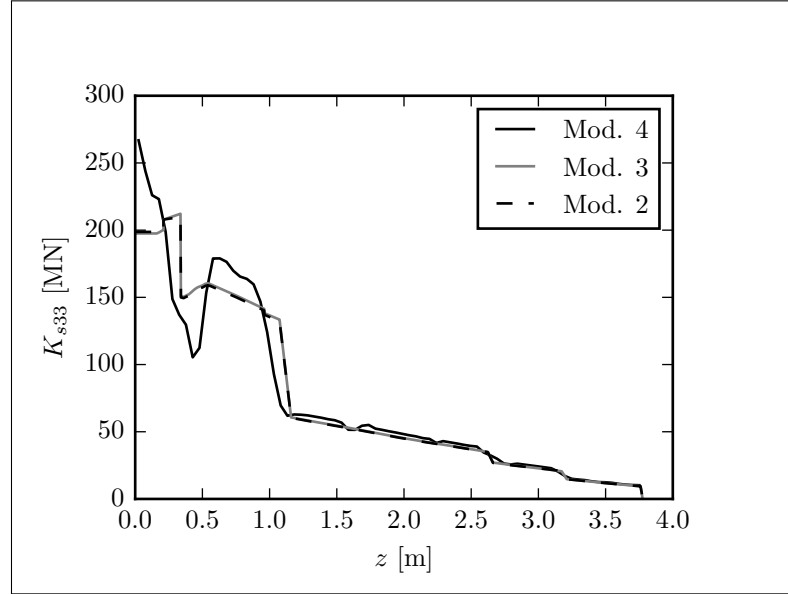
Figure 5.7   Axial stiffness K_{s33}
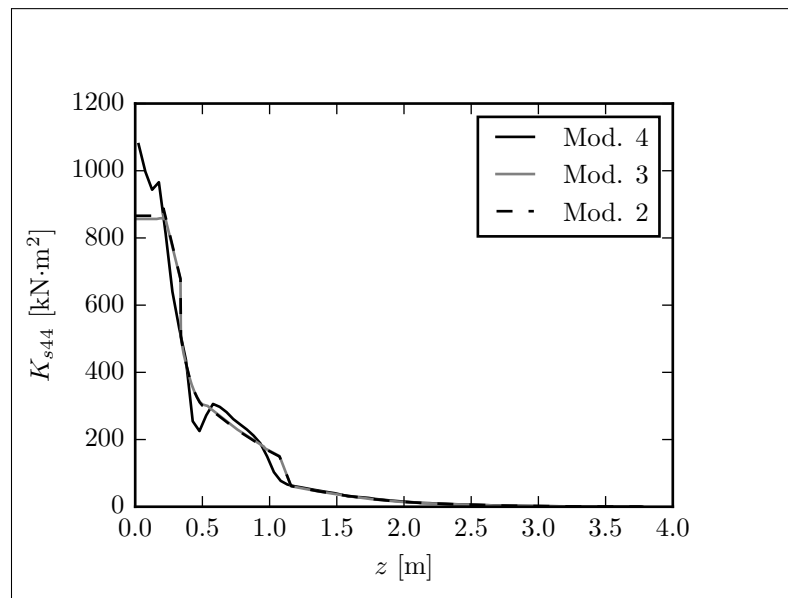
Figure 5.8   Out-of-plane bending stiffness K_{s44}
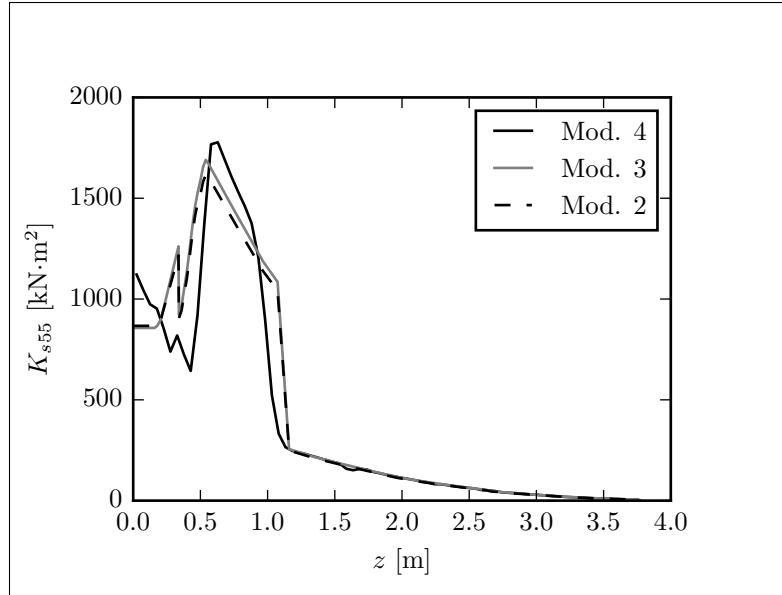
Figure 5.9   In-plane bending stiffness K_{s55}

As the tests performed do not include axial loads on the blade, the extension-bending couplings can not be evaluated. So, the results of models 2, 3 and 4 have to be transferred to the elastic centre (see Figures 5.12 and 5.13 for the elastic centre position) to be compared with the experimental results. This is shown in Figures 5.10 and 5.11 where we can see a difference of up to 30 % for the out-of-plane bending stiffness (K_{s44}) and of up to 20 % for the in-plane bending stiffness (K_{s55}).
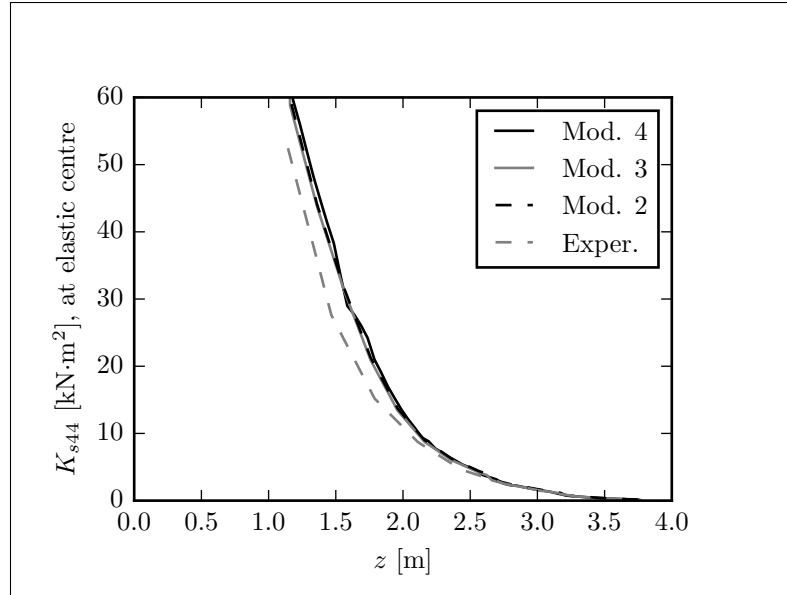
Figure 5.10   Out-of-plane bending stiffness K_{s44}
transferred to elastic centre
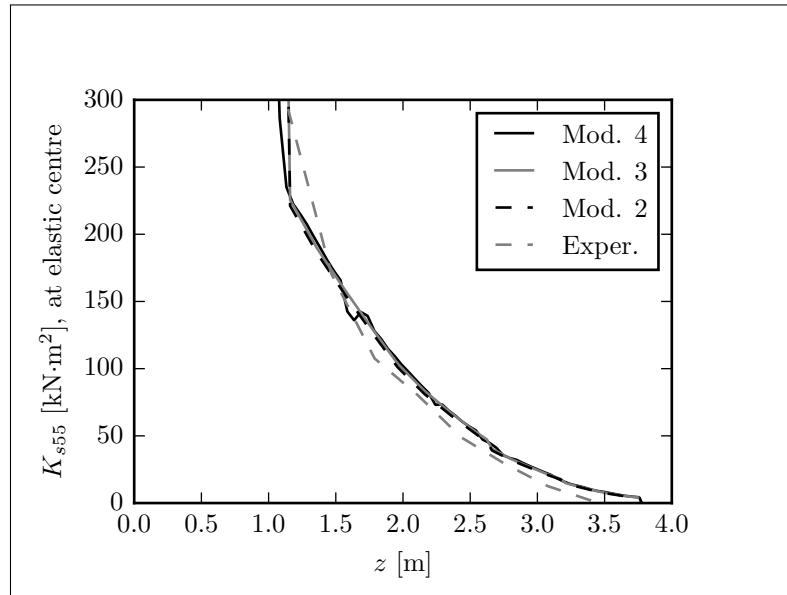
Figure 5.11   In-plane bending stiffness K_{s55} transferred
to elastic centre
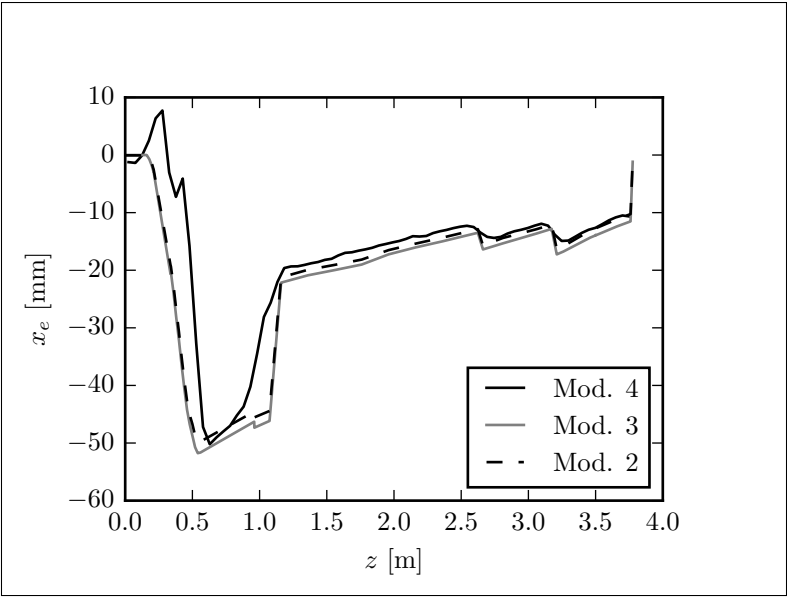
Figure 5.12   Elastic centre location along the x-axis x_e
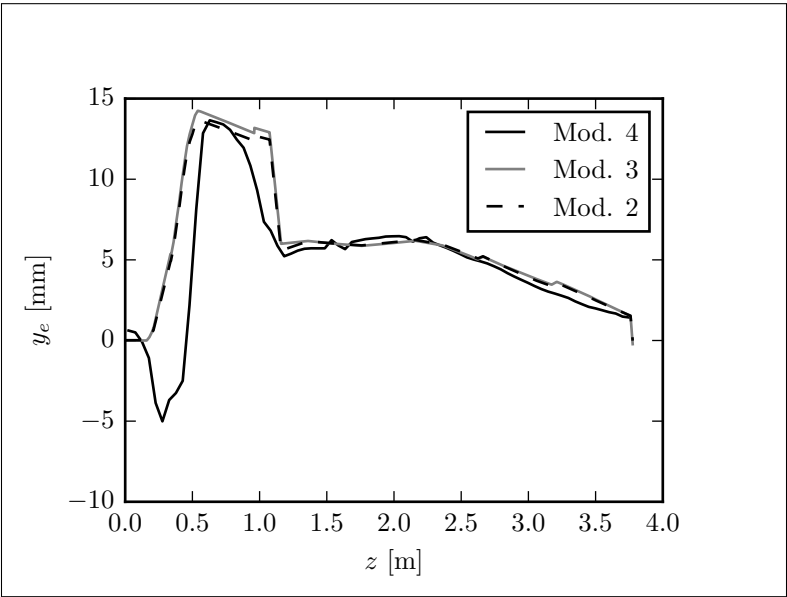
Figure 5.13   Elastic centre location along the y-axis y_e

Starting from the cross-sectional stiffness matrices computed at the elastic centre, it is possible to compute the orientation of the principal axes of bending. The results of the angle θ_1 between the x-axis and the flapwise principal axis of bending are shown in Figure 5.14. All models return values close to each other. Transferring the K_{s44} term to this axis allows to compare with the flapwise bending stiffness obtained from model 1. As shown in Figure 5.15, model 1 return values that are really close to those of the other models in the outboard region of the blade. In fact, model 1 computes values that are approximately 2 to 3 % smaller than those of the other models. A higher difference is observed from blade root to $z = 1$ m. This is because, in that region, the aerodynamic shells outside the spar caps are as thick as the spar cap, contributing to the blade stiffness, which is not taken into account in model 1. However, we can say that model 1 gives conservative results that are pretty close to the values obtained from the other models.
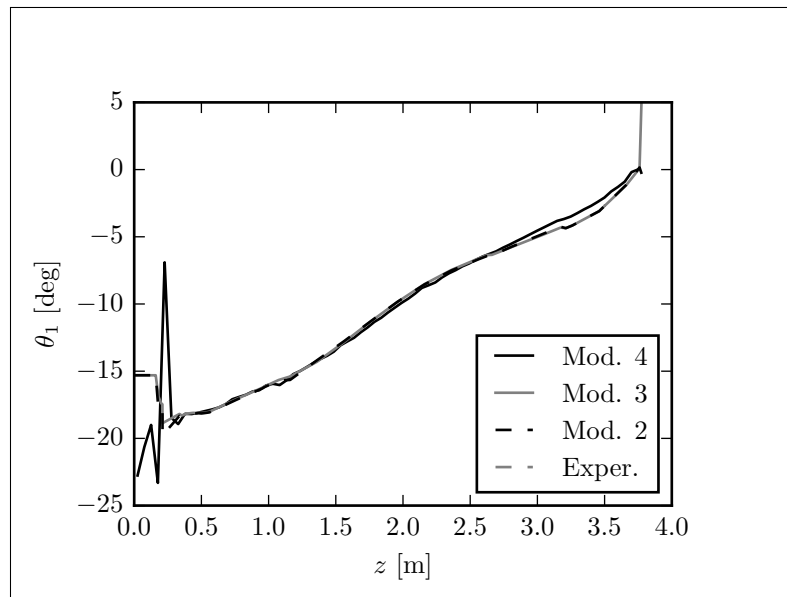
Figure 5.14   Orientation of the principal axes of bending θ_1
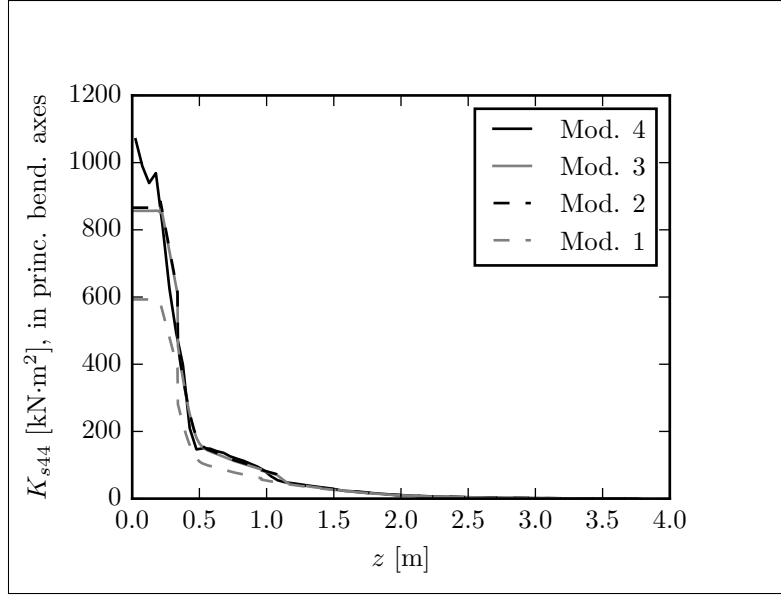
Figure 5.15   Out-of-plane bending stiffness K_{s44}
transferred to elastic centre and rotated to the principal
axes of bending (flapwise bending stiffness)

The results of torsional stiffness are presented in Figure 5.16, where they are transferred to the shear centre for models 3 and 4 in order to be able to compare with model 2 and the experimental results. The results from models 2, 3 and 4 show similar trends. Around $z = 0.5$ m, Model 4 differs from the two others. This is due to the fact that this model takes into account the changing cross-sectional shape. When zooming in the outboard section of the blade (see Figure 5.17), we can observe differences between the different models of up to 50 %. At the opposite of what was observed for bending, model 4 underestimates the torsional stiffness. This can be explained by the difficulty of obtaining good results for torsion from a shell finite element model using offset shells as reported by Fedorov and Berggreen (2014), Branner et al. (2007) and Laird et al. (2005).
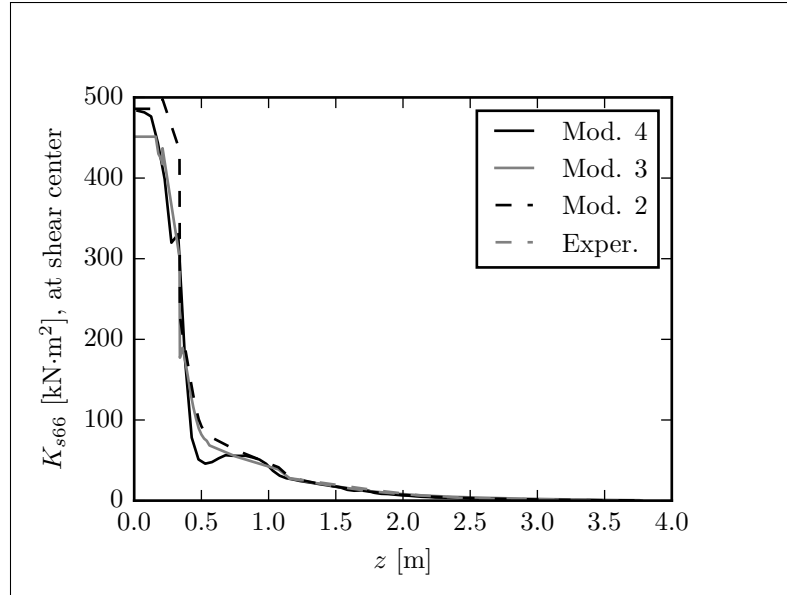
Figure 5.16   Torsional stiffness K_{s66} transferred to shear
centre
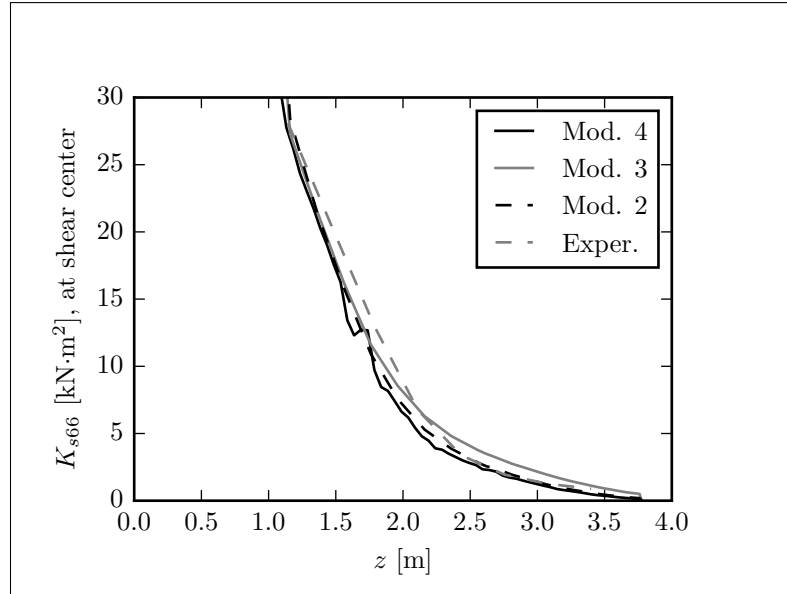
Figure 5.17   Torsional stiffness K_{s66} transferred to shear
centre, closer view of the outboard values

As shown in Figures 5.18 and 5.19, the shear centre position as computed by models
3 and 4 are quite different. However, theses differences are still small relative to the

cross-sectional dimensions. It illustrates the difficulties associated with the computation of the transverse shear properties using the 3D shell finite element model.
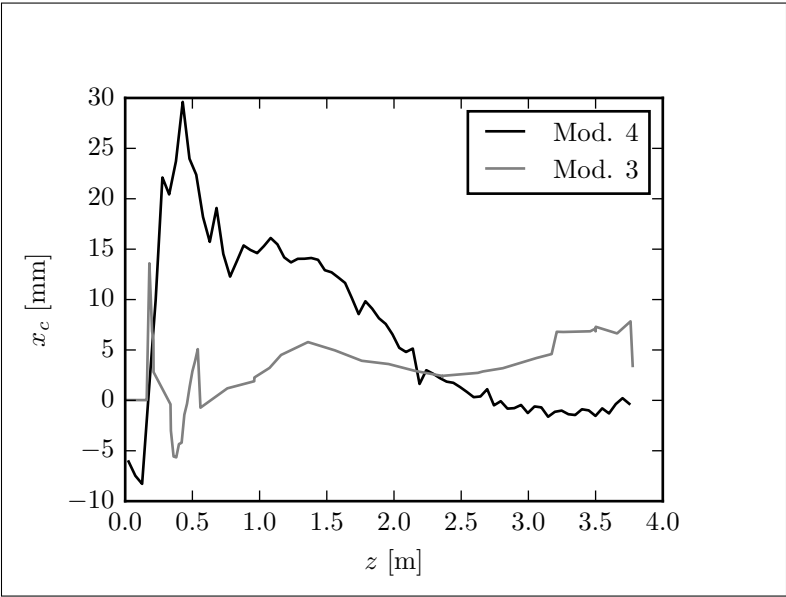
Figure 5.18   Shear centre location along the x-axis x_c
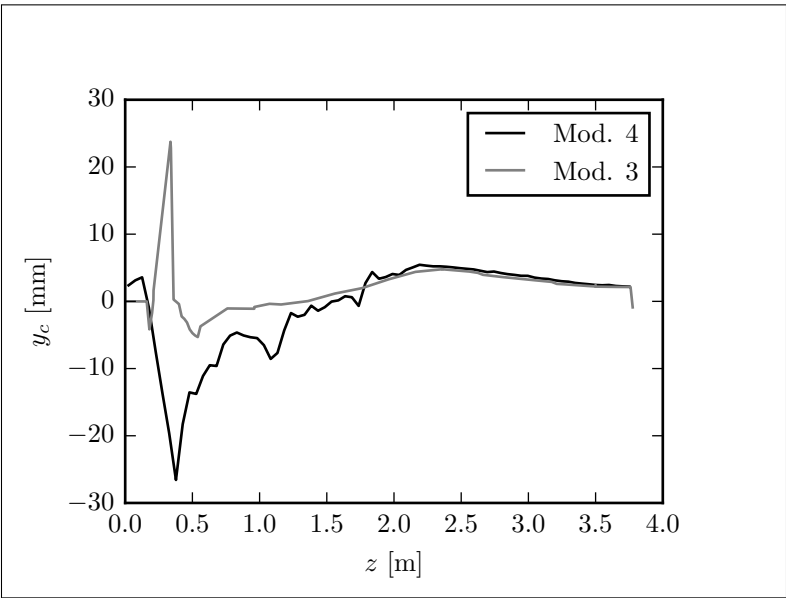
Figure 5.19   Shear centre location along the y-axis y_c

Results for the K_{s16}, K_{s26}, K_{s34}, K_{s35} and K_{s45} terms are not presented here as they are used to compute the elastic and shear centre as well as the orientation of the principal axes of bending.

Comparing the blade cross-sectional properties from the different numerical models against the experimental data, all models seem to overestimate the blade stiffness. This could be explained by the fact that the materials' elastic moduli used in the models (see Table 1.3) are in fact higher than the real material stiffnesses. Another reason for the difference in stiffness can be the fact that the bonded joints were not modeled and can reduce the blade stiffness. Model 1 gives a conservative but pretty good estimation of the flapwise bending properties at low calculating cost. Model 2 gives really good results for extension, bending and torsion. Model 3 seems to be the most reliable according to the validation performed on it. Model 4 gives really good results for axial and bending behaviours. For a wind turbine blade with no bend-twist coupling, models 2, 3 and 4 are correct. Model 1 is usable for preliminary analysis based on flapwise bending behaviour.

5.3 Natural frequencies

Blade natural frequencies computed using models 2, 3, and 4 are now compared with the experimental data. Figure 5.20 shows an example of experimental modal testing. The upper part of the figure shows the time-domain signal of one of the strain gauges after deflecting and then releasing suddenly the blade tip. The lower part of the Figure shows the Fourier transform of the strain gauge's time-domain signal. Two natural frequencies can clearly be identified at 6.4 Hz and 15.0 Hz. Both blades instrumented with strain gauges give the same results.

Table 5.10 shows the comparison of model data with experimental data. In each model, the materials' density was adjusted to get a blade mass of 21.6 kg, equivalent to the real blade. This mass does not include the 6.40 kg of steel parts at blade root (so the experimental blade mass properties are computed from total blade mass and known steel parts
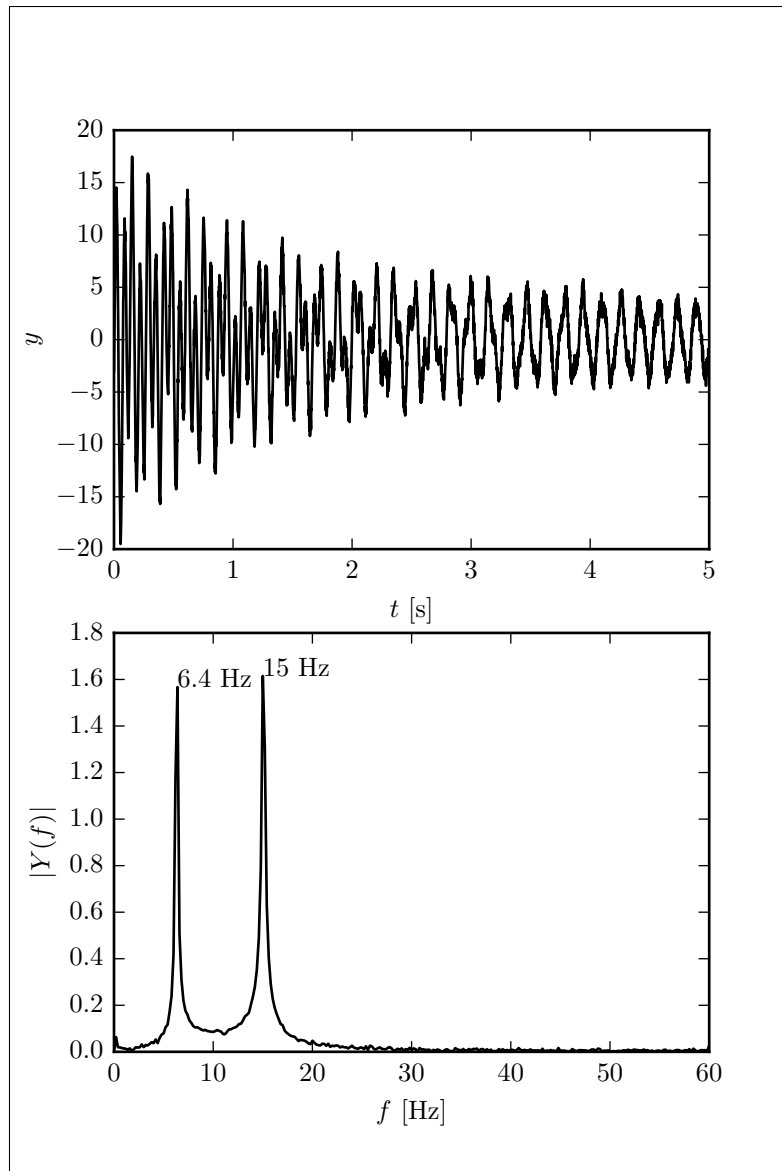
Figure 5.20   Example of experimental modal analysis of
the blade. y is the signal from a strain gauge and Y is its
Fourier transform. t is time and f is the frequency

mass). Each of these models predict a similar centre of gravity location, but these values are approximately 3 % lower than the one of the real blade. For the first blade natural frequency, all three models are within 3.5 % difference relative to the experimental value. This difference increases up to 14.6 % for the second natural frequency. In each case, the models predict higher natural frequencies than the experimental data, confirming the

fact that the models overestimate blade stiffness. The differences between models 2, 3 and 4 are within a 2 to 3 % range and they are satisfactorily predicting the experimental data.

Table 5.10   Results of the blade modal analysis. m is the blade mass, Z_{cg} is the distance from its root to its centre of gravity along its length and f_i are the first 5 blade natural frequencies. δ_j is the relative difference (in %) between model j and experimental data

		Experimental	Model 2	Model 3	Model 4	δ_2	δ_3	δ_4
m	[kg]	21.60	21.60	21.60	21.60	0.0	0.00	0.00
Z_{cg}	[m]	1.180	1.143	1.143	1.140	-3.1	-3.1	-3.4
f_1	[Hz]	6.400	6.616	6.474	6.559	3.4	1.2	2.5
f_2	[Hz]	15.00	17.19	17.05	16.72	14.6	13.7	11.5
f_3	[Hz]	-	20.86	20.32	20.21	-	-	-
f_4	[Hz]	-	42.69	40.42	40.55	-	-	-
f_5	[Hz]	-	58.32	57.08	56.18	-	-	-

As we can see in Figures 5.21 to 5.25 each models predict mode shapes that are really similar to each other. Figure 5.26 shows the blade mode shapes as computed by model 4.
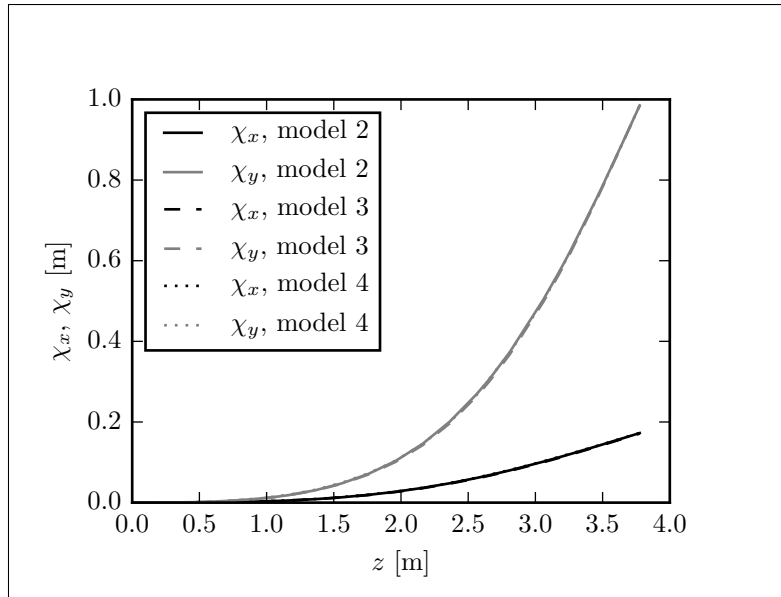
Figure 5.21 Comparison of the 1st blade mode shape.
χ_x and χ_y are respectively the in-plane and out-of-plane
deflections
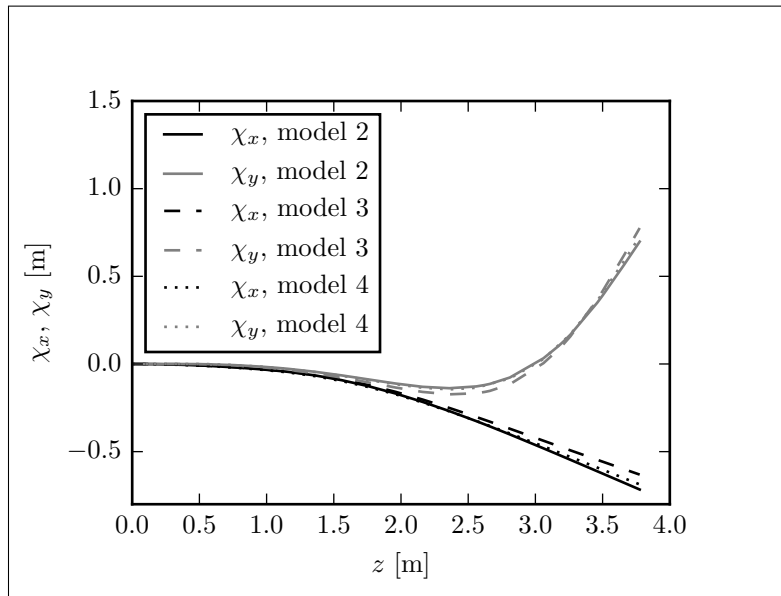
Figure 5.22 Comparison of the 2nd blade mode shape.
χ_x and χ_y are respectively the in-plane and out-of-plane
deflections
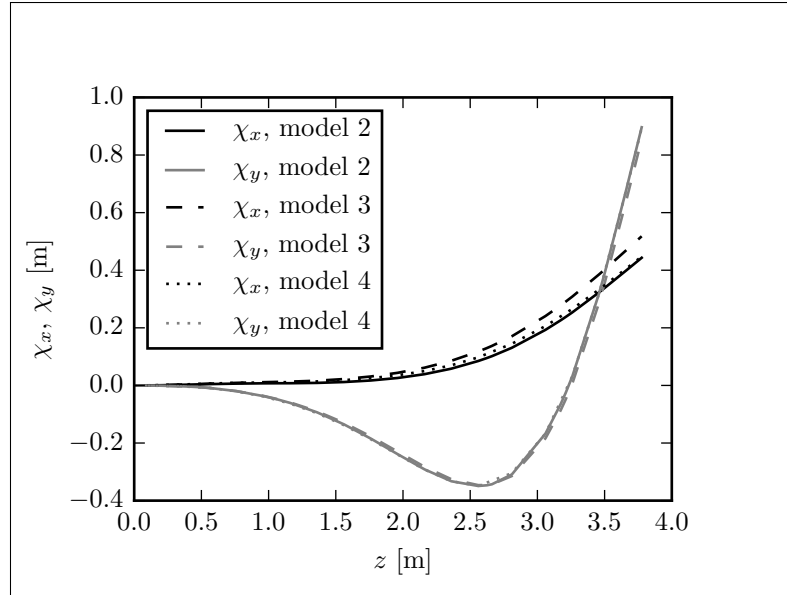
Figure 5.23 Comparison of the 3rd blade mode shape.
χ_x and χ_y are respectively the in-plane and out-of-plane
deflections
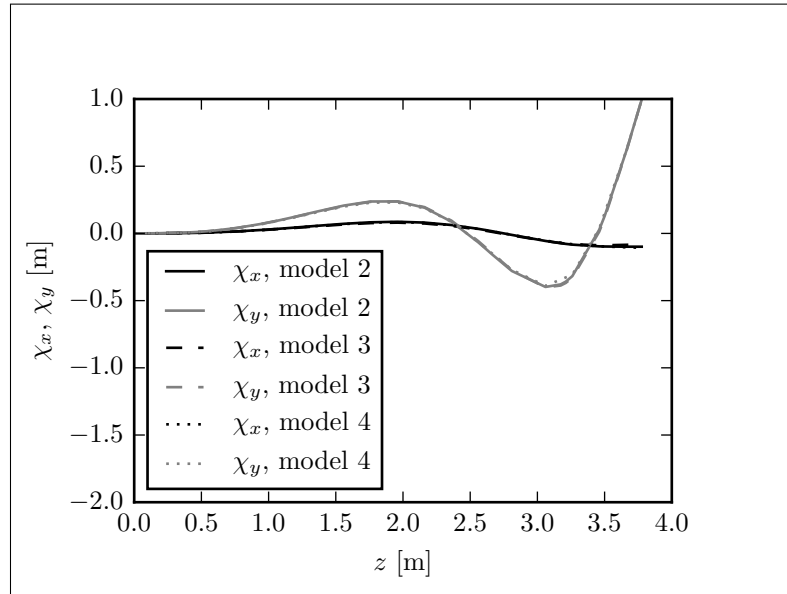
Figure 5.24 Comparison of the 4th blade mode shape.
χ_x and χ_y are respectively the in-plane and out-of-plane
deflections
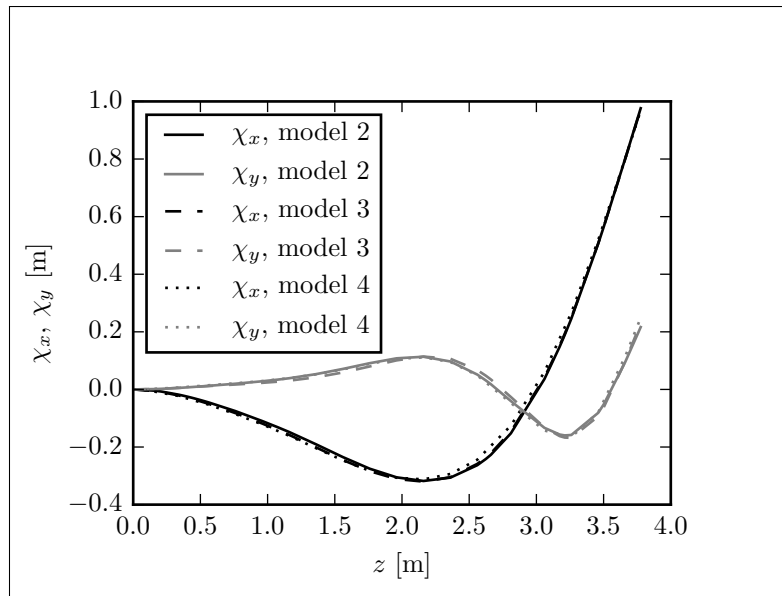
Figure 5.25 Comparison of the 5th blade mode shape. χ_x and χ_y are respectively the in-plane and out-of-plane deflections

(a) Mode 1

(b) Mode 2

(c) Mode 3

(d) Mode 4
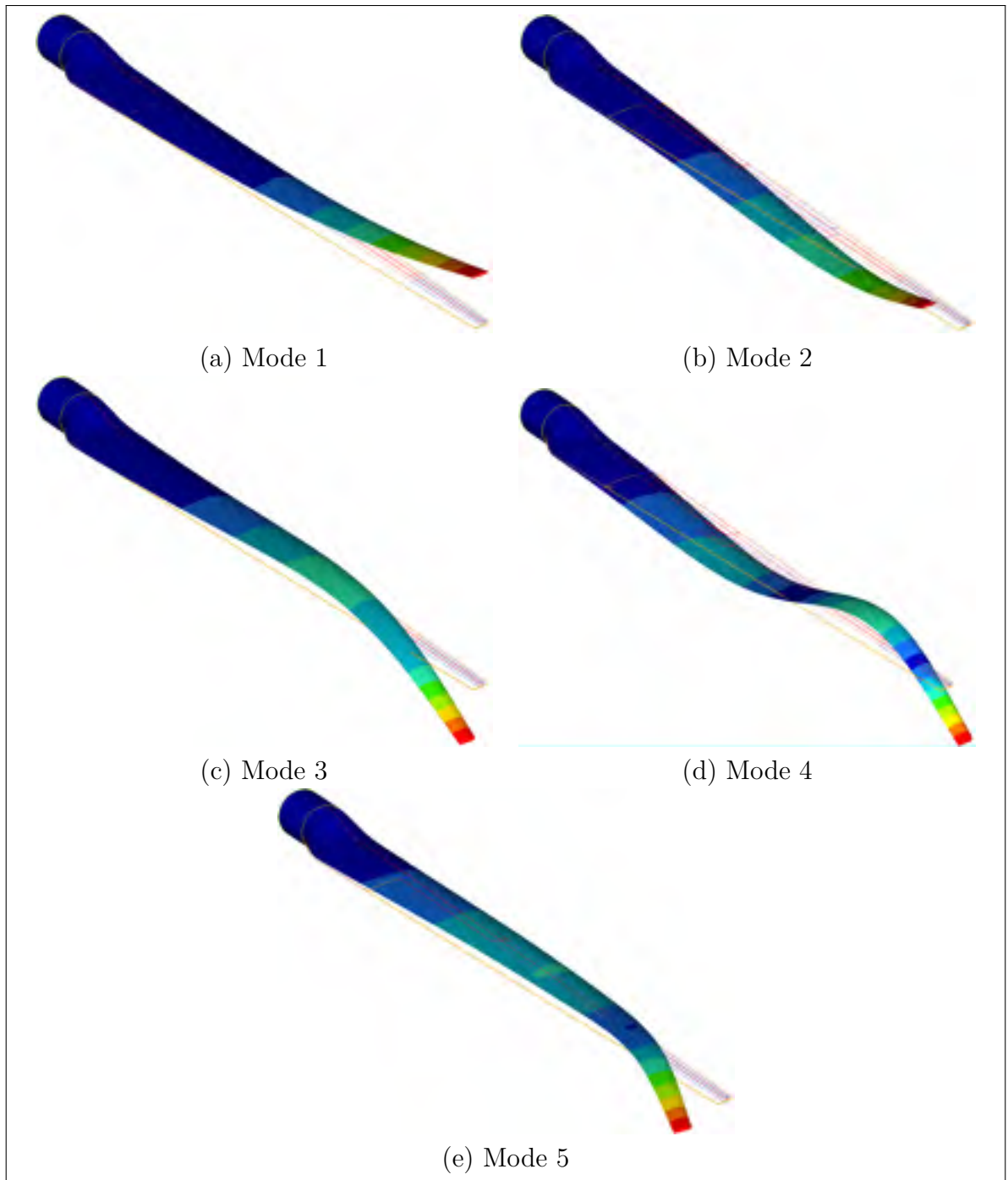
(e) Mode 5

Figure 5.26   Blade mode shapes from model 4

5.4 Deflection

Looking now at the blade deflections during the design load test (defined in Section 1.7.2), we can see in Figure 5.27 that all models predict well the out-of-plane deflection. At tip, all values are within a 10 % interval. The experimental data were obtained from tests on 4 different blades (results for all 4 blades are shown in Figure 5.27). For the in-plane deflection, we can observe some scatter in the experimental data, which is normal due to the low deflection values and to the precision of the method used to compute them (see Section 1.7).
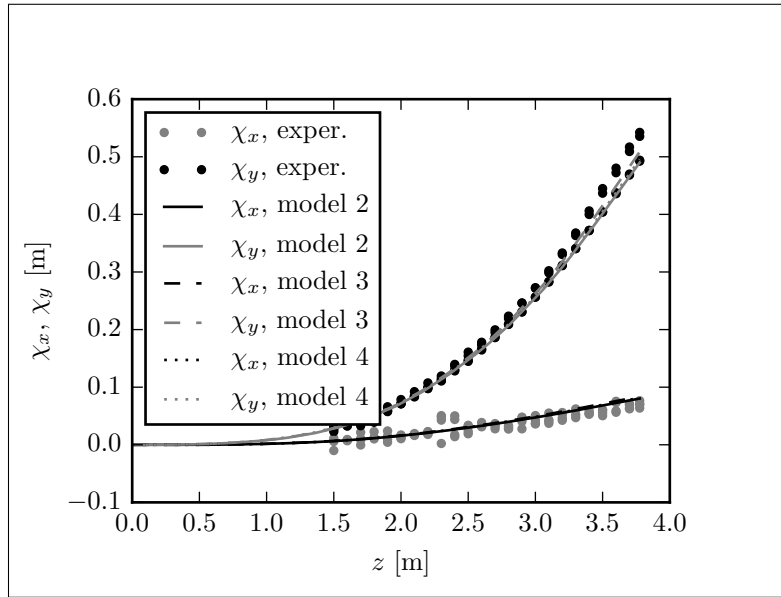
Figure 5.27   Comparison of experimental and models blade deflection under the design load. χ_x and χ_y are respectively the in-plane and out-of-plane deflections

5.5 Strains

All four models allow computing the blade strains. Figure 5.28 shows the maximum and minimum longitudinal strains computed over the blade length by these four models for the design load (defined in Section 1.7.2). In addition to these data, the experimental

results from the two blades that were equipped with strain gauges are shown. The strain gauges were placed on the upper and lower blade surface at 30 % of the chord length (which correspond to the chordwise blade reference axis location). As seen in Figure 5.28, models 2, 3 and 4 predict relatively well the strains obtained from the experiments (within a 10 % range). As expected and desirable, model 1 gives a conservative evaluation of the strain levels by overestimating them.
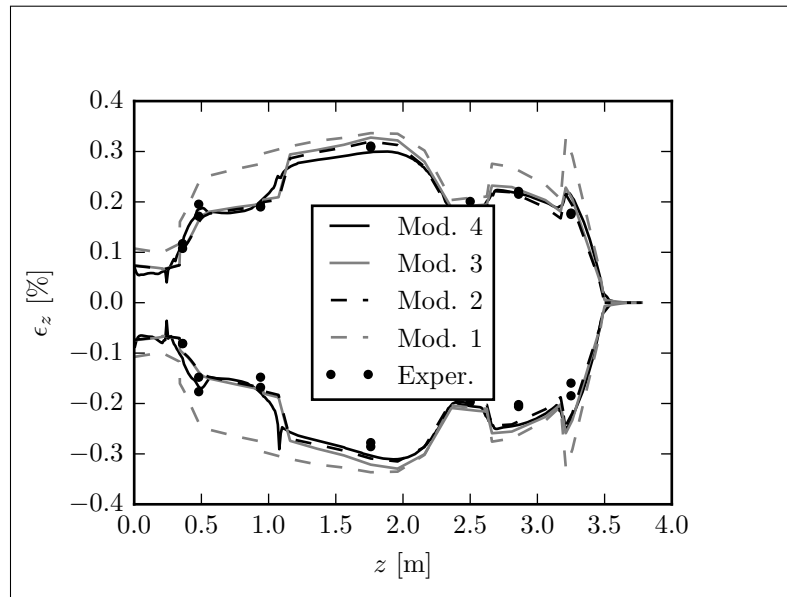
Figure 5.28 Comparison of experimental and models blade strains under the design load. Top curves are lower surface data and lower curves are upper surface data

5.6 Buckling

During the experimentations, buckling has been observed in both steps of the destructive tests (performed on both blades instrumented with strains gauges).

During the first step (where the blade was simply supported at $z = 2360$ mm and loaded at $z = 3500$ mm), buckling was observed on the first blade tested at location $z = 2800$ mm, on the panel near the trailing edge on the upper side. From the 3D

scanner data, we know that buckling occurs between 2000 and 2250 N of load applied on the blade. Figure 5.29 shows the blade buckling as observed by the 3D scanner. When looking at the signal of the strain gauge closest to the buckling location (gauge at the right-hand side of Figure 5.29), we can see a change in the signal at a load of 2160 N (see Figure 5.30).

For the second blade tested, no buckling was observed with the 3D scanner before the blade failure under a load of 2000 N. But when looking at the signal of the strain gauge closest to the buckling location (for blade 1), a change of slope is observed at a load of around 1800 N as seen in Figure 5.31. This value corresponds to the intersection point between a line passing through the initial slope and a line passing throught the final slope.

For the second step of the destructive test (where the force was applied at $z = 2360$ mm), the 3D scanner indicates that buckling occurs between 4000 and 6000 N applied on the blade, and this is the case for both blades. Figure 5.32 shows the buckling of blade 1 as recorded by the 3D scanner (blade 2 is similar). As we can see, the centre of the wave that has the maximum amplitude is located at $z = 1200$ mm, where a strain gauge was installed. Again, buckling occurs on the panel near the trailing edge on the upper side of the blade. When looking at the signal of this strain gauge for both blades, we can see a change in the slope (intersection point between lines passing through the initial and the second linear parts of the curve) at a load of 4600 N for blade 1 and at a load of 5500 N for blade 2 as shown in Figures 5.33 and 5.34.

As summarized in Table 5.11, for the first step of the destructive tests, buckling occurs at a load level between 1800 and 2160 N at a radial location $z = 2800$ mm. For the second step of the destructive tests, buckling begins at a load between 4600 and 5500 N at 1200 mm from the blade root.

The shell finite element model of the blade (model 4) allows computing buckling loads. Figure 5.35 shows the first buckling mode for both steps of the destructive test. The
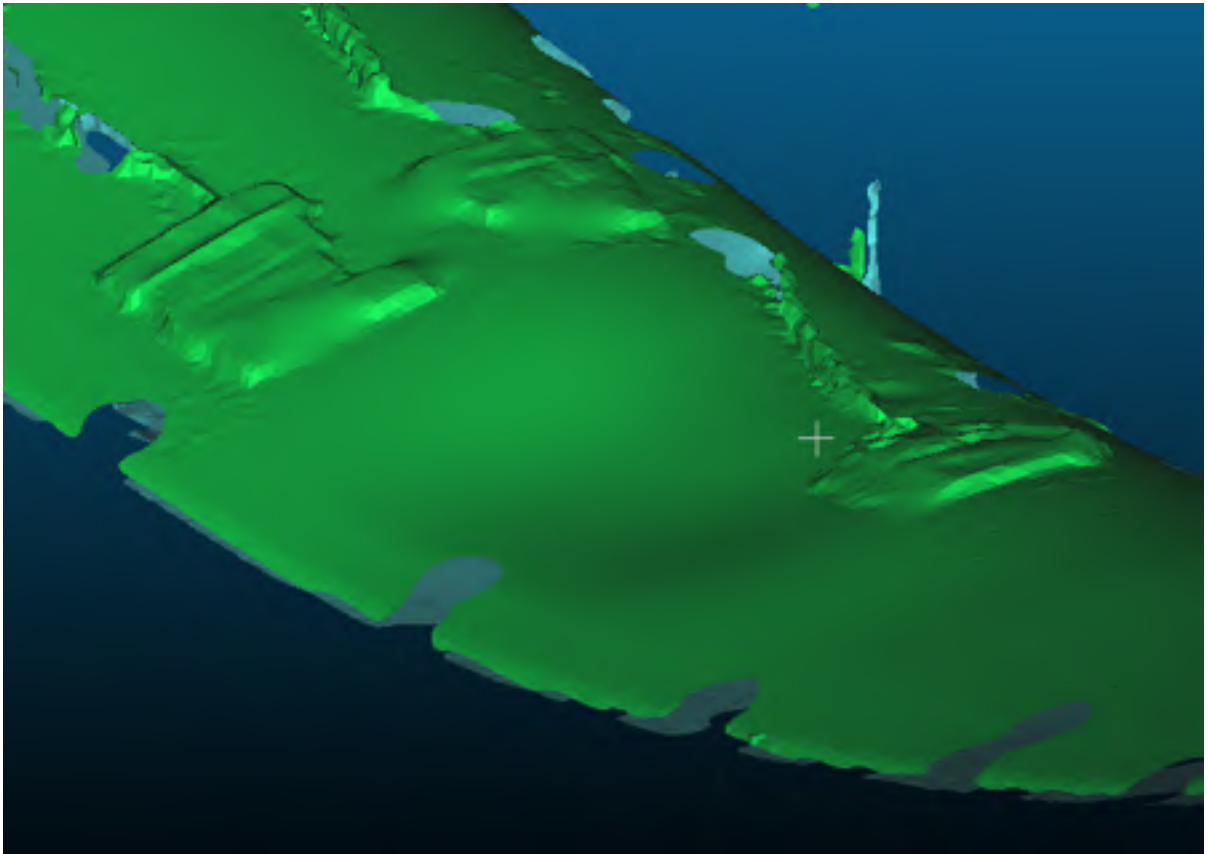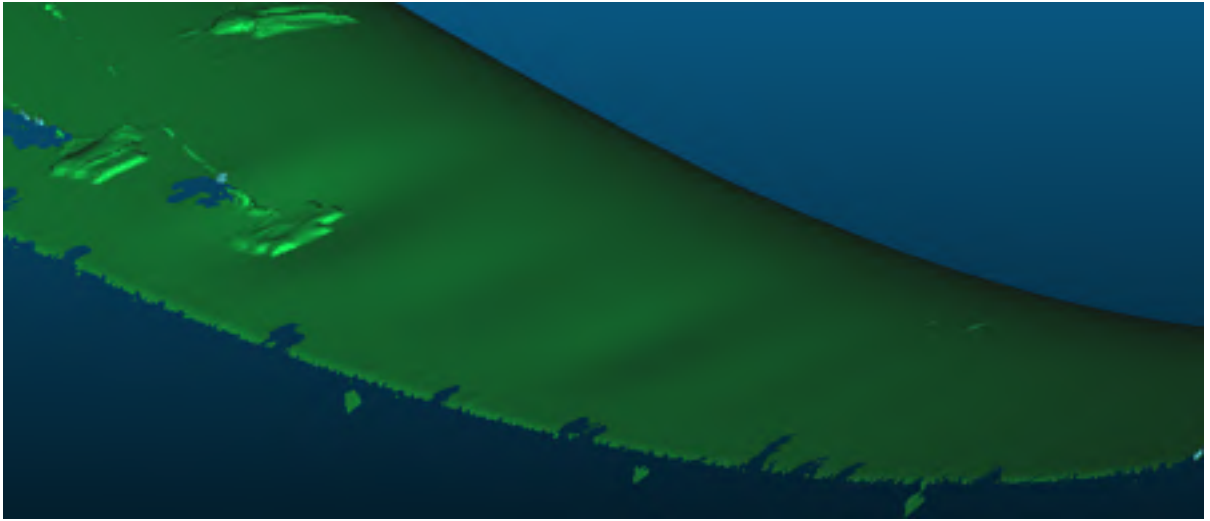
Figure 5.29   Buckling at $z = 2800$ mm on blade 1 during the first step of the destructive test recorded by the 3D scanner

buckling loads are 3066 N and 6059 N for the first and second steps of the destructive test respectively. These results are also presented in Table 5.11.

The only other model able to compute buckling loads is the classical strength of materials model (model 2). For the first step of the destructive test, this model predicts a buckling load of 2326 N at the section located at 2662 mm from the blade root (see Figure 5.36). For the second step, buckling occurs at 1160 mm from the root at a load level of 3702 N (see Figure 5.37). These results are also summarized in Table 5.11.

When comparing the buckling results, we can first see that the buckling locations are relatively well predicted by both models. All results are within ranges of 105 mm for step 1 and 65 mm for step 2. If we compare the buckling loads, we can see that model
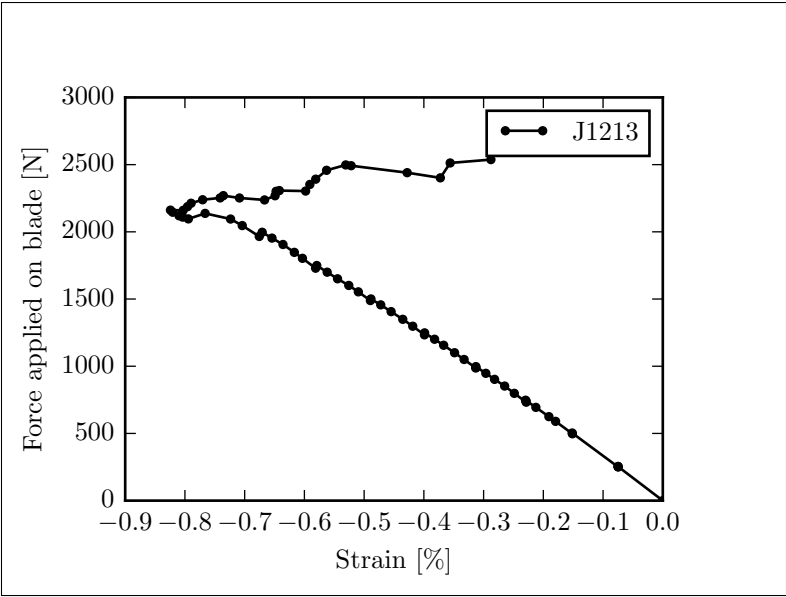
Figure 5.30   Signal of the strain gauge close to the buckling location on blade 1 for the first step of the destructive test
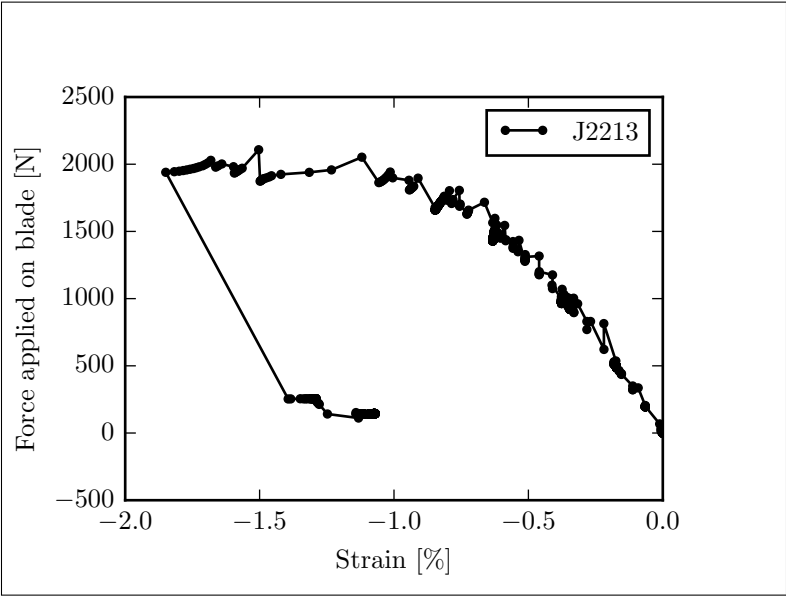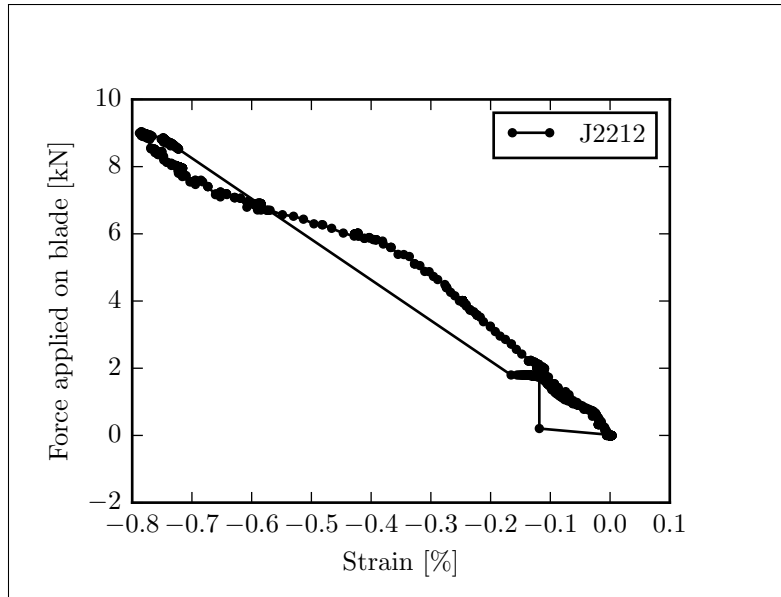

Figure 5.31   Signal of the strain gauge close to the buckling location on blade 2 for the first step of the destructive test

Figure 5.32   Buckling at $z = 1200$ mm on blade 1 during the second step of the destructive test recorded by the 3D scanner
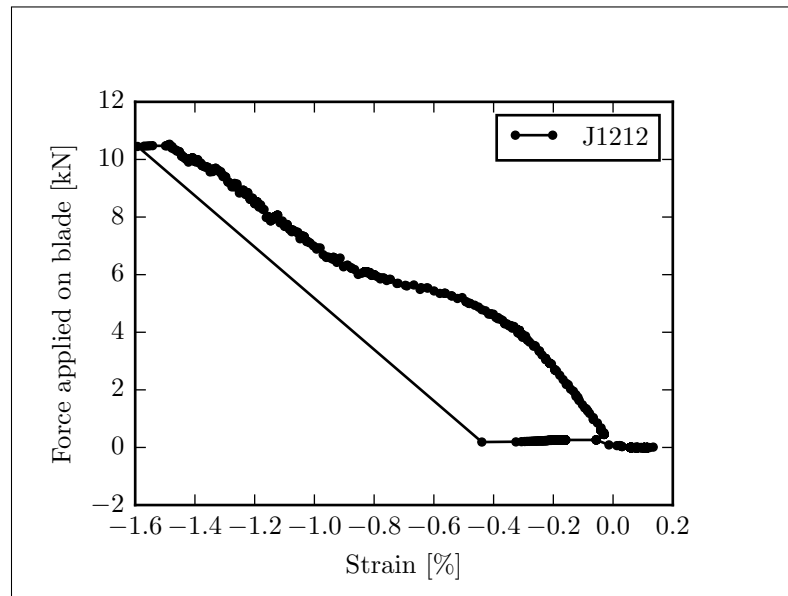
Figure 5.33   Signal of the strain gauge at the buckling location on blade 1 for the second step of the destructive test

2 predict lower loads than model 4, which is normal due to the conservative hypotheses of model 2 (infinitely long flat plates). However, the experimental data for step 1 show

Figure 5.34   Signal of the strain gauge at the buckling
location on blade 2 for the second step of the destructive
test
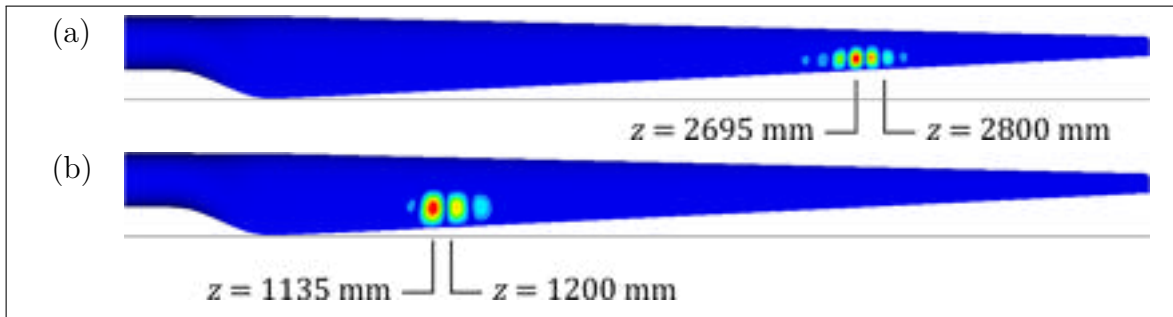
Figure 5.35   Buckling results from model 4. (a) step 1, (b) step 2

that buckling occurs at a load that is lower than the one predicted by both models. For
the second step, the experimental results range between the results of models 2 and 4.

The differences between the experimental data and the results from the shell finite element
model (model 4) can be explained by the fact that finite element linear buckling analyses
are non-conservative. This is formalized in some standards (Germanischer Lloyd, 2010;
DNV GL, 2015) where a partial safety factor of 1.25 is specified when a linear finite
element model is used for buckling analysis. As seen in the previous results (frequencies,
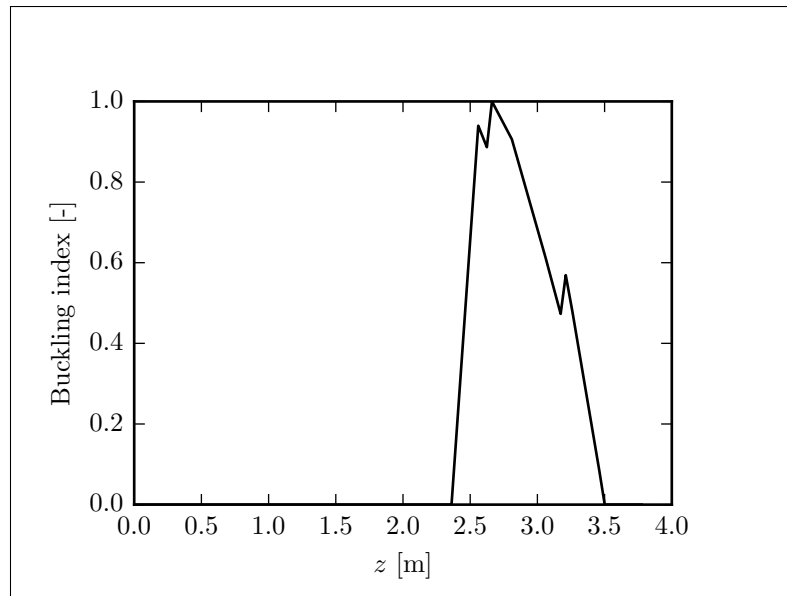
Figure 5.36   Buckling index (inverse of safety factor) results of model 2 for the first step of the destructive test under a force of 2326 N
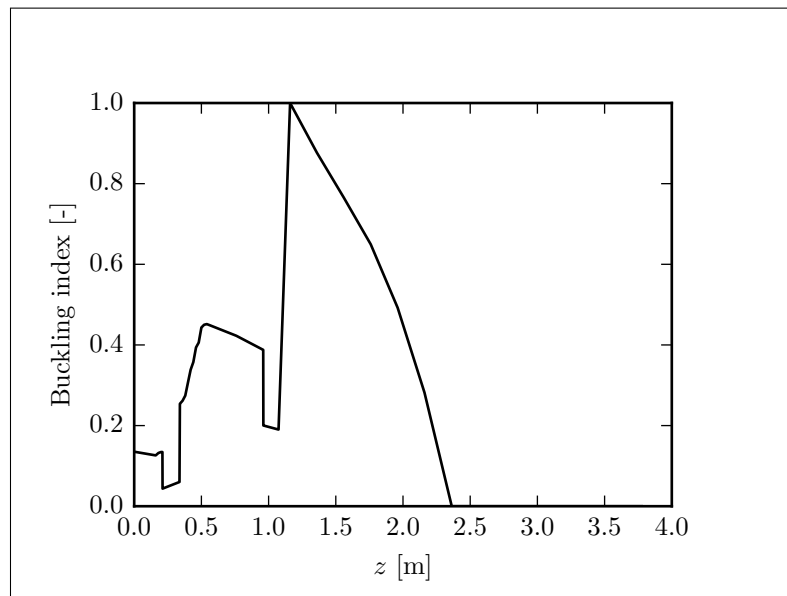
Figure 5.37   Buckling index (inverse of safety factor) results of model 2 for the second step of the destructive test under a force of 3702 N

Table 5.11   Comparison of buckling results

Model	Step 1		Step 2	
	Buckling force [N]	Buckling location, z [mm]	Buckling force [N]	Buckling location, z [mm]
Experimental	1800–2160	2800	4600–5500	1200
Model 2	2326	2662	3702	1160
Model 4	3066	2695	6059	1135

deflections, strains), the models overestimate the blade stiffness. The buckling results go in the same way. The ratio of shell finite element buckling load to experimental minimum buckling load is 1.70 for step 1 and 1.32 for step 2. The value of step 2 seems reasonable as the cited standards prescribe a total reduction factor around 1.5 to 1.6 for a buckling analysis using a linear finite element model. For step 1, the ratio is high. This may be caused by a problem with the bonded joint between blade web and skin that reduce the panel support. However, we can note that these buckling behaviours occur in non-structural areas and do not lead to blade failure.

5.7   Composite Strength

The last object of comparison between the different blade structural models is about the blade strength. For the first step of the destructive test, both blades fail in similar ways. A compressive failure occurs in the spar cap on the upper side. For blade 1, the failure occurs for a load around 2650 N (continuous recording of the load cell data was not available so an estimate of the failure load is given) at 2760 mm from the root. Blade 2 fails at a load level of 2110 N and the failure is located at 2690 mm from the root. These values are summarized in Table 5.13 presented at the end of this section. Figure 5.38 shows images of the failure of blade 1.

During the second step of the test, blade 1 fails at a load level of 10 528 N and the failure is located at 1210 mm from the blade root in the spar cap of the upper side (see Figure 5.39).
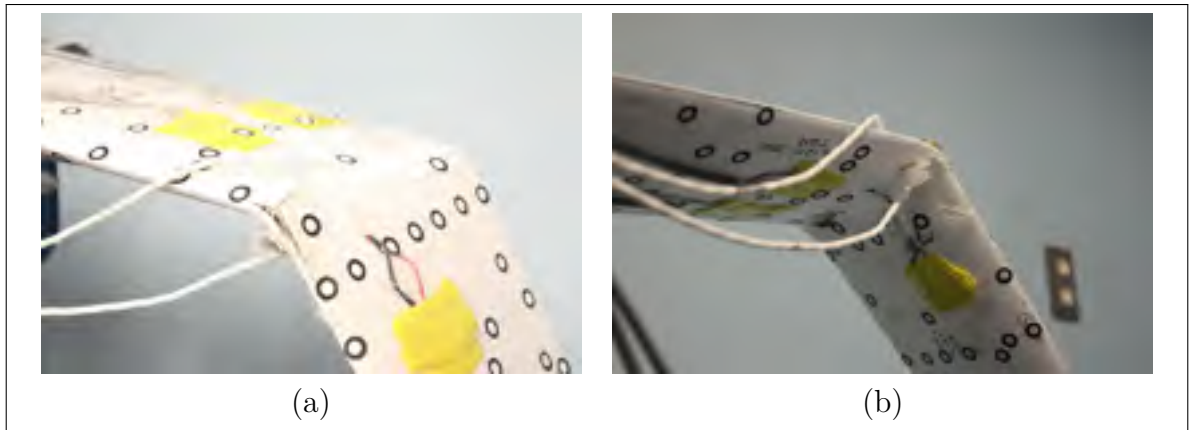
Figure 5.38   Failure of blade 1 at $z = 2760$ mm in the first step of the destructive test. (a) lower side, (b) upper side
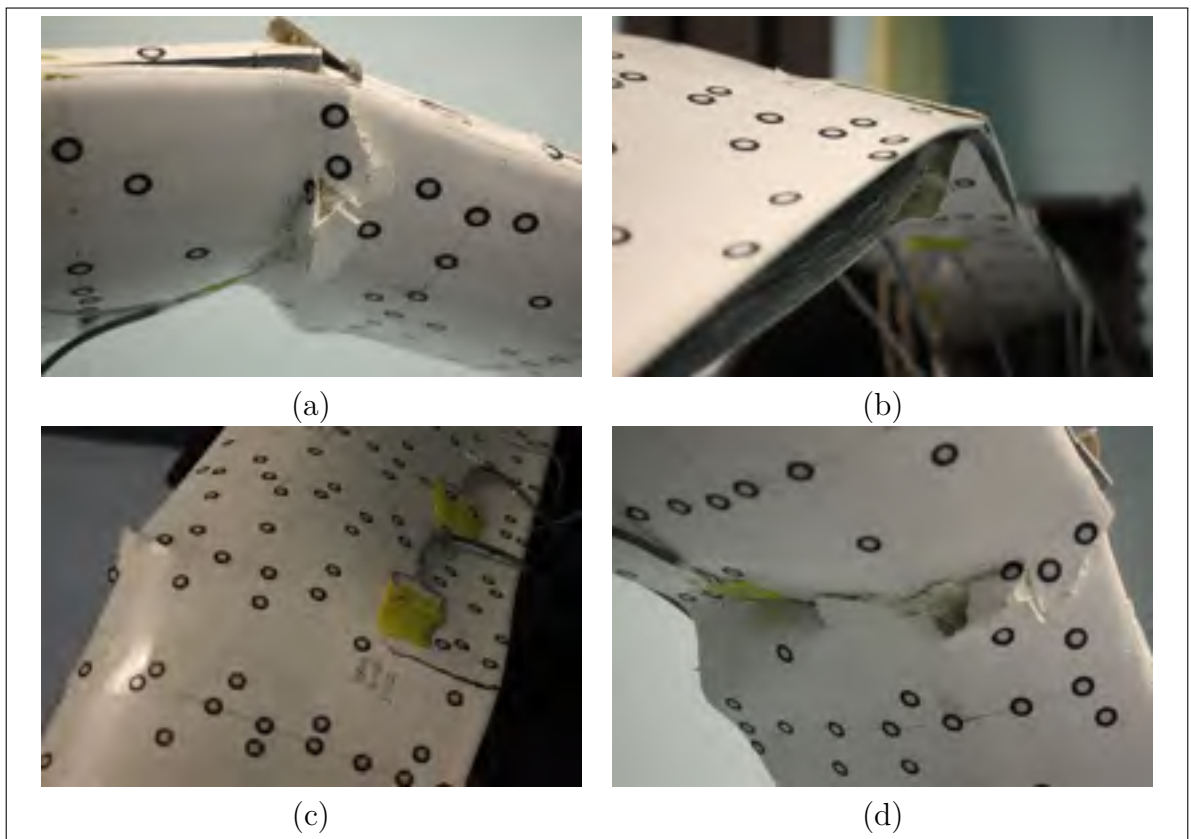

Figure 5.39   Failure of blade 1 in the second step of the destructive test. (a) leading edge and upper side, (b) trailing edge, (c) lower side, (d) upper side

The second blade fails in a different way. The failure process starts by a crack appearing on the leading edge around 450 mm from the root at a load level of 8450 N (Figure 5.40a). After reaching a maximum load of 9040 N, the trailing edge suddenly opens at 700 mm from the blade root (Figure 5.40b). At this moment, the load slightly decreases. After a small increase in the applied load, the blade fails at 500 mm from the root. This results in a failure of the shear web and of both upper and lower skins near the trailing edge (Figure 5.40c and d).

(a)

(b)

(c)

(d)
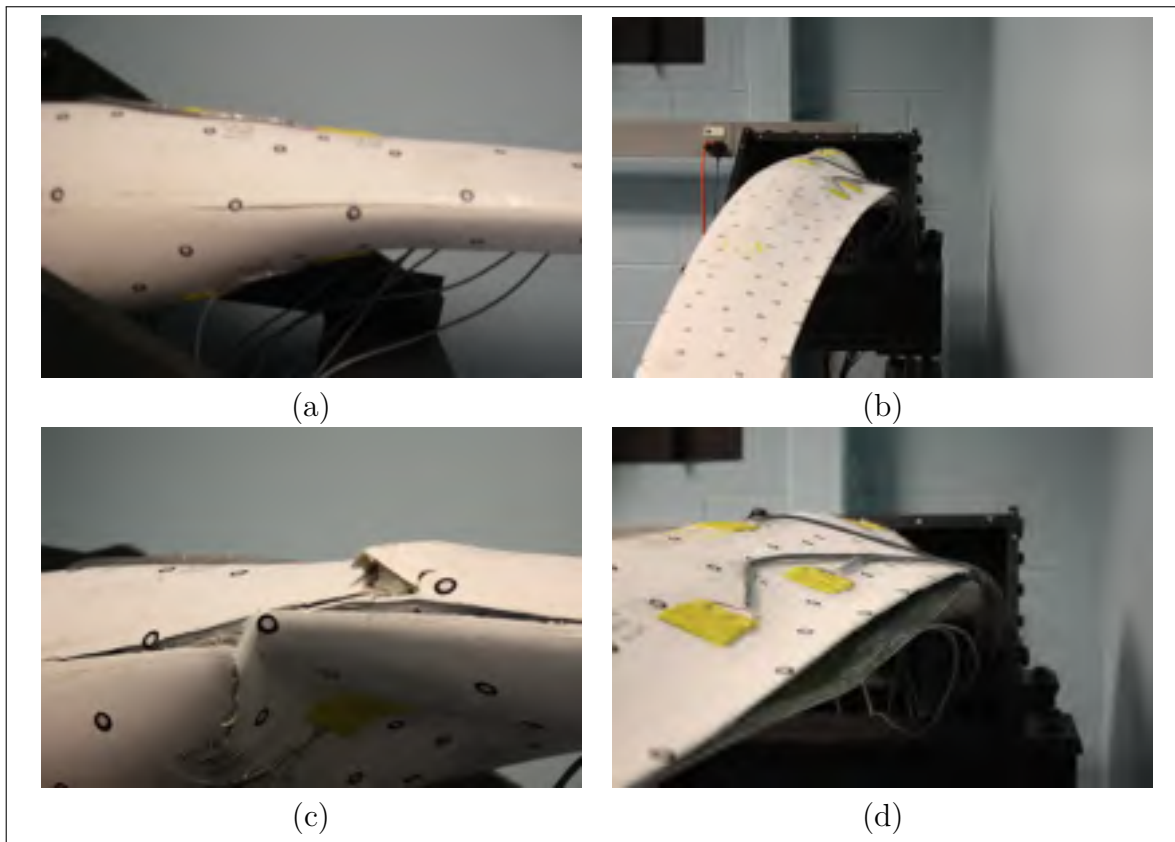
Figure 5.40   Failure of blade 2 in the second step of the destructive test

As the failure process of the second blade during step 2 of the destructive test is hard to analyze with the numerical model used in this thesis, only the results of the first blade are used for the comparison of this section. They are reported in Table 5.13.

For the evaluation of the blade strength with models 1 and 2, the strength of the different laminates is needed. This is obtained by using the classical lamination theory with the following procedure as proposed in composite textbooks (Gibson, 2007; Berthelot, 2012, for instance) :

- The first ply failure stress is computed using the Tsai-Wu criterion.

- For that ply, the maximum stress failure criterion is used to get the failure mode (longitudinal tension, longitudinal compression, transverse tension, transverse compression or shear).

- If the failure mode is in the transverse direction or in shear, the stiffness dominated by the matrix properties (E_2, G_{12} and ν_{12}) are set to 0. If the failure mode is in the longitudinal direction, the stiffness dominated by the fibre properties (E_1, and ν_{12}) are set to 0.

- This process is repeated until the maximum load is reached.

- The failure strain is computed as the failure stress divided by the initial longitudinal modulus.

- The failure analysis is applied to the 0° and ±45° plies only.

An example of this process is given in Figure 5.41, presenting the longitudinal tensile behaviour of the spar cap laminate ranging from $z = 960$ mm to $z = 2624$ mm. At a stress level of 169 MPa, the ±45° plies fail in transverse tension. This is the first ply failure. The laminate stiffness is then slightly reduced and the stress can be increased to 449 MPa before failure occurs in the 0° plies, which is the failure stress. The failure strain corresponding to this value is 1.59 %.

Table 5.12 summarizes the tension and compression longitudinal failure strains for all laminates along the blade length. All compressive strains are lower than tensile strength.
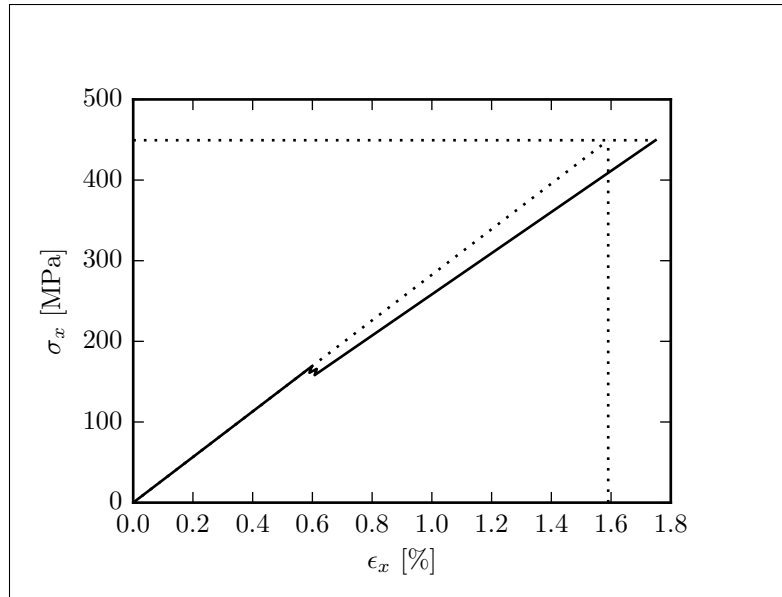
Figure 5.41   Stress-strain curve of the spar cap laminate
in the region 960 mm $< z <$ 2624 mm loaded in the
longitudinal direction

It is interesting to note that when using the first ply failure data, the opposite result is
obtained.

Table 5.12   Failure strains of the laminates
along the blade length. e_x^T and e_x^C are
respectively the tensile and compressive
longitudinal failure strains

longitudinal position	e_x^T [%]	e_x^C [%]
$z <$ 337 mm	1.32	0.89
337 mm $< z <$ 960 mm	1.61	1.02
960 mm $< z <$ 2624 mm	1.59	1.01
2624 mm $< z <$ 3173 mm	1.45	0.94
3173 mm $< z$	1.07	0.84

When using the compressive failure strains within structural model 1, for the first step of
the destructive test, the blade failure is predicted at $z = 3211$ mm under a force of 1288 N
as shown in Figure 5.42. A second possible failure point is located at $z = 2662$ mm and
arise when the force reaches a value of 1705 N. This second failure point is interesting

because it is located near the failure location observed during the tests. For the second step of the destructive test, the failure is predicted at $z = 1360$ mm under a force of 9661 N as shown in Figure 5.43. These results are reported in Table 5.13.
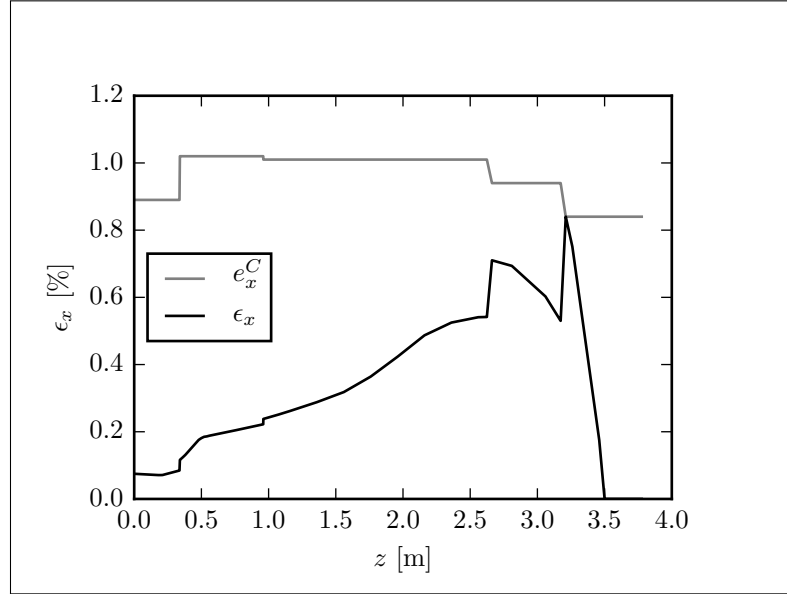

Figure 5.42   Results of structural model 1 for the strain
distribution from the first step of the destructive test
under a force of 1288 N

As shown in Figures 5.44 and 5.45, the results obtained from structural model 2 are similar to those of model 1. For model 2, due to the asymmetry of the blade cross section, the extremum cross-sectional strains are not the same in tension and in compression. The predicted failures are in compression due to the fact that the failure strains are smaller in compression than in tension. As presented in Table 5.13, the predicted failures of structural model 2 are at the same locations as those of model 1, but for higher load values. So, as for the bending stiffness evaluation, model 1 gives conservative estimation of the failure load.

For models 3 and 4, the method used for the evaluation of blade failure load is based on a method described in Barbero (1999). In order to get the failure loads, all the ma-
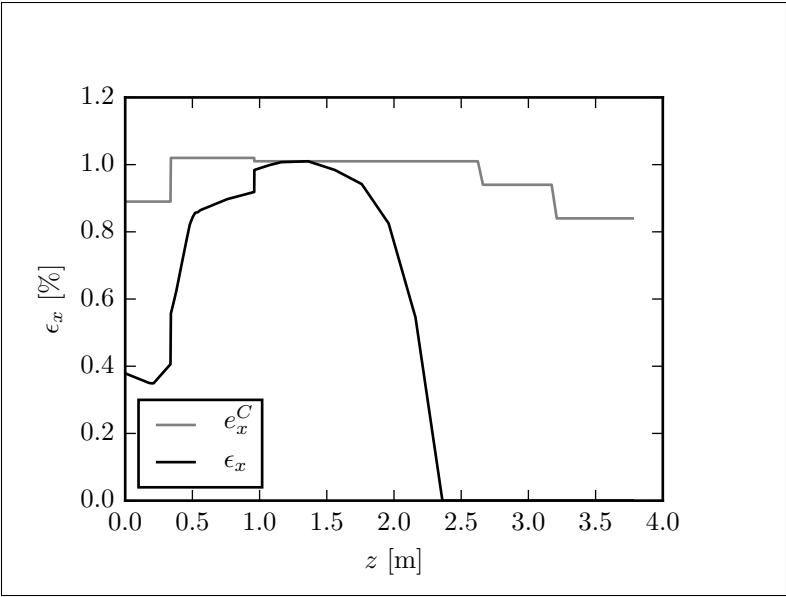
Figure 5.43 Results of structural model 1 for the strain distribution from the second step of the destructive test under a force of 9661 N
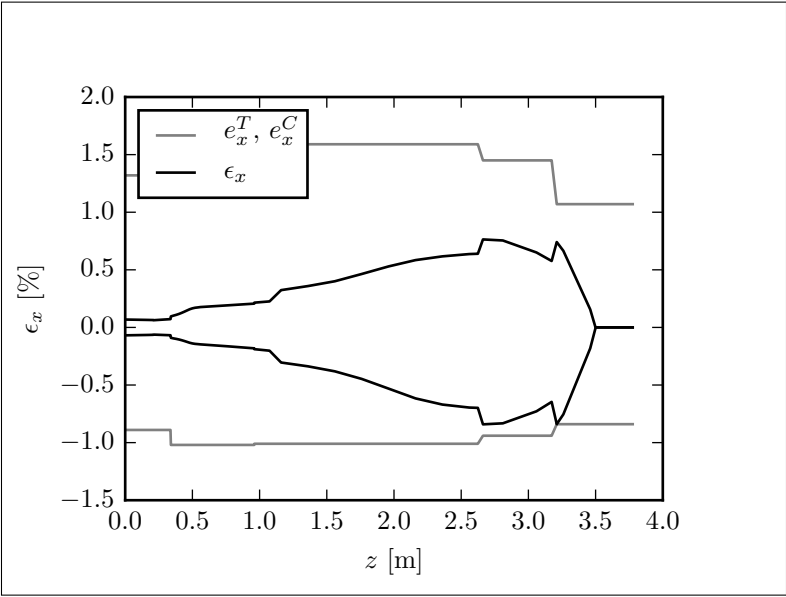

Figure 5.44 Results of structural model 2 for the strain distribution from the first step of the destructive test under a force of 1723 N
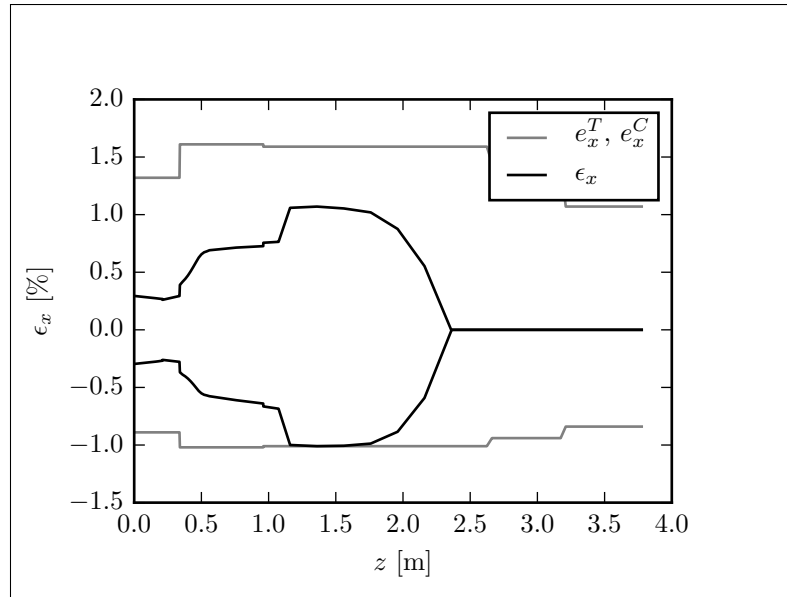
Figure 5.45   Results of structural model 2 for the strain
distribution from the second step of the destructive test
under a force of 11 006 N

terials' stiffnesses were given a value close to zero, except the longitudinal properties of the glass/epoxy unidirectional plies, the transverse shear of the glass/epoxy unidirectional plies and the core material properties. By doing so, the blade behaves as if transverse failures have occurred so that all the load is carried by the fibres. To avoid numerical problems associated with zero stiffness deformation modes, the transverse shear properties of the glass/epoxy unidirectional plies and the core properties were also kept unchanged. All the material strengths were set to really high values excepted the tensile and compressive longitudinal strength of the glass/epoxy unidirectional plies to force the software to compute failure indices associated with these failure modes. The Tsai-Wu failure index F_{TW} is used. This index is the inverse of the safety factor. Note that, in this case, Tsai-Wu and maximum stress failure criterion give the same results. This gives a conservative estimation of the last ply failure strength by using a linear model.

When performing this analysis with structural model 3, the obtained composite failure indices for both steps of the destructive test are as presented in Figures 5.46 and 5.47. For

the first step of the test, a failure is predicted at $z = 3211$ mm under a force of 1452 N. Another possible failure point is located at $z = 2662$ mm and the failure occurs at a 1942 N load level. For the second step of the destructive test, a failure is predicted under a force of 11 270 N at 1360 mm from the blade root. For both steps of the test, the failure occurs in compression on the upper side's spar cap. As an example, Figure 5.48 shows the distribution of the composite failure index in the cross section located at $z = 1360$ mm for the second step of the destructive test under a unit load. The failure results from model 3 are presented in Table 5.13.
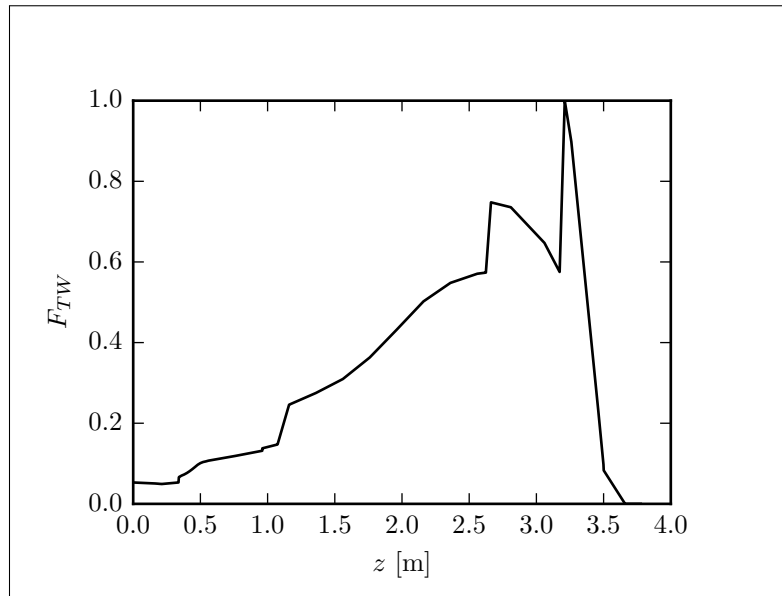

Figure 5.46   Results of structural model 3 for the composite failure index from the first step of the destructive test under a force of 1452 N
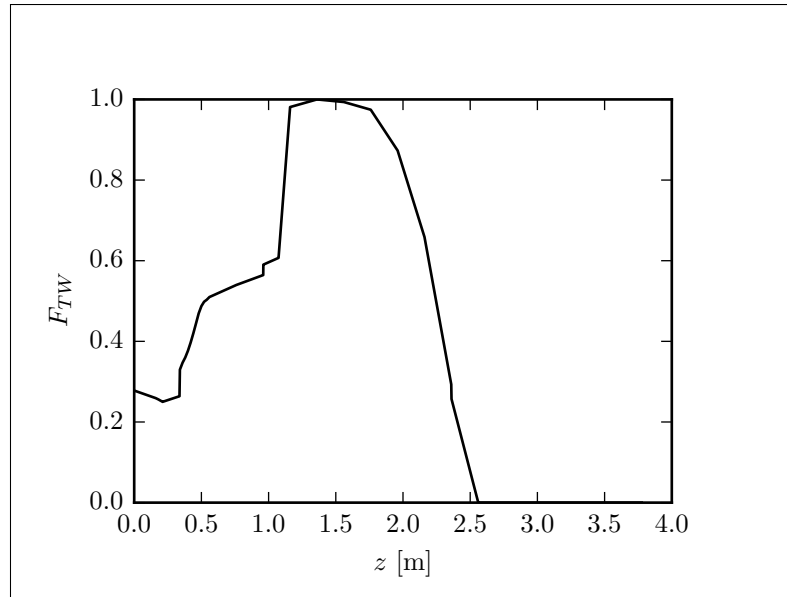
Figure 5.47   Results of structural model 3 for the composite failure index from the second step of the destructive test under a force of 11 270 N
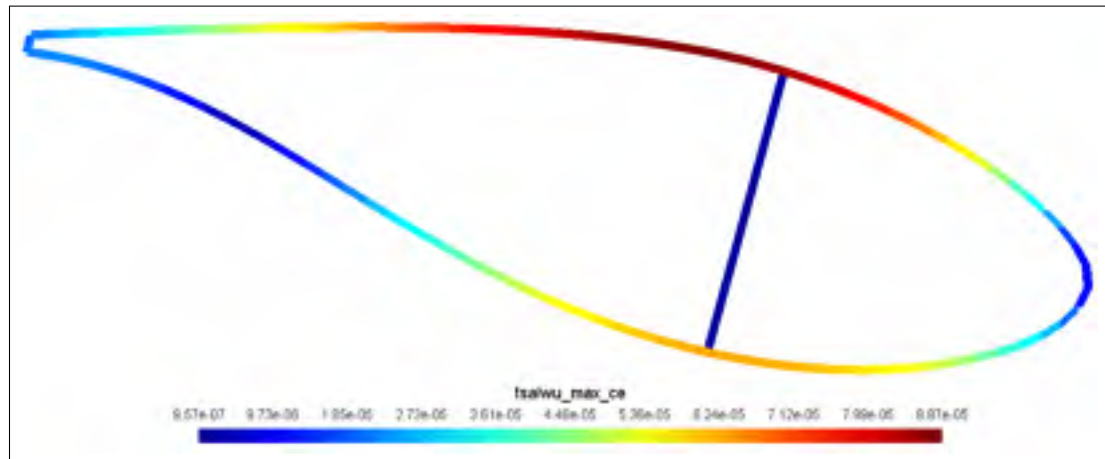

Figure 5.48   Distribution of the composite failure index from model 3 (maximum value among each layer) in the cross section located at $z = 1360$ mm for the second step of the destructive test under a unit load. The inverse of the maximum failure index gives the failure load: $1/8.87 \times 10^{-5} = 11\ 270$

The failure results from model 4 are summarized in Figure 5.49, showing the composite failure index distribution for unit loads. For both steps, a compressive failure is predicted on the upper side of the blade. Two points are identified for both steps, they correspond to

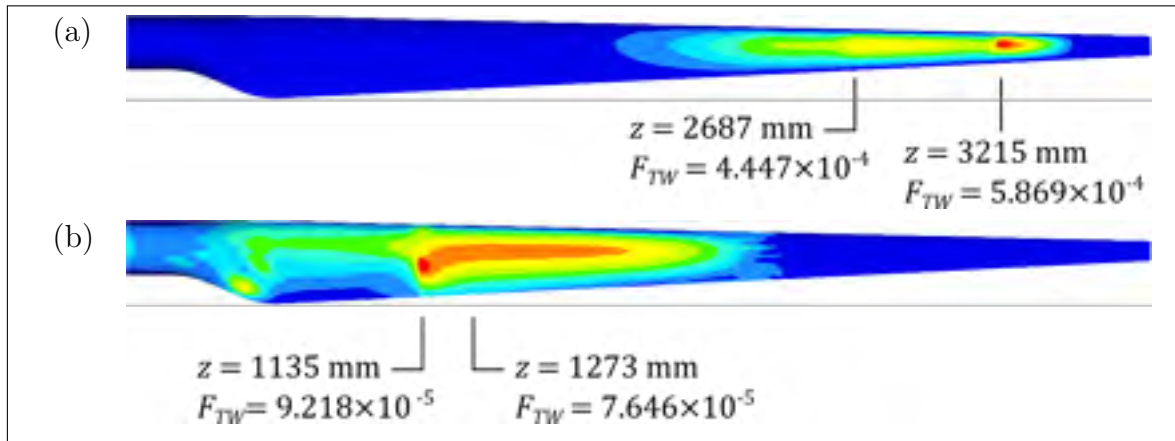the two highest values of the failure index. The failure results of model 4 are summarized in Table 5.13

Figure 5.49   Failure indices from model 4 (maximum value among each layer) under unit loads. The failure load can be computed as the inverse of the failure index. (a) step 1, (b) step 2

When comparing the results of Table 5.13, we can see that the failure locations are relatively well predicted by all models. Sometimes, the first failure predicted is not exactly at the real failure point, but a second point of high failure index is located close to the real failure point. The predicted failure loads are conservative or really close to the observed values. As expected, the results from model 1 are the most conservative, but give really good insight on the failure behaviour despite the model simplicity. As also expected, model 4 is the most precise.

Table 5.13   Comparison of blade strength results

Model	Step 1		Step 2	
	Failure load [N]	Failure location, z [mm]	Failure load [N]	Failure location, z [mm]
Experimental	2110–2650	2690–2760	10 530	1210
Model 1	1288, 1705	3211, 2662	9661	1361
Model 2	1723, 1925	3211, 2662	11 010	1360
Model 3	1452, 1942	3211, 2662	11 270	1360
Model 4	1704, 2249	3215, 2687	10 850, 13 080	1135, 1273

5.8   Conclusion

In conclusion, for this section, a summary of the capabilities of each model is presented. The simple model (model 1), despite its simplicity, gives pretty good results for cross-sectional properties (the one it allows computing), the strain distribution and the blade failure. In addition to that, it returns conservative results. However, this model does not allow the evaluation of the blade's natural frequencies, deflection (a really conservative evaluation of the deflection of the untwisted blade could be performed, but was not done here) and buckling. This model is really well suited for preliminary design based on blade strength.

The classical strength of materials model (model 2) gives good results for cross-sectional properties, natural frequencies, deflection, strain and composite failure. Buckling has to be handled with care as non-conservative results are obtained despite the conservative hypothesis of the model. Also, this model is limited to blades using orthotropic laminates (i.e., no material couplings at the laminate level). Care must also be paid to the region where the shape of the cross section is varying quickly. The stress, strain and failure index are not really accurate in these regions.

The cross-sectional finite element model (model 3) gives the more reliable results for the cross-sectional properties, especially for properties associated with transverse shear. This model is really well suited for beams that use material coupling (bend-twist coupling for

wind turbine blades for instance). It gives good results for natural frequencies, deflections, strains and composite strength, but as the classical strength of materials model, it suffers from a lack of precision in the region where the shape of the cross section is varying quickly. No buckling analysis was implemented within model 3, but it could be possible to implement something similar to model 2, with similar results.

The 3D shell finite element model (model 4) is the more precise and is the only one that can manage the regions of the blade where the cross-sectional shape changes quickly. However, it is less reliable than model 3 for the computation of cross-sectional properties associated with transverse shear. The results of the buckling analysis also have to be used with caution since they are not conservative.

CONCLUSION AND RECOMMENDATIONS

The purpose of this thesis was to address certain issues related to the structural design process of wind turbine blades. This structural design process consists of three iterative steps as summarized in Figure 0.4: (1) aeroelastic analysis of the wind turbine; (2) blade structural dimensioning and validation and (3) computation of blade cross-sectional properties and then; return to step 1. These steps are parts of an iterative process and the starting step depends on the information available to the designer and on the hypothesis made. Each of the three specific objectives of this thesis was on one of the steps of the design process.

The first objective of this thesis was to develop tools to transfer the blade loads obtained from an aeroelastic model of the wind turbine to a 3D shell finite element model of the blade. It was addressed in Chapter 2. This has been done by developing a generic kinematic model of a wind turbine blade. This allows first to get a set of analytical equations to compute the blade loads from the wind turbine operation parameters and the blade mass properties. It also allows the definition of a procedure to apply the gravitational and inertial loads as body loads by defining position and orientation of the blade rotation and acceleration vectors. This method has the advantage to allow defining gravitational and inertial loads for any rotor coning, tilt and azimuth angle.

The second objective of this thesis was to compare blade structural models of different levels of complexity with respect to their efficiency at the different steps of the design process. These different models were presented in chapters 3 and 4 and then compared in Chapter 5. This comparison, based on experimental data obtained on the 10 kW WESNet wind turbine blade, leads to the following conclusion for each of the presented model. The simple model (made of two rectangular strips for the spar caps) gives conservative but surprisingly good results for flapwise cross-sectional properties, strain distribution and

failure loads. The capabilities of this model are limited to these properties. The quality of the results that can be achieved using this model made it well suited for preliminary blade design based on strength criteria.

The classical strength of materials model gives excellent results for cross-sectional properties, natural frequencies, deflection, strain and failure load of orthotropic thin-walled beams. However, results can be erroneous at stress concentrations and at the locations where the blade cross-section shape changes quickly. Also, the results of the proposed buckling analysis give good indications but are unconservative, pointing out the importance of the partial safety factors for linear buckling that are defined in the wind turbine standards. The same conclusion can be drawn about the cross-sectional finite element model (excepted for buckling which was not implemented). However, this model has the capability to analyse thin-walled beams with nonsymmetrical and unbalanced layups. It performs really well to evaluate coupling between the different blade deformation modes including transverse shear effects. These latter two models are well suited for more detailed design and for providing the blade cross-sectional properties needed for the aeroelastic analysis without having to build a 3D shell finite element model, which is much more time consuming.

The 3D shell finite element model performs well for all types of analysis with an exception for the prediction of behaviour associated with transverse shear deformation and torsion (when using offset nodes). As, for most blade designs, these behaviours are not of great importance, the 3D finite element model is the ideal model for the final validation of the blade.

Finally, the third objective (addressed in Chapter 4) was to develop a tool for the cross-sectional analysis of thin-walled composite beams. This was done by proposing a thin-walled implementation of the Nonhomogeneous Anisotropic Beam Section Anal-

ysis (NABSA) method. It uses 3-node line elements having translational and rotational degrees of freedom. This tool has shown to perform well for a variety of validation cases including geometric and material coupling, open sections, multicell sections and offset nodes.

The contributions of this thesis are :

- The development of a set of analytical equations to compute the blade loads as a function of the wind turbine operating parameters and blade mass parameters.

- The development of a method to transfer the loads computed by an aeroelastic model of a wind turbine to a 3D finite element model of a blade.

- The comparison of blade structural models of different levels of complexity against experimental data. This leads to the conclusion that simple models based on the strength of materials theory can be used for preliminary design, early detailed design and for the computation of cross-sectional properties needed for aeroelastic simulations. However, 3D finite element models are still needed for final detailed design and validation of the blade.

- The development of a tool for structural analysis of thin-walled composite beams cross sections of arbitrary layups. This tool is based on a thin-walled implementation of the NABSA method using 3-node line elements.

In conclusion of this thesis, the wind turbine blade design process presented in Figure 6.1 is proposed. The inner circle represents the very first stages of the design process where model 1 can be used to validate the feasibility of an aerodynamic design and get an idea of the mass distribution. A set of loads can be obtained on a standstill blade under the extreme wind model without information about the blade mass or stiffness. Once the

aerodynamic design seems feasible, the process can go to the second circle. If no blade stiffness information is available, an aeroelastic model with rigid blades can be used to get the loads. Model 2 or 3 can be used to get a preliminary structural design and to compute the blade stiffness properties. The process can then enter the outer circle, where model 4 is used for the blade dimensioning and validation and where the aeroelastic model uses flexible blades.
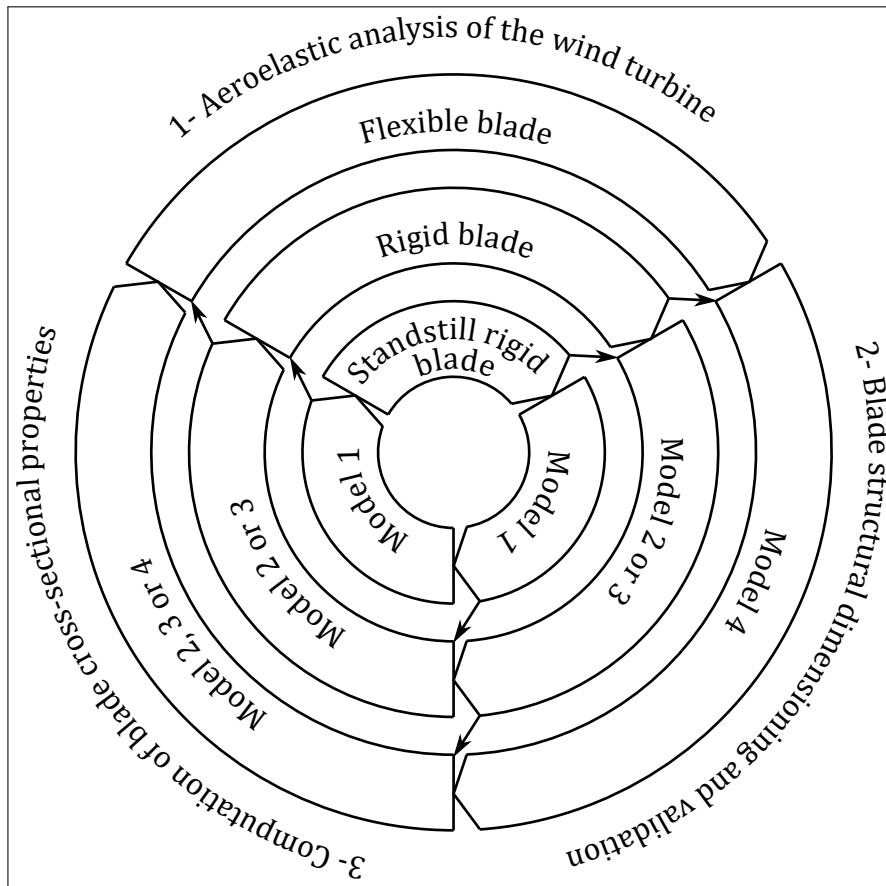

Figure 6.1   Proposed wind turbine blade design process: The inner circle represents the very first stages of the design process that will evolve towards the outer circles as the blade design refines.

APPENDIX I

NASTRAN'S RBE3 ELEMENT

The NASTRAN's RBE3 element is a series of kinematic contraints between the degrees of freedom of a reference node and those of connected nodes. Its utility is to transfer loads applied at the reference node to the connected nodes. However, knowing the kinematic relations implied, it can be used to compute the displacements and rotations of the references nodes when these quantities are known for the connected nodes. This gives the mean displacement and rotation of the connected nodes.

The following description of this element is based on Reese et al. (2011) and Delmas (2012).

In the general case where all the degrees of freedom of nodes (3 translation and 3 rotations per nodes), the kinematic constraints are:

$$\mathbf{R}_{qi} \begin{bmatrix} \mathbf{u}_q \\ \mathbf{u}_i \end{bmatrix} = \mathbf{0} \qquad \text{(A I-1)}$$

In fact, these are MPC (multi point constraint) type kinematic relations, i.e., linear relations between degrees of freedom.

$\mathbf{u}_q$ is a column vector of shape (6×1) containing the degrees of freedom of the reference nodes. $\mathbf{u}_i$ is a column vector of shape $(6c \times 1)$ containing the degrees of freedom of the c connected nodes. The $\mathbf{R}_{qi}$ matrix of shape $(6 \times (6 + 6c))$ contains the kinematic relation coefficients and is computed as:

$$\mathbf{R}_{qi} = \begin{bmatrix} -\mathbf{I}_{qq} & \mathbf{G}_{qi} \end{bmatrix} \qquad \text{(A I-2)}$$

where $\mathbf{I}_{qq}$ is a 6×6 unit matrix. If the displacements of the connected nodes are known, the displacements of the reference node can be computed as

$$\mathbf{u}_q = \mathbf{G}_{qi}\mathbf{u}_i \tag{A I-3}$$

with

$$\mathbf{G}_{qi} = \mathbf{T}_i\mathbf{A}^{-1}\mathbf{S}^T\mathbf{W} \tag{A I-4}$$

where $\mathbf{T}_i$ is a 6×6 identity matrix excepted for the case, not discussed here, where the coordinate systems used to express the displacements of reference and connected nodes are not the same. The $\mathbf{A}$ matrix is

$$\mathbf{A} = \mathbf{S}^T\mathbf{W}\mathbf{S} \tag{A I-5}$$

where $\mathbf{W}$ is a $6c \times 6c$ matrix formed by the assembly of $\mathbf{W}_i$ matrices on its diagonal:

$$\mathbf{W} = \begin{bmatrix} \mathbf{W}_1 & \mathbf{0} & \mathbf{0} & \dots & \mathbf{0} & \mathbf{0} \\ \mathbf{0} & \mathbf{W}_2 & \mathbf{0} & \dots & \mathbf{0} & \mathbf{0} \\ \vdots & \vdots & \ddots & \dots & \vdots & \vdots \\ \mathbf{0} & \mathbf{0} & \mathbf{0} & \mathbf{W}_i & \mathbf{0} & \mathbf{0} \\ \vdots & \vdots & \vdots & \dots & \ddots & \vdots \\ \mathbf{0} & \mathbf{0} & \mathbf{0} & \dots & \mathbf{0} & \mathbf{W}_c \end{bmatrix} \tag{A I-6}$$

The $\mathbf{W}_i$ matrices, of shape 6×6 are associated with each connected nodes:

$$\mathbf{W}_i = \begin{bmatrix} w_1 & 0 & 0 & 0 & 0 & 0 \\ 0 & w_2 & 0 & 0 & 0 & 0 \\ 0 & 0 & w_3 & 0 & 0 & 0 \\ 0 & 0 & 0 & w_4L_c^2 & 0 & 0 \\ 0 & 0 & 0 & 0 & w_5L_c^2 & 0 \\ 0 & 0 & 0 & 0 & 0 & w_6L_c^2 \end{bmatrix} \tag{A I-7}$$

where w_i are weight associated with each degree of freedom. Generally, $w_i = 1$ is used. The **S** matrix, of shape $6c \times 6$ is formed as:

$$\mathbf{S} = \begin{bmatrix} \mathbf{S}_1 & \mathbf{S}_2 & \dots & \mathbf{S}_i & \dots & \mathbf{S}_c \end{bmatrix}^T \qquad \text{(A I-8)}$$

where the $\mathbf{S}_i$ matrices, associated with each reference nodes, are

$$\mathbf{S}_i = \begin{bmatrix} 1 & 0 & 0 & 0 & L_{i,z} & -L_{i,y} \\ 0 & 1 & 0 & -L_{i,z} & 0 & L_{i,x} \\ 0 & 0 & 1 & L_{i,y} & -L_{i,x} & 0 \\ 0 & 0 & 0 & 1 & 0 & 0 \\ 0 & 0 & 0 & 0 & 1 & 0 \\ 0 & 0 & 0 & 0 & 0 & 1 \end{bmatrix} \qquad \text{(A I-9)}$$

Finally, for a given connected node i,

$$L_{i,x} = x_i - x_q$$
$$L_{i,y} = y_i - y_q \qquad \text{(A I-10)}$$
$$L_{i,z} = z_i - z_q$$

where x_i, y_i and z_i are the coordinates of the ith connected node and x_q, y_q and z_q are the coordinates of the reference node. The characteristic length used for the calculation of the $\mathbf{W}_i$ matrices is

$$L_c = \sum_{i=1}^{c} \frac{|L_i|}{c} \qquad \text{(A I-11)}$$

where

$$L_i = \sqrt{L_{i,x}^2 + L_{i,y}^2 + L_{i,z}^2} \qquad \text{(A I-12)}$$

To remove degrees of freedom to the connected nodes, corresponding lines in $\mathbf{S}_i$ and corresponding lines and columns in $\mathbf{W}_i$ have to be removed. For instance, in this work, the rotation degrees of freedom of the connected nodes are not used for the computation

of the displacement of the reference node. So, lines 4 to 6 of $\mathbf{S}_i$ and lines and columns 4 to 6 of $\mathbf{W}_i$ are removed. To remove degrees of freedom to the reference node, corresponding lines in $\mathbf{G}_{qi}$ have to be removed. For instance, if the translational degrees of freedom are the only one to be computed for the reference node (this is not the case in this work), lines 4 to 6 of $\mathbf{G}_{qi}$ have to be removed.

BIBLIOGRAPHY

Ahmad, S., Irons, B. M., and Zienkiewicz, O. C. (1970). Analysis of thick and thin shell structures by curved finite elements. *International Journal for Numerical Methods in Engineering*, 2:419–451.

Altair Engineering (2008). *Optistruct User Manual.* Altair Engineering, Troy (Michigan, United States).

Barbero, E. J. (1999). *Introduction to Composite Materials Design.* Taylor & Francis, New York (New York, United States).

Bathe, K. J. (2006). *Finite Element Procedures.* K. J. Bathe, Cambridge (Massachusetts, United States).

Batoz, J.-L. and Dhatt, G. (1992). *Modélisation des structures par éléments finis, volume 3: coques.* Les Presses de L'Université Laval, Sainte-Foy (Québec, Canada).

Bazergui, A., Bui-Quoc, T., Biron, A., McIntyre, G., and Laberge, C. (2002). *Résistance des matériaux.* Presses internationales Polytechnique, Montréal (Québec, Canada), 3rd edition.

Bazilevs, Y., Hsu, M.-C., Akkerman, I., Wright, S., Takizawa, K., Henicke, B., Spielman, T., and Tezduyar, T. E. (2011a). 3D simulation of wind turbine rotors at full scale. Part I: Geometry modeling and aerodynamics. *International Journal for Numerical Methods in Fluids*, 65(1-3):207–235.

Bazilevs, Y., Hsu, M.-C., Kiendl, J., Wüchner, R., and Bletzinger, K.-U. (2011b). 3D simulation of wind turbine rotors at full scale. Part II: Fluid–structure interaction modeling with composite blades. *International Journal for Numerical Methods in Fluids*, 65(1-3):236–253.

Berggreen, C., Branner, K., Jensen, J. F., and Schultz, J. P. (2007). Application and analysis of sandwich elements in the primary structure of large wind turbine blades. *Journal of Sandwich Structures and Materials*, 9:525–551.

Berry, D. S. (2008). Blade system design studies phase II: Final project report. Technical Report SAND2008-4648, Sandia National Laboratories, Albuquerque (New Mexico, United States).

Berthelot, J.-M. (2012). *Matériaux composites: Comportement mécanique et analyse des structures.* Lavoisier, Paris (France), 5th edition.

Bir, G. (2006). User's guide to PreComp (pre-processor for computing composite blade properties). Technical Report NREL/TP-500-38929, National Renewable Energy Laboratory, Golden (Colorado, United States).

Blasques, J. P. (2011). *Optimal Design of Laminated Composite Beams*. PhD thesis, Technical University of Denmark, Lyngby (Denmark).

Blasques, J. P. (2012). User's Manual for BECAS : A cross section analysis tool for anisotropic and inhomogeneous beam sections of arbitrary geometry. Technical Report Risø-R-1785(EN), Risø DTU – National Laboratory for Sustainable Energy, Roskilde (Denmark).

Blasques, J. P., Bitsche, R. D., Fedorov, V., and Lazarov, B. S. (2016). Accuracy of an efficient framework for structural analysis of wind turbine blades. *Wind Energy*, 19:1603–1621.

Blasques, J. P. and Stolpe, M. (2012). Multi-material topology optimization of laminated composite beam cross sections. *Composite Structures*, 94(11):3278–3289.

Bossanyi, E. A. (2003). GH Bladed Theory Manual. Technical Report 282/BR/009 issue 11, Garrad Hassan and Partners Limited, Bristol (United Kingdom).

Branner, K., Berring, P., Berggreen, C., and Knudsen, H. W. (2007). Torsional performance of wind turbine blades – part II: Numerical validation. In *16th International Conference on Composite Materials*, Kyoto (Japan), 8–13 July.

Caous, D., Lavauzelle, N., Valette, J., and Wahl, J.-C. (2018). Load application method for shell finite element model of wind turbine blade. *Wind Engineering*, 42(5):467–482.

Cardoso, J. B., Benedito, N. M., and Valido, A. J. (2009). Finite element analysis of thin-walled composite laminated beams with geometrically nonlinear behavior including warping deformation. *Thin-Walled Structures*, 47:1363–1372.

Cesnik, C. E. S. and Hodges, D. H. (1997). VABS: A new concept for composite rotor blade cross-sectional modeling. *Journal of the American Helicopter Society*, 42(1):27–38.

Chen, H., Yu, W., and Capellaro, M. (2010). A critical assessment of computer tools for calculating composite wind turbine blade properties. *Wind Energy*, 13(6):497–516.

Cook, R. D., Malkus, D. S., Plesha, M. E., and Witt, R. J. (2002). *Concepts and Applications of Finite Element Analysis*. John Wiley & Sons, Hoboken (New Jersey, United States), 4th edition.

Cormier, L., Joncas, S., and Nijssen, R. P. (2016). Effects of low temperature on the mechanical properties of glass fibre-epoxy composites: Static tension, compression, $R = 0.1$ and $R = 1$ fatigue of $\pm45°$ laminates. *Wind Energy*, 19:1023–1041.

Couturier, P. J., Krenk, S., and Høgsberg, J. (2015). Beam section stiffness properties using a single layer of 3D solid elements. *Computers and Structures*, 156:122–133.

Cowper, G. R. (1966). The shear coefficient in Timoshenko's beam theory. *Journal of Applied Mechanics*, June:335–340.

Cárdenas, D., Escárpita, A. A., Elizalde, H., Aguirre, J. J., Ahuett, H., Marzocca, P., and Probst, O. (2012). Numerical validation of a finite element thin-walled beam model of a composite wind turbine blade. *Wind Energy*, 15(2):203–223.

Delmas, J. (2012). Relations cinématiques linéaires de type RBE3. Technical Report R3.03.08, Code_Aster, Électricité de France, Paris (France).

Dhatt, G., Touzot, G., and Lefrançois, E. (2005). *Méthode des éléments finis*. Lavoisier, Paris (France).

DNV GL (2015). Rotor blades for wind turbines. Standard DNVGL-ST-0376 Edition December 2015, DNV GL, Høvik (Norway).

Fedorov, V. and Berggreen, C. (2014). Bend-twist coupling potential of wind turbine blades. In *The Science of Making Torque from Wind 2014*, Lyngby (Denmark), 17–20 June.

Ferede, E. A. and Abdalla, M. M. (2014). Cross-sectional modelling of thin-walled composite beams. In *55th AIAA/ASME/ASCE/AHS/ASC Structures, Structural Dynamics, and Materials Conference*, National Harbor (Maryland, United States), 13–17 January.

Fernandes da Silva, G., Marín, J. C., and Barroso, A. (2011). Evaluation of shear flow in composite wind turbine blades. *Composite Structures*, 93:1832–1841.

Forcier, L.-C. (2010). Conception d'une pale d'éolienne de grande envergure à l'aide de techniques d'optimisation structurale. Master's thesis, École de technologie supérieure, Montréal (Québec, Canada).

Forcier, L.-C. and Joncas, S. (2012). Development of a structural optimization strategy for the design of next generation large thermoplastic wind turbine blades. *Structural and Multdisciplinary Optimization*, 45(6):889–906.

Forcier, L.-C. and Joncas, S. (2019). On the wind turbine blade loads from an aeroelastic simulation and their transfer to a three-dimensional finite element model of the blade. *Wind Engineering*, In press.

Forcier, L.-C., Sumner, J., Gagnon, T., Charron, J.-F., and Joncas, S. (2013). Structural design and validation of a 10 kW wind turbine blade. In *19th International Conference on Composite Materials*, Montréal (Québec, Canada), 28 July – 2 August.

Germanischer Lloyd (2010). Guideline for the certification of wind turbines. Guideline Edition 2010, Germanischer Lloyd, Hamburg (Germany).

Geuzaine, C. and Remacle, J.-F. (2009). Gmsh: A 3-D finite element mesh generator with built-in pre- and post-processing facilities. *International Journal for Numerical Methods in Engineering*, 79:1309–1331.

Giavotto, V., Borri, M., Mantegazza, P., and Ghiringhelli, G. (1983). Anisotropic beam theory and applications. *Computers & Structures*, 16(1–4):403–413.

Gibson, R. F. (2007). *Principles of composite material mechanics.* CRC Press, Boca Raton (Florida, United States), 2nd edition.

Giguère, P. and Selig, M. S. (2000). Blade geometry optimization for the design of wind turbine rotor. In *2000 ASME Wind Energy Symposium*, Reno (Nevada, United States), 10–13 January.

Griffin, D. A. (2001). WindPACT turbine design scaling studies technical area 1 – Composite blades for 80- to 120-meter rotor. Technical Report NREL/SR-500-29492, National Renewable Energy Laboratory, Golden (Colorado, United States).

Griffith, D. T. and Ashwill, T. D. (2011). The Sandia 100-meter all-glass baseline wind turbine blade: SNL100-00. Technical Report SAND2011-3779, Sandia National Laboratories, Albuquerque (New Mexico, United States).

Gúnay, M. G. and Timarci, T. (2017). Static analysis of thin-walled laminated composite closed-section beams with variable stiffness. *Composite Structures*, 182:67–78.

Gupta, M. and Hodges, D. H. (2017). Modeling of thin-walled beams using VAM. In *58th AIAA/ASCE/AHS/ASC Structures, Structural Dynamics, and Materials Conference*, Grapevine (Texas, United States), 9–13 January.

Hansen, M. O. L. (2008). *Aerodynamics of Wind Turbines.* Earthscan, London (United Kingdom), 2nd edition.

Hillmer, B., Borstelmann, T., Schaffarczyk, P., and Dannenberg, L. (2007). Aerodynamic and structural design of multiMW wind turbine blades beyond 5 MW. In *The Science of Making Torque from Wind*, Lyngby (Denmark), 28–31 August.

Hodges, D. H. and Yu, W. (2007). A rigorous, engineer-friendly approach for modelling realistic, composite rotor blades. *Wind Energy*, 10:179–193.

International Electrotechnical Commission (2005). Wind turbines – Part 2 : Design requirements for small wind turbines. Standard IEC 61400-2 Edition 2, International Electrotechnical Commission, Geneva (Switzerland).

Jackson, K., Zuteck, M., van Dam, C., Standish, K. J., and Berry, D. (2005). Innovative design approaches for large wind turbine blades. *Wind Energy*, 8:141–171.

Jensen, F. M. (2008). *Ultimate Strength of a Large Wind Turbine Blade.* PhD thesis, Risø National Laboratory for Sustainable Energy and Technical University of Denmark, Roskilde and Lyngby (Denmark).

Jonkman, J. M. (2003). Modeling of the UAE Wind Turbine for Refinement of FAST_-AD. Technical Report NREL/TP-500-34755, National Renewable Energy Laboratory, Golden (Colorado, United States).

Jonkman, J. M. and Buhl Jr., M. L. (2005). FAST User's Guide. Technical Report NREL/EL-500-38230, National Renewable Energy Laboratory, Golden (Colorado, United States).

Knill, T. J. (2005). The application of aeroelastic analysis output load distributions to finite element models of wind. *Wind Engineering*, 29(2):153–168.

Knowledge Centre WMC (2012). FOCUS6: The integrated wind turbine design suite. Knowledge Centre WMC, Wieringerwerf (The Netherlands). http://www.wmc.eu /WMC_FOCUS6_folder2012.pdf (accessed March 13, 2013).

Kollár, L. and Pluszik, A. (2002). Analysis of thin-walled composite beams with arbitrary layup. *Journal of Reinforced Plastics and Composites*, 21(16):1423–1465.

Kollár, L. P. and Springer, G. S. (2003). *Mechanics of Composite Structures.* Cambridge University Press, Cambridge (United Kingdom).

Laird, D. L., Montoya, F. C., and Malcolm, D. J. (2005). Finite element modeling of wind turbine blades. In *2005 ASME Wind Energy Symposium / 43rd AIAA Aerospace Sciences Meeting and Exhibit*, Reno (Nevada, United States), 10–13 January.

Larsen, T. J. and Hansen, A. M. (2007). How 2 HAWC2, the user's manual. Technical Report Risø-R-1597(ver. 3-1)(EN), Risø National Laboratory, Roskilde (Denmark).

Librescu, L. and Song, O. (2006). *Thin-Walled Composite Beams. Theory and Application.* Springer, Dordrecht (The Netherlands).

Lillo, P. (2011). Static and fatigue analysis of wind turbine blades subject to cold weather conditions using finite element analysis. Master's thesis, University of Victoria, Victoria (British Columbia, Canada).

Lindenburg, C. (2005). PHATAS release "NOV-2003" and "APR-2005" user's manual. Technical Report ECN-I--05-005, Energy Research Center of The Netherlands, Petten (The Netherlands).

Lindenburg, C. and de Winkel, G. D. (2005a). Buckling load prediction tools for rotor blades. mode description of tools for buckling of thin-walled beams. Technical Report ECN-C--05-103, Energy Research Center of The Netherlands, Petten (The Netherlands).

Lindenburg, C. and de Winkel, G. D. (2005b). State of the art of rotor blade buckling tools: Inventory of the Dutch BLADKNIK project. Technical Report ECN-C--05-054, Energy Research Center of The Netherlands, Petten (The Netherlands).

Lobitz, D. W. and Veers, P. S. (1998). Aeroelastic behavior of twist-coupled HAWT blades. In *1998 ASME Wind Energy Symposium*, Reno (Nevada, United States), 12–15 January.

Malcolm, D. J. and Laird, D. L. (2007). Extraction of equivalent beam properties from blade models. *Wind Energy*, 10:135–157.

Massa, J. C. and Barbero, E. J. (1998). A strength of materials formulation for thin walled composite beams with torsion. *Journal of Composite Materials*, 32(17):1560–1594.

Mikkelsen, L. P. (2016). A simplified model predicting the weight of the load carrying beam in a wind turbine blade. In *37th Risø International Symposium on Materials Science*, Roskilde (Denmark), 5–8 September.

Nijssen, R. (2006). OptiDAT database reference document. Technical Report OB_TC_-R018 rev. 005, Optimat Blades, Wieringerwerf (The Netherlands).

Ning, S. (2013). Airfoilprep.py documentation. Technical Report NREL/TP-5000-58817, National Renewable Energy Laboratory, Golden (Colorado, United States).

Paquette, J. A. and Veers, P. S. (2008). Increased strength in wind turbine blades through innovative structural design. In *AWEA Windpower 2008*, Houston (Texas, United States), 1–4 June.

Pluszik, A. and Kollár, L. (2002). Effects of shear deformation and restrained warping on the displacements of composite beams. *Journal of Reinforced Plastics and Composites*, 21(17):1517–1541.

Reese, G. M., Walsh, T. F., and Bhardwaj, M. K. (2011). Salinas – Theory manual version 4.22. Technical Report SAND2011-8272, Sandia National Laboratories, Albuquerque (New Mexico, United States) and Livermore (California, United States).

Rivello, R. M. (1969). *Theory and Analysis of Flight Structures*. McGraw-Hill, New York (New York, United States).

Saravanos, D., Varelis, D., Plagianakos, T., and Chrysochoidis, N. (2006). A shear beam finite element for the damping analysis of tubular laminated composite beams. *Journal of Sound and Vibration*, 291:802–823.

Saravia, C. M. (2014). A large deformation–small strain formulation for the mechanics of geometrically exact thin-walled composite beams. *Thin-Walled Structures*, 84:443–451.

Saravia, M. C., Machado, S. P., and Cortínez, V. H. (2012). A consistent total Lagrangian finite element for composite closed section thin walled beams. *Thin-Walled Structures*, 52:102–116.

Sheikh, A. H. and Thomsen, O. T. (2008). An efficient beam element for the analysis of laminated composite beams of thin-walled open and closed cross sections. *Composites Science and Technology*, 68:2273–2281.

Sørensen, B. F., Jørgensen, E., Debel, C. P., Jensen, F. M., Jensen, H. M., Jacobsen, T. K., and Halling, K. M. (2004). Improved design of large wind turbine blade of fiber composites based on studies of scale effects (phase 1) – Summary report. Technical Report Risø-R-1390(EN), Risø National Laboratory, Roskilde (Denmark).

Tarfaoui, M., Khadimallah, H., Imad, A., and Pradillon, J. Y. (2012). Design and finite element modal analysis of 48m composite wind turbine blade. *Applied Mechanics and Materials*, 146:170–184.

Timmer, W. and van Rooij, R. (2003). Summary of the Delft University wind turbine dedicated airfoils. *Journal of Solar Energy Engineering*, 125:488–496.

Victorazzo, D. S. and De Jesus, A. (2016). A Kollár and Pluzsik anisotropic composite beam theory for arbitrary multicelled cross sections. *Journal of Reinforced Plastics and Composites*, 35(23):1696–1711.

Volovoi, V. V. and Hodges, D. H. (2000). Theory of anisotropic thin-walled beams. *Journal of Applied Mechanics*, 67:453–459.

Volovoi, V. V. and Hodges, D. H. (2002). Single- and multicelled composite thin-walled beams. *AIAA Journal*, 40(5):960–965.

Wang, L., Liu, X., Guo, L., Renevier, N., and Stables, M. (2014). A mathematical model for calculating cross-sectional properties of modern wind turbine composite blades. *Renewable Energy*, 64:52–60.

Wang, Q., Sprague, M. A., Jonkman, J., Johnson, N., and Jonkman, B. (2017). Beamdyn: A high-fidelity wind turbine blade solver in the fast modular framework. *Wind Energy*, 20:1439–1462.

Wang, S. and Zhang, C. (2014). Structure mechanical modeling of thin-walled closed-section composite beams, part 2: Multi-cell cross section. *Composite Structures*, 113:56–62.

Wilson, R. E., Walker, S. N., and Heh, P. (1999). Technical and User's manual for the FAST_AD Advanced Dynamics Code. Technical Report OSU/NREL report 99-01, Oregon State University and National Renewable Energy Laboratory, Corvallis (Oregon, United States) and Golden (Colorado, United States).

Yu, W., Hodges, D. H., and Ho, J. C. (2012). Variational asymptotic beam sectional analysis – An updated version. *International Journal of Engineering Science*, 59:40–64.

Yu, W., Hodges, D. H., Volovoi, V., and Cesnik, C. E. (2002a). On Timoshenko-like modeling of initially curved and twisted composite beams. *International Journal of Solids and Structures*, 39(19):5101–5121.

Yu, W., Hodges, D. H., Volovoi, V., and Cesnik, C. E. S. (2002b). On Timoshenko-like modeling of initially curved and twisted composite beams. *International Journal of Solids and Structures*, 39:5101–5121.

Yu, W., Hodges, D. H., Volovoi, V. V., and Fuchs, E. D. (2005). A generalized Vlasov theory for composite beams. *Thin-Walled Structures*, 43:1493–1511.

Yu, W., Volovoi, V. V., Hodges, D. H., and Hong, X. (2002c). Validation of the variational asymptotic beam sectional analysis. *AIAA Journal*, 40(10):2105–2112.

Zhang, C. and Wang, S. (2014). Structure mechanical modeling of thin-walled closed-section composite beams, part 1: Single-cell cross section. *Composite Structures*, 113:12–22.

Zhang, H., Maheri, A., Daadbin, A., and Hackney, P. (2012). An analytical model for deformation analysis of wind turbine adaptive blades. *WIT Transactions on The Built Environment*, 124:13–25.